Fabrication of Zinc Oxide Based Nanostructures for Light Emission and Gas Sensing Applications

Thesis submitted to

UNIVERSITY OF CALICUT

for the award of the degree of

DOCTOR OF PHILOSOPHY IN PHYSICS

by

SHAHEERA.M

Under the guidance of

Dr. V. Geetha

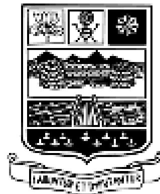

RESEARCH DEPARTMENT OF PHYSICS

GOVERNMENT VICTORIA COLLEGE

PALAKKAD KERALA -678001

INDIA

JANUARY 2020

Fabrication of Zinc Oxide Based Nanostructures for Light Emission and Gas Sensing Applications

Thesis submitted to

University of Calicut in partial fulfillment of the
requirements for the award of the degree of

Doctor of Philosophy
in Physics under the Faculty of Science
by

SHAHEERA.M

Under the guidance of

Dr. V. Geetha
Research Guide
Govt. Victoria College
Palakkad

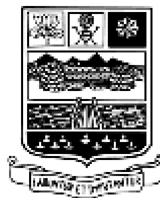

RESEARCH DEPARTMENT OF PHYSICS
GOVERNMENT VICTORIA COLLEGE
PALAKKAD KERALA -678001
INDIA

JANUARY 2020

CERTIFICATE

This is to certify that the thesis entitled “Fabrication of Zinc Oxide Based Nanostructures for Light Emission and Gas Sensing Applications” which is being submitted herewith for the award of the degree of doctor of Philosophy in Physics of University Calicut is a bonafide record of the original research work completed by Mrs. Shaheera.M under my supervision and guidance and to the best of my knowledge and belief the work embodied in this thesis has not formed earlier the basis for the award of any Degree or similar title of this or any other University or examining body.

Dr. V. Geetha
(Research guide, Department of Physics,
Govt. Victoria College, Palakkad)
Principal
Govt. Arts and Science College,
Palakkad

Dr. Pradeesh.K
Research Co-Guide
Associate Professor
Department of Physics,
Govt. Victoria College,
Palakkad

Place: Palakkad
Date: 24/01/2020

CERTIFICATE

Certified that the thesis titled "Fabrication of Zinc Oxide Based Nanostructures for Light Emission and Gas Sensing Applications" submitted by Mrs. Shaheera. M have incorporated the suggestions/ corrections from the adjudicators.

Dr. V. Geetha
Research guide,
Department of Physics,
Govt. Victoria College,
Palakkad

DECLARATION

I hereby declare that the dissertation entitled **"Fabrication of Zinc Oxide Based Nanostructures for Light Emission and Gas Sensing Applications"** submitted for the Degree of Doctor of Philosophy is the original work carried out by me under the guidance and supervision of Dr. V. Geetha (Guide) and Dr. Pradeesh. K (co- Guide) and the dissertation have not formed the basis for the award of any degree, diploma, associateship, fellowship of similar titles. It has not been submitted to any other institution for the award of any degree or diploma.

Place: Palakkad   Signature of scholar

Date:

ACKNOWLEDGEMENTS

A journey is easier when you travel together. Many people have been involved in helping me to complete this dissertation. My gratitude is beyond words. It is really a pleasant task to express my thanks to all those who contributed in various ways to the success of my PhD study and made it a memorable experience for me.

At first I express my gratefulness to the Almighty Allah-Rabbul Alamin, who has given me the strength and energy to fulfill this research work.

I would like to express my overwhelming gratitude to my research guide, ***Dr. V. Geetha****, for her expertise shown in guiding my work and the willingness to share his knowledge and experience. She has given immense freedom for developing ideas and she is always willing to listen patiently and acknowledge sincere efforts. Her profound practical skills, immense knowledge and critical but valuable remarks led me to do a good research.*

It is a great pleasure for me to express my profound sense of gratitude, indebtedness and deep appreciation to my Co- Guide ***Dr. Pradeesh. K*** *From his constant guidance, inspiring collaboration, vast knowledge and experience, I have benefited very much.*

I am thankful to Mr. ***O.K. Ramesan*** *and all the former principals of Govt. Victoria College for their immense support and for providing me with the necessary facilities to carry out my research. I would like to thank all the teaching and non-teaching staff of Department of Physics and office staff for their support during the research. I extend my special thanks to* ***Mrs. Ambily Krishnan****, Assistant Professor and fellow researcher of the same department for her help, motivation, love and care during my work*

I would like to express my sincere thanks and heartfelt gratitude to ***Dr. S. C. Gadkari****, former Head, Technical Physics Division (TPD), Bhabha Atomic Research Centre (BARC) for giving me permission to do part of research work at Thin film device section (TFDS), TPD, BARC.I am very thankful to* ***Dr. K.P. Muthe*** *Head, TFDS for his constant encouragement and motivation during the work.*

I am greatly indebted to ***Dr. Manmeet Kaur, Scientific Officer (F)*** *TFDS, BARC, who taught me a lot about sensors and guided me tirelessly during the work at BARC. The blessing, help and*

motherhood guidance given by her time to time shall carry me a long way in the journey of life on which I am about to embark.

*I am most grateful to **Dr. K. G. Girija** Scientific Officer (G) Chemistry Division, BARC her constant supervision, inspiring guidance, sagacious advice, active help, enthusiastic encouragement, co-operation, fruitful suggestions and encouragements throughout the course of my research work.*

*I would like to thank **Dr. R. K. Vatsa, Scientific Officer (G) Chemistry Division, BARC** who has supported and given me permission to carry out film deposition in Chemistry Division. I would like to thank **Dr. A. K. Debnath**, Scientific Officer (G), TFDS, BARC who helped me for XPS analysis. I am grateful to **Dr. J. B. Singh**, (Head), **Malavika Kari** and **Manoj Kumar thota** (Scientific Assistants) Metallurgy Department, BARC, for their help in XRD and FESEM analysis.*

*I am content to extended gratitude to my lab mates **Lisha. C. L**, **Resmi. K. R** and **O. K. Nimisha** for extending help during my work. I am also grateful to all my friends right from my school days and college days.*

I am indebted to my parents, In Laws, brother and sisters for their love, encouragement and support, for the fulfillment of my dream. I humbly remember hardship of my husband and daughter and thank them for their love and support which helped me to ease the toughest moments in this research journey.

Shaheera. M

Contents

Preface **i**

List of Figures **iii**

List of Tables **x**

List of Publications **xi**

List of papers presented in conferences **xii**

Chapter 1 **1-42**

Introduction: Brief historical review of research and basic characteristics of ZnO

1.1. Introduction 2

1.2. Zinc oxide -a multifunctional semiconductor 3

1.2.1. Properties of ZnO

1.2.1.1. Physical properties 4

1.2.1.2. Electrical properties 4

1.2.1.3. Magnetic properties 5

1.2.1.4. Optical properties 5

1.2.1.5. Piezoelectric properties 5

1.2.2. Crystal structure 6

1.2.3. Doping in ZnO

1.2.3.1. Donor impurities 9

1.2.3.2. Acceptor impurities 13

1.2.4. Defects in ZnO 19

1.3. Applications of ZnO

1.3.1. ZnO as Light Emitting Diode 25

1.3.2. ZnO as Transparent conducting Oxide (TCO) 30

1.3.3. Transparent thin film transistors (TTFT) 30

1.3.4. ZnO as Gas sensors 32

1.3.5. Photodetector 34

1.3.6. Solar cells 35

1.3.7. Photocatalysis 37

1.4. Motivation and Objectives 41

1.5. Conclusion 42

Chapter 2 **43-85**

Experimental and Characterization techniques

2.1. Film deposition and fabrication

2.1.1. Introduction 44

2.1.2. Sputtering 47

2.1.2.1. DC/RF sputtering 47

2.1.2.2. Magnetron sputtering 49

2.1.2.3. Advantages of sputtering over other deposition methods 49

2.1.2.4. Sputter deposition of doped and undoped ZnO thin films 50

2.1.3. Thermal evaporation 53

2.1.4. Sol gel 55

2.1.5. Hydrothermal 58

2.2. Film Analysis

2.2.1. Structure determination

2.2.1.1. X-ray Diffraction (XRD) 58

2.2.1.2. Raman spectroscopy 61

2.2.2. Surface morphology

2.2.2.1. Field Emission Scanning electron Microscope (FESEM) 64

2.2.2.2. Atomic Force Microscopy (AFM) 65

2.2.3. Chemical composition

2.2.3.1. Energy Dispersive spectrum (EDS) 66

2.2.3.2. X-Ray Photoelectron Spectroscopy (XPS) 67

2.2.4. Optical Measurements: UV Spectrophotometer 70

2.2.5. Film Thickness Measurement by Ellipsometry 71

2.2.6. Photoluminescence Measurements 72

2.2.7. Current- Voltage measurements 75

2.2.8. Device fabrications: Gas Sensors 76

2.3. Conclusion 85

Chapter 3 **86-94**

Growth and characterization of undoped and Lithium doped ZnO nanocrystalline thin films

3.1. Introduction 87

3.2. Material and Methods 87

3.3. Result and Discussion

3.3.1. Structural Properties 88

3.3.2. Morphological Properties 89

3.3.3. Compositional Analysis 89

3.3.4. Absorption and optical band gap 91

3.3.5. Photoluminescence Properties 92

3.4. Conclusion 94

Chapter 4

Group V elements doped ZnO nanocrystalline thin films (Antimony and Phosphorous) **95-109**

4.1. Antimony doped ZnO nanocrystalline thin films (SZO)

4.1.1. Introduction 96

4.1.2. Material and Methods 96

4.1.3. Result and Discussion

4.1.3.1. Structural Properties 96

4.1.3.2. Morphological Properties 98

4.1.3.3. Compositional Analysis 98

4.1.3.4. Absorption and optical band gap 101

4.1.3.5. Photoluminescence Properties 102

4.1.4. Conclusion 103

4.2. Phosphorous doped ZnO nanocrystalline thin films (PZO)

4.2.1. Introduction 104

4.2.2. Material and Methods 104

4.2.3. Result and Discussion

4.2.3.1. Structural Properties 104

4.2.3.2. Morphological Properties 105
4.2.3.3. Compositional Analysis 106
4.2.3.4. Absorption and optical band gap 108
4.2.3.5. Photoluminescence Properties 108
4.2.4. Conclusion 109
Chapter 5 **110-155**
Group III elements doped ZnO nanocrystalline thin films
(Indium, Gallium and In and Ga codoped)
5.1. Indium doped ZnO nanocrystalline thin films (IZO)
5.1.1. Introduction 111
5.1.2. Materials and Methods 112
5.1.3. Result and Discussion
5.1.3.1. Structural Properties 112
5.1.3.2. Morphological Properties 115
5.1.3.3. Compositional Analysis 117
5.1.3.4. Absorption and optical band gap 119
5.1.3.5. Photoluminescence Properties 121
5.1.3.6. Homojunction Devices 124
5.1.3.7. Gas sensing measurements 125
5.1.4. Conclusion 129
5.2. Gallium doped ZnO nanocrystalline thin films (GZO)
5.2.1. Introduction 131
5.2.2. Materials and Methods 131
5.2.3. Result and Discussion
5.2.3.1. Structural Properties 131
5.2.3.2. Morphological Properties 134
5.2.3.3. Compositional Analysis 136
5.2.3.4. Absorption and optical band gap 139
5.2.3.5. Photoluminescence Properties 140
5.2.3.6. Homojunction Devices 143
5.2.4. Conclusion 145

5.3. Indium and Gallium codoped ZnO nanocrystalline thin films (IGZO)

5.3.1. Introduction 146

5.3.2. Materials and Methods 146

5.3.3. Result and Discussion

5.3.3.1. Structural Properties 146

5.3.3.2. Morphological Properties 148

5.3.3.3. Compositional Analysis 150

5.3.3.4. Absorption and optical band gap 152

5.3.3.5. Photoluminescence Properties 153

5.3.4. Conclusion 155

Chapter 6 **156-170**

Solution processed Zinc Oxide nanostructures as NO_2 gas sensor

6.1. Introduction 157

6.2. Material and Methods

6.2.1. Synthesis of ZnO nanostructures: Hydrothermal method 158

6.2.2. Deposition of ZnO thin films : sol-gel methods 159

6.2.3. Fabrication of gas sensors 159

6.3. Result and Discussion

6.3.1. Structural Properties 160

6.3.2. Morphological Properties 161

6.3.3. Compositional Analysis 163

6.3.4. Photoluminescence Properties 164

6.3.5. Gas sensing Measurements 165

6.4. Conclusion 170

Chapter 7

Summary and future work **171**

References **175**

Preface

Nanostructured zinc oxide plays a fundamental role in the fabrication of new devices. Zinc oxide is an inorganic material present in a variety of structures, stoichiometry, physical and chemical properties. These properties can be tailored by a variety of synthesis techniques and doping. Our ability to manipulate structures and its properties by doping is helpful to design innovative fundamental system. Also we can modify the optical and physical properties by adding suitable dopants of the material. Zinc oxide is an important semiconducting material with wide band gap (3.37eV) and large exciton binding energy 60 meV. It is the most attractive material due to its unique properties and wide range of applications. It has chemical stability, biocompatibility and non- toxicity. It is used in a variety of application such as window layer and n type electrode in solar cell, sensors, biotechnology and engineering. Now a days different synthesis technique are designed to get ZnO structures for devices applications. Inspite of last few decades of research, some of the basic properties of the ZnO material have remained unclear.

Doped ZnO has attracted considerable attention because of its tunable optical properties. Hence it is very important to understand the effect of dopants on the various properties of ZnO structures. By enhancing the various properties, we can effectively use it as optoelectronic light emission and gas sensing applications. This research covers the synthesis and characterization of pure and doped nanocrystalline thin films by RF sputtering using powder target. In addition, techniques such as sol-gel and hydrothermal methods are also used to grow nanostructures of ZnO. The various dopants such as Lithium, indium, Gallium, antimony and phosphorous were used for synthesizing nanocrystalline thin films. The influence of dopants on various properties of ZnO was systematically studied. We have designed and fabricated homojunction devices. The performance of these devices can be quantitatively analyzed by measuring I-V characteristics.

Chapter 1 gives general introduction and brief general properties of doped and undoped ZnO nanostructures and defect formations. Next section of this chapter is devoted to recent progress in optical and gas sensing properties of ZnO and a review of critical issues of realization of ZnO based devices like gas sensors, TCO etc.

Chapter 2 describes the process of sample preparation and fabrication. The description of the procedure involved as well as the characterization techniques used to investigate the structural,

morphological, chemical composition of the ZnO thin films such as XRD, FESEM, AFM, EDS, Raman , UV Vis spectrophotometer, XPS, PL and I-V are presented.

Chapter 3 deals with the growth and characterization of lithium doped ZnO (LZO) using RF magnetron reactive sputtering. The sputtering is optimized by changing the deposition parameters namely: sputtering power, substrate temperature, sputtering pressure and Ar: O_2 ratio etc.

Chapter 4 has two sections. The first section deals about the preparation and characterizations of antimony doped ZnO (SZO) nanocrystalline thin films by RF sputtering. The concentration of Sb was varied from 1 to 10 wt% and their properties like structure, morphology, composition, optical and luminescent properties were presented. The second session focuses on the influence of phosphorous doping on the structure, morphology, composition, optical and luminescent properties of PZO films deposited by RF sputtering.

Chapter 5 consists of 3 parts. Part 1 reports investigations and analysis of the effect of indium doping on the structural, morphology, composition, optical and luminescent properties IZO nanocrystalline thin films prepared by RF sputtering. It also includes homojunction fabrication by SZO and IZO layers. Gas sensing properties of IZO films also explained in this part. Part 2 focuses on the properties of gallium doped ZnO (GZO) nanocrystalline thin films. The influences of gallium on the different properties are presented. The p-n junction was fabricated by SZO and GZO layers and its properties are presented in it. Part-3 investigates the synergetic effect of indium and gallium codoping on the physical properties and optical properties. Defect emission is explained with the help of PL.

Chapter 6 Focus on the NO_2 gas sensors based pure ZnO nanostructures prepared by chemical methods such as hydrothermal and sol-gel. This chapter also contains properties of ZnO nanostructures.

Chapter 7 summarizes the general conclusions drawn from this research and gives suggestions for future work.

List of Figures

Figure.1.1 Investigation into the Properties of ZnO 3

Figure.1.2 (a) ZnO structures and (b) the polar and non-polar faces view 7

Figure.1.3 ZnO unit cell with Wurtzite structure b) different types of crystal planes of ZnO Wurtzite Structure 8

Figure.1.4 A simple sketch of the bonding in ZnO and the creation of the band gap (b) Band structure of bulk ZnO obtained from tight binding calculations. 9

Figure.1.5 Geometry of possible charge state of Oxygen vacancy in ZnO (blue balls represent oxygen atoms and grey represent zinc 21

Figure.1.6 (a) Geometry of Zinc vacancy in-2 charge state (V_{Zn}^{2-}) (b) Geometry of Zinc interstitial in +2 charge state (Zn_i^{2+}) (c) Geometry of the zinc antisite in the +2 charge state (Zn_o^{2+}) 23

Figure.1.7 Geometries for (a) oxygen interstitial in the split-interstitial configuration O_i^o (split); (b) oxygen interstitial in the octahedral configuration O_i^{2-} (oct); (c) oxygen antisite O_{Zn}^{2-}, showing a large displacement off the substitutional site 24

Figure.1.8 Positions of native point defects within the ZnO lattice, left shows zinc rich conditions and right shows oxygen rich conditions. The 0 eV position of the Fermi level represents the valance band maximum, the position at ~3.4 eV represents the conduction band minimum. 25

Figure.1.9 (a) Working principles of a nanowire-based photoelectrochemical water splitting device, with ZnO nanowires as the photoanode and Pt plate as the cathode (b) Linear sweep volt ammograms, collected at a scan rate of 10 mV/s at applied potentials from 0.5 to 1.3 V from undoped ZnO nanowires in the dark (black line), undoped ZnO nanowires, and 3.7% ZnO:N nanowires (red line) at 100 mW/cm^2 39

Figure.1.10 (a) Schematic illustration of the architecture of double-sided CdS/ZnO/ZnO/CdSe nanowire arrayed photoanode and (b) the corresponding energy diagram. (c) LSV curves of double sided nanowire samples at a scan rate of 10 mV/s at applied potentials from -0.7 to +0.4 V, under 100 mW/cm^2 illumination. (d) The IPCE

spectra of double-sided nanowire samples obtained with an incident wavelength of 310-650 nm at 0 V versus Ag/AgCl. 40

Figure.2.1 A diagram showing the Thin Films Deposition Techniques 44

Figure.2.2 Pulsed Laser Deposition Technique 45

Figure.2.3 Block diagram of (a) DC and (b) RF sputtering system 48

Figure.2.4 Block diagram of Magnetron sputtering 50

Figure.2.5 Photograph of the Two target Sputtering System 51

Figure.2.6 Photograph of the plasma when shutter is (a) closed & (b) open 53

Figure.2.7 Block diagram of Thermal Evaporation System 54

Figure.2.8 Photograph of the thermal evaporation system 55

Figure.2.9 Schematic of various routes in the sol-gel process, a metal oxide film can be produced by spin-coating a precursor solution or sol to form a dried gel (xerogel), and then using a thermal treatment to densify the film. 56

Figure.2.10 Schematic representation of typical spin-coating process: First the solution is applied to the substrate; then the substrate is rotated with the desirable rotational speed; the solution spread over the substrates and finally uniform thin film will be obtained. 57

Figure.2.11 Schematic of (a) XRD setup and (b) Bragg's law 59

Figure.2.12 Actual picture of X-ray diffraction machine 62

Figure.2.13 (a) & (b) Schematic representation of the theory of Raman Spectroscopy 63

Figure.2.14 Possible vibrational modes in ZnO crystal 64

Figure.2.15 Principle of FESEM operations 65

Figure.2.16 Schematic diagram of atomic force microscopy 66

Figure.2.17 The photoemission on the XPS system process 69

Figure.2.18 The working principle of the XPS spectroscopy (a) and (b) binding energy diagram 70

Figure.2.19 (a) Schematic diagram of an UV-Vis spectrophotometer (b) actual photograph72

Figure.2.20 Schematic diagram of spectroflurometer 74

Figure.2.21 Radiative transition with PL 75

Figure.2.22 (a) Schematic diagram and (b) photograph of fabricated p-n junction devices76

Figure.2.23 General Classification of sensors 78

Figure.2.24 Gas sensing mechanism of n-type semiconducting oxide upon interaction with (a) air, in which an electron depletion layer (EDL) is formed on the surface of the metal oxide, upon interaction with O_2 molecules and subsequent adsorption and ionisation of oxygen species on its surface and (b) the target analyte CO (a reducing gas), which interacts with the adsorbed ionic oxygen species on the surface of the metal oxide, forming the product CO_2 and releasing electrons in the process. This induces a decrease in the width of the electron depletion layer, and resultantly increases the conductivity of the n-type metal oxide. The gold percolation arrows illustrate the direction of electron conduction in the material 80

Figure.2.25 Typical response signal from metal oxide semiconductor gas sensor upon exposure to test gas. The diagram indicates when the pulse of gas is switched on and when it is switched off. Further, t90 represents the response time of the sensor device to reach 90% of its maximum response and t-90 is the recovery time of the sensor device to be within 10% of the baseline value. 81

Figure.2.26 Flow diagram of gas sensor fabrication, characterization and gas sensing 83

Figure.3.1 (a) XRD pattern of undoped (ZnO) and Li doped ZnO (LZO) thin films. Inset shows the shifting of diffraction peak due to Li doping and (b) Room temperature Raman spectra of undoped ZnO and LZO films 89

Figure.3.2 FESEM micrographs of (a) Undoped (ZnO) and (b) lithium doped zinc oxide thin films (LZO) (c) EDX spectrum 90

Figure.3.3 XPS spectra of undoped ZnO and LZO films: (a) Survey spectra of LZO films (b) high resolution selective spectra of Zn-2p (c) high resolution spectra of O-1s (d) high resolution selective spectra of Li-1s. Peak at 52.5 eV corresponds to Fe-3p from sample holder 91

Figure.3.4 (a) Optical absorbance spectra and the inset shows the typical $(\alpha h\nu)^2$vs ($h\nu$) plot (b) optical transmittance/Reflectance spectra of undoped and LZO thin films 92

Figure.3.5 Room Temperature Photoluminescence spectra (black line) along with fitting (red line) and the Deconvoluted peaks in different colors for (a) undoped (ZnO) and (b) LZO films (c) Schematic energy level of defects state in band gap of Li doped ZnO films with possible emissions. (d) Chromaticity diagram undoped and LZO films 93

Figure.4.1 (a) XRD pattern and (b) Raman spectra of undoped and SZO nanocrystalline thin films 97
Figure.4.2 FESEM micrograph of (a) 0% SZO (b) 1% SZO (c) 5% SZO and (d) 10% SZO nanocrystalline thin films 98
Figure.4.3 EDS spectra of (a) undoped and (b) 10 wt% SZO nanocrystalline thin films 99
Figure.4.4 The chemical state of (a) sb3d (b) O1s (c) Zn 2P (d) survey spectra SZO nanocrystalline thin films and (e) The deconvoluted chemical state of Sb in 1% SZO films for Sb 3d $_{5/2}$ state. 100
Figure.4.5 (a) Absorbance and (b) transmittance spectra of undoped and SZO thin films. The inset shows variation of the optical band gap with doping content 101
Figure.4.6 (a) Room temperature PL spectra of undoped and SZO thin films (inset shows deconvoluted spectra) (b) chromaticity diagram of SZO films based on PL data 102
Figure 4.7 (a) XRD patterns of PZO thin films and (b) shifting of diffraction angle of (002) plane of PZO thin films 105
Figure.4.8 FESEM micrograph of (a) 0% (b) 1% (c) 3% and (d) 5% PZO thin films 106
Figure 4.9 (a) Deconvoluted O1s spectra (b) Zn2P spectra and (c) 2P spectra of PZO thin films 107
Figure.4.10 (a) Absorbance spectra (Inset shows the band gap) and (b) Transmittance spectra (Inset shows the variation of band gap with P concentration) of PZO thin films 108
Figure.4.11 (a) Room temperature PL spectra and (b) CIE diagram of (1) 0 wt% (2) 1 wt% (3) 3 wt% (4) 5 wt% PZO thin films at an excitation wavelength of 325 nm 109
Figure.5.1 Schematic diagram of homojunction device configuration 112
Figure.5.2 (i) XRD pattern of IZO thin films at various indium contents and (ii) Variation of (a) Micro strain (b) peak position and FWHM (c) Crystallite size and Dislocation density and with various indium content of ZnO films. 113
Figure.5.3 Raman spectra of undoped and indium doped ZnO thin films. 115
Figure.5.4 FESEM Micrograph of (a) 0wt% (b) 1wt% (c) 5wt% and (d) 10wt% indium doped ZnO thin films 116

Figure.5.5 (a) 2D and (b) 3D Atomic force Microscope (AFM) images of ZnO thin films doped: 0%, 1%, 5%, and 10% of Indium 116

Figure.5.6 (a) 0wt% (b) 1wt% (c) 5wt% and (d) 10wt% shows EDS spectra of undoped and indium doped ZnO thin films and the inset shows the elemental composition of films 117

Figure.5.7 Deconvoluted high resolution XPS spectra (a) Survey spectra (b) Zn 2P region (c) O 1s region and (d) In 3d region of indium doped Zinc oxide thin film. 119

Figure.5.8 (a) Optical absorbance spectra (b) Optical Transmittance/Reflectance spectra (c) Variation of $(\alpha h\nu)^2$ vs hν curve and (d) Variation of band gap with concentration of IZO films. 121

Figure.5.9 (a-d) Deconvoluted room temperature Photoluminescence spectra of IZO thin films 123

Figure.5.10 (a) The schematic energy band diagram of IZO film with possible radiative transition and (b) The CIE diagram of IZO film with different concentration 124

Figure.5.11 (a) I-V characteristic curve, (b) ln(I)-V characteristics curve with different IZO content and (c) schematic band diagram of the IZO/SZO homojunction structure 125

Figure.5.12 (a) Static gas sensing set up and (b) Inter-digited IZO gas sensor 126

Figure.5.13 Variation in response of (a) 10 wt% IZO sensor towards different gas concentration at 250°C (b) IZO sensors at different temperature for 50 ppm H_2S gas, (c) IZO sensor with indium content & (d) IZO sensor at different gas concentrations. 128

Figure.5.14 Response and recovery time of 10 wt% IZO sensor (a) with gas concentration (b) with indium content and (c) Relative response of 10wt% IZO sensor for various gases at 250°C 129

Figure.5.15 Schematic diagram of homojunction device fabricated using GZO and SZO layers 132

Figure.5.16 (i) X-ray diffraction patterns of the (a) undoped ZnO (b-e) GZO nanocrystalline thin films. (ii) Variation of crystallite size, FWHM, and 2theta with Ga concentration of GZO nanocrystalline thin films. 133

Figure.5.17 (a) Raman spectrum and (b) shows the shift in E_2 high peak of undoped and doped ZnO thin films 134

Figure.5.18 FESEM images of (a) undoped ZnO and (b-e) GZO ((b) 1% (c) 3% (d) 5% and (e) 10%)) nanocrystalline thin films 135

Figure.5.19 AFM 2D and 3D images of (a) undoped ZnO (b) 1% GZO and (c) 5% GZO) nanocrystalline thin films 136

Figure.5.20 EDS spectra of (a) undoped ZnO (b) 1% (c) 3% (d) 5% and (e) 10% GZO nanocrystalline thin films 137

Figure.5.21 High resolution XPS (a) survey scan spectra of ZnO nanocrystalline thin films (b) the chemical state of Ga in GZO films for Ga $3d_{5/2}$ states 138

Figure.5.22 Deconvoluted High resolution XPS spectra for core level Zn 2P of (a) undoped ZnO (b) 1% (c) 3% (d) 5% and (e) 10% GZO nanocrystalline thin films 139

Figure.5.23 The O1s core level peaks of (a) undoped ZnO (b) 1% (c) 3% (d) 5% and (e) 10% GZO nanocrystalline thin films 140

Figure.5.24 (a) Absorbance spectra and the inset shows the tauc's plot and (b) Optical transmittance and inset shows the band gap variation with concentration of dopants spectra of ZnO thin films 141

Figure.5.25 Room temperature Photoluminescence spectra of (a) undoped ZnO (b) 1% GZO (c) 3% GZO (d) 5% GZO and (e) 10% GZO nanocrystalline thin films 142

Figure.5.26 (a) Energy level diagram showing some of the principal defect levels in ZnO thin films and (b) Chromaticity diagram undoped and doped ZnO thin films in the visible spectral range 143

Figure.5.27 (a) Current-Voltage characteristics curve and (b) Ln (I) vs Voltage graph of GZO/SZO homojunction diode with Ga content and the inset shows the band diagram of GZO/SZO structure 144

Figure.5.28 X-ray Diffraction pattern of pristine ZnO, IZO, GZO and IGZO nanocrystalline thin films 147

Figure.5.29 (a) Raman spectra ((b) enlarged view) of single and codoped ZnO thin films 149

Figure.5.30 FESEM micrograph of (a) ZnO (b) IZO (c) GZO and (d) IGZO nanocrystalline thin films 149

Figure.5.31 EDS spectra of (a) ZnO (b) IZO (c) GZO (d) IGZO nanocrystalline thin films 150

Figure.5.32 XPS (a) Deconvoluted O1s spectra and (b) Zn 2p spectra of ZnO, IZO, GZO and IGZO thin films 151

Figure.5.33 XPS spectra of (a) In 3d in IZO, (b) Ga $3d_{5/2}$ in GZO and (b & c) In 3d and Ga $3d_{5/2}$ in IGZO thin films 152

Figure.5.34 UV-visible (a) Absorbance spectra (b) Transmittance spectra in the wavelength range 300-900 nm and inset shows the plot of $(\alpha h\nu)^2$vs$h\nu$ of the pristine, single and co doped ZnO thin films 153

Figure.5.35 Deconvoluted room temperature photoluminescence spectra of (a) ZnO (b) IZO (c) GZO and (d) IGZO thin films 154

Figure.6.1 Schematic diagram of deposition of Zinc oxide nanorods by hydrothermal method 158

Figure.6.2 (a) Schematic diagram and (b) flow chart showing the steps for depositing ZnO thin films 159

Figure.6.3 Photograph of (a) gas sensing chamber and (b) PID controller 160

Figure.6.4 XRD pattern of ZnO samples prepared by (a) hydrothermal and (b) Sol–gel techniques 161

Figure.6.5 Raman spectra of (a) Z1 (b) Z2 thin films 162

Figure.6.6 SEM micrographs (a) Z1 nanorod (inset shows the enlarged view of hexagonal shaped nanorod) and (b) Z2 thin films 162

Figure.6.7 EDS spectra of (a) Z1 nanorod and (b) Z2 thin films, inset shows the composition of Zn and O present in the samples 163

Figure.6.8 The XPS survey spectra of (a) Z1 and (b) Z2 samples 164

Figure.6.9 XPS images of (a) Deconvoluted O1s spectra and (b) Zn2p spectra of Z1 and Z2 thin films 164

Figure.6.10 Room temperature PL spectra of (a) Z1 and (b) Z2 samples excited at a wavelength of 325 nm. 165

Figures.6.11 (a-f)) correspond to sensitivity plots of Z1 samples on exposure of NO_2 gas at different temperature & different concentrations 168

Figures.6.12 (a-f)) correspond to sensitivity plots of Z2 samples on exposure of NO_2 gas at different temperature & different concentrations 169

List of tables

1.1 Basic Physical properties of ZnO at room temperature 4

1.2 Summary of published results on gas sensing characteristics of ZnO –review 33

2.1 The optimized parameters for the deposition of RF sputtered undoped and doped ZnO thin films 53

2.2 Long-Term Exposure Limit for 8 hr (LTEL), Short-Term Exposure Limit for 10 minutes (STEL) and impact of these toxic gases on human health and environment 84

3.1 Structural parameters of pure and Lithium doped ZnO thin films 88

4.1. Structural parameters of PZO thin films 106

5.1. Values of 2 theta values, FWHM, crystallite size D,'d'spacing and lattice parameters of IZO films at various dopant concentrations 115

5.2. Values of dislocation density, strain along c axis and micro strain of IZO films at various dopant concentrations 114

5.3. Relative surface composition Zn:O:In as calculated from the XPS 118

5.4. The optical parameters values IZO thin films 120

5.5. Variation in lattice parameters, unit cell volume, Zn-O bond length, crystallite size and grain size of ZnO and GZO nanocrystalline thin films. 134

5.6 Structural parameters of ZnO and GZO nanocrystalline thin films 134

5.7. Lattice parameters of single and codoped ZnO thin films calculated along (002) orientation 148

5.8. Compositional ratio of ZnO, IZO, GZO and IGZO thin films from EDS 150

List of Publications

1. **Shaheera.M**, K.G.Girija, Manmeet Kaur, V.Geetha, A.K.Debnath, R.K.Vatsa, K.P.Muthe and S.C.Gadkari., ***"Characterization and device application of indium doped ZnO homojunction prepared by RF magnetron sputtering"***, Optical Materials 101 (2020) 109723 https://doi.org/10.1016/j.optmat.2020.109723
2. **Shaheera M**., K. G. Girija, ManmeetKaur, V. Geetha, A. K. Debnath, R. K. Vatsa, K. P. Muthe, and S. C. Gadkari, "***Elucidation of structural, morphological, optical and photoluminescence properties of single and (In, Ga) co-doped ZnO nanocrystalline thin films"***Bull. Mater. Sci. (2019) 42:266 https://doi.org/10.1007/s12034-019-1945-7
3. **Shaheera M**., K. G. Girija, ManmeetKaur, V. Geetha, A. K. Debnath, R. K. Vatsa, K. P. Muthe, and S. C. Gadkari, ***"Influence of P content on the structural and physical properties of P-doped ZnO nanocrystalline thin films synthesized by RF magnetron sputtering***"AIP Conference Proceedings 2082 (2019) 040007; https://doi.org/10.1063/1.5093859
4. **Shaheera M**., K. G. Girija, ManmeetKaur, V. Geetha, A. K. Debnath, Malvika Karri, Manoj Kumar Thota, R. K. Vatsa, K. P. Muthe, and S. C. Gadkari , ***"Synergistic effect of indium and gallium co-doping on the properties of RF sputtered ZnO thin films***", AIP Conference Proceedings 1942, 080054 (2018); https://doi.org/10.1063/1.5028888
5. **Shaheera.M**, K.G.Girija, Manmeet Kaur, V.Geetha, A.K.Debnath,, Manoj Kumar Thota, R.K.Vatsa, K.P.Muthe and S.C.Gadkari., ***"Creation of multiple defect states in RF sputtered Li doped ZnO nanocrystalline thin films"*** *(under review)*

List of papers presented in conferences

1. **Shaheera M**., K. G. Girija, ManmeetKaur, V. Geetha, A. K. Debnath, R. K. Vatsa, K. P. Muthe, and S. C. Gadkari ,***"Influence of P content on the structural and physical properties of P-doped ZnO nanocrystalline thin films synthesized by RF magnetron sputtering***", 3rd International Conference on Optoelectronic and Nano Materials for Advanced Technology (icONMAT 2019) Jointly Organized by Centre of Excellence in Advanced Materials Inter University Centre for Nanomaterials and Devices CUSAT January 1-5 2019.
2. **Shaheera M**., K. G. Girija, ManmeetKaur, V. Geetha, A. K. Debnath, R. K. Vatsa, K. P. Muthe, and S. C. Gadkari***"Tuning of Photoluminescence Emission of (In, Ga) Co-Doped ZnO Nano Crystalline Thin Films*** Materials & Technologies for Energy Conversion and Storage (M-TECS 2018) Bhabha Atomic Research Centre, Mumbai September 26-29 2018.
3. **Shaheera M**., K. G. Girija, Manmeet Kaur, V. Geetha, A. K. Debnath, R. K. Vatsa, K. P. Muthe, and S. C. Gadkari "***Effect of Doping and Post Annealing on the Optical Properties of Nanocrystalline ZnO Thin film,*** International Conference on Advanced Semiconductor Materials and Devices (ICASMD-2018) C-MET Hyderabad March 10-13 2018
4. **Shaheera M**., K. G. Girija, Manmeet Kaur, V. Geetha, A. K. Debnath, R. K. Vatsa, K. P. Muthe, and S. C. Gadkari, ***"Synergistic effect of indium and gallium co-doping on the properties of RF sputtered ZnO thin films"*** **62nd DAE Solid State Symposium (DAE SSPS 2017)** Bhabha Atomic Research Centre, Mumbai December 26-30 2017.
5. **Shaheera M**., K. G. Girija, Manmeet Kaur, V. Geetha, A. K. Debnath, R. K. Vatsa, K. P. Muthe, and S. C. Gadkari "***Growth and Characterization of RF sputtered Lithium doped ZnO thin films"*** **17th International Conference on Thin films (ICTF 2017)** CSIR National Physical Laboratory, New Delhi, November 13-17 2017 **.**
6. S.Kailasa Ganapathi, **Shaheera M**, Steffi Edilbert, ManmeetKaur,A. K. Debnath, K. P. Muthe, and S. C. Gadkari **"*Palladium functionalized ZnO thin films as faster CO Sensor",*** **17th International Conference on Thin films (ICTF 2017)** CSIR National Physical Laboratory, New Delhi, November 13-17 2017**.**

CHAPTER 1

Introduction

Brief historical review of research and basic characteristics of ZnO

1.1. Introduction

1.2. Zinc oxide -a multifunctional semiconductor

1.2.1. Properties of ZnO

1.2.1.1. Physical properties

1.2.1.2. Electrical properties

1.2.1.3. Magnetic properties

1.2.1.4. Optical properties

1.2.1.5. Piezoelectric properties

1.2.2. Crystal structure

1.2.3. Doping in ZnO

1.2.3.1. Donor impurities

1.2.3.2. Acceptor impurities

1.2.4. Defects in ZnO

1.3. Applications of ZnO

1.3.1. ZnO as Light Emitting Diode

1.3.2. ZnO as Transparent conducting Oxide (TCO)

1.3.3. Transparent thin film transistors (TTFT)

1.3.4. ZnO as Gas sensors

1.3.5. Photodetector

1.3.6. Solar cells

1.3.7. Photocatalysis

1.4. Motivation and Objectives

1.5. Conclusion

In this section, the fundamental physical properties of the ZnO material system employed in this work are introduced. It provides some background on the doping and defects in ZnO. A brief overview of the applications of ZnO structures is also provided. In the last part of this chapter, motivation and objectives of the work are discussed.

CHAPTER 1

Introduction

Brief historical review of research and basic characteristics of ZnO

1.1. Introduction

In recent years optoelectronic devices and electronic sensors based on semiconductor have attracted considerable attention due to wide range in our daily life. Now a days every electronic gadget like photovoltaic cell, bio sensors, defence system, robotics, smart vehicle, mobiles and many more are equipped with advanced electronic devices with quick response and high performance. For over a decade, II-VI semiconductors have attracted growing interest owing to their possible application in optoelectronics. The wide band gap II-VI semiconductors are efficient emitters in the blue to ultraviolet region and are likely candidate to replace materials like GaN in light emitting laser diodes [1-3]. Despite some similarities, each of II-VI semiconductors demonstrates their own unique and novel physical properties.

Zinc Oxide (ZnO) is one of the II-VI compounds with some exceptional properties. Over the last few decades, there has been growing interest in ZnO as a material for wide variety of devices and applications. In 1954 ZnO was confirmed as an n-type material characteristically [4] and light emission from ZnO was also drawing attention among researchers in Germany [5]. Figure 1.1 shows the steady growth of investigations on ZnO in every ten years. For practical applications, doping of semiconductors is fundamentally necessary in order to control their properties depending on purpose. For making low cost electronic devices ZnO is one of the most promising semiconductors which can be utilized in semiconducting sensors and optoelectronic device technologies. ZnO has impressive electronic and optical properties. Due to these properties, ZnO has received considerable attention in a wide range of applications such as transparent conductive oxide, optoelectronic, and piezoelectric devices. Recently, ZnO has attracted increasing interest in organic and amorphous semiconductors for plastic electronic, LEDs, photodetector (PD), solar cells (SCs), and transparent thin film transistors [7]. Doping is an important and effective way of improving semiconductor properties. Up to now, it is well-known that the most suitable dopant for p-type doping in ZnO are the Group 5 elements [nitrogen (N), phosphorus (P), arsenic (As), and antimony(Sb)] substituting for oxygen. In comparison to Group 5, there have been few p-type reports discussing Group 11[copper (Cu),

silver (Ag), and Gold (Au)] doping at the Zn sites that offer +1 valency. The Group 11 elements can assume a valency of either +1 or +2, depending upon their chemical configuration. Thus in this thesis, influence of various dopants such as lithium, indium, gallium, phosphorous and antimony on the different properties are depicted, especially focused on luminescent properties for light emission application.

Metal oxide semiconductor-based gas sensors have been extensively investigated for the purpose of monitoring environmental biodiversity and detection of explosive and toxic gases at their lower concentrations. Zinc oxide is a well-known semiconductor, which is very promising for application in sensor devices due to its good electrical, structural and environment-friendly properties as well as high response to different reducing and oxidizing gases. On the other hand, high response to different gases is responsible for the lack of selectivity in the ZnO based gas sensors and this problem has motivated researchers to improve selectivity of ZnO-based gas sensors. Thus in this thesis, a part of the work is based on gas sensing properties of doped and undoped ZnO nanostructures.

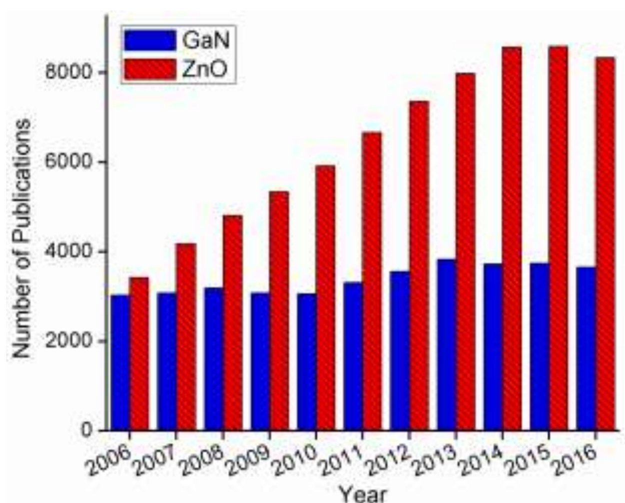

Figure 1.1: Investigation into the Properties of ZnO [8]

1.2. Zinc oxide (ZnO): a multifunctional semiconductor

Currently, Zinc oxide is the most studied material among metal oxides due to its broad applications related to its semiconducting, optical and piezoelectric properties. From the exciting new developments in several key areas, pure or doped ZnO films appear to be highly promising new and advanced functional materials.

1.2.1. Properties of ZnO

ZnO is a wide band gap semiconductor with a large number of attractive properties for electronic and optoelectronic devices. For instance, ZnO based devices can be used in optoelectronics, sensors and lasers etc. Here some of the properties are highlighted.

1.2.1.1. Physical properties

Some basic physical properties of ZnO at the room temperature are listed in Table.1.1. There is still some uncertainty in the values of the thermal conductivity due to the presence of some defects in the material. Pure ZnO is white in colour and turns yellow on heating. Its molecular weight is 81.37. ZnO has relative density of 5.607. Under high pressure, the melting point of ZnO is 1900℃ and its heat capacity is 9.62cal/deg/mole at 25℃. It is insoluble in water but soluble in acid. In addition a stable and reproducible p-type doping in ZnO is still a challenge there is also uncertainty in the values of the hall mobility and effective mass.

Table.1.1 Basic Physical properties of ZnO at room temperature [9-11].

Parameters	Values
Lattice constant	a= 0.32495 nm, c= 0.52069 nm
Density	5.67526 g/cm^3
Molecular mass	81.389 g/mol
Melting point	1975°C
Electron effective mass	0.28 m_o
Hole effective mass	0.59 m_o
Static dielectric constant	8.656
Refractive index	2.008, 2.029
Band gap energy	3.37 eV
Exciton binding energy	60 meV
Thermal conductivity	0.6-1.16 w/km
Specific heat	0.125 cal/J^{o}C
Electron mobility	~210 cm^2/Vs
Hole mobility	~10 cm^2/Vs

1.2.1.2. Electrical properties

To comprehend completely the electronical behavior of ZnO nanostructures prior to utilize them in fabrication of nano device /nanoelectronics is very important. Inherently, the

undoped ZnO nanostructures is n-type in nature and it has been reported in the literature that it is due to the presence of native defects in its crystal structure like oxygen vacancies and Zinc interstitials [12-13]. ZnO has a wide band gap of 3.3 eV at room temperature. This wide band gap has many advantages like higher breakdown voltage, ability to sustain large electrical fields, lower electronic noise, high temperature and high-power operation. These properties make ZnO nanomaterial fit for wide varieties of electrical applications. The numerical values of electron mobility in doped and hole mobility in ZnO are estimated~ 210 cm^2/Vs and~ 10 cm^2/Vs respectively at room temperature [14], which varies with method of preparations.

1.2.1.3. Magnetic properties

Various reports show that room temperature magnetism can be achieved by doping magnetic impurity in ZnO like Fe, Pb, Co etc. But preserving magnetism at room temperature in this material is still a challenge. Despite of many experimental results, the reason behind origin of magnetism in this material is not clear. In some cases, it is explained in terms of segregation of metallic clusters [15] while in other cases it is due to double exchange [16, 17]. Double exchange occurs between ions of different oxidation state which predicts the way by which electrons are transferred between two species.

1.2.1.4.Optical properties

As reported in different literature, the optical band gap of ZnO is 3.44 eV at low temperature and 3.37 eV at room temperature which corresponds to energy of 375.75 Å photons. So, Zinc oxide is transparent to visible light but strongly absorbs ultra violet light below 375.75 Å. Due to this reason, ZnO is used in varieties of optoelectronic applications like Light Emitting Diode (LED's), Solar Cells, photo detectors etc. [18-20]. The band gap of ZnO depends upon the carrier concentration; Band gap tends to decrease as there is an increase in carrier concentration. Photoluminescence of ZnO represents a relatively sharp absorption peak at 380nm (due to band to band transitions) and a wider yellow-green emission band (due to presence of oxygen vacancies and other related defects). Due to number of intrinsic and extrinsic radiative defects levels ZnO emit light in spectral range with in visible region [21]. There are different experimental techniques to study of optical transition in ZnO such as reflection, transmission, optical absorption, photoluminescence etc..

1.2.1.5. Piezoelectric properties

In case of Wurtzite ZnO nanostructures, the origin of the piezoelectricity can be explained as follows: consider an atom with a negative charge that is surrounded tetrahedrally by

positive charges, in which the oxygen atoms and Zinc atoms are tetrahedrally bonded. When an external force is exerted on the crystal along the direction of the tetrahedron, the center of the positive charge and the negative charge can be displaced due to lattice distortion. This distortion can cause the center of positive charge and negative charge to displace from each other, which induces local dipole moments. If the whole crystals have the same orientation, the crystals will possess macroscopic dipole moments, while it is experiencing the external force or external pressure [10]. The ZnO nanostructure comprises alternating layers of Zn^{+2} and O^{-2} atoms stacking along the c-axis with a lack of center of symmetry in ZnO, leading ZnO to possesses a strong piezoelectricity property providing a relatively large electromechanical coupling. This offers significant potential for applications in nano-electromechanical systems, sensor development and electromechanically coupled sensors and transducers [9-11].

1.2.2. Crystal structure

Depending on the crystallization condition, ZnO has three crystal structures Wurtzite, Zinc blende and rock salt as schematically shown in Figure.1.2 If ZnO is grown on the surface of a cubic crystal, a Zinc blende structure is expected; while rock salt structure can be only achieved under high pressure [22-23]. According to the first principle periodic Hartree-Fock linear combination of atomic orbitals theory, the hexagonal Zinc Wurtzite is found to be the most thermodynamically stable form [24]. It belongs to the space group of P63mc [25] which has two lattice parameters; a = 3.25 Å, c = 5.20 Å and is characterized by two interconnecting sub lattices of Zn^{2+} and O^{2-} where each anion is surrounded by four cations at the corners of a tetrahedron with a typical sp^3 covalent bonding. The numbers of alternating planes of tetrahedrally coordinated O^{2-} and Zn^{2+} ions which are pilled alternately along c-axis (Figure 1.2) describe the structure of ZnO. The Zinc and oxide center in the Wurtzite ZnO is tetrahedral and this tetrahedral symmetry plays an important role for polarity of ZnO. Piezoelectricity and pyroelectricity are the direct consequences of polar symmetry of ZnO along hexagonal axis [22, 25-26].

The structure consists of alternating diatomic (0001) planes with a stacking sequence of AaBbAaBbCcBbAaBbAaBb …in the (0001) direction [24]. The two interpenetrating sub lattices of the Wurtzite structure are hexagonal close packed (hcp). This means that each Zn atom is surrounded by four oxygen atoms placed at the edges of a tetrahedron and vice versa. These tetrahedrons are generally of sp^3 covalent bonding, but the II-VI semiconductors make the bonds with the combination of ionic and covalent. A mechanical deformation of the tetrahedral

structures leads to a polarization, i.e., the formation of electric dipole of the microscopic scale, which results in the piezoelectric nature. ZnO has polar and non- polar surfaces. Some of the polar surfaces are entirely terminated with Zinc cations (Zn^{2+}) or oxygen anions (O^{2-}) surface respectively. The ZnO has four common surfaces, the polar Zn (0001) and (0001) terminated faces and the non-polar (1120) and (1010) faces. The (1120) and (1010) surfaces contain equal numbers of Zn and O atoms controlling the growth conditions and tuning the growth rate along the polar and non-polar surfaces give unique ability to form different nanostructures.

ZnO has a six-fold symmetry about the c-axis, and its Wurtzite structure has no inversion symmetry, i.e. the (0001) plane is different from the (0001^{-}) plane, which means that the crystal exhibits crystallographic polarity. The positive z direction for the crystal is the [0001] axis which points from the face of the oxygen plane to the Zinc plane. Bonds along the c direction going from an Zinc cation to an oxygen anion has a Zn polarity, and the opposite is true for bonding from oxygen to Zinc and the two sides of the crystal is called Zn-face [0001] and O-face [0001].

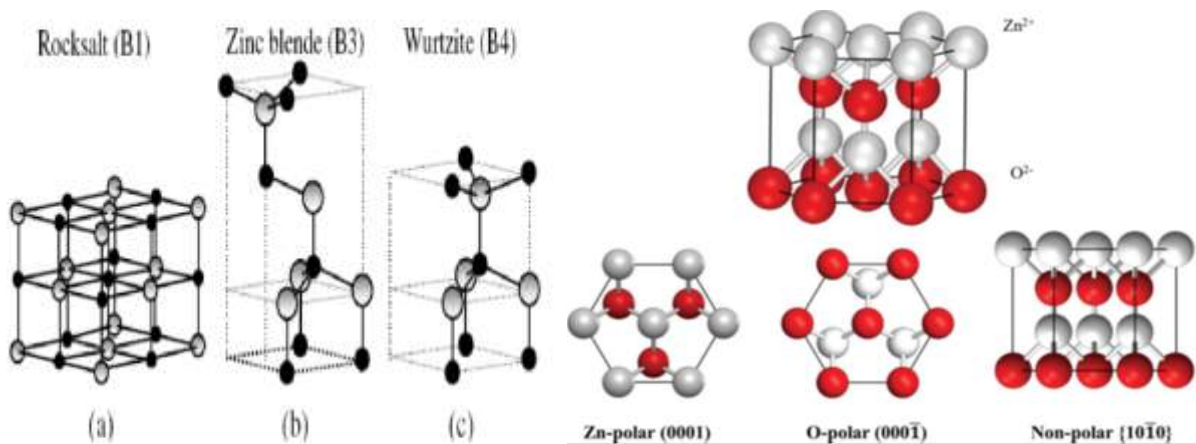

Figure.**1.2** (a) ZnO structures and (b) the polar and non-polar faces view

The hexagonal ZnO Wurtzite structure is a polar crystallite with (0001) positive polar planes rich in Zn, (0001) negative polar planes rich in O, and a (1010) nonpolar plane. Each Zn atom is adjacent to four O atoms as tetrahedral lattice. Zn^{2+} and O^{2-} ion layers are alternatively arranged in [0001] or the c-axis direction (Figure1.3) As a result, the inherent asymmetry along the c-axis leads to the anisotropic crystallite growth. The polar face of the crystallite can also be the atomic layer of Zn or O which have different properties. Polarity is a property of crystal which is determined by the sequence of the attachments inside the crystallite while the termination of the plane is determined by the last atom on the plane. So, there are four types of

(0001) plane structure in ZnO; Zn polar planes with the O or Zn terminal atom, and O polar planes with the O or Zn terminal atoms [27].

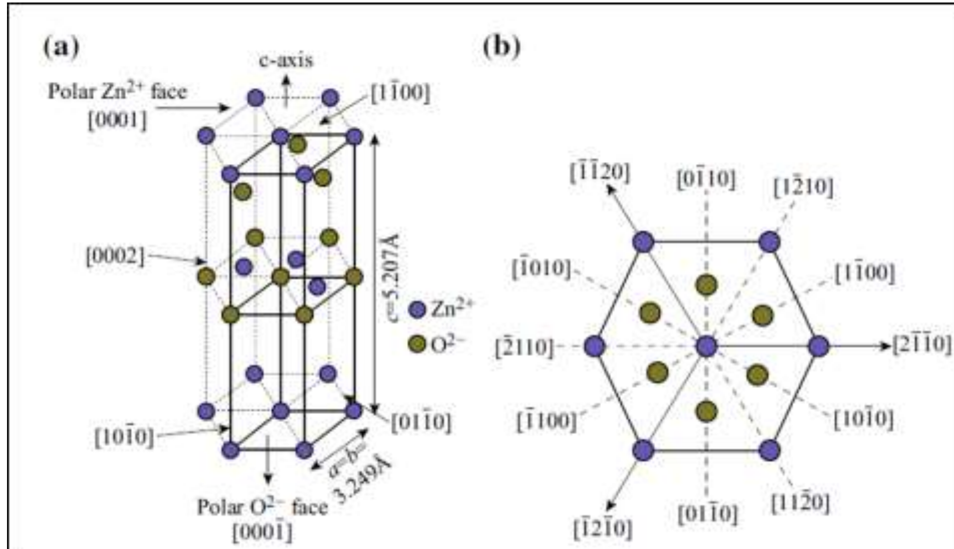

Figure.**1.3** ZnO unit cell with Wurtzite structure b) different types of crystal planes of ZnO Wurtzite Structure (28)

Band structure of ZnO

Figure 1.4 shows single element lattices, ZnO however, is made up of two elements in a tetrahedrally bonded structure. The bonding between the Zinc and the oxygen is derived from the overlap of the Zinc 4s orbital and the oxygen 2p orbital. These form four sp3 hybrid orbitals with the valance and conduction bands based on the energies of the atomic orbitals, shown in Figure 1.4(a). The hybridization allows the electrons to exactly fill bonding orbital and they do not enter the antibonding orbitals. This gives results in a full valance band and empty conduction band. In the case of ZnO, this gap is relatively small and allows easy excitation from the valance band to the conduction band. As such, it displays semiconducting behavior. Using the tight binding approximation a detailed description of the band structure can be obtained. This is achieved by calculating the wave functions across a series of high symmetry routes across its reciprocal lattice the band edges of ZnO can be shown. Figure 1.4(b) gives a detailed description of the band structure of ZnO calculated using the tight binding approach [29]. Electrons fill the states up to the zero energy position of Figure 1.4 showing that ZnO has a direct band gap at the Γ position of roughly 3.4 eV. Stoichiometric ZnO is a wide bandgap semiconductor, however for use in TCO applications it is required to show near metallic conductivity

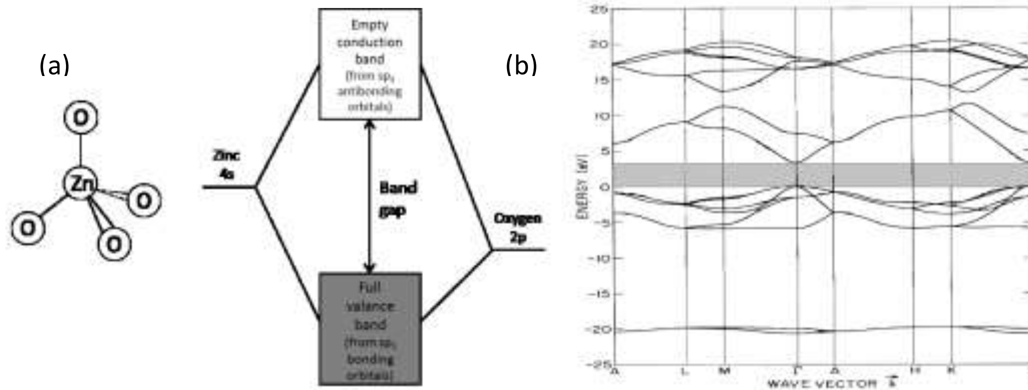

Figure.**1.4** (a) A simple sketch of the bonding in ZnO and the creation of the band gap. (b) Band structure of bulk ZnO obtained from tight binding calculations. The band gap is shown in grey [29]

1.2.3. Doping in ZnO

ZnO is an important for its multifunctional properties for optoelectronics. One of the requirements for these applications is doping of ZnO with various elements for improving and controlling its properties. Several elements are doped in ZnO films like group-I elements, group III elements and group VII elements and so forth. Undoped semiconductor often shows n type conductivity due to its native defects. For the sake of controlling the n-type conductivity in ZnO it is also relevant to investigate dopants that act donors/acceptors and can be used to make n - type/ p-type conductivity in stable manner. In ZnO obtaining p type doping has proved to be very challenging task. A few research groups have reported the p type conductivity in ZnO and research still going on. In the following section details of review based donor dopants and acceptor dopants in ZnO are mentioned.

1.2.3.1. Donor impurities

The group III impurities B, Al, Ga and In when substituted on Zn site act as shallow donors in ZnO. The extra valence electron of these impurities is loosely bound and occupies effective mass states near the conduction band maximum at low temperature. As the temperature raises this extra electron is excited to the conduction band and is free to move.

Transparent conducting aluminium- and gallium-doped Zinc oxide (AZO and GZO) layers have been deposited by spin coating on glass substrates by Naji Al Dahoudi [30]. The coatings have been sintered in air at 450 °C for 30 min and then post-annealed at 350 °C in a reducing atmosphere for 30 min. The electrical, optical and morphological properties of both coatings have been studied and compared. The conventional sols lead to very thin coating,

typically 24 nm for a single layer of AZO and 32 nm of GZO with electrical resistivity of 0·72 and 0·35 Ω cm, respectively. The value however, drastically decreases down to a minimum of $2{\cdot}6 \times 10^{-2}$ Ω cm for AZO and $1{\cdot}76 \times 10^{-2}$ Ω cm for GZO, when five multilayer coatings are made. The origin of these differences is due to the different morphology of the coatings showing different electron scattering process. The GZO sol leads to denser smoother structure (porosity of 5%) layers with an average roughness of 2·76 Å, while the AZO coating is formed by a more porous assembly (porosity of 20%) with an average roughness of 3·46 Å. Both coatings exhibit high transparency (T > 85%) in the visible spectrum range with a slight shift of the absorption energy gap.

Seyda Horzum et al [31] experimentally and theoretically studied how the structural and vibrational properties of Zinc oxide (ZnO) are modified upon Gallium (Ga) doping. For atomic-level understanding of the experimental findings state-of-the-art density functional theory (DFT) based calculations are also performed. DFT calculations reveal that both the substitution and adsorption of Ga atoms in ZnO are energetically possible and substitutional doping in ZnO is the most favorable scenario. XRD measurements show that all the films are in Wurtzite structure and the crystallite size of the films decreases with increasing Ga doping. In addition, Raman analysis show that strong vibrational modes at about 100 and 441 cm^{-1} are associated with E_2^{low} and E_2^{high} phonon branches of ZnO, respectively. While the frequency of the E_2^{high} mode downshifts with increasing Ga concentration, the E_2^{low} phonon mode is not affected by the Ga doping. Furthermore, Ga phonon branch, stemming from the substituted Ga atoms, emerges at low frequencies. It is also seen that the Raman intensity of the E_{Ga} peak linearly increases with increasing Ga concentration.

Properties and energy levels of In-doped ZnO (IZO), Ga-doped ZnO (GZO), and In- and Ga-doped ZnO (IGZO) crystals, were investigated by L. C. Kuang Liau and J. S. Huang [32]. Metal-doped ZnO with different dopants were prepared by sol-gel processing. Results showed that the lattice crystal of the doped ZnO was distorted and the average grain sizes of the crystals decreased. The resistivity and mobility of all doped samples decreased, but the carrier concentration increased in the presence of In and Ga. The energy levels of all crystals were varied depending on the dopants in ZnO. Although the conduction band energy (Ec) and valence band energy (Ev) of IZO apparently shifted to lower energy levels, the bandgap energy (Eg) varied little. The Eg of GZO was widened with respect to ZnO because its Ev was altered. The

Eg of IGZO was widened because the Ec was significantly shifted by In and the Ev was mainly varied by Ga.

Mg, Al and Ga co-doped ZnO (AGMZO) thin films were deposited by Yang Liua et al [33], on flexible substrates by rf magnetron sputtering using ceramic targets at room temperature. The effect of Mg content on structural, morphological, electrical and optical properties of the films was investigated in detail. X-ray photoelectron spectroscopy measurements indicated that the Mg content in the films was substantially consistent with that of corresponding targets. XRD results revealed that the films had the hexagonal Wurtzite structure. The (002) preferred orientation of the crystallites detected by XRD suggested that the grains grew perpendicular to the surface of the film, which was confirmed by the cross-section image. The average transmittance in the visible range was above 82% for all the films. The lowest resistivity of 2.8×10^{-3} Ω cm with carrier concentration of 1.54×10^{20} cm^{-3} and Hall mobility of 14.6 cm^2/Vs can be obtained. The optical transmission spectra revealed that when the Mg concentration increased, the UV absorption edge moved toward the shorter wavelength direction and the optical band gap increased from 3.4 to 3.5 eV.

Alireza Samavati et al investigated [34] the characteristics of laser annealed thin films of Al–Ga co-doped Zinc oxide (ZnO:Al–Ga) nanoparticles on top of SiO_2/glass. The studies on the structural, optical and electrical properties of the pre-annealed sample and samples annealed at different power densities are conducted using a variety of characterization techniques. The samples exhibit a hexagonal Wurtzite structure. Spectroscopic and nano-imaging techniques confirm that by increasing the laser power density, the crystallinity the samples is improved and the nanoparticle size is enhanced from ∼10 nm to ∼35 nm. The resistivity exhibits a minimum value at 440 mJ cm^2. Results demonstrate that the optical band gaps of the samples are between 3.29 and 3.41 eV, which are greater than that of pure bulk ZnO (band-gap of 3.21 eV). Several vibrational modes occur as a result of the dopant combination in the ZnO lattice.

Chen-Hui Zhai et al [35] investigated the structural, optical, and electrical properties of ALD-based AZO films with doping concentrations ranging from 3.7 to 12.7 at.% for applications as transparent conductor materials. The measured surface roughness is within 1.00 nm, whch shows the high morphological quality of the films deposited by ALD technology. The diffraction peak shifts from ZnO (002) to ZnO (100) with increasing Al content indicate that Al doping can change the growth mode of ZnO films. SE analysis has been adopted to reveal the thickness,

optical constants, and band gap of samples. A blue shift of absorption edge of extinction coefficient appears with a growing trend of optical band gap energy due to Burstein-Moss effect. Meanwhile, the blue shift is also shown in optical transmission spectra with the average transmittance that is beyond 85 % in the visible region. Moreover, the lowest resistivity, 1.28×10^{-2} Ω cm, is found for AZO 20:1 film with an Al content of 4.9 at.%. The results of this study can be a useful reference for practical applications and engineering design.

M. U. Shahid [36] deduced that aluminum doping in ZnO thin films greatly affects the crystallite morphology in the thin films. The doping of 'Al' up to 1 at% produced more regular shaped crystallites by sol–gel process. The lowest electrical resistivity (4.27 9 10^{-3} X cm) and higher carrier concentration (5.21 - 10^{19} cm^{-3}) were achieved in 1 at% 'Al' doping in ZnO. The high resistivity and low charge carrier concentration in pure ZnO and 2 at% 'Al'doped films were attributed to the formation of Al_2O_3 precipitates and anisotropic behavior of elongated crystallites.

M. K. Hamza Taha investigated [37] the improvement of the dopant activation in ZnO-based nanocrystals for mid IR plasmonics. For that purpose, we have synthesized Al-doped and Ga-doped ZnO nanocrystals in O-rich and O-poor environments. We show that the free carrier concentration can be doubled for the samples grown in an O-poor environment. Accordingly, the plasmon resonance shifts from 5 mm to 3.1 mm. In analogy with previous results from Ga-doped ZnO thin films, we discuss the effect of the possible reduction of the concentration of acceptor-like complexes such as Al_{Zn}–V_{Zn} and Al_{Zn}–O_i (resp. Ga_{Zn}–V_{Zn} and Ga_{Zn}–O_i) on the activation improvement. Besides, whether long or rapid, thermal annealing does not improve the compensation ratio. Consequently, the control of O content during synthesis remains the most valuable tool to achieve the highest dopant activation in doped ZnO nanocrystals.

S. Edinger et al [38] focused on developing a solution recipe based on water as solvent, with only minor acetic acid content, as well as keeping the substrate temperature as low as possible at 360°C. The process is therefore environment friendly and energy efficient. Despite the challenging conditions, the resulting IZO films were highly transparent and conductive. Their texture deviates strongly from the (002) texture of ZnO and depends on the indium content, which also influences the resistivity. The latter attains its minimum for an indium concentration of 4 at.% in the solution and decreases for increasing film thickness, reaching the value of (5.0 ± 0.1) 10^{-3} X cm, mainly due to the increase in carrier mobility. The stability of the resistivity after

high dose of UV irradiation was found to increase with the carrier density and the film thickness. Thick, highly doped films show minimal resistivity modification even after a total dose of 12.1 kJ/cm^2 UVA/ UVB irradiation. Finally, to demonstrate its applicability in devices, the IZO electrode was used for the fabrication of a lead-perovskite absorber solar cell, yielding an energy conversion efficiency of 6% and 910 mV open-circuit voltages.

Wenliang Zhu et al [39] applied cathodoluminescence (CL) spectroscopy to evaluate the defect-induced luminescence within ZnO and Ga-doped ZnO (GZO) nanoparticle. The observed emissions from defect sites present in the GZO lattice exhibited a strong dependence on both dopant content and synthesis methods. The strong and broad defect-induced emissions and inhomogeneous population of intrinsic defects in nanosized ZnO particles could effectively be suppressed by Ga doping, although large dopant amounts caused the generation of negatively-charged defects, V_{Zn} and Oi, with a subsequent increase of the luminescence. Upon deconvolution of the retrieved CL spectra into individual sub-bands, the physical origin of all the sub-bands could be clarified, and related to sample composition and synthesis protocol. This study lays the foundation of quantitative CL evaluation of defects to assess the quality of GZO optoelectronic devices.

1.2.3.2. Acceptor impurities

Several groups have reported Group-I (Li, Na and K) impurities as acceptor in ZnO. Lithium may behave as donor as well as acceptor in ZnO. The donor behaviour arises when lithium occurs as an interstitial impurity; the acceptor behaviour is exhibited when lithium substitute on a Zn site. Despite the size difference between Li and Na, it is expected that Na also shows a dual behaviour, acting as an acceptor when substitute for Zn and as a donor when occupying interstitials sites.

The optical and structural properties of Li-doped ZnO nanowires grown by a hydrothermal method are reported by Sang Hyo Lee et al [40]. The low-temperature and temperature-dependent photoluminescence spectra clearly exhibited emission peaks that confirmed the presence of a lithium impurity as an acceptor dopant. Particularly, the acceptor energy level of the Li dopant was estimated to be 121 meV from the PL spectra.

Mahajan et al [41] reported optical and electrical properties of lithium doped ZnO nano films. The XRD spectrum reveals that all the synthesized samples have single crystal structure having strong intense peak oriented along (002) c-axis. Crystalline size of undoped and Li doped

ZnO nano films were deduced to be 34.66 nm and 32.59 nm respectively. FESEM exhibits uniform chromosome type structure. Nano films show transmittance above 90% in the range of wavelength 350nmto 800 nm. I–V characteristic shows linear and ohmic behavior.

Jun Seok Lee et al [42] described the growth of vertically aligned p-type ZnO:Li NWs based on a simple hydrothermal technique with a Li dopant in aqueous solution followed by post annealing. TEM measurements of the c -axis oriented and highly vertically aligned NWs demonstrated that Li defects in as-grown ZnO:Li NWs can occupy the empty cages of the Wurtzite structure at octahedral sites, and that Li substitution of Zn occurred because of thermally induced migration due to post-annealing in the presence of oxygen. Also, they confirm the stable formation of p-type ZnO:Li NWs using a NW field-effect transistor and a simple n-type ZnO thin film/p-type annealed ZnO:Li NWs homojunction diode.

Undoped and group- I elements doped ZnO nanowires were synthesized using a thermal evaporation method by A. Sa′aedi et al [43]. FESEM results showed that, the undoped ZnO nanowires were ultra-long with uniform diameters. On the other hand, the length of the doped ZnO nanowires was in the range of some hundred of nanometers. XRD patterns clearly indicated hexagonal structures for all of the products. XPS studies confirmed the oxidation states of Li, Na, K, in the ZnO lattice. An asymmetric O 1s speak indicated the presence of oxygen in an oxide layer. The Raman spectra of the product indicated a strong E_2 (high) peak. The PL spectra exhibited a strong peak in the ultraviolet (UV) region of the electromagnetic spectrum for all of the ZnO nanowires. The UV peak of the doped ZnO nanowires was red-shifted compared to the undoped ZnO nanowires. In addition, the UV–vis spectra of the samples showed similar results compared to the PL results.

LuYue et al [44] fabricated Na-doped ZnO nanorod arrays on Si substrate by a simple hydrothermal method for the first time. With the increase of nNa/nZn, the diameter of ZnO nanorod gradually increased from 30 nm to70 nm, and the length decreased from 754 nm to 71 nm. The p-type carrier concentrations and mobility of Na-doped ZnO nanorod arrays arranged from 3.1×10^{16} cm^{-3} to 1.7×10^{17} cm^{-3} and 41.9 cm^{2} v^{-1} s−1 to10^{6} cm^{2} v^{-1} s^{-1}, respectively.

Linhua Xua et al [45] prepared 1at% K doped ZnO thin films by sol–gel method on Si substrates. The results showed that the films had a hexagonal Wurtzite structure and were preferentially oriented along the c-axis perpendicular to the substrate surface. All the samples showed a strong ultraviolet emission and a weak blue emission. With the increase of annealing

temperature, the ZnO grains gradually grew up; at the same time, the blue emission gradually decreased. The sample annealed at 500 ^{o}C showed the best crystalline quality and strongest ultraviolet emission. The authors think that the blue emission in these samples is mainly connected with K interstitial defects. When the 1 at.% K-doped ZnO thin film is annealed at high temperatures ($\geq$ 600 ^{o}C), most of K interstitials move into ZnO lattice sites replacing Zn. emission resulting from K interstitial defects also decreased.

Among Group -V acceptor impurities (N, P, As, Sb) that substitute for oxygen in ZnO. Min-Suk Oh et al [46] reported, the influence of hydrogen incorporation on the conductivity of phosphorous (P) doped ZnO thin films grown by using radio-frequency (RF) magnetron sputtering. The P dopant is an oxide form of P_2O_5, which is introduced into ZnO thin films using RF plasma with oxygen ambient to suppress the generation of O vacancies. It was observed that the P_2O_5-doped ZnO thin films annealed at 800^0 C exhibited the best electrical property with p-type behavior. Hydrogen atoms in ZnO thin films play an unusual role since it acts as a shallow donor and it may control the n-type conductivity in undoped material. It was observed that the P_2O_5-doped ZnO thin films annealed at 800 ^{o}C exhibited the best electrical property with an acceptor concentration of 3.23 x 10 $^{-17}$ cm^{-3}, mobility of 0.5 cm^2 V^{-1} s^{-1} and resistivity of 35.7 ohm per cm. The activation energies calculations revealed that the acceptor compensating H atoms in P_2O_5-doped ZnO thin films make a strong bond to P and/or O atoms.

K. Zhang et al [47] reported the low temperature magneto-transport properties and electron dephasing mechanisms of phosphorus doped ZnO thin films grown on (111) Si substrates with Lu_2O_3 buffer layers using pulsed laser deposition by quantum interference and weak localization theories under magnetic fields up to 10 T. The dephasing length follows the temperature dependence with an index pE1.6 at higher temperatures indicating electron–electron interaction, yet becomes saturated at lower temperatures. Consistent with photoluminescence measurements and the multi-band simulation of the electron concentration, such behavior was associated with the dislocation densities obtained from x-ray diffraction and mobility fittings, where charged edge dislocations acting as inelastic Coulomb scattering centers were affirmed responsible for electron dephasing. Owing to the temperature independence of the dislocation density, the phosphorus-doped ZnO film maintained a Hall mobility of 4.5 cm^2 V^{-1} s^{-1} at 4K.

Jang-Won Kang et al[48] reported on p-type conductivity in antimony (Sb)-doped ZnO (ZnO:Sb) nanorods which have self-corrugated surfaces. The p-ZnO:Sb/n-ZnO nanorod diode

shows good rectification characteristics, confirming that a p–n homojunction is formed in the ZnO nanorod diode. The low-temperature photoluminescence (PL) spectra of the ZnO:Sb nanorods reveal that the p-type conductivity in p-ZnO:Sb is related to the Sb_{Zn}–$2V_{Zn}$ complex acceptors. Transmission electron microscopy (TEM) analysis of the ZnO:Sb nanorods also shows that the p-type conductivity is attributed to the Sb_{Zn}–$2V_{Zn}$ complex acceptors which can be easily formed near the self-corrugated surface regions of ZnO:Sb nanorods. These results suggest that the Sb_{Zn}–$2V_{Zn}$ complex acceptors are mainly responsible for the p-type conductivity in ZnO:Sb nanorods which have corrugated surfaces.

S. K.Pandey et al reported [49] the effect of in-situ annealing ambient on the performance of p-type SZO films grown on c-plane sapphire substrates by DIBSD system. XRD spectra showed (002) preferred crystal orientation in all SZO films. SZO film annealed in 100% of $O_2/(O_2/N_2)$% was found out to have the highest hole concentration of 1.356 x 10^{17} cm^3 with the lowest resistivity of 6.842 X cm and mobility of 6.737 $cm^2V^{-1}s^{-1}$ at room temperature. Sb_{Zn}–$2V_{Zn}$ complex was found to be responsible for p-type conduction in SZO films. It was also confirmed that the Sb5þ states were more preferable in comparison to Sb3þ states for Sb_{Zn}-$2V_{Zn}$ complex formation.

Doping of ZnO with suitable dopants is a well-known method for achieving the desired material properties. The idea of co-doping is not new. Co-doping allows the benefits of two dopants to be exploited simultaneously. The strengths of one dopant can compensate for the weaknesses of another. Many dopants have been used to improve the physical properties of ZnO. The following section discussed about the brief review of codoped ZnO structures.

Aluminum and indium co-doped Zinc oxide (AIZO) thin films were prepared by direct current (dc) magnetron sputtering on glass substrate in pure argon atmosphere. Three inches of Zinc oxide ceramic with 0.5 wt.% of aluminum and indium doping was used as a target in static mode. The influence of sputtering conditions i.e.substrate–target distance, pressure and power on AIZO films was studied. The electrical resistivity and microstructure of thin films were investigated by the four point probe technique and the scanning electron microscope, respectively. The optical transmittance of AIZO films was measured by UV visible spectrophotometer in the wavelength of 300–1100 nm. Depending on the deposited conditions, highly transparent films up to 80% with low resistivity in the range of 2.6 –7.9×10^{-4} Ω cm were

achieved at room temperature. Possible mechanism in the processing which, ultimately, determines the physical properties of AIZO films will be discussed [50].

Indium and gallium co-doped Zinc oxide (IGZO) thin films were deposited on glass substrates by ultrasonic spray pyrolysis. Physical properties such as structural, morphological, optical and electrical properties were examined on IGZO thin films with respect to the changes in the substrate temperature (425, 450 and 475 °C). Structural results showed that IGZO films were crystalline and presented hexagonal Wurtzite structure. Morphological studies proved that the substrate temperature changed the sizes of hexagonal nanostructures of IGZO. Optical transmittance in the UV–vis region and electrical measurements confirmed that IGZO films were transparent (>70%) with a minimum electrical resistivity ~10.5×10^{-3} Ω cm [51]

Al and F co-doped ZnO thin films were deposited on glass substrates at RT, 100 °C, and 200 °C using a 1.5 wt% ZnF_2 and 1 wt% Al_2O_3 co-doped ZnO target by rf magnetron sputtering. All the AFZO thin films exhibited a typical Wurtzite structure with a strong (002) preferred orientation regardless of substrate temperature. As the substrate temperature increased from RT to 200 °C, the grain size increased from 24.6 to 34.7 nm, the surface RMS rough-ness decreased from 4.25 to 2.90 nm, and the residual film stress changed from compressive to tensile type. The film resistivity significantly decreased by Al and F co-doping in comparison with single-dopant (either Al or F) doping in the ZnO films, revealing that the effectiveness of Al and F co-doping on electrical properties of ZnO thin films was higher than those of the Al or F-doped ZnO films. The electrical properties were also enhanced with the increase of substrate temperature and the lowest resistivity of the AFZO thin film was 2.88×10^{-4} cm at the substrate temperature of 200 ^{o}C, accompanying by the carrier concentration of 9.86×10^{20} cm^{-3}andthe Hall mobility of 22 cm^2/V-s. The XPS, XRD, and SIMS data revealed the enhancement of carrier concentration and conductivity is due to better Al doping effectiveness, F doping/passivation effect, less chemisorbed oxygen or OH species on the film surface, and more oxygen vacancies. The developed AFZO thin films had very high optical transmittances, that is, more than 92% in the visible range (λ= 400–800 nm) and more than 80% in the NIR region (λ = 1200 nm). The optical band gap was broadened from 3.767 to 3.791 eV with the increasing carrier concentration as the substrate temperature increased from RT to 200°C, which conformed to the Burstein–Moss effect [52].

D. S. Y. Jayathilake, reports the microwave-assisted fabrication of highly conducting Al-doped ZnO (AZO), Ga doped ZnO (GZO), and Al, Ga codoped ZnO (AGZO) materials as cheaper earth abundant alternatives to indium tin oxide (ITO) for transparent conducting applications. All three doped ZnO powder samples were compressed into pellets, and their electrical properties were evaluated after the post synthesis heat treatment. The heat treatment was performed by sintering the pellets at 600 °C in a reducing atmosphere using either conventional radiant annealing for 3 h or microwave annealing for 90 s. The Al and Ga dopant levels were systematically varied from 0.5 to 2.5 at. %, and it was found that the lowest resistivity values for the pelleted singly doped ZnO powders exist when the doping level is adjusted to 1.5 at. % for both AZO and GZO, giving resistivity values of 4.4×10^{-3} and 4.3×10^{-3} Ω·cm, respectively. The lowest resistivity of 5.6×10^{-4} Ω·cm was achieved for the pelleted codoped AGZO powder using the optimized Al and Ga dopant levels. Notably, this value is one magnitude lower than the best literature reported value for conventionally synthesized codoped AGZO powder. The resistivity values obtained for the pellets after radiant and microwave post synthesis heat treatments are comparable, although the microwave heat treatment was performed only for 90 s, compared to 3 h for conventional radiant heat treatment. Hence, significant gains were made in the post annealing step by reducing time, cost, and energy required, benefiting our thrust for finding sustainable routes toward alternative low-cost transparent conducting oxides. As a proof of concept, transparent conducting thin films were fabricated via a simple aerosol assisted deposition technique using our best conducting AGZO nanoparticles. The films exhibited a visible transmittance as good as 90% and a resistivity of 5.7×10^{-3} Ω·cm, which can compete with the existing high cost ITO films [53].

Dymitr Snigurenko [54] demonstrated experimental results on p-type ZnO films grown by atomic layer deposition (ALD) and co-doped with aluminum and nitrogen (ANZO). The films were obtained at low temperature (100 °C) with different N to Al ratio and show conductivity type, which depends on the N and Al content. N1s core levels which appear at binding energies of 396.1, 397.4 and around 399 eV were confirmed by XPS. Based on ANZO and undoped ZnO films, both grown by the ALD technique, the ZnO homojunction was obtained in one technological process without any post-growth high temperature processing. The rectification ratio as high as 4×10^{4} at $\pm$ 2V was achieved when an ultrathin Al_2O_3 layer was inserted between

p- and n-type ZnO and a n type ZnO buffer layer deposited on an insulating Si substrate was applied.

Aluminium/gallium co-doped ZnO (AGZO), indium/gallium co-doped ZnO (IGZO), and aluminium/ indium co-doped ZnO (AIZO) thin films were synthesized on glass substrates via aerosol assisted chemical vapour deposition (AACVD). The AGZO film displayed the lowest resistivity (1.3 x 10^{-2} Ω cm) and highest carrier mobility (7.9 cm^2 V^1 s^1), due the relatively low amount of disorder in the structure. The incorporation of In3+ resulted in the most disorder in the structure due to its large radius, which led to an increase in optical absorption, and a decrease in resistivity [55]

C. L. Heng [56] studied the photoluminescence (PL) properties of (Ce + Yb) co-doped ZnO thin films as a function of high temperature annealing. The films were fabricated by magnetron sputtering. After 1000-1100°C annealing, the near band edge (NBE) emissions of the films were dozens to a hundred times stronger than that of undoped ZnO, while the Yb^{3+} emission (~980 nm) was quite weak, indicating that energy transfers from the ZnO host to Yb^{3+} ions in the films were not efficient. X-ray diffraction analysis and scanning electron microscopy observations demonstrated that the (Ce + Yb) co-doping had a large effect on the morphology and crystallinity of the films. The crystallinity enhancement of the films is considered to be the main reason for the strong NBE enhancements of the co-doped ZnO films.

1.2.4. Defects in ZnO

Regulation of defects and its engineering are most important factor for potential application of ZnO in various fields. However, in spite of many reports published on ZnO, the relationship between defects, processing, and properties has not received much attention. Defect studies in ZnO have been done from last few years, but now there is need to retreat again in the perspective of its novel applications. A subtle balance of various defects in ZnO, gives rise to fundamentally new and newer material characteristics. Understanding of defects in doped ZnO with covalent ions is critically important to attain certain functionality. The concentration of defects in a lattice depends on its formation energy. If there are N atoms, the equilibrium defect concentration n is given by [57].

$$\frac{n}{N-n} = \exp\left(-\frac{E^f}{k_B T}\right) \quad \ldots\ldots 1.1$$

where E^f is the formation energy, k_B the Boltzmann constant and T is the temperature. This equation can be derived by considering free energy model of the system without taking into account defect-defect interaction.

In the limit $n << N$, the above equation reduces to a simple form

$$n \approx N \exp(-\frac{E^f}{k_B T}) \qquad \text{.......} 1.2$$

This equation indicates two important facts: The equilibrium vacancy concentration decreases with increase of temperature and Defects having high formation energies will occur in low concentrations.

Impurity defects and native defects can be described using the Kroger-Vink notation [58] which details species (M), the electric charge (q), and the lattice site (s) of the defect in the form: . 'M' can be an atom, vacancy or electron. 'q' can be neutral given by an x, positive given by a '-', and negative given by a '+'. If a charge is greater than one it is given by that number of marks. The site details which atom would usually be present at the lattice site given as an 'i'. (if the defect is in an interstitial site). Defects introduce levels in the band gap of semiconductors and transition from bands to these levels is responsible for green, blue, violet, yellow and orange-red emissions, but the chemical natures of the defects responsible for these emissions have not been conclusively established.

Native defects are imperfections in the crystal lattice. They include vacancies, interstitials and antisites. The basic native defects which are present in the ZnO are oxygen vacancies (Vo), Zinc Vacancies (V_{Zn}), Zinc interstitials (Zn_i), Oxygen interstitials (O_i), Oxygen antisite (O_{zn}) and Zinc antisite (Zn_O).These defect strongly influences the optical and electrical properties of a semiconductor. Understanding the incorporation and behavior of point defects in ZnO is therefore essential to its successful application in semiconductor devices. As grown, ZnO is usually n- type, a property that was historically ascribed to native defects. Possible defects in ZnO are given below, the charge on the defects are determined by the position within the band gap.

Oxygen Vacancies (V_0)

In defining the physical and chemical properties of ZnO, oxygen vacancies play vital roles, which are a common native point defect. The oxygen vacancy is the source of unintentional n-type conductivity [59]. Although there are many controversial reports on this fact

as few reports suggested that oxygen vacancy (Vo) in ZnO are +2 charged near the conduction band minimum which establish the fact that oxygen vacancies are dominant donor type defect and responsible for n-type conductivity in ZnO. Other reports suggested that Vo is a deep rather than shallow donor and therefore cannot contribute to the n-type conductivity [60]. An oxygen vacancy possesses three possible charge states: the neutral oxygen vacancy (V_o), the singly ionized oxygen vacancy (V_o^+), and the doubly ionized oxygen vacancy (V_o^{++} or V_o^{2+}) (Figure 1.5)

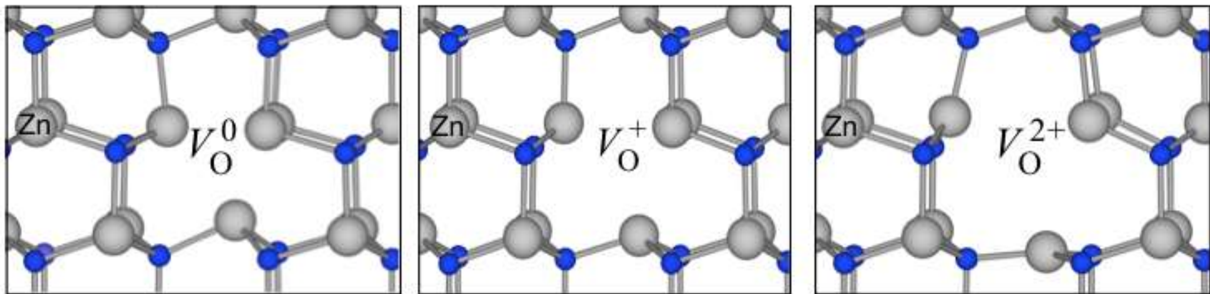

Figure.**1.5** Geometry of possible charge state of Oxygen vacancy in ZnO (blue balls represent oxygen atoms and grey represent Zinc) [60]

First principle calculations predict that the oxygen vacancies are negative-U centers [61]. As a result, the singly ionized state is thermodynamically unstable, and therefore oxygen vacancies will be either in neutral or doubly charged state, depending on the Fermi level position. The neutral oxygen vacancies have the lowest formation energy, and thus will dominate. The green luminescence band centred around 2.4 eV (510 nm) has been attributed to O vacancies due to an excited-to-ground state transition. In case of oxygen vacancy in ZnO, formation energy is given by [62]

$$E^f(V_o^q) = E_{total}(V_o^q) - E_{total}(ZnO) + \mu + q(E_f + E_{VBM}) \quad \ldots\ldots 1.3$$

where $E_{total}(V_o^q)$ is the total energy of a supercell containing the oxygen vacancy in the charge state q, E_{tot} (ZnO) is the total energy of a ZnO perfect crystal in the same supercell and μ_0 is the oxygen chemical potential. Expressions similar to equation (1.3) apply to all native point defects. The chemical potential varies with the experimental conditions, which can be either Zn-rich, O-rich or in between, and is, therefore, explicitly regarded as a variable in the formalism. Thus oxygen vacancies are plays an important role in determining functionality of synthesized ZnO material.

Zinc Vacancies (V_{Zn}):

Electronic structure of Zinc vacancies (V_{Zn}) can be created by removal of a Zn atom from the ZnO lattice which results in four oxygen dangling bonds and a total of six electrons [63] (Figure 1.6). These four oxygen dangling bonds combine into a doubly occupied symmetric state located deep in the valence band and three almost degenerate states in the band gap, close to the valence band maxima (VBM). Only four electrons are present in these three states which therefore can accept up to two additional electrons showing acceptor behavior of V_{Zn} in ZnO. With increasing up Fermi level energy the formation energy of acceptor-type defects decreases there by V_{Zn} can easily be formed in n-type materials. Whereas, in case of p-type ZnO formation energy of V_{Zn} is very high hence concentration of V_{zn} should be negligible in p-type ZnO. First principle calculation revealed that V_{Zn} /V_{Zn}^{-1} and V_{Zn}^{-1}/V_{Zn}^{-2} acceptor levels lies 0.1eV-0.2eV and 0.9-1.2 eV above the valence band maxima respectively [60]. According to full potential linear muffin tin orbital potential, transition from conduction band or Zinc interstitial to Zinc vacancy (V_{Zn}) leads to blue emission.

Zinc Interstitials (Zn_i):

Zinc interstitial might be the source of n-type conductivity of ZnO. There are two main sites for Zn_i in the Wurtzite structure i.e., one at tetrahedral site and another at octahedral site [60, 63]. At the tetrahedral site, Zn_i has one Zn and one O as nearest-neighbour atoms; at a distance of ∼0.833 d_0 (d_0 is the Zn–O bond length along the c axis). At the octahedral site, the Zn_i has three Zn and three O atoms as nearest neighbours at a distance of ∼1.07d_0.

It has been reported that octahedral site is the most stable site for Zn_i, while Zn_i at the tetrahedral site is 0.9 eV higher in energy and highly unstable. Zn_i defects induce a state with two electrons above the CBM. These two electrons are transferred to conduction-band states, stabilizing the +2-charge state (Zn_i^{2+}) (Figure 1.6). Hence, Zn_i donate electrons to the conduction band, thus acting as a shallow donor [60, 63]. Formation energy of Zni in n-type ZnO, where Fermi level lies near the conduction band minimum, is high. Therefore, concentration of Zn_i defect in n-type ZnO is very low and unlikely to be responsible for n-type conductivity. While formation energy of Zn_i^{2+} decreases rapidly when the Fermi level lies near the Valence band Minima, making Zn interstitials a potential source of compensation in p-type ZnO. According to full potential linear muffin tin orbital potential, Zni lies ~0.22 eV below conduction band and transition from Zinc interstitial (Zn_i) to valence band leads to Violet emission.

Zinc antisites (Zn_O):

Zinc antisites (Zn_O) defect originates when Zinc atom substitutes at oxygen atom site (Figure 1.6). ZnO is a double donor in n-type ZnO, but its high formation energy indicates that it is an unlikely source of unintentional n-type conductivity [60, 63]. Electronic structure of ZnO involves both deep and shallow donor levels [64]. It has shallow level of (Zn_O^{+2}/Zn_O^{+1}/Zn_O) near the conduction band maxima and deep level of (Zn_O^{+4} /Zn_O^{+3}) and (ZnO^{+3}/ Zn_O^{+2}) levels located below the middle of the band gap. Formation energy of Zn_O is even higher than that of Zn_i under n-type condition. While formation energy of Zn_O is lower in case of p-type ZnO because of the preference of the highly positive charge states, as is seen in the case of O vacancy and Zn interstitial. Hence, ZnO is unlikely to form at a substantial concentration in *n*-type ZnO.

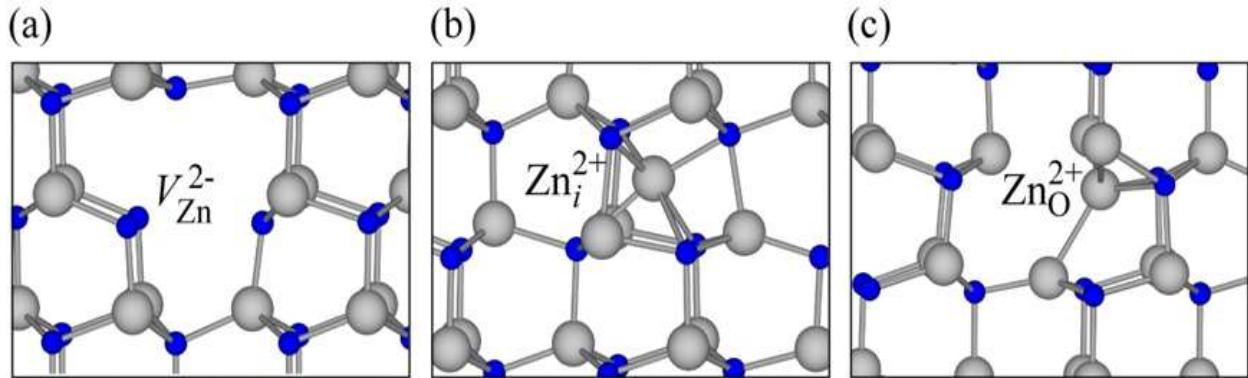

Figure 1.6 (a) Geometry of Zinc vacancy in -2 charge state (V_{Zn}^{2-}) (b) Geometry of Zinc interstitial in +2 charge state (Zn_i^{2+}) (c) Geometry of the Zinc antisite in the +2 charge state (Zn_o^{2+}) [60].

Oxygen Interstitials (Oi):

There are two non-bonded sites for oxygen interstitial (O_i) in the Wurtzite ZnO i.e., tetrahedral site and octahedral site (Figure 1.7). Density functional theory calculations revealed that O_i at tetrahedral site is unstable and relaxes into a split-interstitial configuration. The calculated O-O bond length in this case is 1.46 Å [60-63]. O_i at the octahedral site is stable and introduces states in the band-gap that could accept two electrons, so transition levels of (O_i/ O_i^{-1}) and (O_i^{-1}/ O_i^{-2}) are located at 0.5 eV and 1.4 eV above the valance-band maximum, respectively. O_i do not contribute to n-type conductivity in ZnO. DFT calculation revealed the Zn-O_i distance is 2.19Å which is somewhat greater than the 1.98Å for the host Zn–O bond-length.

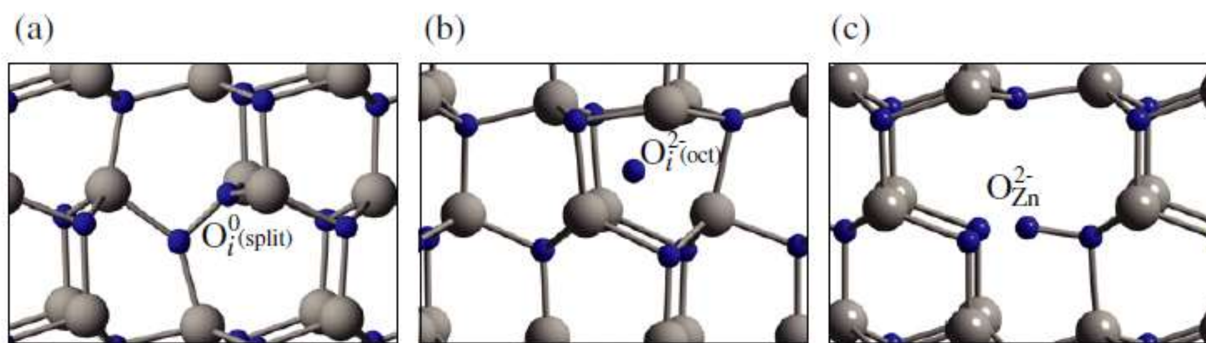

Figure1.7 Geometries for (a) oxygen interstitial in the split-interstitial configuration O_i^o (split); (b) oxygen interstitial in the octahedral configuration O_i^{2-} (oct); (c) oxygen antisite O_{Zn}^{2-}, showing a large displacement off the substitutional site [63].

First-principles studies suggest that the O interstitial is very high in formation energy and/or electrically inactive [61]. According to full potential linear muffin tin orbital potential, transition from conduction band to O_i and Zn_i to O_i leads to yellow and orange-red colour emission.

Oxygen antisites (O_{Zn}):

Oxygen antisites (O_{Zn}) defect originates when oxygen atom substitutes at Zinc atom site (Figure 1.7). The oxygen antisite (O_{Zn}) is an acceptor-type defect having very high formation energy and electrically inactive, even under the most favorable O-rich conditions. Therefore, concentrations of O_{Zn} defects are very low in ZnO at equilibrium. However, O_{Zn} could potentially be formed under non-equilibrium conditions such as under irradiation or ion implantation. It was found that O on the ideal Zn site is unstable and spontaneously relaxes to an off-site configuration [60-63]. DFT calculation suggested that O–O bond length is 1.46 Å in the −2 charge state and 1.42Å in the neutral charge state. The distances between O_{Zn} and other nearby oxygen atoms are ∼2.0 Å, much larger than twice the oxygen covalent radius of 0.73 Å, thus indicating the absence of bonding. O_{Zn} are deep acceptors with transition levels O_{Zn}/O_{Zn}^{-1} and O_{Zn}^{-1} / O_{Zn}^{-2} at 1.52 and 1.77 eV above the VBM. A breakdown of the formation energies across the band gap is shown Figure 1.8.

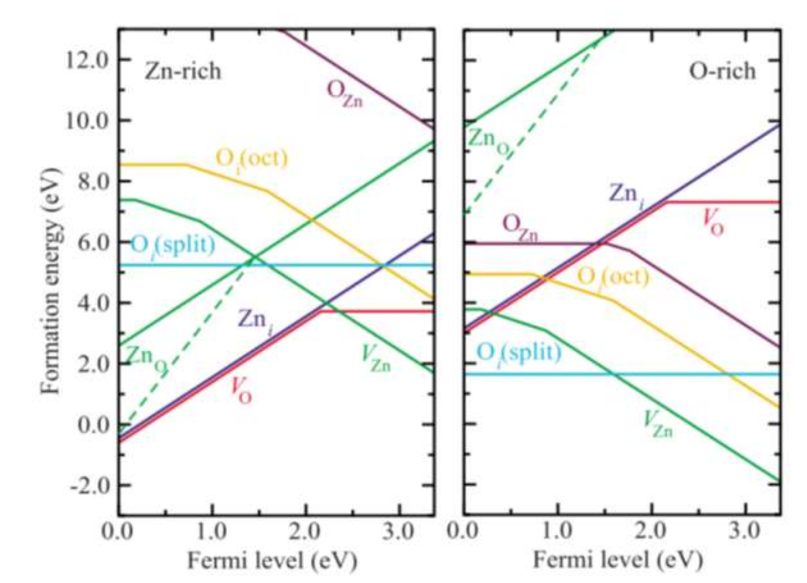

Figure 1.8 Positions of native point defects within the ZnO lattice, left shows Zinc rich conditions and right shows oxygen rich conditions. The 0 eV position of the Fermi level represents the valance band maximum, the position at ~3.4 eV represents the conduction band minimum [60]

1.3. Applications of ZnO

Due to multi functionality and versatility nature of ZnO, creates more attention in the research field related to its applications. It has wide range of applications ranging from paint, paper, rubber, food and drug industries. Also it is a promising material in nano electronics and nano-robotic technology. Its wide band gap, high exciton binding energy, can be utilized for electronic and photonic devices, as well as for high frequency applications. ZnO nanostructures or thin films have been used in various devices like solar cell, gas sensors, antireflection coatings, super capacitor and in many applications.

1.3.1. ZnO as Light Emitting Diode

Reiterating, ZnO is considered as a potentially attractive material for light emitting devices emitting in the ultraviolet region, because of its large exciton binding energy (60 meV). Since initially p-type ZnO has not yet been developed widespread fabrication of ZnO p-n junction based LEDs has not possible. In the interim, n type ZnO on other available and comparable p-type materials was used for investigating the particulars of junctions formed by ZnO. One of the first if not the first ZnO based hybrid heterostructure LEDs was fabricated by Drapak in 1968 who used Cu_2O as the p-type layer [65]. Reports on all ZnO based light emitting

diodes have also started to appear as p-type ZnO began to become available. Near band edge electroluminescence also been observed from ZnO homojunction LED structures fabricated using phosphorous doped p-ZnO on gallium doped n-ZnO grown by radio frequency (RF) sputtering on c-sapphire [66]. Sheng-Po Chang et al [67] fabricated the ZnO NW/p-GaN heterostructure by thermal chemical vapor deposition using a quartz tube furnace and packaged an LED with ITO/glass by a simple process. The photoluminescence spectrum of the p- GaN film exhibited broad bands at 432 and 583 nm; these bands are attributed to near-band edge emission by ZnO with a wide band gap. The current-voltage characteristics of the fabricated diode indicated that the turn-on voltage was large (approximately 5.5V), which may indicate that the thermal chemical vapor deposition procedure produces a high density of defects at the interface. The room temperature EL emission peak at 425nm was attributed to the recombination of electrons and holes in ZnO, causing an unexpected defect to occur in ZnO or at the interface between ZnO and GaN. Furthermore, there has been the yellow band in the EL spectrum; it is attributed to the deep defect level in the heterojunction.

W. Z. Xu [68] reported a breakthrough in fabricating ZnO homojunction light-emitting diode by metal organic chemical vapor deposition. Using NO plasma, they are able to grow p-type ZnO thin films on n-type bulk ZnO substrates. The as-grown films on glass substrates show hole concentration of 10^{16}–10^{17} cm^{-3} and mobility of 1–10 cm^2 V^{-1} s^{-1}. Room-temperature photoluminescence spectra reveal nitrogen-related emissions. A typical ZnO homojunction shows rectifying behavior with a turn-on voltage of about 2.3 V. Electroluminescence at room temperature has been demonstrated with band-to-band emission at I=40 mA and defect-related emissions in the blue-yellow spectrum range.

Mazhar Ali Abbasi et al [69] developed heterojunction LEDs based on the well-aligned ZnO nanorod and nanotubes on the p-type GaN with the insertion of the NiO buffer layer that showed enhancement in the light emission. The cathodoluminescence spectra represent strong and broad visible emission peaks compared to the UV emission and a weak peak at 425 nm which is originated from GaN. Electroluminescence study has shown highly improved luminescence response for the LEDs fabricated with NiO buffer layer compared to that without NiO layer. Introducing a sandwich-thin layer of NiO between the n-type ZnO and the p-type GaN will possibly block the injection of electrons from the ZnO to the GaN.

An electrically pumped Sb-doped ZnO nanowire/Ga-doped ZnO p–n homojunction random laser is demonstrated by [70]. Catalyst-free Sb-doped ZnO nanowires were grown on a Ga-doped ZnO thin film on a Si substrate by chemical vapor deposition. The morphology of the as-grown titled nanowires was observed by scanning electron microscopy. X-ray photoelectron spectroscopy results indicated the incorporation of Sb dopants. Shallow acceptor states of Sb-doped nanowires were confirmed by photoluminescence measurements. Current–voltage measurements of ZnO nanowire structures assembled from p- and n-type materials showed a typical p–n diode characteristic with a threshold voltage of about 7.5V. Very good photoresponse was observed in the UV region operated at 0V and different reverse biases. Random lasing behavior with a low threshold current of around 10mA was demonstrated at room temperature. The output power was 170 nW at 30 mA.

ZnO thin films were fabricated by spray pyrolysis (SP) method with p-ZnO:N/n-ZnO:Ga/ITO structure. The X-ray results show that the deposited films have hexagonal Wurtzite structure. The EDS results observed that the composition of Ga in ZnO:Ga and N in ZnO:N was 3.73% and 27.73% respectively. The photoluminescence (PL) with excitation wave length of 260 nm shows that ZnO:Ga and ZnO:N films emitted UV emission at ~393 and ~388 nm, respectively and the films resistivity was 7.12 and 12.80 Ohm-cm respectively. The electroluminescence of the p-ZnO:N/n-ZnO:Ga/ITO structure was obtained by applying forward bias of 5 volt with 30 mA current, resulting in a 3.35 volt threshold bias with the peak electroluminescence in UV-blue range.[71].

The incorporation of doping elements in ZnO nanostructures plays an important role in adjusting the optical and electrical properties in optoelectronic devices. They fabricated 1-D ZnO nanorods (NRs) doped with different In contents (0% ~ 5%) on p-GaN films using a facile hydrothermal method, and also investigated the effect of the In doping on the morphology and electronic structure of the NRs and the electrical and optical performances of the n-ZnO NRs/pGaN heterojunction light emitting diodes (LEDs). As the In content increased, the size (diameter and length) of the NRs increased, and the electrical performance of the LEDs improved. From the electroluminescence (EL) spectra, it was found that the broad green-yellow-orange emission band significantly increased with increasing In content due to the increased defect states (oxygen vacancies) in the ZnO NRs, and consequently, the superposition of the emission bands centered at 415 nm and 570 nm led to the generation of white-light. These results

suggest that In doping is an effective way to tailor the morphology and the optical, electronic, and electrical properties of ZnO NRs, as well as the EL emission property of heterojunction LED [72].

Ultraviolet light-emitting diodes based on ZnO/NiO heterojunctions were fabricated on commercially available n+-GaN/sapphire substrates using a radio frequency magnetron sputtering system. Near band edge emission of ZnO peaking at 370 nm with a full-width at half maximum of 7 nm was achieved at room temperature when the devices were under sufficient forward bias. With the help of an electron blocking i-$Mg_{1-x}Zn_xO$ layer inserted between the ZnO and NiO layers, the emission intensity has been much enhanced and the threshold current drops down to 23 from 70 mA [73].

A simple and efficient combustion method was used to synthesize undoped ZnO and europium (Eu^{3+}) doped ZnO or ZnO:Eu^{3+}nanophosphors (NPr). The X-ray diffraction pattern shows that the ZnO:Eu^{3+}consists of a single phase Wurtzite structure. The XPS spectra suggest that there were Eu^{3+}ions present in the matrix of the sample at the lower concentration of $Eu^{3+}$and confirmed the formation of Eu_2O_3at higher doping concentrations. ZnO native defect and Eu^{3+} f–f transition related emissions were observed under excitation by a 325 nm He–Cd laser. The Judd–Ofelt intensity parameters (Ω_t (t = 2, 4)) were estimated from the photoluminescence data. The value of Ω_2 at higher doping concentration (5and 6 mol% of Eu^{3+}) was found to be higher than Ω_4, pointing to more covalency and asymmetricity of Eu^{3+}ions with ligands in the ZnO host. These ZnO:Eu^{3+}NPrs have the potential for applications as source of red light in light emitting devices [74].

The low-temperature solution process-based seed-layer-free ZnO p−n homojunction light emitting diodes (LED) were reported. In order to obtain p-type ZnO nanodisks (NDs), antimony (Sb) was doped into ZnO by using a facile chemical route at 120 °C. The XPS spectra indicated the presence of ($Sb_{Zn}-2V_{Zn}$) acceptor complex in the Sb-doped ZnO NDs. Using these NDs as free standing templates, undoped n-type ZnO nanorods (NRs) were epitaxially grown at 95 °C to form ZnO p−n homojunction. The homojunction with a turn-on voltage of 2.5 V was found to be significantly stable up to 100 s under a constant voltage stress of 5 V. A strong orange-red emission was observed by the naked eye under a forward bias of 5 V. The electroluminescence spectra revealed three major peaks at 400, 612, and 742 nm which were attributed to the

transitions from Zn_i to VBM, from Zn_i to O_i, and from V_O to VBM, respectively. The presence of these deep-level defects was confirmed by the photoluminescence of ZnO NRs [75].

Zinc oxide (ZnO) homojunction-based light-emitting diodes (LEDs), with variable emission wavelengths depending on the bias polarity, have been fabricated using a simple hydrothermal growth method. The p-type doping of ZnO nanorods (NRs) was achieved using Sb in the precursor solution and the homojunction was fabricated by epitaxial growth of the Sb-doped p-type ZnO NRs on top of n-type ZnO NRs. The fabricated devices emitted light under forward and reverse bias with a turn-on voltage of 2.7 V and a breakdown voltage of – 3.7 V. The emission wavelength of the devices was dependent on the bias polarity, owing to changes in the types of carrier recombinations. Under forward bias, mixed violet, yellow, and red colored emissions were mainly observed, corresponding to emission peaks at 475, 625 and 700 nm respectively, whereas only red colored emission was prominent under the reverse bias, corresponding to a single broad peak centered at 730 nm. Under forward bias, the near-band edge emission (NBE) was red-shifted from 378 to 475 nm, which was attributed to a localized surface plasmon resonance (LSPR) effect due to the presence of silver nanoparticles (Ag NPs) formed after annealing of the Ag top electrode. No NBE was observed under reverse bias owing to carrier recombination with existing defects, leading to discordance in the resonance energy with the Ag NPs, and thus no LSPR effect. [76]

A Ga-doped ZnO nanorod array has been synthesized on a p- GaN/Al_2O_3 substrate by a hydrothermal method at low temperature. The results show that the Ga-doped ZnO nanorods have excellent crystallinity and good epitaxial relationships with the substrate. With increasing Ga doping, the ZnO nanorods will grow along the [001] direction rapidly resulting in a decreasing average diameter. At the same time, the incorporation of Ga also significantly affects the optical and electrical properties of the n-ZnO nanorods/p-GaN heterojunction light-emitting diode. From the photoluminescence spectrum, it was found that Ga doping can be effectively regulated by the UV and visible emission peak intensity ratio of the ZnO nanorods. The I–V characteristics curve indicates that the n-ZnO nanorods/p-GaN heterojunction light-emitting diode will have better conductivity with increasing Ga doping concentration. Finally, the heterojunction light-emitting diode achieves green light emission under forward bias [77].

The origin of red emission in chemically obtained ZnO nanotubes has been investigated by EL spectra. The as-grown samples were annealed in different ambient (argon, air, oxygen,

and nitrogen). It was observed that the post-growth annealing in nitrogen and oxygen ambients strongly affected the green, yellow, orange, and red emissions of ZnO nanotubes. The EL intensities of the green, the yellow, the orange, and the red emissions were gradually increased after annealing in air, oxygen ambients, and decrease in argon ambient. However, in nitrogen ambient, the EL emission of the red peak in the range of 690–750 nm was increased, and in the range of 620-690 nm, it was decreased as compared with the as-grown samples. It was found that more than one deep level defect are involved in producing the red emission in ZnO [78].

1.3.2. ZnO as Transparent conducting Oxide (TCO)

In most optoelectronic devices such as flat panel displays, LEDs and solar cells, it is essential to use a transparent electrode such as thin film transparent conducting oxide (TCO). All the commercial available ITO is widely used today for most transparent electrode applications. ZnO based compounds is also extremely attractive as a transparent contact larger due to its high conductivity and transparency in addition to its low cost, non-toxicity and relatively low deposition temperature. The ability to easily produce high quality thin-films on a transparent substrate (glass or quartz for example) makes ZnO a very attractive material in this field. If its transparency is high thanks to its large band-gap, on the other hand, its conductivity needs to be modulated with doping in order to lower the resistivity of the film. As mentioned before, Al doping is a commonly used technique for the fabrication of conductive ZnO for displays applications [79]. Zinc oxide (ZnO) thin film as a transparent conductive oxide (TCO) for thin film solar cell application was successfully prepared by Muslih, E. Y. Kim, K. H.. They reported the O_2 effect, reaction mechanism, structure, and morphology, optical and electrical properties. ZnO thin film in the work shows a single phase of Wurtzite, with n-type semiconductor and has band gap, carrier concentration, mobility, and resistivity as 3.18 eV, 1.21×10^{-19}cm^3, 11 cm^2/Vs, 2.35×10^{-3} Ωcm respectively which is suitable for TCO at thin film solar cell [80].

1.3.3. Transparent thin film transistors (TTFT)

Thin film transistors made with amorphous and poly silicon have become the key part of electronic industry in the last ten years. Nevertheless these TFTs actually present some similarities. One possible way to overcome such problems is the utilization of efficient and reliable oxide based TFTs. ZnO is one of a few oxides that can be grown as a crystalline material at relatively low deposition temperatures on various substrate like glasses and plastics. Because it can be made at room temperature and thus, there is compatibility with flexible substrate

materials. Based on these characterizations it is possible to fabricate the ZnO thin film transistor at room temperature.

High performance homo-junction field-effect transistor memory devices were prepared using solution processed transparent lithium-doped Zinc oxide thin films for both the ferroelectric and semiconducting active layers. A highest field-effect mobility of 8.7 cm^2/Vs was obtained along with an Ion/Ioff ratio of 106. The ferroelectric thin film transistors showed a low sub-threshold swing value of 0.19 V/dec and a significantly reduced device operating voltage (64V) compared to the reported hetero-junction ferroelectric transistors, which is very promising for low-power non-volatile memory applications [81].

Kyongjun Kim et al [82]developed a new direct patterning method, drop-casting with a new developing method, through the combination of an aqueous ammonia–ZnO process with the doping of Na ions and surface engineering for high n-type semiconducting performance with good operational stability at low temperature. In particular, the effective decomposition and removal of the residual ammonia compounds using methanol have a successful effect on both intrinsic and Na doped ZnO precursor processes for TFTs and they showed the extensive possibility of ammonia based metal oxide precursor solutions. The Na doped ZnO TTFTs showed good operational stability even with the process of low temperature sintering. The mobility 0.80 $cm^2\ V^{-1}\ s^{-1}$ was obtained at 200 ^oC sintering and the mobility 0.10 $cm^2\ V^{-1}\ s^{-1}$ at 100 ^oC sintering. In addition, in ambient conditions, the patterned Na doped ZnO TTFT exhibited high electron mobility is 1.84 $cm^2\ V^{-1}\ s^{-1}$ with excellent device operational stability and scant hysteresis with sintering at 300 ^oC. This method is not only simple as compared with photolithography and inkjet printing, but is also a sophisticated patterning process with good fidelity for solution-processed ZnO TFTs. Moreover, the proposed method can be extended to plastic substrates on a large scale because of the low temperature development process of the ammonia ZnO precursor using methanol and continuous patterning at ambient conditions. We believe that this method can be adapted to the advanced process toward future printed transparent electronic devices.

ZnO semiconducting thin films were fabricated using a sol-gel method under standard atmospheric conditions and acetates as precursors. The performances of thin-film transistors (TFT) with a ZnO active channel layer and effects of indium doping on the threshold voltage of ZnO TFTs were evaluated at a low temperature (300 °C). By examining the electrical

characteristics of thin films and TFTs while doping a ZnO system with increasing indium concentrations from 0.01 to 0.1M, reductions at the threshold voltage of 5.3 V and an increase of an order of magnitude of the on/off current ratio were observed. Oxygen vacancies increase when the indium concentration increases, thus releasing electrons and increasing the channel carrier concentration. At 300 °C, the indium-doped Zinc oxide (IZO) device performance showed a mobility of 0.06 cm^2/V-s, a threshold voltage of 5.3 V, and an on/off current ratio of 10^6 [83].

Han.D et al [84] have successfully fabricated bottom gate fully transparent tin-doped zinc oxide thin film transistors (TZO TFTs) on flexible plastic substrate at low temperature by RF magnetron sputtering. The effect of O_2/Ar gas flow ratio during channel deposition on the electrical properties of TZO TFTs was investigated, and found that the O_2/Ar gas flow ratio have a great influence on the electrical properties. TZO TFTs on flexible substrate has very nice electrical characteristics with a low off-state current (Ioff) of 3 pA, a high on/off current ratio of 2×10^7, a high saturation mobility (μ_{sat}) of 66.7 cm^2/V x s, a steep subthreshold slope (SS) of 333 mV/decade and a threshold voltage (V_{th}) of 1.2 V. Root-Mean-Square (RMS) roughness of TZO thin film is about 0.52 nm. The transmittance of TZO thin film is about 98%. These results highlight that the excellent device performance can be realized in TZO film.

1.3.4. ZnO as Gas sensors

Gas sensors play an indisputable role in most fields of technology in the modern world; they are broadly used for public safety, pollution monitoring, quality control, breath analysis, smart homes and automobiles, and so on. Due to their low cost, high sensitivity, compact size, online detection, ease of use, portability, and low power consumption, metal oxide (MO) gas sensors have exceptional potential for detection of more than 150 gases [85] . ZnO is of interest for application in different types of sensors including gas sensors and bio sensors. The utilization of ZnO as a gas sensor has a long history because of its chemical sensitivity to different adsorbed gases, high chemical stability, amenability to doping, non-toxicity and low cost. In 1959, Heiland reported on the gas sensitive behavior of ZnO's electrical conductivity [86]. The conductivity of thin layers of ZnO increased by orders of magnitude in vacuum and decreased in an atmosphere even at 500K. From then, the detection of H_2, oxygen and hydrocarbon by means of surface conductivity changes on ZnO crystals and thin films has been proposed and demonstrated [86]. ZnO for flammable gas sensing applications was demonstrated [87]. However sensing mechanism and sensing application have studied more for gas sensors. A simple sensor contains

two metal contacts across the nanostructure network. Sensing is based on the change in conductivity upon gas absorption/desorption. A short review of the gas sensing characteristics of ZnO towards different gases and the effect of doping on the gas sensing properties is discussed in the following section. Table1.2 gives a short summary of ZnO gas sensors used for the detection of various gases.

Table. 1.2 Summary of published results on gas sensing characteristics of ZnO -review

Material	Gas/ concentration (ppm)	Temperature (^oC)	Sensitivity	Method of preparation	References
ZnO:Ag	Methanol/200 ppm	370°C	15.831	hydrothermal method	88
ZnO:In	CO/80 ppm	300°C	5.5	Sol-gel method	89
ZnO:Ga	H_2S /5ppm	250-300°C		RF sputtering	90
ZnO:In	Acetone/37.5 ppm	275°C	714	Chemical vapor deposition	91
ZnO:Na	CO_2/50 sccm	Room temperature	81.9%	Spin coating	92
ZnO	NO /40 ppm	Room temperature	500%	Dielectrophoresis	93
ZnO:In	H_2/5 ppm	300°C	15	Sol-gel	94
ZnO:Al	NO_2/0.5 ppm	250°C	13.7	Sputtering	95
ZnO	NO_2/500 ppm	270°C	218.1	Photolithiography RF sputtering	96
ZnO	NO_2/7 ppm H_2S/18 ppm	200°C	3.32 1.4	Spray pyrolysis	97
ZnO	NO_2/1000 ppm	150°C	61	Chemical Bath Deposition	98
ZnO/ Graphene	H_2/200 ppm	150°C	3.5	Reduction	99
ZnO/	NO_2/1 ppm	300°C	12.57	Microwave	100

Graphene				irradiation	
ZnO	NO_2/200 ppm	150°C	15.7%	SILAR	101
ZnO:Al	CO/50 ppm	300°C	80%	Sol gel method	102
ZnO:Al	NH_3/100 ppm	350°C	350	Sol gel method	103
SiNW/ZnO core shell	H_2S/50 ppm	300°C	11.22	MACE & thermal evaporation	104
ZnO nanosheets	H_2S/100 ppm	70°C	22.5	Co precipitation method	105
p-CuO/n-ZnO nanofibres	H_2S/100 ppm	250°C	60	Electrospinning Atomic layer deposition method	106
ZnO:La Fibrous	H_2S/90 ppm	175°C	6485%	Electrospinning	107
ZnO:Cr	CO/500 sccm	50°C	64.45%	Sol-gel	108
Pt/ZnO:Al	NH_3/1000 ppm	300°C	2183	Sputtering	109
ZnO:Al	H_2S/600 ppm	200°C	13	Spray Pyrolysis	110
ZnO:Ag	NO/21.6 ppb	200°C	78.95%	Hydrothermal	111
ZnO:In, Ga	NO_2	250°C		wet-chemical method	112

1.3.5. Photodetector

There have been many reports regarding the photo response properties of the ZnO based heterojunction. Buddha Deka Boruah [113] presented an overview of the photoresponse characteristics of UV PDs and potential ZnO nanostructures from the conventional to self-powered device designs. Both the conventional and self-powered ZnO-based UV PDs were precisely categorized based on device structure and working mechanism, where recently introduced novel phenomena such as piezo-electric, pyro-electric and plasmonic effects for efficient photoconduction were presented.

A simple and low-cost fabrication of ZnO p-n homojunction was demonstrated. The junction consists of n-type ZnO nanowires array by a hydrothermal method covered with p-type Al, N co-doped ZnO film by a sol-gel method. The junction exhibits good rectification characteristics, with reverse leakage current and rectification ratio of 5 μ A and 150 at bias of 3 V, respectively. The junction is operated as a photodetector when light radiation is shined on the glass-side of the device. The photodetector shows peak responsivity at 384 nm with UV-visible responsivity ratio R384 nm/R550 nmof 70 at an operating bias of 3 V [114]

Hydrothermally grown ZnO NR-based UV detectors with an MSM configuration were fabricated on glass substrates. Pd was used as the electrode metal for the MSM devices. The crystal and optical properties of the ZnO NRs were investigated by SEM and UV–vis spectroscopy. The SEM images showed that an array of high-density ZnO NRs was grown on the glass substrate. From the I-V characteristics, it was observed that the value of the photocurrent was twice that of the dark current. The responsivity and contrast ratios were 0.19 and 2.10 A/W, respectively, for the MSM detectors. These results provide greater insight into the design and simple fabrication of MSM detectors for various optoelectronics applications [115].

The highly dense n-type Zinc oxide (ZnO) nanowires (NWs)/p-type ZnO:Sb nanoparticles (NPs) was grown on glass substrate. An energy dispersive X-ray mapping demonstrates that Sb element is present in the nanostructures (NSs) and the doping Sb concentration is 1.52 atomic %. The XRD spectrum reveals ZnO Wurtzite and Sb_2O_3 cubic structures. Additionally, the PL spectrum of the ZnO:Sb sample includes strong peaks at approximately 390 and 521 nm. HRTEM images indicate that p-ZnO:Sb NPs and n-ZnO NWs are polycrystalline and single crystalline structures, respectively. The I–V curve reveals that the measured currents in the ZnO NWs to ZnO:Sb NSs were increased by a factor of ~13 at 5 V. The UV-to-visible rejection ratio of the ZnO:Sb sample was ~3.19 at 5 V. The maximum quantum efficiency of the ZnO:Sb sample was approximately 46.5% when the incident light was 390 nm. Furthermore, the dynamic response of the ZnO:Sb sample UV photodetector was stable and reproducible. The measured current under UV light exceeded the dark current by around 11 μA [116].

1.3.6. Solar cells

Solar cells represent a very promising renewable energy reducing technology because they provide clean and renewable energy reducing our dependence on fossil oil and our impact

on the environment. Among the various semiconducting metal oxide materials, the most convenient conducting oxide for solar energy application is Zinc oxide. Recently Al doped ZnO thin films have attracted attention as a replacement for ITO due to their low resistivity, high transmission, non-toxicity and low cost.

The low pressure chemical vapor deposition (LP-CVD) of Al doped ZnO thin film was investigated for transparent electrode of thin film solar cell Doyoung Kim et al [117]. The haze factor of ZnO:Al films drastically increased with the introduction of TMA precursor. However, it is observed that the excessive increase of FAr, TMA deteriorates the haze factor and film resistivity. Based on the characterization of ZnO:Al films, we fabricated the superstrate p-i-n a-Si:H solar cell with optimized LP-CVD ZnO TCO. In spite of contact problem between ZnO:Al and p+ a-Si:H, ZnO:Al TCO solar cell showed higher efficiency of 7.77% than SnO_2:F. Thus, LP-CVD Al doped ZnO thin films prepared can be applied to improve the properties of Si thin film solar cells.

O. Lupan et al [118] observed that all ZnO/Si heterojunction devices fabricated using ZnO films deposited by the SCSD method exhibit enhanced rectifying current–voltage characteristics after RPP at 600–700 ^oC. The variation found in the I–V characteristics can because by the changes in the electrical properties of n-ZnO layer as well as interface region between the nanostructured film and Si substrate. The improvement shown in rectifying characteristic may be assigned partially to the reduction of the defect density in the films after RPP. They fabricated a solar cell with a conversion efficiency of 6.8% (V_{OC} = 0.335V; J_{SC} = 28 mA/cm^2; FF = 0.721) for Al–ZnO/SiO2/Si/Al. The area of the fabricated cell was about1cm^2 and no antireflection coatings were employed.

A photoanode with Ga-doped ZnO nanorods has been prepared on F-doped SnO_2 (FTO) coated glass substrate and its application in dye-sensitized solar cells (DSSCs) has been investigated. Ga doped ZnO nanorods have been synthesized by an electric-field-assisted wet chemical approach at 80˚C. Under a direct current electric field, the nanorods predominantly grow on cathodes. The results of the X-ray photoelectron spectroscopy and photoluminescence verify that Ga dopant is successfully incorporated into the ZnO Wurtzite lattice structure. Finally, employing Ga-doped ZnO nanorods with the length of ~5 μm as the photoanode of DSSCs, an overall energy conversion efficiency of 2.56% is achieved. The dramatically

improved performance of Ga-doped ZnO based DSSCs compared with that of pure ZnO is due to the higher electron conductivity [119].

Cu_2O/ZnO heterojucntion solar cells were successfully obtained by a magnetron sputter deposition method. The Cu_2O thin film was deposited by the method using a sintered Cu_2O ceramics target. Crystalline phases of the films were controlled by adjusting an O_2 flow rate ratio (O_2/(Ar+O_2)) precisely during the sputtering process and Cu_2O single phase polycrystalline films were obtained at room temperature. The Cu_2O films qualities were improved by a rapid thermal annealing for 30 s in an Ar atmosphere of 1 atm. Hall mobility, carrier density, and resistivity of annealed films reached the values of 16.6 $cm^2/V/s$, $3.5x10^{15}$ cm^{-3}, and 10^7 Ωcm at 600 °C, respectively. The conversion efficiency of the Cu_2O/ZnO heterojucntion solar cell was 0.24 % with the open circuit voltage of 0.69 V [120].

1.3.7. Photocatalysis

Another application of ZnO is in Photocatalysis. 'Photocatalysis' means the use of photon energy in the catalytic activity reactions. In the last few years Photocatalytic process involving semiconductor ZnO nanostructures under UV light illumination have been shown to be potentially beneficial and helpful in the treatment of various hazardous pollutants. Different studies have proved this with different pollutants like dyes, drugs, surfactants, pesticides etc. that can be completely mineralized in the presence of ZnO nanostructures. Photocatalytic efficiency of ZnO is strongly depends on its morphology and properties.

Pal M [121],Ga doped nanostructured Zinc oxide thin films on pure silica glass substrate were prepared from Zinc acetate based precursor solutions by varying Ga doping level (0 to 6%). The presence of quasi-spherical nanocrystalline hexagonal ZnO with a decreased trend in crystallite/particle size vis-à-vis an enhancement of direct band gap energy of the films found on increasing the doping level. Root means square (RMS) film surface roughness was found maximum in 1% doped film (G1ZO). Photoluminescence (PL) emission study revealed that the formation of various intrinsic/extrinsic defects along with the presence of characteristics band edge emission of ZnO at ~ 385 nm (UV-PL) and a lowest relative intensity of the UV-PL emission was found in 1% doped film (G1ZO), indicating an appreciable decrease in the recombination rate of photogenerated charge carriers in the semiconductor. The photocatalytic activity (PA) of the films towards degradation of rhodamine 6G dye was performed under UV (254 nm) and obtained the maximum value of dye degradation first order reaction rate constant

in 1% doped film. On increasing doping level, the trend in change of defect concentration (oxygen vacancies) as analyzed by Raman spectra was found identical with the dye photodegradation activity of the films. Thus, a synergic effect of the maximum RMS surface roughness and the maximum defect concentration in G1ZO film could be responsible for its highest PA. The G1ZO film would expect to decompose micro-organisms even under exposure of visible light.

A moderate electrodeposition synthesis was developed in this work to prepare a ZnO film. The target of this research is to determine the best photoelectrochemical response for solar-induced water decomposition. On the basis of the acquired results, a nanostructured ZnO film was developed on the surface of a substrate. The photocatalytic and photoelectrochemical responses of the obtained Wurtzite type ZnO film were monitored and assessed for comparison with those of the commercial ZnO. In respect to the newly formed ZnO thin film, light current densities of 17.14 mA/cm^2 under ultraviolet light and 13.71 mA/cm^2 under visible light were observed. The ZnO film was believed to possess excellent capacity to absorb more incident photons from the illumination to produce more photoinduced charge carriers, giving rise to the photocatalytic and photoelectrochemical reactions. In addition, incident rays from any orientation can be caused by light-scattering effects and the high specific surface area of 2D nanostructures [122].

In addition to Photocatalytic water splitting and pollutant degradation, another Photocatalytic application of interest is Photocatalytic disinfection, due to increasing antibiotic resistance and the need for water treatment. Some research groups demonstrated the antibacterial activity of ZnO and it was shown that ZnO has higher activity compared to more commonly used TiO_2 [123].

Semiconductor metal oxides, such as ZnO and TiO_2, have been extensively studied as photoelectrodes for water splitting applications to produce hydrogen [123], making it a more popular choice of material for photoelectrochemical applications. However, because of the wide bandgap nature of ZnO, the power conversion efficiency of pure ZnO is limited by its poor visible light absorption. In this case, doping and sensitization are effective strategies to further enhance the photoelectrochemical activities of 1D ZnO nanostructures. Yang et al. (2009) [124] reported a rational synthesis of nitrogen-doped ZnO nanowire arrays (ZnO:N) and studied their applications as photoanodes for photoelectrochemical hydrogen generation. The uniform and

well-aligned ZnO nanowires were prepared using a hydrothermal approach, followed by an annealing process in ammonia to incorporate nitrogen as a dopant. The ZnO:N nanowire arrays showed enhanced photoresponse within the visible light region, as the incorporation of nitrogen could introduce intermediate energy levels in the bandgap of ZnO, thus leading to a redshift of the absorption spectrum of ZnO. Compared to the pristine ZnO nanowires synthesized under similar conditions, the ZnO:N nanowires demonstrated increased photocurrent density(Figure 1.9) and photo-to-hydrogen conversion efficiency.

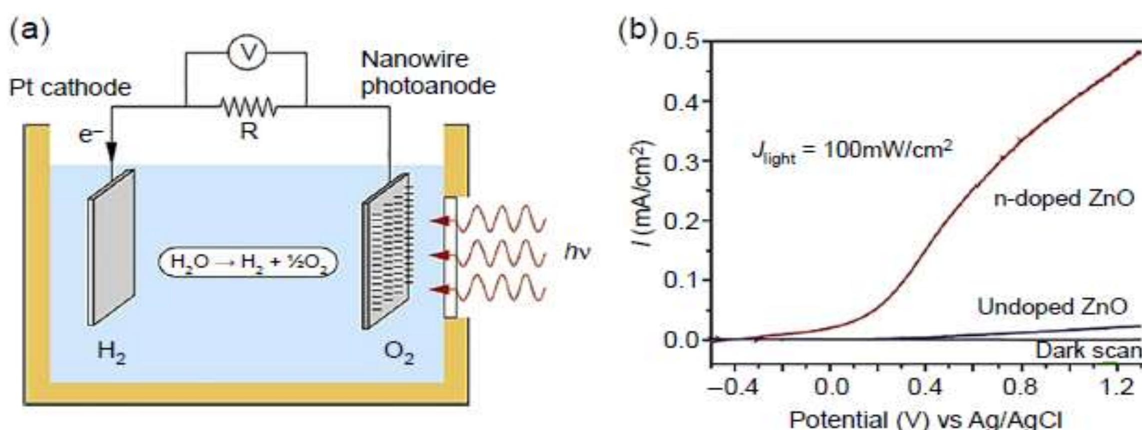

Figure 1.9 (a) Working principles of a nanowire-based photoelectrochemical water splitting device, with ZnO nanowires as the photoanode and Pt plate as the cathode. (b) Linear sweep voltammograms, collected at a scan rate of 10 mV/s at applied potentials from 0.5 to 1.3 V from undoped ZnO nanowires in the dark (black line), undoped ZnO nanowires, and 3.7% ZnO: N nanowires (red line) at 100 mW/cm^2 (124).

To further maximize the solar light absorption, tandem structures, in which semiconductors with different bandgap energies are combined to form optimum band structure, were developed and utilized in photoelectrochemical devices. Wang, Yang et al [125] reported that the fabrication of novel photoanodes consisted of double-sided CdS and CdSe QD-cosensitized ZnO nanowire arrays for PEC hydrogen generation. ZnO nanowire arrays were first grown on both sides of ITO-coated glass substrate using the hydrothermal approach, after which CdS and CdSe QDs were sequentially deposited onto ZnO nanowires using chemical bath deposition (Figure 1.10). The cosensitized photoelectrode shows significantly enhanced visible light absorption up to 650 nm. Both CdS and CdSe QDs possess conduction band edges higher than that of ZnO, thus leading to the efficient transfer of photogenerated electrons from QDs to ZnO. The photoelectrochemical measurements were carried out in a three-electrode setup, using

coiled Pt wire and Ag/AgCl electrode as the counter- and reference electrodes, respectively. The electrolyte contains 0.25 M Na_2S and 0.35 M Na_2SO_3, which acts as a sacrificial reagent to prevent CdS and CdSe from photocorrosion.

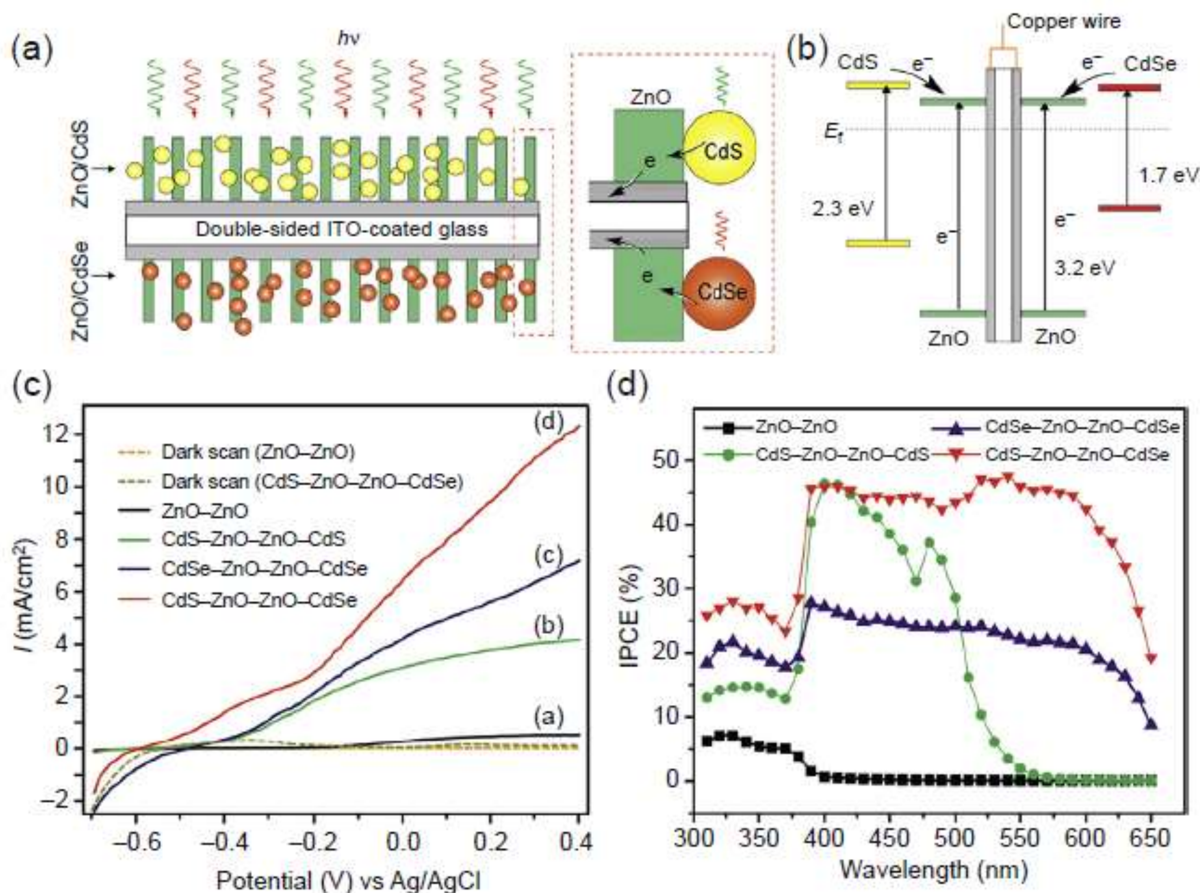

Figure 1.10 (a) Schematic illustration of the architecture of double-sided CdS/ZnO/ZnO/CdSe nanowire arrayed photoanode and (b) the corresponding energy diagram. (c) LSVcurves of double sided nanowire samples at a scan rate of 10 mV/s at applied potentials from -0.7 to +0.4 V, under 100mW/cm^2 illumination. (d) The IPCE spectra of double-sided nanowire samples obtainedwith an incident wavelength of 310-650 nm at 0 V versus Ag/AgCl [125]

As shown in Figure 1.10(c), the double-sided CdS and CdSe QD-cosensitized ZnO nanowire arrays can generate a pronounced photocurrent density of 12 mA/cm^2 at 0.4 V versus Ag/AgCl, which is twice the value of samples sensitized with a single type of QDs. Incident-photon-to-current measurements were performed to quantitatively probe the photoactivity of different photoanodes, and the cosensitized CdS/ZnO/ZnO/CdSe photoanode yields an almost constant IPCE of about 45% within the whole visible light region (400-650 nm), which is overwhelmingly better than other samples. The pronounced performance of this unique

photoanode is mainly attributed to the integration of the advantage of QD sensitization and tandem cell configuration, which simultaneously enhanced the charge carrier collection and visible light absorption.

Miao et al. reported [126] a facile all-electrochemical approach for the fabrication of arrayed ZnO-CdSe coreeshell nanorods for efficient photoelectrochemical water splitting. In this work, both the ZnO nanorods core and the CdSe QDs shell were electrochemically deposited on ITO-coated glass substrates. SEM images of the ZnO-CdSe core shell nanorod arrays show that the CdSe nanocrystals are homogeneously distributed along the entire surface of ZnO nanorods, forming a uniform and dense outer shell. The X-ray diffraction analysis indicates that the organic phase-based CdSe deposition did not affect the crystalline structure of ZnO nanorods. The thickness of the shell can be well tuned through controlling the CdSe deposition duration. In the photoelectrochemical tests, the optimized ZnO-CdSe nanorod arrays can generate a promising photocurrent density of 14.9 mA/cm^2 in 0.2 M Na_2S. Compared to undecorated ZnO nanorod arrays, the ZnO-CdSe nanorods exhibit a significantly enhanced photoresponse within the visible light region, reaching a maximum IPCE value of~34.9%.

1.4. Motivation and Objectives

During the past decade, nanostructured metal oxides with semiconducting properties are very attractive for fabricating low cost optoelectronic devices and chemical gas sensors with high response to hazardous gases. Among the various semiconductor metal oxides, ZnO is most widely investigated because of their attractive properties. Zinc oxide is a semiconductor having wide band gap of 3.37eV and large exciton binding energy of 60meV at room temperature. It shows piezoelectricity and it is nontoxic material. Due to these properties ZnO is a material of huge technological importance; it has application in optoelectronics devices such as solar cell, optical wave guide, LED, transparent thin film transistor and photo detectors. Furthermore, ZnO is inexpensive, chemically stable, easy to prepare and etch, and nontoxic, which also make fabrication ZnO based optical devices an attractive prospect.

Objectives:

Recently, Zinc oxide (ZnO) materials have attracted much interest, for promising application in optoelectronics devices and gas sensors. The main objectives of the work are to synthesis and characterize ZnO based nanostructures for light emission and gas sensing applications. The specific objectives of the work are summarized below:

- Synthesis of pure and doped ZnO nanostructures/ thin films by physical methods such as RF magnetron sputtering and chemical methods such as sol-gel and hydrothermal techniques
- Extensive characterization of structural, optical and luminescent properties of the undoped and doped ZnO films (pure, doped (Li, In, Ga, P and Sb) and co doped (In & Ga)) towards light emission.
- Gas sensing studies of as prepared nanostructures / thin films for toxic gases.

1.5. Conclusion

Zinc oxide is a multifunctional material because of its many interesting properties (piezo- and pyroelectric), a wide range of UV absorption, and high photostability, biocompatibility and biodegradability. ZnO can also be obtained with a variety of particle structures, which determine its use in new materials and potential applications in a wide range of fields of technology. Therefore the development of a method of synthesizing crystalline Zinc oxide which can be used on an industrial scale has become a subject of growing interest in science as well as industry.

As can be seen from the survey of recent literature presented here, particles of Zinc oxide both nano and thin films can be produced by many different methods. Due to the rich basic properties of ZnO, it can be doped by different group member on the periodic table to tune its properties and thus can be very useful applicant for several nano-electronic devices. It can be expected that interest in Zinc oxide will continue to grow, and that this will lead to the development of new possibilities for its application.

CHAPTER 2

Experimental and Characterization techniques

2.1. Film deposition and fabrication

2.1.1. Introduction

2.1.2. Sputtering

2.1.2.1. DC/RF sputtering

2.1.2.2. Magnetron sputtering

2.1.2.3. Advantages of sputtering over other deposition methods

2.1.2.4. Sputter deposition of doped and undoped ZnO thin films

2.1.3. Thermal Evaporation

2.1.4. Sol gel

2.1.5. Hydrothermal

2.2. Film Analysis

2.2.1. Structure determination

2.2.1.1. X-ray Diffraction (XRD)

2.2.1.2. Raman spectroscopy

2.2.2. Surface morphology

2.2.2.1. Field Emission Scanning electron Microscope (FESEM)

2.2.2.2. Atomic Force Microscopy (AFM)

2.2.3. Chemical composition

2.2.3.1. Energy Dispersive spectrum (EDS)

2.2.3.2. X-Ray Photoelectron Spectroscopy (XPS)

2.2.4. Optical Measurements: Spectrophotometer

2.2.5. Film Thickness Measurement by Ellipsometry

2.2.6. Photoluminescence Measurements

2.2.7. Voltage-Current Measurements

2.2.8. Device fabrications: Gas Sensors

2.3. Conclusion

This part is mainly composed of two sections; the first is fabrication and film growth, where the deposition parameters and conditions are illustrated. The second is the film characterization, where the characterization tools and their data interpretation methods are explained

CHAPTER 2

Experimental and Characterization techniques

2.1.Film deposition and fabrication

2.1.1. Introduction

The defect and structural features in ZnO, and thus the film properties, are highly dependent on the method of deposition and specific parameters of that method. Thin films can be synthesized by many different processes. The deposition technique involves three basic steps: (i) Creation of atomic/molecular/ionic species, (ii) transfer of these species through a medium, and (iii) deposition of the species on a substrate. Deposition techniques fall mainly under three categories, depending on the state (physical or chemical) of the materials deposited. Deposition techniques can be broadly classified into three categories and are presented in the Figure. 2.1. First one is the Physical Vapor Deposition (PVD), where the material is ejected from a target and then transferred to the substrate through the vacuum.According to the type of target excitation that causes the ejection of the atoms, different systems are used. Under this category many methods are there, few of them are mentioned below [127]

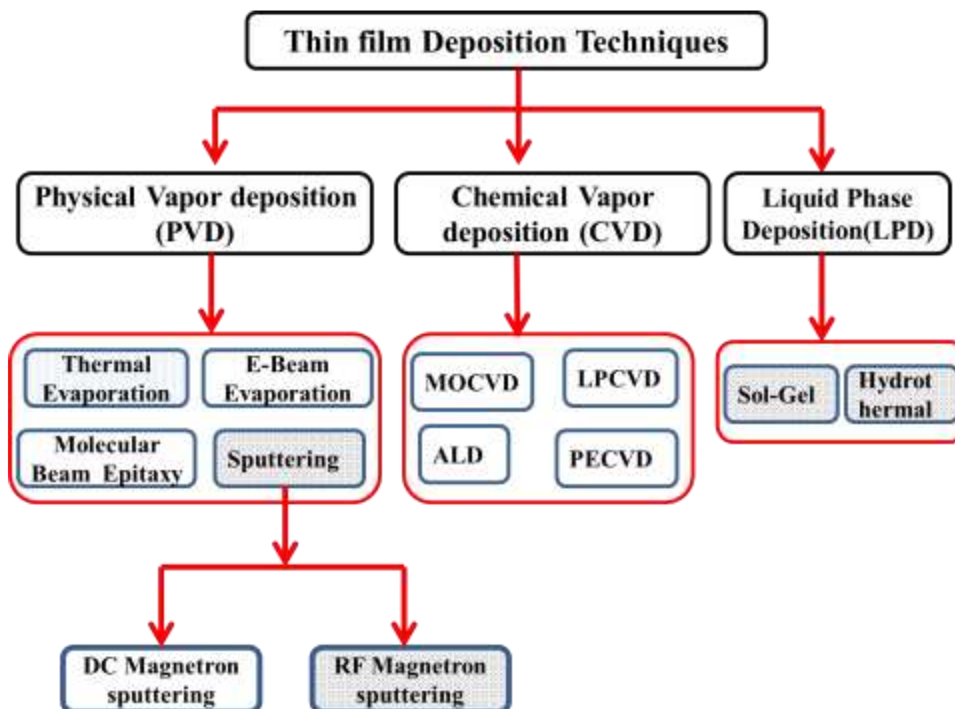

Figure: 2.1 A diagram showing the Thin Films Deposition Techniques

- Thermal Evaporation: The source material to be deposited is evaporated in a vacuum by using an electron beam or resistive heating inside a high vacuum coating chamber. The vacuum allows the vapor particles to travel directly to the substrate where they condense back to a solid state to form a thin film
- Electron-beam Evaporation: This type of evaporation is another method of physical deposition where the intensive beam of electrons is generated from a filament and steered through both electric and magnetic fields to hit the target and vaporize it under vacuum environment. Thin films prepared by electron beam evaporation are of good quality and purity [128]
- Molecular Beam Epitaxy (MBE): is a particular sophisticated form of thermalevaporation.In this technique, slow streams of an element are directed at the substrate, sothat material deposits one atomic layer at a time. The beam of material can begenerated by either physical means or by a chemical reaction (chemical beam epitaxy) [129]
- Sputtering: is a popular method and one of the most flexible deposition techniques for adhering thin films onto a substrate. In this method material targets are bombarding by Argon ions to eject the atoms. The sputtered atoms are condensed on a substrate to form a film [127]
- Pulsed Laser Deposition (PLD): It is an ablation process. High power pulses of laser light are focused on the surface of the target material in a vacuum chamber [127]. This results in vaporization of the target material. The atoms ablated from the target material get deposited on the substrate. Figure 2.2 shows pulsed laser deposition technique.

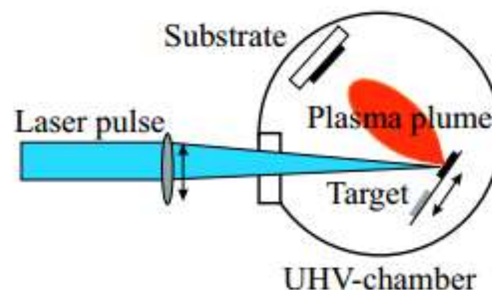

Figure 2.2: Pulsed Laser Deposition Technique

Second category is the Chemical Vapor Deposition (CVD), where the materials are in gas form as it under goes a series of decompositions and reactions before reaching the substrates.

Precursor gases are moved into a chamber with the substrate. The chemical reaction between the substrate and the precursor is continued at high temperature till the desired thickness of the film is obtained. Under this group many methods are there, few of them are mentioned below;

- Plasma Enhanced Chemical Vapor Deposition (PECVD): In PECVD, plasma is formed in a reaction chamber that transforms the gaseous precursors into reactive radicals, ions, neutral atoms and molecules. These atomic and molecular fragments interact with a substrate and this chemical reaction cause to develop a solid layer on the surface at the substrate [127-128]. In PECVD, lower temperatures (300~350 ^{o}C) are used for thin film deposition while in CVD high temperatures (600~90 ^{o}C) are used to develop thin films.
- Low Pressure Chemical Vapor Deposition (LPCVD): is a chemical vapor deposition technology that uses heat to initiate a reaction of a precursor gas on the solid substrate. This reaction at the surface is what forms the solid phase material. Low pressure (LP) is used to decrease any unwanted gas phase reactions, and also increases the uniformity across the substrate.
- Metal-Organic Chemical Vapor Deposition (MOCVD): is a chemical vapour deposition technique using organo-metallic precursors. The principle of MOCVD is to realize the contact between volatile compound material to be deposited and a substrate heated under vacuum. Precursors are transported to the substrate by the carrier gas (argon, nitrogen) and then are adsorbed on the substrate surface. The reactive species thus diffuse at the surface to preferential sites and react in heterogeneous phase to give rise to the formation of the film.
- Atomic layer Deposition (ALD): In Atomic layer deposition, two or more gaseous precursors are used to react with the substrate sequentially one at a time. The thin films obtained by this process are conformal. The process of ALD is divided into two half reactions. These reactions include deposition of precursor and evacuation of the reaction chamber that run in sequence and repeated for each precursor [129]. This chemical reaction occurs on the substrate resulting in the formation of desired film thickness. ALD is a stepwise procedure; therefore it is slower one but can run even on lower temperature.

The third category is the Liquid Phase Deposition (LPD), such as Sol-gel and hydrothermal. Each of the previously mentioned categories has its advantages over the others.

2.1.2. Sputtering

Sputtering is a vital and prominent procedure among the PVD processes. When a solid surface is bombarded with energetic ions, surface atoms of the solid are scattered due to collisions between the surface atoms and the energetic particles. This process of ejecting atoms from the surface by bombardment of positive ions (usually inert gas ions), by momentum transfer process between the sputter gas and target atoms is commonly known as sputtering (cathode sputtering) [130-131].The ejected atoms can be made to condense on a substrate at an optimal distance from the target to form a film.

In a typical sputtering deposition process, a chamber is first evacuated to high vacuum to minimize the partial pressures of all background gases and potential contaminants. After base pressure has been reached, sputtering gas which comprises the plasma is flowed into the chamber and the total pressure is regulated – typically in the milli Torr range – using a pressure control system. To initiate plasma generation, high voltage is applied between the cathode – commonly located directly behind the sputtering target – and the anode – commonly connected to the chamber as electrical ground. Electrons which are present in the sputtering gas are accelerated away from the cathode causing collisions with nearby atoms of sputtering gas. These collisions cause an electrostatic repulsion which 'knock off' electrons from the sputtering gas atoms, causing ionization. The positive sputter gas atoms are now accelerated towards the negatively charged cathode, leading to high energy collisions with the surface of the target. Each of these collisions can cause atoms at the surface of the target to be ejected into the vacuum environment with enough kinetic energy to reach the surface of the substrate. In order to facilitate as many high energy collisions as possible – leading to increased deposition rates – the sputtering gas is typically chosen to be a high molecular weight gas such as argon or xenon. If a reactive sputtering process is desired, gases such as oxygen or nitrogen can also be introduced to the chamber during film growth. The sputtering yield 'S' (number of atoms ejected from the target surface per incident ion) depends on the target material composition, binding energy, characteristics of the incident ion and the experimental geometry. It also depends on the voltage and current (sputter power) at which sputtering takes place.

2.1.2.1. DC/RF sputtering

Depending on the type of power supply used in the sputtering process, it is classified into DC or RF sputtering. Magnetron sputtering using DC power is an effective and economical

choice for depositing conductive materials such as metals or transparent conductive oxides (TCOs). For magnetic materials such as Fe (iron), Ni (nickel), or Co (cobalt), DC magnetrons can be configured with magnets specifically selected for generating plasma within a strong magnetic field. Sputter deposition of insulating materials cannot be done with DC power. Materials such as oxides, nitrides, and ceramics have very large DC impedance and require prohibitively high voltages to ignite and maintain plasma. Using power delivered at radio frequencies (RF) – typically at 13.56 MHz – and an automatic impedance matching network, the total impedance of the circuit can be regulated to 50 Ω which is suitable for plasma ignition in typical sputtering environments. RF sputtering has to be used to avoid charge build-up when an insulating target is used. In case of insulators after the ions strike the surface, their charge will remain localized and with passage of time positive charge will build up on the target, making it impossible to further bombard the surface. This can be prevented by bombarding the insulator by both positive ions and electrons simultaneously [130-133]. It is done by applying a RF potential to the target. The RF potential provides sufficient energy to the electrons oscillating in the alternating field to cause ionizing collisions, and a self-sustained discharge is maintained (Figure 2.3). As electrons have higher mobility compared to ions, more electrons will reach the insulating target surface during the positive half cycle than the positive ions during the negative half cycle. Hence the target will be self-biased negatively. This repels the electrons from the vicinity of the target and forms a sheath enriched in positive ions in front the target surface. These ions bombard the target and sputtering is achieved. At a frequency less than 10 kHz such an ion sheath will not be formed. Typical RF frequencies are employed in the range from 5 to 30 MHz. However, 13.56 MHz is the most general frequency used for RF sputtering.

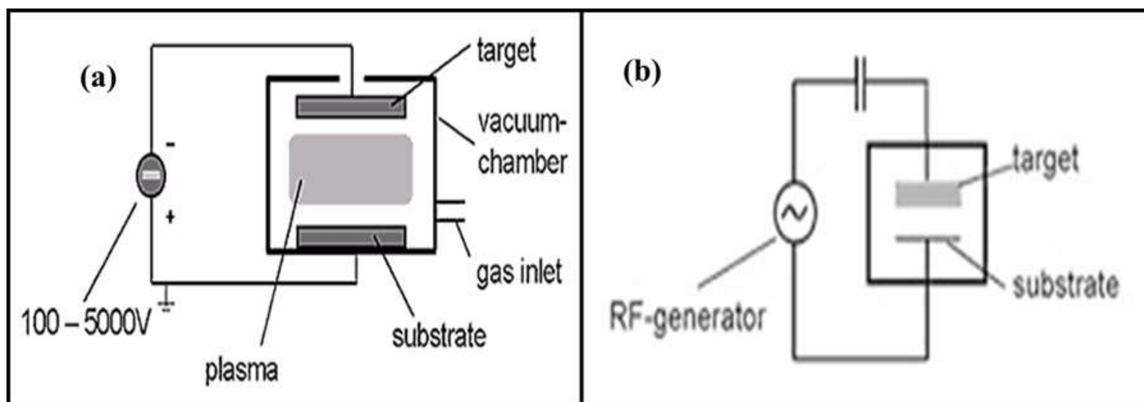

Figure 2.3 Block diagram of (a) DC and (b) RF sputtering system

2.1.2.2. Magnetron sputtering

Magnetron sputtering is considered as the most effective process for the deposition of a wide range of thin film materials [130]. In many cases, magnetron sputtered films now overtake films deposited by other physical vapour deposition processes, and can offer the same functionality as much thicker films produced by other surface coating techniques. Magnetron sputtering systems generate a strong magnetic field near the target area, which causes the travelling electrons to spiral along magnetic flux lines near the target. This arrangement confines the plasma near the target area without causing the damage to the thin films being formed on the substrate, and maintains the stoichiometry and thickness uniformity of the deposited thin film. Moreover, in an R.F. magnetron sputtering systems, the generated electrons travel a longer distance, hence increasing the probability of further ionizing the inert gas atoms (Ar^+) and generating stable high-density plasma that improves the sputtering process efficiency. Figure 2.4 illustrates the basic components of an R.F. magnetron sputtering system and Figure 2.5 shows actual photograph two target sputtering system. Briefly, ionized Ar atoms bombard a sputtering target, thus releasing the molecules/atoms that form thin layers on a substrate. R.F. magnetron sputtering offers additional advantages, including the use of non-conductive targets, charge-up effects and reduced arching due to the use of alternating electric field (R.F. frequency). It is important to note that R.F. magnetron sputtering has advantageous in the deposition of thin films using non-conductive target materials. This is at the cost of R.F. power supplies and an impedance matching network between the R.F. generator and the sputtering target. It should also be noticed that without the use of a magnetron, the non-conducting materials may have more difficulty forming into a thin film as they become positively charged. Reactive sputtering can also be used, whereby the deposited film is formed by chemical reaction between the target material and the gas introduced into the vacuum chamber [131,134]. The work presented in thesis (chapter 3-6) was prepared by RF magnetron sputtering.

2.1.2.3. Advantages of sputtering over other deposition methods

In sputtering, the entire surface of the target act as the source, unlike evaporation process where a point (where electron beam hits) on the target is the source. In sputtering the evaporated atoms bombard the substrate surface, rearrange themselves and then condense on the substrate. Higher kinetic energy of the sputtered particles (~ tens of eV) giving rise to better adhesion to the substrate. By incorporating target cooling provision in sputtering, higher melting point

elements can be deposited. Some of the main advantages of sputtering as a thin film deposition technique are due to high kinetic energy of the sputtered atoms, causing their re-distribution on the substrate, leading to (a) high uniformity, density and interface roughness of the deposited film (b) deposition over large surface area [130]. By incorporating target cooling provision in sputtering, higher melting point elements can be deposited. With a better understanding of the sputtering processes, it has become one of the versatile methods for preparing high quality thin solid films of any material.

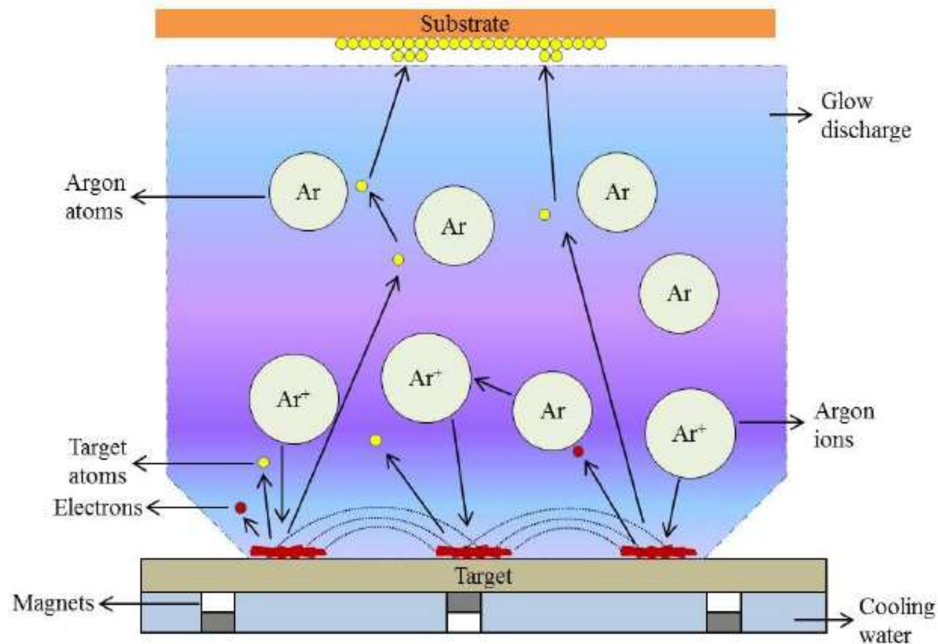

Figure.**2.4** Block diagram of Magnetron sputtering

Many parameters that affect the deposition process in sputtering such as: base vacuum, sputter gas pressure during deposition, sputter power, target and substrate temperature etc. The microstructure of the film or its quality which includes surface roughness, adhesion, impurity, density of the film produced by sputtering process is a result of interplay of the above parameters [130]. Contribution of such a large number of parameters makes the process complex but also provides a large degree of control over the film growth process, if optimized properly.

2.1.2.4.Sputter deposition of doped and undoped ZnO thin films

- **Substrate Cleaning**

In this study, the undoped and doped ZnO films were deposited on glass substrates, Silicon wafers (for Raman measurements) and ITO (for devices) substrates. Before use for sputtering deposition, the substrates were cleaned in an ultrasonic bath using by tri-chloro

ethylene, methanol and acetone around 10 minutes, then rinsed by deionized water around 10 minutes in order to ensure that no organic material remaining on the glass surface. After that the substrate was dried. Then the substrate was introduced to a load-lock chamber for depositions.

Figure.**2.5** Photograph of the Two target Sputtering System

- **Target preparation**

Doped and undoped ZnO films were fabricated on glass and p type Si (100) substrate by RF magnetron sputtering using a powder target under O_2 and Ar ambient. A host of commonly deployed targets are available commercially but the target preparation becomes very expensive and difficult which limit the choice of using complex or mixed oxides. To overcome such constraints, we have used in-house made powder targets to achieve the desired doping levels in ZnO films.

Sputtering targets were prepared in-house using powders of ZnO and other oxides like Sb_2O_3, P_2O_5, Ga_2O_3, etc for doped ZnO films. Stoichiometric quantities of metal oxides (99.99%, May and Baker Ltd) and ZnO (99.9%, May and Baker Ltd) powders were weighed, mixed and ground for few hours. Then the mixture was evenly spread on a copper holder of 2" diameter and made compact by manually pressing with a solid piece of stainless steel. No further processes

were involved in the target preparation. Thus the preparation of sputter target was simple and economical, in addition to the flexibility of changing the composition for doped films.

- **Film deposition**

After the substrate and targets were prepared, the next step is to deposit ZnO film on substrate. Once the target is mounted in the sputter head, a power supply applies a high voltage to the sputter head and target. This voltage ionizes Ar gas in the chamber. The Ar ions bombard the target, knocking material off which then travels down to the substrate and forms a film. To improve efficiency, the sputter head contains a large magnet which confines the plasma near the target. Additionally, the applied voltage is actually an oscillating rf signal, which prevents charge buildup on the surface of the target to allow sputtering of insulating materials. Here are more specific steps regarding operating the sputtering system. First, turn on the water cooling and open the Ar, O_2 gas. Next, place the substrate on the substrate heater. Close the lid and evacuate the system and leave the vacuum running and open to the chamber. Set the substrate heater to the desired temperature and turn on the high voltage. Next, open the valves on the Ar and O_2 gas tanks, which should both be set to required amount for proper flow controller function. If either of the lines had lost pressure before opening the valves, they should be purged by flowing with no voltage on the sputter head for 15 min before sputtering.

The next step is striking plasma (Figure 2.6). Turn on the rf sputter power supply to 75 W and turn on the matching network as well. Turn on the flow controllers. Since the shutoff valves located above the flow controller box are still off, the flow controllers open wide but no gas flows yet. Next, when the shutoff valves are opened, they at first allow much more gas into the chamber than the settings dictate, but then quickly fall to the desired level. This pressure spike makes it much easier to strike plasma. At this point, there should be bright violet plasma visible in front of the sputter head. If so, sputtering is underway, and the user need only wait several minutes until the film has reached the desired thickness. To shut off the system, turn off the flow controllers and shutoff valves, power down the sputter power supply, and turn off the substrate heater. When it has cooled somewhat, turn off the vacuum system (ensuring that the turbo pump is isolated from the chamber) and the chamber can then be vented and opened. Inside is a reflective, often intriguing ZnO film ready for characterization. The optimized parameters for the deposition was given in the table: 2.1

Table.2.1 The optimized parameters for the deposition of RF sputtered undoped and doped ZnO thin films

Base pressure	**1.5 x 10^{-2} mbar**
RF Power	**75 W**
Substrate Temperature	**100 ^{o}C**
Sputtering time	**120 minutes**
Gas flow rate (Ar + O_2)	**20+ 20 sccm**
Pre- sputtering	**10 minutes**

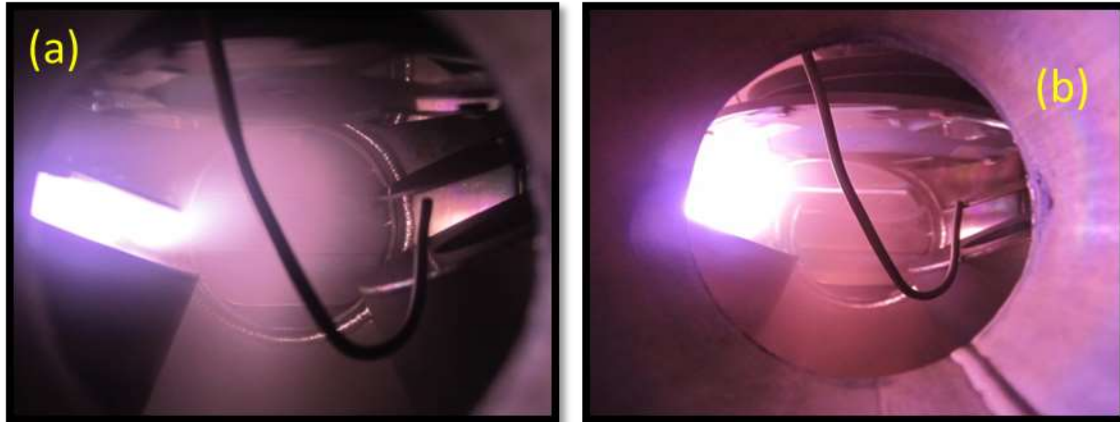

Figure 2.6 Photograph of the plasma when shutter is (a) closed & (b) open.

2.1.3. Thermal evaporation

Thermal Evaporation is a common method of thin-film deposition. The source material is evaporated in a vacuum. The vacuum allows vapor particles to travel directly to the target object (substrate), where they condense back to a solid state. Evaporation is used in micro fabrication, and to make macro-scale products such as metalized plastic film [135]. Figure 2.7 refers to the block diagram of Thermal Evaporation System.

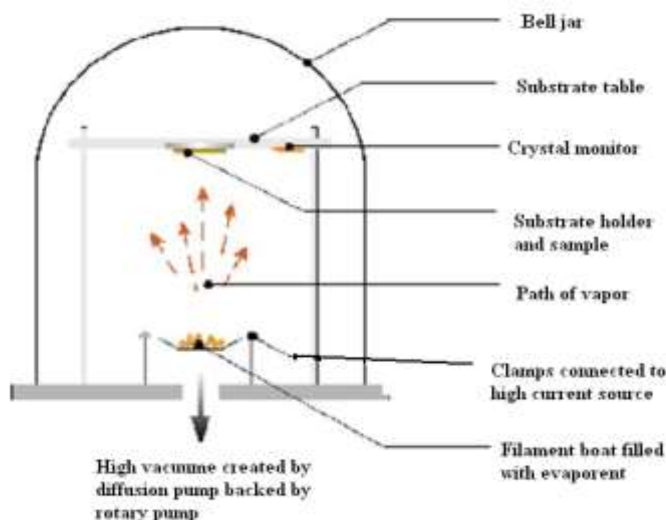

Figure 2.7 Block diagram of Thermal Evaporation System

A thermal evaporator uses an electric resistance heater to melt the material and raise its vapor pressure to a useful range. This is done in a high vacuum, both to allow the vapor to reach the substrate without reacting with or scattering against other gas-phase atoms in the chamber, and reduce the incorporation of impurities from the residual gas in the vacuum chamber. Thermal evaporation is the simplest way of depositing material onto a substrate. One major disadvantage of this is that a lot of material is lost in the process. Thin film deposition is done in two steps, first evaporation of material by means of an electrical current passing through a filament or metal plate where the material is loaded (Joule effect) and recondensation of vapours on the substrates desired. Usually low pressures are used, about 10^{-6} or 10^{-5} Torr, to avoid reaction between the vapour and atmosphere. At these low pressures, the mean free path of vapour atoms is of the same order as the vacuum chamber dimensions, so these particles travel in straight lines from the evaporation source towards the substrate. In thermal evaporation techniques the average energy of vapour atoms reaching the substrate surface is generally low (order of kT, i.e. tenths of eV). This affects the morphology of the films, often resulting in a porous and less adherent material. Typical metals used as filaments or boats (heating resistance) are tantalum (Ta), molybdenum (Mo) and tungsten (W), with vapour pressure practically zero at the evaporation temperature (T_{evap} = 1000-2000 °C). In the present work contacts on devices are

prepared using HIND HIVAC make thermal evaporation system. Figure 2.8 show the picture of the thermal evaporation system used for this work.

Figure 2.8 Photograph of the thermal evaporation system

2.1.4. Sol gel

Sol-gel processing is one of the main solution deposition techniques of thin films. It is a self-assembly process which employs a series of hydrolysis and condensation reactions. In solution, precursor monomers cross link to form clusters which grow into nanoparticles, producing a colloidal suspension [136]. The liquid is then applied onto the substrate to form a thin film, via spin or dip coating processes. After coating, heat is applied to hasten evaporation of the solvents causing the final stage of gelation to occur rapidly. The coating can be repeated a number of times to increase the film thickness. Often this will be followed by additional thermal treatments at higher temperatures, to anneal the coating. The annealing process allows the constituent atoms to diffuse through the material to form a dense polycrystalline film [137], and allows defect and impurities to migrate to the surface and out of the material. ‘Sol’ includes metal alkoxides or metal salts as precursors (starting material) and their appropriate solvents. Moreover, sol may contain some functional additives such as stabilizers that chemically improve the homogeneity of sol. The liquid-filled solid network called ‘gel’ is originated by the linking

colloidal particles with one another in 3D structure. The transformation from sol to gel is most commonly induced by changing the pH value of the sol via catalysts such as acids and bases. The catalysts initiate the sol to gel transformation by affecting the overall hydrolysis and condensation rates. As a result, characteristic of gel, such as structure of the chains or groups, time required for gelation. In addition sol-gel offers low temperature route for production of complex/functional oxide structures and deposition of sol onto complex-shaped or large surfaces [136,138]. It has several chemical and physical steps which are hydrolysis, condensation, drying and densification. It is possible to fabricate high purity products such as micro and nano particles in different size/shape, fibers, membranes, powders and coatings by sol gel process as shown in Figure 2.9. This technique is promising with its low cost, simple equipment requirement and scalability. In addition, it allows stoichiometry-controlled production of multicomponent materials and the reproducible deposition of high purity thin films, practiced by spray, dip and spin coating techniques for the fabrication of thin film.

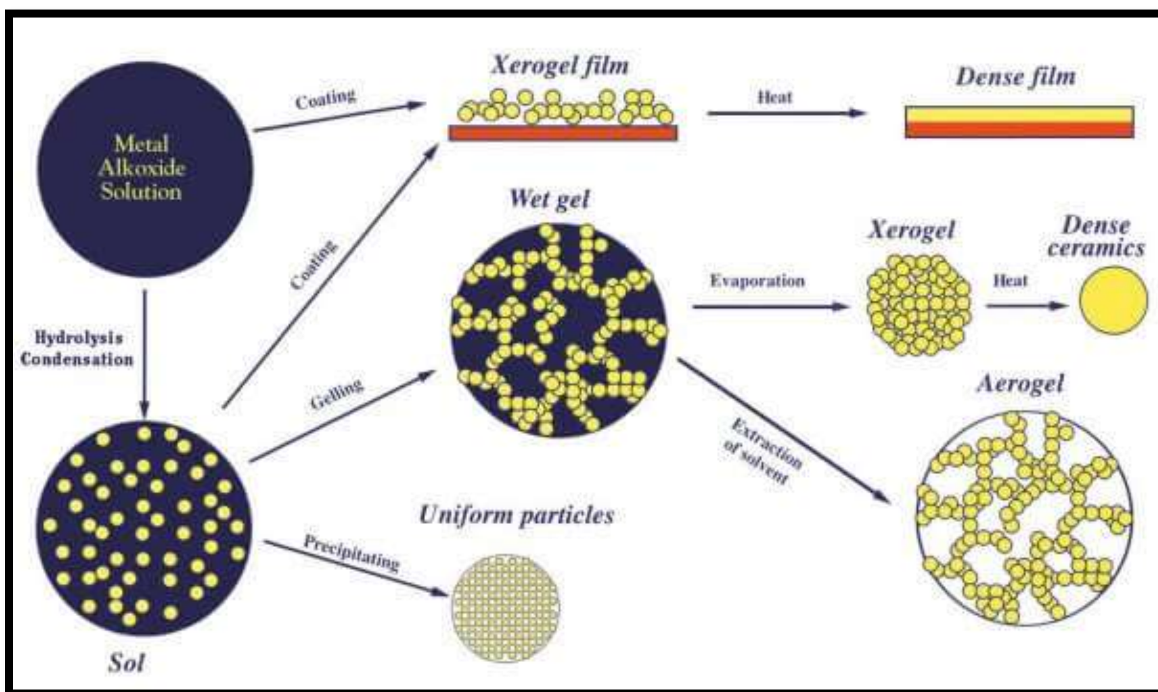

Figure.**2.9** Schematic of various routes in the sol-gel process, a metal oxide film can be produced by spin-coating a precursor solution or sol to form a dried gel (xerogel), and then using a thermal treatment to densify the film.

The schematic of sol-gel method, retrieved from Spin coating is widespread practice to obtain quite dense and uniform thin films from few nanometers to few micrometers in thickness

on flat surfaces. Spin coating enables the production of single/multi-layered thin films quick, easy and reproducible; therefore, it is widely used in variety of industries and technological applications. However, the foremost weakness of this technique is that spin coating is applicable on flat surfaces only. This technique is mainly based on the draining by centrifugal force and evaporation of solvent deposited thin film. Duration and speed of spin, viscosity and surface tension of sol, volatility of the solvent used in formation of sol are detrimental parameters to achieve dense, smooth and uniform coatings [136]. Spin coating process is composed of four steps which are deposition, spin-up, spin-off and evaporation. These steps are given in Figure 2.10 schematically.

i. Deposition: to get completely wet surface, surface of the substrate is coated by excess amount of sol.

ii. Spin-up: substrate is accelerated up to the final selected speed for desired time; therefore, by the effect of centrifugal force, sol covers all over the surface and excess of the sol is flung off the surface.

iii. Spin-off: substrate starts spinning at constant speed. In this step, viscous forces lead to fluid thinning mechanism and edge effects are commonly observed due to the high spin speed.

iv. Evaporation: coating thinning mechanism dominates and almost all solvent evaporates simultaneously in this step of the processing; since, a solvent used in composition of sol is typically volatile, such as alcohols. Transformation from sol to gel starts following evaporation of solvent. The detailed description of sol-gel process used in this thesis is given in chapter-6.

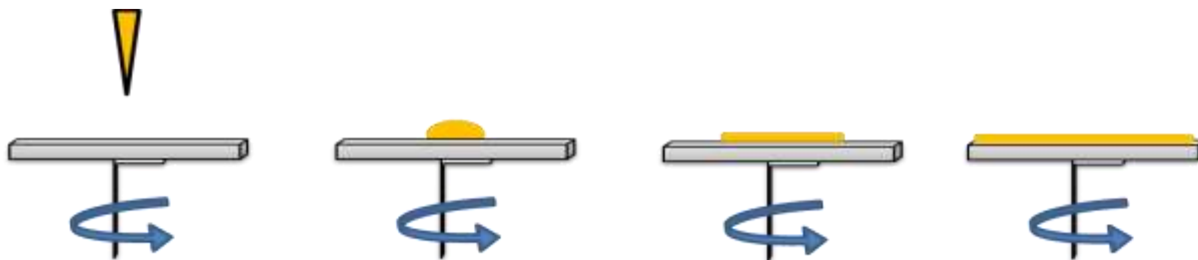

Figure .2.10. Schematic representation of typical spin-coating process: First the solution is applied to the substrate; then the substrate is rotated with the desirable rotational speed; the solution spread over the substrates and finally uniform thin film will be obtained.

2.1.5. Hydrothermal

Hydrothermal technique is a promising method because of the low process temperature and very easy to control the particle size. The hydrothermal process have several advantages over other growth processes such as use of simple equipment, catalyst-free growth, low cost, large area uniform production, environmental friendliness and less hazardous. The low reaction temperatures make this method an attractive one for microelectronics and plastic electronics [139]. This method has also been successfully employed to prepare nano-scale ZnO and other luminescent materials. The particle properties such as morphology and size can be controlled via the hydrothermal process by adjusting the reaction temperature, time and concentration of precursors. Generally, this method includes chemical reactions in aqueous solutions. These reactions can be considered to be in reversible equilibrium and the driving force is the minimization of the free energy of the whole reaction system.

2.2. Film Analysis

In general, Characterization of thin films is carried out to investigate their optical, electrical and mechanical properties along with their crystallinity, microstructure and chemical composition. A brief discussion about X-raydiffraction (XRD), Scanning electron microscope (SEM), Atomic force microscope (AFM), Energy dispersive X-rays (EDX), and Ultraviolet-visble (UV-VIS) spectrophotometer has been included here.

2.2.1. Structure determination:

2.2.1.1. X-ray Diffraction (XRD)

X-ray diffraction (XRD) analyses were performed to examine crystalline state and to determine the crystal structure of doped and undoped nanostructured ZnO films. X-rays diffraction (XRD) is a rapid and a powerful technique used to study the phase of a crystalline material, information on unit cell lattice parameters, crystal structure, crystal orientation and crystallite size. The working principle of the XRD technique is depends on constructive interference of X-rays and a crystalline sample. In a crystal, the atoms distribute regular in space, which comes into being crystal lattices. These lattices form a series of parallel planes with spacing distance d. The x-rays are generated by a cathode ray tube (X-ray produced by the impact of accelerated electrons with heavy metal such as Cu), filtered to produce monochromatic X-ray radiation which directed toward the sample [140]. When X-rays light with wavelength λ is

incident onto a crystal lattice at an angle θ, the interaction of the incident X-rays with the sample provides constructive interference if the conditions satisfy Bragg's law

$$n\lambda = 2d_{hkl} \sin\theta \qquad \textbf{2.1}$$

where n is an integer 1, 2, 3….. (Usually n =1), λ is wavelength in angstroms (1.5418 Å for CuKα), d_{hkl} is spacing between the planes, the θ is the angle between the incident light and the lattice planes, the 2θ is angle between the incident and scattered beams, the angle 2θ of maximum intensity is called the Bragg angle. All diffraction directions of the lattice will be generating by scanning through a range of 2θ angles on the sample. Figure 2.11 illustrates the reflection of X-rays from two planes of atoms in a crystal solid.

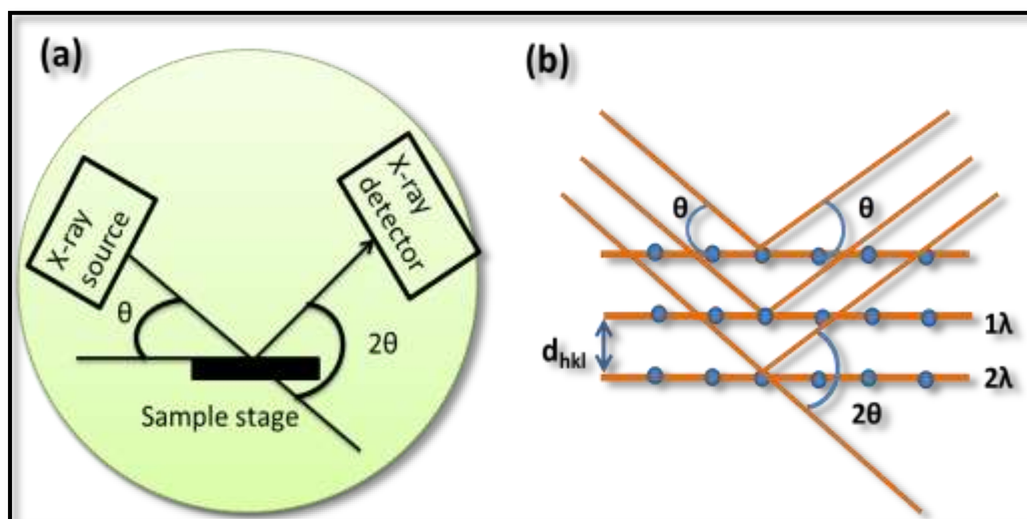

Figure.**2.11** Schematic of (a) XRD setup and (b) Bragg's law

In XRD, a collimated beam of X-rays typically ranging from 0.5-2.5 Å is used as a source. For diffraction a monochromatic X-ray source is needed and the source is generally a metal anode bombarded by high energy electrons which gives off both characteristics line spectrum X-rays and continuum (bremsstrahlung) radiation (Figure 2.11). Generally the stronger Kα characteristic line radiation is used, and the Kβ radiation is filtered. In the Bruker system a Cu Kα X-ray source is used in which $\lambda = 1.54 \times 10^{-10}$ m is produced. The purpose of the Göbel mirror (a curved mirror) is to collimate the divergent beam coming from the point-like source in the X-ray tube anode. The mount in the diffractometer where the sample sits is called the goniometer. The goniometer allows the altering of orientation of the sample. Depending on the number of degrees of freedom of goniometer, and the allowed movement of the source and/or the detector the XRD system can be called a 'one-circle', 'two-circle' diffractometer …etc. The

diffractometer used for this thesis work is a 'four-circle' diffractometer, a three circle goniometer plus a movable detector. The function of the soller slit is to remove any randomly scattered nonparallel X-rays. The detector used is a scintillation detector, which is a single photon detector. When the incident X-ray strikes the fluorescent crystal (scintillator) at the front of the detector a visible photon is produced. A photocathode struck by a photon ejects an electron. A series of dynodes after the scintillator/photocathode amplifies the electron into a detectable electrical pulse.

The grain size was determined via the known scherrer's equation as shown:

$$D = \frac{0.9\lambda}{\beta\cos\theta} \qquad \textbf{2.2}$$

Where D is the grain size, (λ=0.154 nm) is the x-ray wavelength, β is the FWHM in radians and θ is the Bragg's diffraction angle. From these XRD pattern, the lattice parameter of the samples can be estimated by equations. 2.3-2.10.The lattice constants 'a' and 'c' and the spacing d_{hkl} for the wurtzite structure of ZnO can be calculated using the relations [141-144]

$$a = \sqrt{\frac{1}{3}}\frac{\lambda}{\sin\theta} \qquad \textbf{2.3}$$

$$c = \frac{\lambda}{\sin\theta} \qquad \textbf{2.4}$$

$$\frac{1}{d_{hkl}^2} = \frac{4}{3}\frac{h^2 + hk + k^2}{a^2} + \frac{l^2}{c^2} \qquad \textbf{2.5}$$

$$\delta = \frac{1}{D^2} \qquad \textbf{2.6}$$

$$\varepsilon = \frac{\beta\cos\theta}{4} \qquad \textbf{2.7}$$

where D is grain size, β is full width at half maxima, δ is dislocation density, ε is lattice strain.

Bond length was calculated by the relation as

$$l = \sqrt{\frac{a^2}{3} + (1/2 - u)^2 c^2} \qquad \textbf{2.8}$$

where a and c are lattice parameters, and u is defined as positional parameter of the wurtzite structure which is given by

$$u = a^2 / 3c^2 + 0.25 \quad \textbf{2.9}$$

The cell volume and the number of atoms per unit cell for the ZnO samples with hexagonal form are estimated using equations [145]

$$V = \frac{3\sqrt{3}}{2} a^2 c$$

$$n = \frac{4\pi}{3V}\left(\frac{D}{2}\right)^3 \quad \textbf{2.10}$$

where a and c are lattice parameters, D is the crystallite size (nm).

In this work, XRD (Bruker D8 Discover advance high resolution XRD with CuKα and λ = 1.5406 Å) was used for all measurements (Figure 2.12). The sample was mounted on a rotating stage using double-sided tape. However, θ offset correction was required during the alignment procedure. After the initial alignment and positioning of the sample took place, θ-2θ measurements performed. Intensities of the reflected x-ray radiation were recorded for the preferred range of θ and 2θ angles. Each observed peak corresponds to a set of planes perpendicular to the sample surface. The measurement has been done in the range of 2θ from 20° to 80° using a Ni filter to cut Kβ radiation, with sampling step of 0.05°. The scan speed was adjusted depending on measured samples in order to obtain enough signals to noise ratio of each peak. The spectra provide information about the crystal structure, thin film texture, grain size, and lattice parameters. All peaks match well with the positions reported for wurtzite ZnO [ICDD No. 36-1451].

2.2.1.2. Raman spectroscopy

Raman spectroscopy was used for investigation of vibrational, rotational and low frequency modes in the crystal in order to confirm the thin film formation and determine the crystal structure. The general setup for Raman scattering experiments is shown in Figure.2.13 and consists of a monochromatic light source for excitation, optical equipment to bring the laser beam on the sample and collect the scattered light, a spectrometer to analyze the scattered light and a detector to collect the signal. Monochromatic laser light is focused on a sample; the scattered light is collected, and analyzed by a spectrometer and a CCD detector. The Raman spectra were recorded on undoped and doped multi-layer ZnO thin films deposited on silicon wafer substrates. Moreover, the spectra were acquired on the bare substrates as a reference.

Figure 2.12. Actual picture of X-ray diffraction machine

The measurements were performed at room temperature on an instrument (Jobin Vyon Labram HR800 Spectrometer) equipped with an optical microscope of 100 X objectives, in a frequency range of 200-900 cm^{-1}. He-Ne laser operating at 632.8 nm was used for excitation of the Raman signal with appropriate holographic notch filters for eliminating the laser line after excitation. The slit width of the spectrometer was typically set at 100 μm. A holographic grating having 1800 grooves/ mm and a charge-coupled device (CCD) detector were used for the collection of all Raman spectra. The resolution was ±1 cm^{-1}. When the sample is excited by a laser, scattering will occur. Two kinds of scattering can be distinguished: the Rayleigh scattering and Raman scattering. For Rayleigh scattering, the scattering light has the same frequency as the incident one, as the elastic interaction happens between the incident photons and the atoms in the sample system. On the contrary, for the Raman scattering, the energy of the scattered light is different from the incident one. If the light beam loses energy during the interaction, the phenomenon is called Stokes scattering, whereas it is referred to as anti-Stokes scattering in the inverse case. The difference between the scattered and incident light can be used to identify the sample in terms of the characteristic vibrational modes [147].

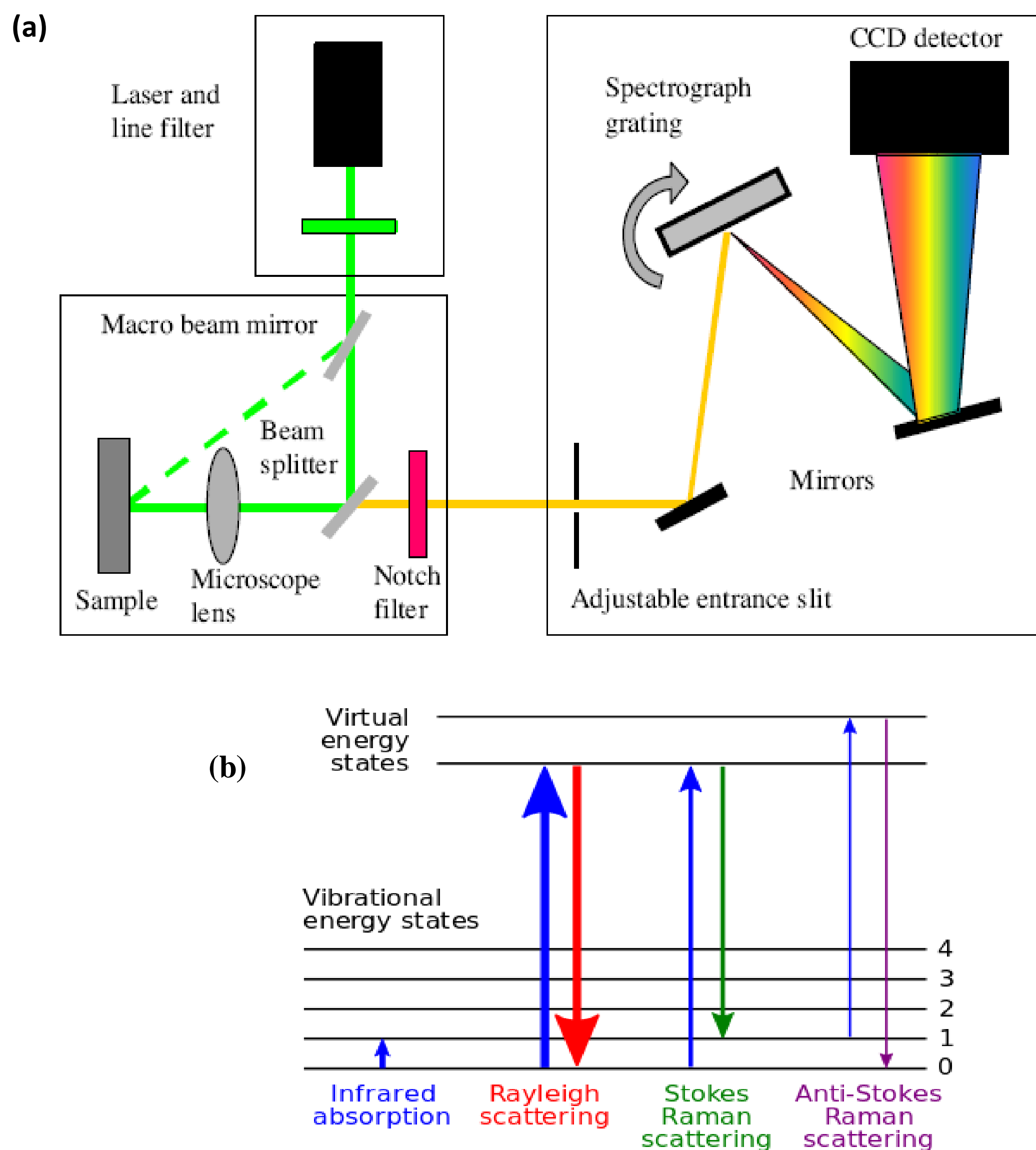

Figure.**2.13** (a) & (b) Schematic representation of the theory of Raman Spectroscopy [147]

ZnO structures grown by different techniques that are often possess a wurtzite crystal structure with C_{6v}^{4} symmetry and two formula units in the primitive cell [148]. The optical phonon modes of ZnO crystals are classified as $A_1+E_1+2E_2+2B_1$, where A_1 and E_1 are polar and split into transverse (TO) and longitudinal (LO) optical phonons. Non-polar phonons with E_2 symmetry show two different frequencies in the Raman spectrum, while B_1 modes are Raman silent. The E_2 phonon modes are related to the oxygen and zinc sub-lattices in the ZnO crystal, also described as E_2(H) and E_2(L), respectively [6]. The possible vibrational modes in ZnO crystal are shown in Figure 2.14.

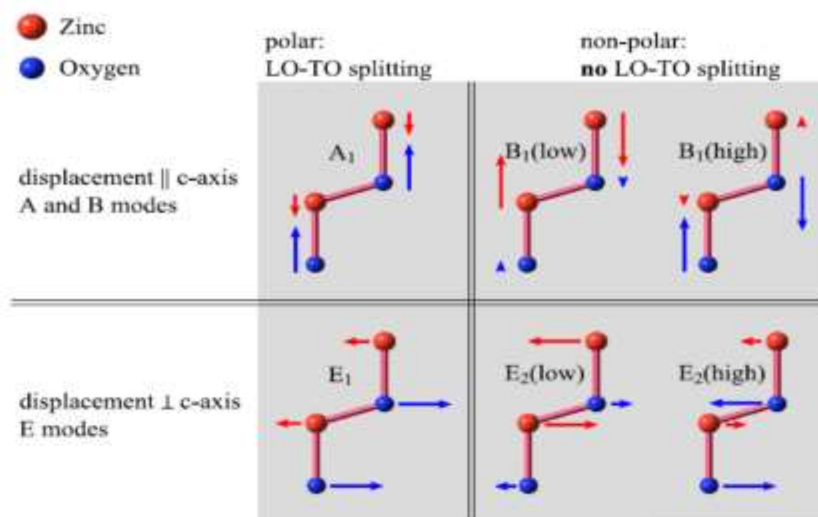

Figure 2.14 Possible vibrational modes in ZnO crystal.

2.2.2. Surface morphology

2.2.2.1. Field Emission Scanning electron Microscope (FESEM)

Field emission scanning electron microscopy (FESEM) generates images from electrons instead of light for conventional optical microscopy. A beam of electron is produced and accelerated from a field-emission cathode in an electron gun. The generated electron beam is then focused onto the sample surface by a series of condenser and objective lenses in a vacuum tube. A scanning coil moves the beam across the sample surface. The electron beam interacts with the sample and produces various types of signals including backscattered electrons, secondary electrons, Auger electrons, characteristic x-rays, etc. The signals, typically secondary electrons signals in standard SEM, are collected by a detector, and amplified and converted to a cathode ray tube image. The contrast in the final image depends on the sample and the equipment setup, providing information on the sample composition, topography and morphology [149].

For principle operation as presented in Figure 2.15, electrons are liberated from a field emission source and accelerated in a high electrical field gradient. Within the high vacuum column these so-called primary electrons are focused and deflected by electronic lenses to produce a narrow scan beam that bombards the object. As a result secondary electrons are emitted from each spot on the object. The angle and velocity of these secondary electrons relates to the surface structure of the object. A detector catches the secondary electrons and produces an

electronic signal. This signal is amplified and transformed to a video scan-image that can be seen on a monitor or to a digital image that can be saved and processed further.

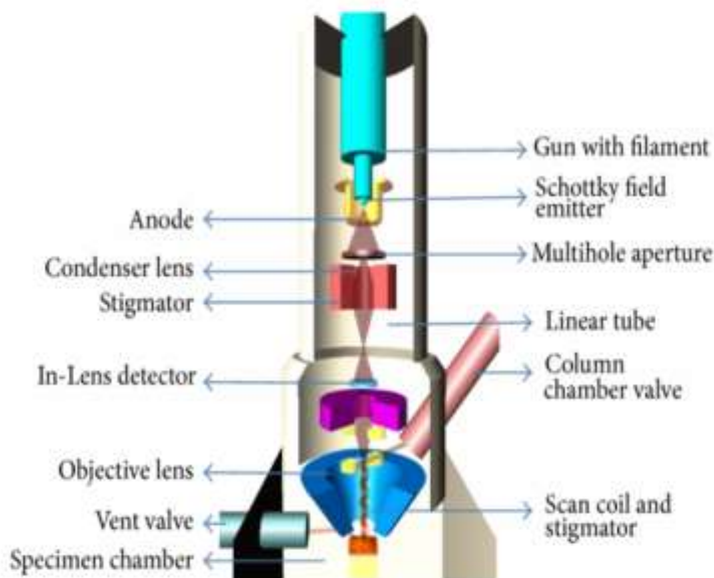

Figure 2.15 Principle of FESEM operations [149]

Compared to the optical microscopy, the main advantages of using electrons for image formation are high resolution (three to six times better), high magnification up to 500,000X, and large depth of fields or effective focus range. Compare to the conventional SEM, the FESEM provides narrower probing beams at both low and high electron energy, resulting in improved spatial resolution down to 1.5 nm (three to six times better). Furthermore, the problem of electrical charging of samples can be minimized by low accelerating voltage (in the range of 0.5 to 30 kV), and the low-kinetic-energy resulted from low accelerating voltage reduces penetration depth into the material. In this work an FESEM Nova device was used to investigate the grown samples, equipped with energy dispersive X-ray analyzer operated at 20 kV. A gold layer of approximately 2-3 nm was deposited onto samples in order to reduce the charging effects during SEM analyses.

2.2.2.2. Atomic Force Microscopy (AFM)

The Atomic Force Microscope (AFM) has been widely used to create a three-dimensional profile of samples' surfaces on a nanoscale. This is achieved by monitoring a deflection of a very fine and flexible cantilever when it is scanned over an uneven surface. Importantly, AFMs are also extensively applied to estimate the sample's surface roughness. Generally, an AFM is composed of a very sharp tip attached to the free end of a flexible cantilever, a laser source, a

photodiode and a piezoelectric scanner as depicted in the simplified Figure 2.16. When the tip is scanned over the surface of the sample various forces such as the Van der Waals, electrostatic and magnetic forces will interact with the tip leading either to a static deflection of the cantilever when the tip is actually in contact with the surface or a change in the fundamental resonant frequency of the cantilever when the tip is brought very close to the sample's surface.[150]. In the first case the AFM is operated in the contact mode where the tip touches the surface as it is moved but when the cantilever is vibrated hence the AFM is said to operate in dynamic or non-contact mode. In the case of the contact mode, the magnitude of the cantilever deflection can be precisely measured by shining a laser beam on the back of the tip and continuously monitoring the reflected beam changes which can be directly related to the deflection magnitude. Therefore, the cantilever displacements can be converted into electrical signals and then processed for creating an image. However, for the non-contact mode the cantilever is mechanically vibrated at or close to its natural resonant frequency utilizing a piezoelectric crystal. The oscillated tip is systematically scanned over the surface of the sample and the oscillation is monitored where any changes in the oscillation wave properties such as frequency, amplitude or phase is attributed to the surface features and hence topographical images can be created [150]. Microstructural details and roughness of the film surface were examined at sampling sizes of 1 x 1 μm using Solver pro SPM.

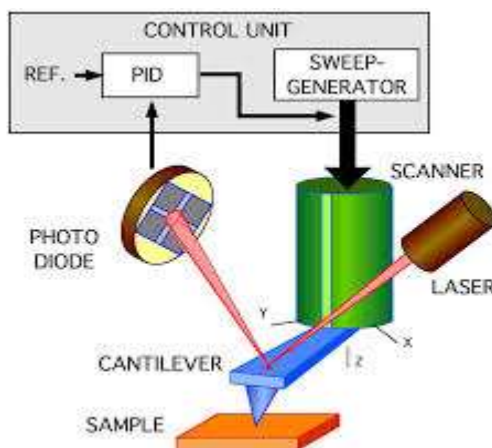

Figure.2.16. Schematic diagram of atomic force microscopy [150]

2.2.3. Chemical composition

2.2.3.1.Energy Dispersive spectrum (EDS)

It is an analytical technique used for the elemental analysis or chemical characterization of a sample. EDS is used for elemental analysis of the bulk. As a type of spectroscopy, it relies

on the investigation of a sample through interactions between electromagnetic radiation and matter, analyzing x-rays emitted by the matter in response to being hit with charged particles. Its characterization capabilities are due in large part to the fundamental principle that each element has a unique atomic structure allowing x-rays that are characteristic of an element's atomic structure to be identified uniquely from each other. EDS involves using an electron beam to bombard a sample ejecting a low energy electron from the core shell leaving behind an electron hole. This hole is filled with an electron from a higher energy shell and the difference in energy between the shells is released in the form of an X-ray. The energy and number of X-rays (characteristic to an element) are measured by the spectrometer, hence elemental composition of a sample can be known. Analytical accuracy for EDS measurements for major elements is ±2% (relative). EDS is widely used to quickly obtain localized compositional information of the top layer of a surface of solid sample. The integrated intensity, the area under the x-ray peak, is proportional to the concentration of the corresponding element. EDS calculations were carried out using the FESEM Nova field emission instrument with an acceleration voltage of 20 kV.

2.2.3.2. X-Ray Photoelectron Spectroscopy (XPS)

Surface chemical natures of the films were investigated by X-ray photoelectron spectroscopy (XPS). XPS analyses were conducted using a monochromatic Al Kα X42 ray source (1486.6 eV) with a PHI 5000 Versa Probe. Nominal binding energy of the C 1s was 284.5 eV.

Introduction

X-ray Photoelectron Spectroscopy (XPS) is a versatile and non-invasivespectroscopic technique which is increasingly applied to a wide range ofmaterials in order to acquire a variety of important analytical informationassociated with the outer surface layers of the materials.X-ray Photoelectron Spectroscopy (XPS) was developed in themid-l960s by Kai Siegbahn and his research group at theUniversity of Uppsala, Sweden. The technique was first knownby the acronym ESCA (Electron Spectroscopy for Chemical Analysis) [151]. The advent of commercial manufacturing of surfaceanalysis equipment in the early 1970 enabled the placementof equipment in laboratories throughout the world. In 1981, Siegbahn was -awarded the Nobel Prize for Physics for his work with XPS.

Surface analysis by XPS involves irradiating a solid in vacuum with mono energetic soft x-rays and analyzing the emittedelectrons by energy. The spectrum is obtained as a plot of the

number of detected electrons per energy interval versus their kinetic energy. Each element has a unique Spectrum. The spectrum from a mixture of elements is approximately the sum of the peaks of the individual constituents. Because the, mean free path of electrons in solids is very small, the, detected electrons originate from only the top few atomic layers, making XPS a unique surface sensitive technique forchemical analysis. Quantitative data can be obtained from peak heights or peak areas, and identification of chemical states often can be made from exact measurement of peak positions and separations, as well as from certain spectral features.

Principle:

Surface analysis by XPS is accomplished by irradiating a sample with mono energetic soft x-rays and analyzing the energyof the detected electrons. Mg Ka (1253.6 eV) or Al K~ (1486.6eV) x-rays are usually used. These photons have limitedpenetrating power in a solid on the order of 1-10 micrometers.They interact with atoms in the surface region, causing electronsto be emitted by the photoelectric effect. The emitted electronshave measured kinetic energies given by [151]:

$$K.E = h\nu - B.E - \phi_s \qquad \textbf{2.11}$$

Where hυ is the energy of photon, B.E is the binding energy of the atomic orbital from of the atomic orbital from which the electron originates, and Φs ,is the spectrometer work function.Binding energy of ejected photoelectron can be indicated by the final stateconfiguration after photoemission. Figure. 2.17 show the XPS emission process for a model atom. The ejected *N* electron was caused by an incoming of incident X-ray (Photon). The kinetic energy of ejected electrons will be analyzed by electronspectrometer. On the practical XPS measurements, graph of count versus bindingenergy of electrons are usually used for analysis.

An electron spectroscopy on the XPS system usually consists of a source of the primary beam, either of X-rays or electron, an energy analyzer and the detection system as shown in Figure 2.18. All of these modules enclosed within a vacuum chamber. In order to comply with the issue of surface sensitivity of the measurement techniques, the vacuum systems are intended to operate in the ultra-high vacuum (UHV) in the order of 10^{-8} Pa. In order to overcome the binding energies of electron core level, the X-ray source on the XPS system must produce enough energetic beams. The most commonly used X-ray source in XPS systems are Mg Kα (1253.6 eV with linewidth 0.7 eV), Al Kα(1486.6 eV with linewidth 0.85 eV) or monochromatic Al Kα (1486.7 eV).Penetrating power as effect of this photon energy is limited on the order of 1-

10micrometers [151-152]. In the case of High Energy XPS (HE-XPS) or hard X-ray XPS(HAX-PES), the Cr Kα line with photon energy of about 5414.87 eV can be used forbulk sensitive analysis reach to 20 nm without any surface treatment. In this study the chemical states of the films were identified by a X-ray photoelectron spectroscopy using Mg-Kα excitation source (1253.6 eV) and a DESA-150 electron analyzer (Staib Instruments, Germany).

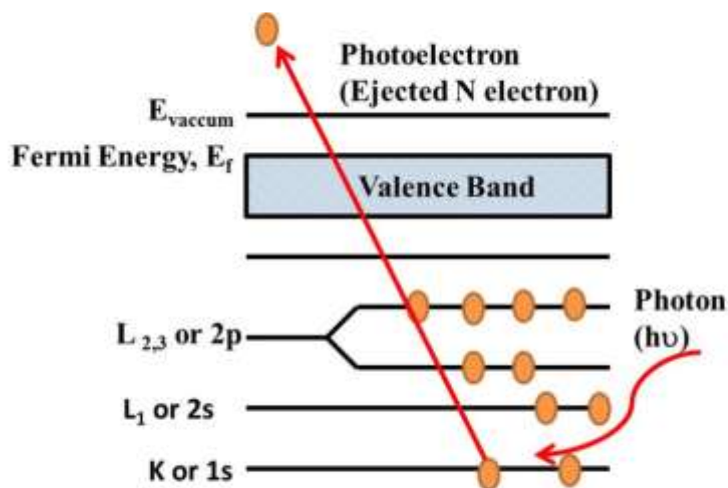

Figure. **2.17** The photoemission on the XPS system process.

By assuming a homogenously distributed sample and taking into account the above-mentioned factors a very simplified mathematical formula which relates the intensity I_i of a photoelectron from element i to the concentration η_i of the element i is given by [153]

$$I_i = J\eta_i\sigma_i\delta\gamma \qquad \textbf{2.12}$$

where J is the x-ray flux, σ_i is the photoemission cross-section of a photoelectron element i, δ is a term which accounts for all spectrometer related factors and γ is the electron attenuation length. By defining elemental sensitivity factor as $S_i = J\sigma_i\delta\gamma$ the concentration of the element i is given by

$$\eta_i = \frac{I_i}{S_i} \qquad \textbf{2.13}$$

The elemental concentration is adequately expressed in terms of atomic percentage as follows [153]

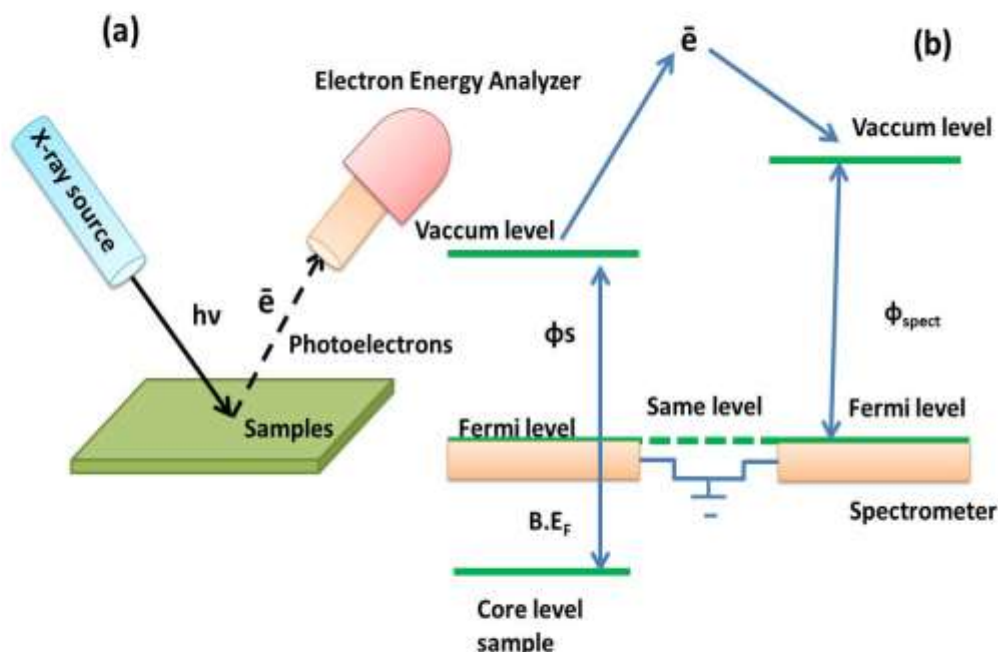

Figure.**2.18** The working principle of the XPS spectroscopy (a) and (b) binding energy diagram

$$C\% = \frac{\frac{I_i}{S_i}}{\sum \frac{I_i}{S_i}} \times 100 \qquad \text{2.14}$$

XPS is mainly considered as a chemical surface sensitive technique since it can only probe the uppermost atomic layers of the sample's surface approximately the first top 10 nm and the concentration of the elements of interest should exist at 0.1 at. % or higher.[154]. The sensitivity of the XPS detection toward the atoms in the surface is caused by the relatively short distance that the photoelectrons can travel to escape the material and arrive at the detector without losing their kinetic energies due to inelastic scattering processes.

2.2.4. Optical Measurements: UV Spectrophotometer

Ultraviolet-visible spectroscopy (UV-vis) is a spectroscopy (absorption or reflectance) in the ultraviolet-visible region. The optical behaviors of a semiconductor are investigated in term of the three phenomena namely transmission, reflection and absorption. When a semiconductor is illuminated by light, photon strikes the surface, a fraction of photons are reflected, some of these are absorbed within the semiconductor and the remainder transmitted into the semiconductor. The UV-vis absorption spectroscopy provides information of light absorption as a function of wavelength, which describes the electronic transitions occurring in the measured

samples. The UV-vis spectrophotometer detects the light intensity passing through a sample and compares the detected intensity to incident light intensity (light before passes through the sample) [155]: The absorbance A is simple expressed as Beer's law:

$$A = -\log\left(\frac{I}{I_o}\right) \quad \text{.......... 2.15}$$

Where the ratio I/I_o is called transmittance, I is the intensity of light passing through the sample and I_0 is the intensity of light before passing through the sample. The optical band gap of the grown samples was estimated using the following equation [156]

$$(\alpha h\nu)^2 = C(h\nu - E_g)^n \quad \text{.......... 2.16}$$

where $\alpha = 2.303x(\frac{A}{d})$ the absorption coefficient, d is thickness of the sample (length of nanorods), n=1/2 for direct band gap semiconductors, h is Planck's constant and hν is the incident photon energy. The optical energy gap of the samples was obtained from the intercept of the linear portion with the x-axis of $(\alpha h\nu)^2$ versus hν curve.

Absorption and transmission spectra of all the samples were recorded using UV-Vis spectrometer and quantitative determination is done. Figure 2.19 shows schematic diagram of UV-Visible spectrometer and Figure 2.19 shows actual photograph of UV-Vis spectrometer. For optical property studies of ZnO, transmittance and absorbance were measured by using a double beam UV spectrophotometer. Measurements were made by placing the sample in the incident beam and another empty glass substrate in the reference beam of the instrument. The optical transmission and reflection spectra of the film with respect to glass substrate were than taken for wavelength range 300 to 900 nm using JASCO V-650 spectrometer. Thin film on glass substrate was used for the characterization and bare glass measurements were taken as a background.

2.2.5. Film Thickness Measurement by Ellipsometry

Ellipsometry is a simple, accurate, non-destructive and non-invasive measurement technique, frequently used for the determination of the refractive index (n) and thickness of thin films. Film thicknesses in this work were measured by an AutoEL-III ellipsometer equipped with a 633.2 nm helium-neon (He Ne) laser at an incident angle of 70^0. The evaluation of ellipsometry data depends on the (intensity-independent) ratios of the amplitudes and phases of the reflected and incident polarized light, and as such it is important that the material to be studied is non-

absorbing at the laser wavelength. For the surface profilometry measurements, a probe or stylus contacts the surface of the sample and records height variations as it scans the surface. The height variations are converted into electrical signals that are used to generate a topographical map of the sample surface. These latter measurements required the creation of a sharp edge between the substrate and the film.

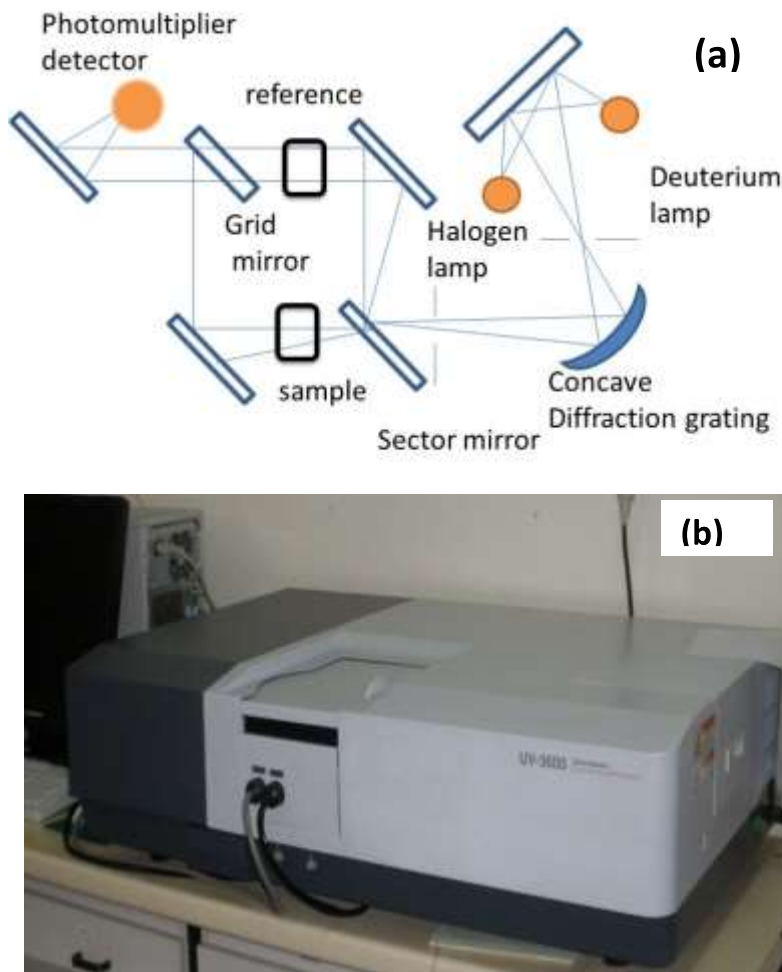

Figure 2.19. (a) Schematic diagram of an UV-Vis spectrophotometer (b) actual photograph

2.2.6. Photoluminescence Measurements

In general luminescence is a collective term and can be broadly classified into several categories based on the type of the excitation source. For instance, photoluminescence (PL) refers to emission of light produced by a luminescent material when it is excited by electromagnetic radiation (photons) while in the thermo luminescence process the excitation process is carried out thermally. Similarly, electroluminescence occurs when an electrical current

is passed through the luminescent material and so on. Investigating the emitted light from an excited material is significantly an important step to assessing the crystal quality, to defining the composition of the material and to exploring the energy levels associated to dopants and active defects present.

Photoluminescence (PL) spectroscopy is an important characterizing technique for analyzing the optical properties of semiconductors. By measuring and analyzing the energy distribution of emitted photons after optical excitation, properties such as the composition of the material, impurities and optical emission efficiencies can be obtained. During photoluminescence laser light of energy greater than the band gap (Eg) of the material is used to excite electrons across the band gap and into the conduction band creating an excess of electron hole pairs. These electron hole pairs (frequently referred to as excitons) recombine within the crystal, sometimes at impurity sites as bound excitons if the semiconductor is extrinsically doped with impurities or recombine at structural defect sites or intrinsic defects (described in Chapter 1), and this recombination can result in the emission of an optically detectable photon.

Excitation is achieved by laser or xenon lamp and after the photoluminescence is spectrally dispersed by a spectrometer it is detected by a photomultiplier tube and is depicted in Figure.2.20. Excited charge carriers can decay to lower energy states through different mechanisms. Band-to-band recombination requires the presence of both an electron and a hole. An electron in the bottom of the conduction band recombining with a hole in the top of the valence band emits a photon with energy equal to the band gap. However, in certain materials this mechanism is relatively unlikely since an exciton is more stable, recombining through free exciton recombination. An exciton is a quasi particle which can be generated through photon absorption, consisting of an electron and a hole separated by the band gap but attracted to each other by the Coulomb interaction energy. The exciton can travel through the periodic structure and can hence transport energy without being electrically charged [157-158].

The main peak in a PL spectrum of a perfect material will be due to free-exciton recombination. Impurities may also serve as recombination centers, with different positions in the band gap depending on its chemical identity and charge state. A donor level lies in close proximity to the conduction band, and a conduction electron can decay to this level before recombining with a hole, and the opposite is true for acceptor levels. There are also so-called deep levels which lie somewhere in the middle of the band gap, and can act as recombination

centers for charge carriers. Thus by analyzing a PL spectrum, different impurities in a thin film can be characterized. The following are the five of the most commonly observed PL transitions: 1) band-to-band recombination (Figure 2.21 a), 2) excitonic recombination (Figure 2.21 b), 3) bound exciton (BE) recombination (Figure 2.21c), 4) free electron recombine with a hole on a neutral acceptor (Figure 2.21 d), and 5) donor–acceptor (D-A) recombination (Figure 2.21 e). Light emission from the recombination reveals the defect types in the examined bulk material. ZnO may have several types of defects (i.e., vacancy and interstitial of oxygen and zinc) near the surface.

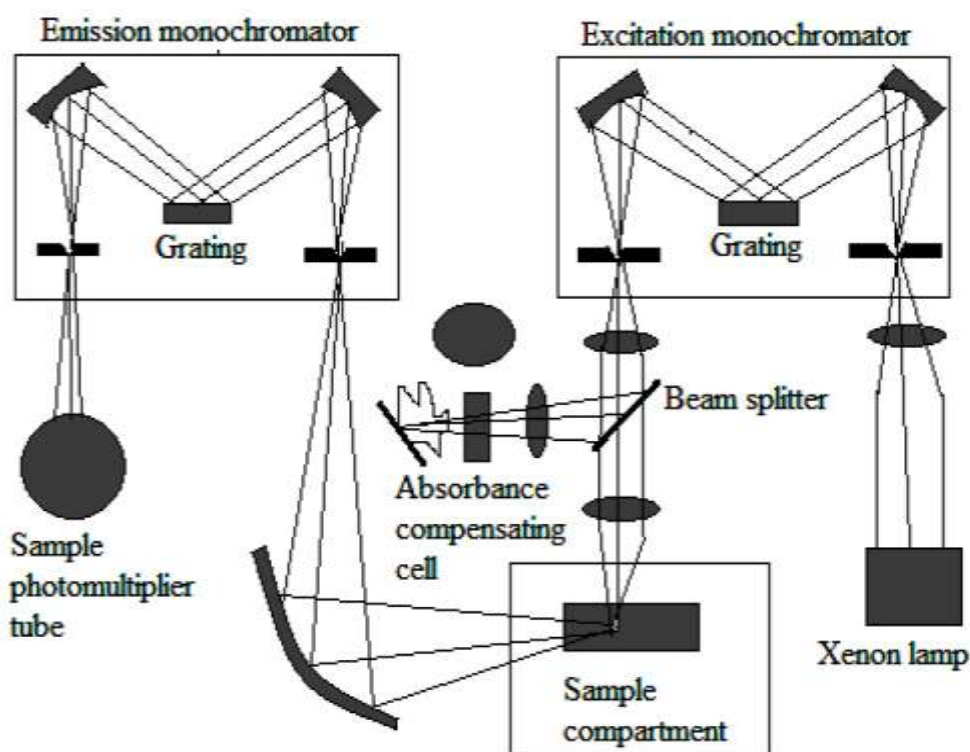

Figure.**2.20** Schematic diagram of spectroflurometer

The PL system used in this work is fluorescence spectrometer (Edinburgh Instrument) with a model of FLSP920. The samples were excited by a continuous Xenon lamp (at 324 nm) at room temperature. The radiative emission was obtained from the samples surface, and was detected by PMT detector (Model: R928) with a spectral range from 300-900 nm.

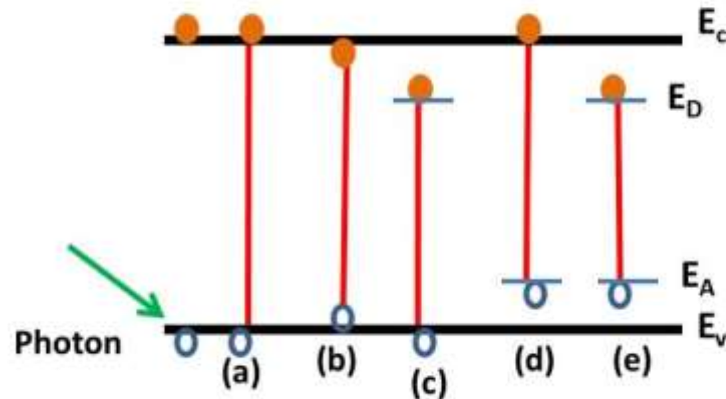

Figure.**2.21** Radiative transition with PL

2.2.7. Current- Voltage measurements

A current-voltage (I-V) measurement is used for p-n junction characterization and confirmation of Homo/Hetero junctions between two semiconductor materials. I-V measurements are carried out by making metallic contacts on two sides of junction. The I-V characteristics of a diode can be written as

$$I = I_0 \exp(\frac{qV}{nkT}) - 1 \quad \textbf{2.17}$$

where q is the elementary charge, k is Boltzmann's constant, T is the absolute temperature, V is the applied voltage, n is ideality factor, and the (−1) term is negligible when V > 0.1 V and I_0 is the reverse saturation current given by [159]

$$I_0 = AA^* T^2 \exp(\frac{-q\phi_B}{kT}) \quad \textbf{2.18}$$

where A* is the effective Richardson constant (theoretically 32 A/cm^2 K^2), A is the contact area and ϕ_B is the barrier height. Under forward bias, the ϕ_B and n can be estimated with a least-squares fit to equation and to the slope of the ln(I/[1-exp(-qV/kT)]) versus V plot.

$$\Phi_B = kT \ln\left(\frac{A.A^* T^2}{I_S}\right) \quad \textbf{2.19}$$

The ideality factor was determined from the slope of the linear region of the forward bias ln(I)-V characteristic through the relation:

$$n = \frac{q}{kT} \frac{dV}{d(\ln I)} \quad \textbf{2.20}$$

In this research work, materials such as Ti/PtAu, were used as the materials to form the contact with ZnO and Indium doped tin oxide (ITO) is used to form the Ohmic contact with ZnO. Then the fabricated diodes are used to study I-V measurements. Figure.2.22 (a) shows a schematic diagram and Figure 2.22 (b) shows photograph of the homojunction diode based on undoped and doped ZnO. During this work the I-V measurement instrument KEITHLEY picoammeter/voltage source 6487 is used. Voltage was swept between negative to positive values and corresponding current values were recorded using a Lab view program.

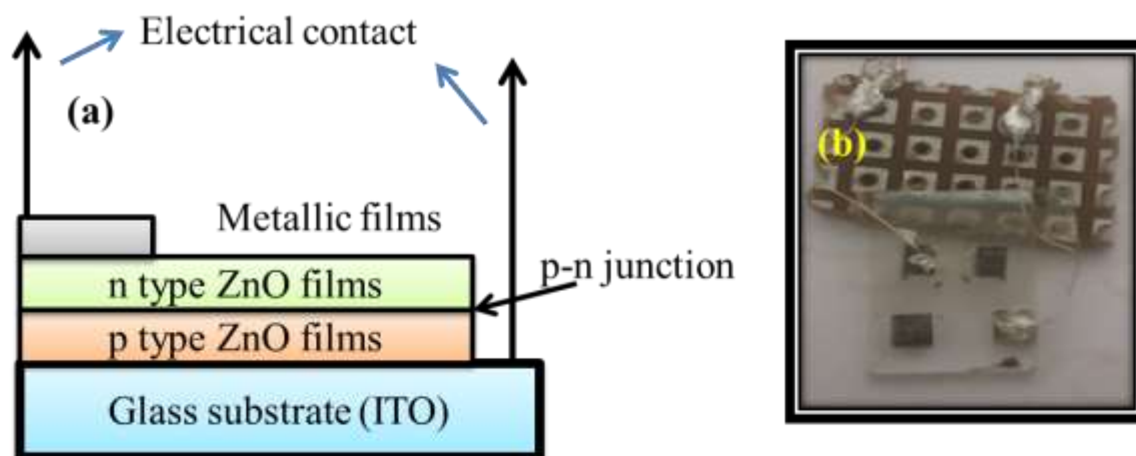

Figure.**2.22** (a) Schematic diagram and (b) photograph of fabricated p-n junction devices

2.2.8. Device fabrications: Gas Sensors

After preparation and characterization processes, the synthesized samples have been used to fabricate gas sensors to detect the toxic gas like H_2S, NO_2 etc. Over the last few years, with the speedy development of industrialization and urbanization, the severe air pollution mainly endorsed to automobile exhaust and factory emission has become a great threat to human survival and development. Meanwhile, a leakage of flammable and explosive gases may result in loss of life and property damage. So, real-time and effective detection of those harmful gases via using gas sensors is in pressing need at present. Off all the numerous semiconductor gas sensors, semiconducting metal oxide based gas sensors have received wide research around the globe by virtue of their high gas response, excellent selectivity, good portability, and low fabrication cost [160-165]. In addition the sensors can also find applications in aerospace, laboratories, factories, fuel cells etc. In the following section a brief descrption about the gas sensors are given:

In general a sensor is a device that responds to any change in physical phenomena or environmental variables like heat, pressure, humidity, movement etc. This change affects the physical, chemical or electromagnetic properties of the sensors which is further processed to a more usable and readable form. On the basis of working principle, the sensors are broadly categorized into physical sensor and chemical sensor as shown in Figure.2.23, the gas sensor comes under the category of chemical sensor. Chemical sensors, based on change in resistance, are termed as resistive sensors. A resistive sensor is based on a sensitive material, in form of bulk/thin film/nanostructure upon which the molecular recognition process takes place. The analytic process occurs either at the surface of the sensing element or in the bulk of the material, leading to a concentration-dependent change in electronic property that can be transformed into an electrical signal. This simple transduction mechanism governs the fabrication of devices with different configurations. In comparison to other sensors like electrochemical and optical, resistive sensors are advantageous due to its small size, low cost, longer lifetime. The resistive gas sensors are further classified according to the sensing material such as metal oxide and conductive polymer.

A gas sensor is a transducer that detects gas molecules and which produces an electronic signal with a magnitude proportional to the concentration of the gas. Long ago in 1938, Wagner et al. observed remarkable change in the electrical properties at high temperatures for semiconductor materials on exposure to reducing or oxidizing gases [166]. Based upon these facts, Seiyama et al. for the first time developed semiconductor-based detector for gaseous components [167]. It was observed that at high temperatures of 400°C, the adsorption and desorption of gases results in a comprehensive change in electrical conductivity and resistivity of semiconductor materials. From the variety of gas sensors, semiconducting metal oxide sensors such as ZnO, SnO_2, WO_3, CuO, Fe_2O_3, In_2O_3, CdO, TeO_2, and MoO_3 have been extensively used.

According to Yamazoe [168], a gas sensor consists of two basic functions, receptor functions and transducer functions. Receptor function includes the recognition the chemical substance, whereas transducer function converts the chemical signal into electrical signals. In many cases, the gas recognition is carried out through gas solid interactions such as adsorption, chemical reactions and electrochemical reactions. On the other hand, the way of transduction is heavily dependent on the materials utilized for the gas recognition. The gas recognition by semi

conducting oxides is conventionally transduced into a sensing signal through the electrical resistance changes of the sensor elements, while capacitance can be used for the elements using dielectric materials. For the basic understanding of the semiconductor gas sensor, therefore, one needs to differentiate these two functions. Actually, the receptor function is provided with the surface of each semiconductor particle. The obtained chemical signal is then transduced through the microstructure of coagulating particles into the resistance of the polycrystalline element.

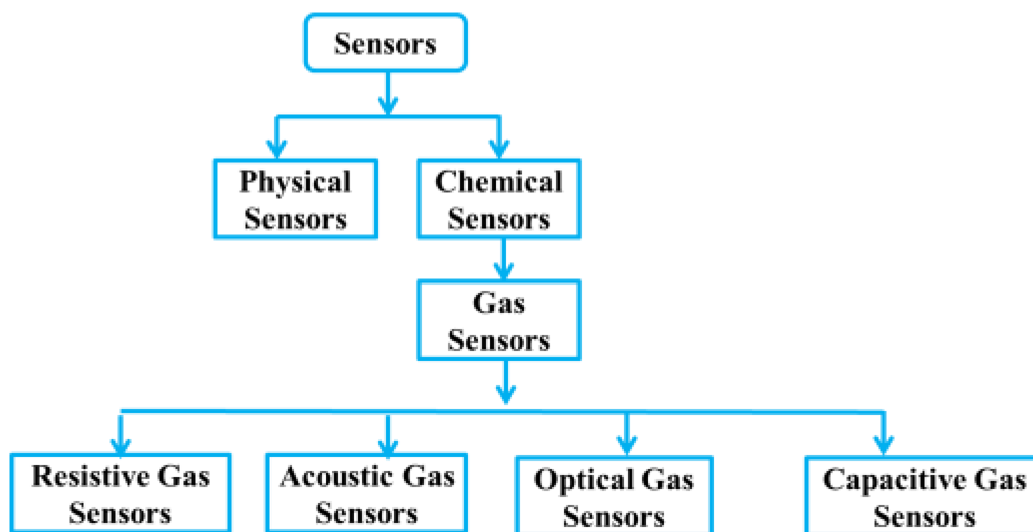

Figure.2.23 General Classification of sensors

Gas Sensing Mechanism in MOS Sensors

The gas - semiconductor surface interaction is based on the gas-sensing mechanism of metal oxide semiconductors occurring at the grain boundaries of the film. They generally include reduction/oxidation processes of the semiconductor, adsorption of the chemical species directly on the semiconductor and/or adsorption by reaction with surface states associated with pre-adsorbed ambient oxygen, electronic transfer of delocalized conduction-band electrons to localized surface states and vice versa, catalytic effects and in general complex surface chemical reactions between the different adsorbed chemical species. The effect of these surface phenomena is a reversible and significant change in electrical resistance. This resistance variation can be easily observed and used to detect chemical species in the ambient. The capture of an atom or molecules on the surface of body is called adsorption. The process is further classified as physical and chemical adsorption. The reverse process of adsorption is called desorption.

i) Physical adsorption - The atoms and molecules retain their individuality. The forces of their interaction with surface are mainly of electronic nature .The physical adsorption and desorption are carried out at relatively low temperature.

ii) Chemical adsorption - The atoms or molecules are chemically bounded with crystal The adsorption takes place at high temperature. The adsorbed atoms or molecules form donor and acceptor surface level regardless of the type of adsorption.

Figure 2.24 illustrates the conduction-oxidation response mechanism of an n-type semiconducting oxide. the reaction initiates with the adsorption of oxygen molecules from the air, on the surface of the n-type particles, in the form of various anionic oxygen species such as O^- or O^{2-}; the exact type of anionic oxygen species is dependent on the operating temperature of the sensor [169]. For these anionic oxygen species to form and stabilize on the surface of the metal oxide, the oxygen molecules from ambient air need to be reduced by the uptake of electrons (i.e. they need to be ionized). These electrons are extracted from the conduction band of the metal oxide and trapped at its surface. This process leads to the formation of an electron depletion layer (EDL) or space-charge layer at the surface of the metal oxide, which is a zone depleted of electrons [169]

Following this, the second part of the reaction may occur, which is illustrated Figure 2.24 (b). Here the target analyte, in this case CO (which is a reducing gas) undergoes oxidation reactions with the adsorbed anionic oxygen species forming CO_2 molecules, which desorb off the surface, and in the process of the oxidation reaction, remnant electrons are released into the EDL / space-charge layer. This reaction causes a decrease in the thickness of the EDL and as a result of this release of electrons back into the bulk of the material, which in effect implies a change in the charge carrier concentration of the material, a decrease in the height of the potential barrier (also called the Schottky barrier) between the two consecutive n-type grains occurs. As such, an increase in the conductance of the material is then observed [169-170].The electron conduction that occurs in the gas sensitive material is represented by the gold percolation arrows observed in Figure 2.24 (b).

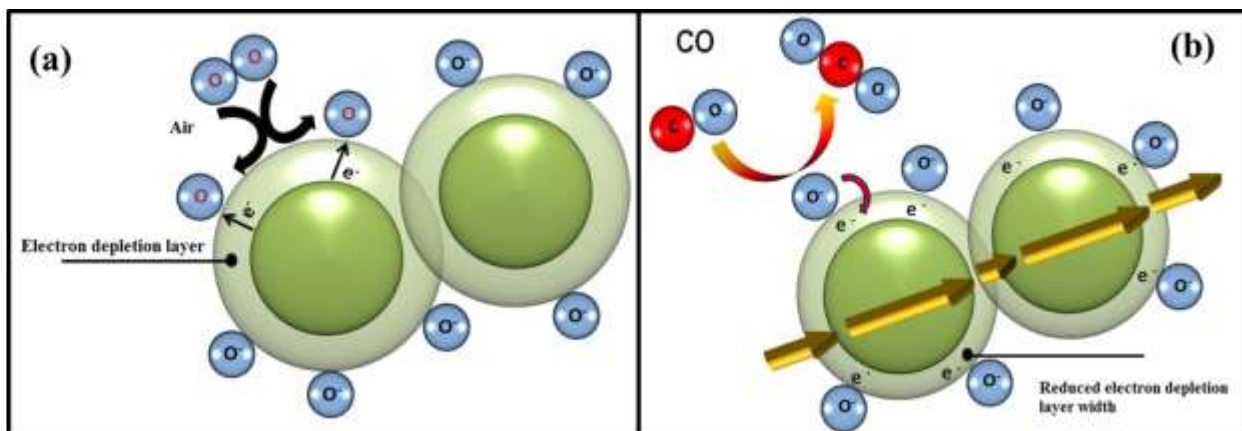

Figure 2.24 Gas sensing mechanism of n-type semiconducting oxide upon interaction with (a) air, in which an electron depletion layer (EDL) is formed on the surface of the metal oxide, upon interaction with O_2 molecules and subsequent adsorption and ionisation of oxygen species on its surface and (b) the target analyte CO (a reducing gas), which interacts with the adsorbed ionic oxygen species on the surface of the metal oxide, forming the product CO_2 and releasing electrons in the process. This induces a decrease in the width of the electron depletion layer, and resultantly increases the conductivity of the n-type metal oxide. The gold percolation arrows illustrate the direction of electron conduction in the material [169].

Gas sensing parameters

The important key in the working of a chemical sensor is the interaction between a gas molecule and the surface of receptor. The major factors in the characterization of nanostructures are morphology, crystal structure and electronic structure of sensing material. From these factors, the performance of a chemical sensor is characterized by different parameters and is described as follows:

(a) Calibration curve

A calibration curve is the relationship between the signal response and the concentration of target gas. The concentration of the gas is usually measured in parts per million (ppm) values.

(b) Baseline

A base line may be defined as the stabilization of sensor signals when it achieves equilibrium with its environment [171]. Normally, there may be large fluctuations of sensor signals before stabilization at the base line; it is essential that this base line be reached before starting the measurements

(c) Gas Response and sensitivity

The electrical resistance of a chemiresistive sensor changes drastically (increase or decrease) when exposed to the molecules of analyzing gas. Increase or decrease in resistance depends on the nature of sensor material (n-type or p-type) and the gas (reducing or oxidizing). A typical response curve, that is, variation of resistance of sensor with time on exposure and withdrawal of analyzing gas, is schematically depicted in Figure 2.25.

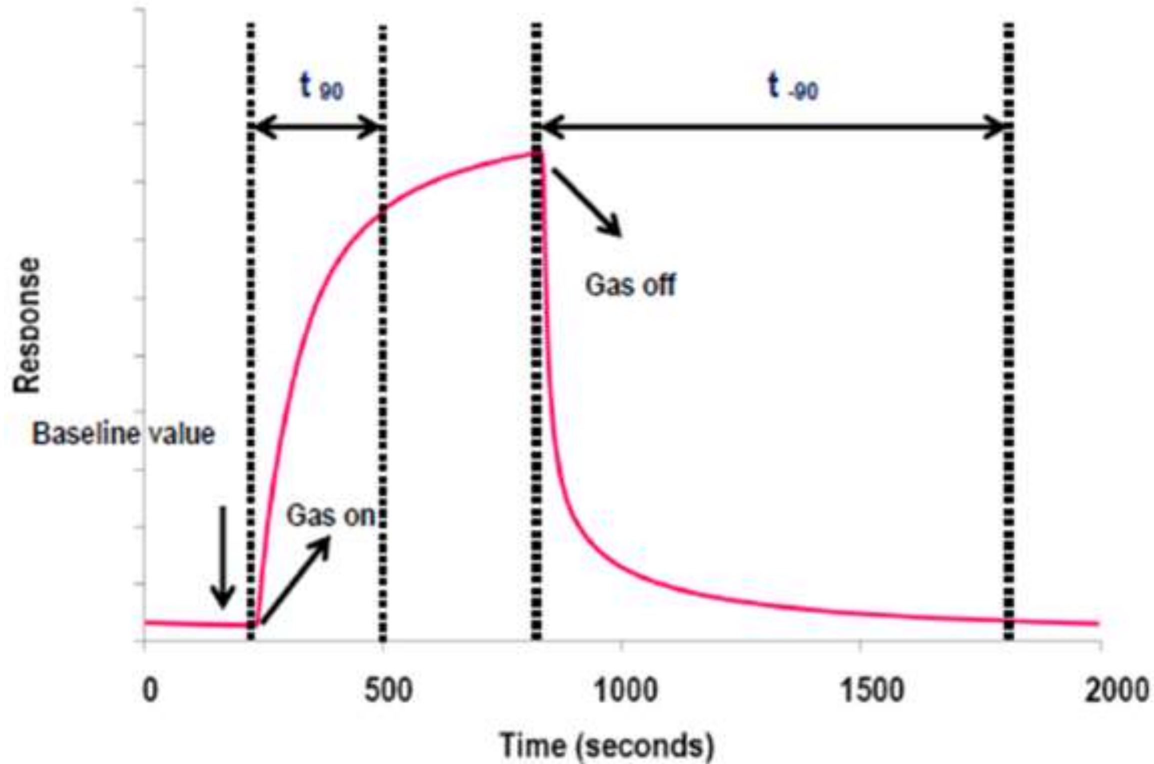

Figure 2.25. Typical response signal from metal oxide semiconductor gas sensor upon exposure to test gas. The diagram indicates when the pulse of gas is switched on and when it is switched off. Further, t90 represents the response time of the sensor device to reach 90% of its maximum response and t-90 is the recovery time of the sensor device to be within 10% of the baseline value.

Gas response of a gas sensor is generally defined as the ratio of the resistance change on the surface of the gas sensor before and after being exposed to the test gas. It is mathematically expressed in different forms. Sensitivity of oxidizing gas by an n-type semiconductor or sensitivity of a reducing gas by p-type semiconductor can be represented as: [172-176]

$$S = \frac{R_g}{R_a}$$

$$S = \frac{R_g - R_a}{R_a} = \frac{\Delta R}{R_a} \times 100$$

$$S = \frac{I_O - I_g}{I_g} = \frac{\Delta I}{I_g} \qquad \ldots\ldots 2.21$$

where Ra is the sensor resistance in presence of ambient dry air and Rg the sensor resistance in the presence of target gas; I_0 the reference value (baseline) of the sensor materials in dry air ambient and I_g the current of the sensor materials in the presence of target gas.

(d) Response characteristics

The response is measured at definite temperature and gas concentration. The response time is time taken by sensor to attain the maximum change in resistance on exposure to the gas. Further, lower the response time better are the sensing properties of the sensor. The response time is short for higher concentrations of target gases. Therefore, care should be taken for monitoring toxic gases at low concentrations as they may take a longer response time.

The recovery time is time taken to attain original resistance when test gas is purged or time required by a sensor so as to return to 90 % of the original baseline signal when the target gas is removed. The recovery of the sensor element is exponential. For good sensor applications, sensor recovery time should be small so that the sensor can be used over and over again.

(e) Selectivity

Selectivity is the ability of a sensor to respond to a certain gas. The selectivity of a sensor in relation to a definite gas is closely connected with its operating temperature

(f) Detection Limit

For high-performance sensor applications, sensor should be capable to detect even very low concentrations of the gases. The minimum concentration of gas which can be detected by a sensor under operative conditions is called its lower detection limit.

(g) Stability and Reproducibility

Stability of the sensor material refers to its ability to maintain its sensing properties repeatedly and even for long durations. Reproducibility is a measure of sensor similarity behavior. In order to compare the reproducibility of two sensor batches on can either calculate

the mean value and the standard deviation of a sensor property for both batches and compare them or calculate reproducibility for each batch.

(h) Working temperature: It is usually the temperature that corresponds to maximum sensitivity.

All these parameters depend on the nature, particle size and morphology of the sensing material, the type of interactions and reactions occurring between the gas and the sensor material, the sensor operating conditions, etc. In order to control these parameters, scientific understanding of gas–sensor interaction and various new technological concepts and novel materials have been developed. Reliable and precise detection of toxic gases is important to prevent or minimize accidents and health hazards. Toxic gases such as CO, H_2S, SO_2, NO_2, NO etc are emitted or used in various industries, automobiles, waste disposal, atmosphere etc. Some of the toxic gases emitted by industries and vehicular exhausts are listed in table2.2 along with their exposure limits and impacts on human health and environment according to American conference of governmental industrial hygienists (ACGIH).

In this study ZnO based gas sensors are fabricated and studied the gas sensing properties and the detailed explanation are given in chapter 5 and 6. The flow diagram of gas sensor fabrication, characterization and sensing process is presented in the Figure.2.26

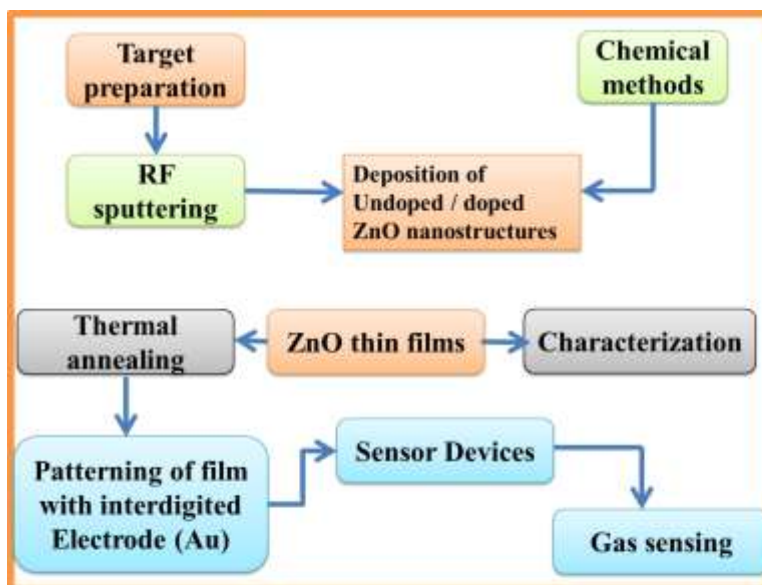

Figure 2.26 Flow diagram of gas sensor fabrication, characterization and gas sensing

Table 2.2 Long-Term Exposure Limit for 8 hr (LTEL), Short-Term Exposure Limit for 10 minutes (STEL) and impact of these toxic gases on human health and environment

Gas/ Vapor	LTEL (ppm)	STEL (ppm)	Impacts on human health and environment
H_2S	10	15	Highly toxic and flammable gas (4.3–46%). At low Conc. (20ppm) – causes eye irritation. 50-500 ppm – affects nervous system
CO	50	300	200 ppm - Slight headache, tiredness, fatigue, nausea and dizziness. 400 ppm - Serious headache-other symptoms intensify. Life threatening after 3 hours.
NO_x	3	5	Small levels of NOx can cause nausea, irritated eyes and/or nose, fluid forming in lungs and shortness of breath. High levels of NOx can lead to rapid burning spasms, swelling of throat, reduced oxygen intake, a larger buildup of fluids in lungs and/or death. Causes acid rain and contributes to global warming.
SO_2	2	5	Irritation of nose, throat, and airways to cause coughing, wheezing, shortness of breath, or a tight feeling around the chest and in extreme cases premature death.
PH_3	-	0.3	Causes damage to lungs, heart, upper respiratory tract, central nervous system (CNS).
NH_3	25	35	Inhalation of lower concentrations can cause coughing, and nose and throat irritation. Exposure to high concentrations of ammonia in air causes immediate burning of the eyes, nose, throat and respiratory tract and can result in blindness, lung damage or death.
CH_3OH	200	250	Methanol vapors cause central nervous system depression. The symptoms of such exposure include headaches, nausea, dizziness, drowsiness, confusion, and unconsciousness. Irritation of the nose, throat, and other tissues of the upper respiratory system may also occur. Inhalation overexposures cause blindness and liver damage.

2.3. Conclusion

In this chapter, the different thin film preparation and characterization techniques relevant to the work presented in this thesis have been discussed. A number of PVD and CVD techniques have been discussed briefly and compared with sputtering deposition, which has been extensively-used in this work. Electrical, optical and physical characterization (UV-Vis spectroscopy, XRD spectroscopy, XPS, FESEM, PL and IV) techniques used for both films and homojunction characterization is briefly presented.

CHAPTER 3

Growth and characterization of undoped and Lithium doped ZnO nanocrystalline thin films

3.1.Introduction

3.2.Material and Methods

3.3.Result and Discussion

3.3.1. Structural Properties

3.3.2. Morphological Properties

3.3.3. Compositional Analysis

3.3.4. Absorption and optical band gap

3.3.5. Photoluminescence Properties

3.4. Conclusion

In this chapter, a detailed description of undoped ZnO and Lithium doped (LZO) nanocrystalline thin film growths and characterization are given. As mentioned in previous chapters, ZnO nanostructures are grown using the RF sputtering technique. The main focus in this chapter is on growth of well-aligned and good crystalline quality LZO nanostructures and methods to achieve this.

CHAPTER 3

Growth and characterization of undoped and Lithium doped ZnO nanocrystalline thin films

3.1.Introduction

The keystone of modern electronic industry is nanostructures of metal oxides. They have been widely used in fabrication of photovoltaic, optoelectronic and photonic devices. Among various metal oxides, zinc oxide (ZnO) which belongs to II-VI group has been extensively explored for its potential application in different fields of science and technology. ZnO has a wide band gap (3.37 eV), large exciton binding energy (60 meV) and is considered to be one of the most important multifunctional semiconductor material for various applications such as solar cells, transducers, light emitting diodes (LED) and laser diodes [176-180].

In order to fabricate optical devices based on ZnO, it is important to achieve both n-type and p-type ZnO thin films. Basically, ZnO exhibits n-type conduction due to its intrinsic donor defects and oxygen vacancies. The semiconducting properties of ZnO can be significantly influenced by adding controlled amounts of selected dopants. In literature, p-type ZnO is reported to be achieved by doping group-I elements (Li, Na and K) at Zn-sites and group-V elements (N, P and Sb) at O-sites [181-184]. However, it is quite challenging to obtain p-type ZnO due to self-compensation effects, which demand higher concentration of dopant source. It has been reported that shallow Li acceptors have a strong influence on the physical properties of ZnO films [185-187] .Though some researchers have reported that partially replacing zinc atoms with lithium in ZnO can aid the formation of p-type ZnO [188], in general, Li-doped ZnO (LZO) films are either n-type or semi-insulating because Li incorporation occurs at interstitials sites as well as substitutional sites. While the doping behavior of Li in ZnO is still uncertain, the resultant defects due to Li incorporation play an important role in determining the optical properties.

3.2. Material and Methods

Undoped and Li doped ZnO nanocrystalline thin films were synthesized using RF magnetron sputtering system (Hind High Vaccum Co. Pvt. Ltd.) on glass and Si (100) substrates using powder targets. Powders of LiCl (99.99%, May and Baker Ltd.) and ZnO (99.9%, May and Baker Ltd.) were used for preparing powder target.

3.3. Result and Discussion

3.3.1. Structural Properties

X-ray diffraction (XRD) patterns of both undoped and Li doped thin films are shown in Figure .3.1 (a). The XRD patterns exhibit the presence of only a strong (002) diffraction peak, suggesting that both the films are crystalline in nature with a wurtzite structure and highly oriented along the c-axis. With Li doping, the (002) diffraction peak shifts towards lower angles due to the difference in ionic radius of Li ion (60 pm) and Zn ion (74 pm) [189-190].To investigate the reasons for this shift, various lattice parameters are estimated. The values of lattice parameters, crystallite size, strain, (002) peak position and FWHM are listed in Table 3.1. From the Table 3.1, it is deduced that crystallite size decreases with Li doping and also strain is developed in film due to incorporation of Li atoms. FWHM value of (002) peak in case of ZnO films is smaller than that in LZO film, indicating an increase in particle size. It has been reported that Li ions can be incorporated either at substitutional sites (Li_{Zn}) or at interstitials sites (Li_i) in ZnO lattice [191]. From Table , the expansion in crystal lattice is evident in LZO films as there is an increase in both "a" and "c" lattice parameters suggesting that Li ions have occupied the interstitials sites (Li_i). Photoluminescence studies which are presented in the following section also strongly support the formation interstitials defects in LZO lattice.

Table.3.1 Structural parameters of pure and Lithium doped ZnO thin films

Film	Lattice parameters		Position 2θ	Plane (hkl)	FWHM	Crystallite size (D) (nm)	Strain ε (10^{-3})	d (Å)
	a(Å)	c (Å)						
ZnO	3.026	5.243	34.177	(002)	0.373	22	1.56	2.621
LZO	3.043	5.270	33.99	(002)	0.895	9	3.74	2.635

Raman spectra of the undoped and LZO films from 200-800 cm^{-1} are shown in Figure.3.1 (b). The Raman spectra of both - undoped and LZO films exhibit a dominant peak at 437 cm^{-1} corresponding to E_2 (high) mode, which confirms the wurtzite hexagonal phase of ZnO and indicates good crystallinity of the films. This result is in accordance with XRD results as the dominant peak at 437 cm^{-1} is at a slightly lower value than 439 cm^{-1} corresponding to stress free

bulk ZnO [191]. The appearance of E_1 (LO) mode indicates that defects including oxygen vacancies are introduced by the doping of lithium in the ZnO films which is further confirmed from photoluminescence spectra. A dominant and intense peak is observed at 521 cm^{-1} in Raman spectra for all samples, due to silicon substrate.

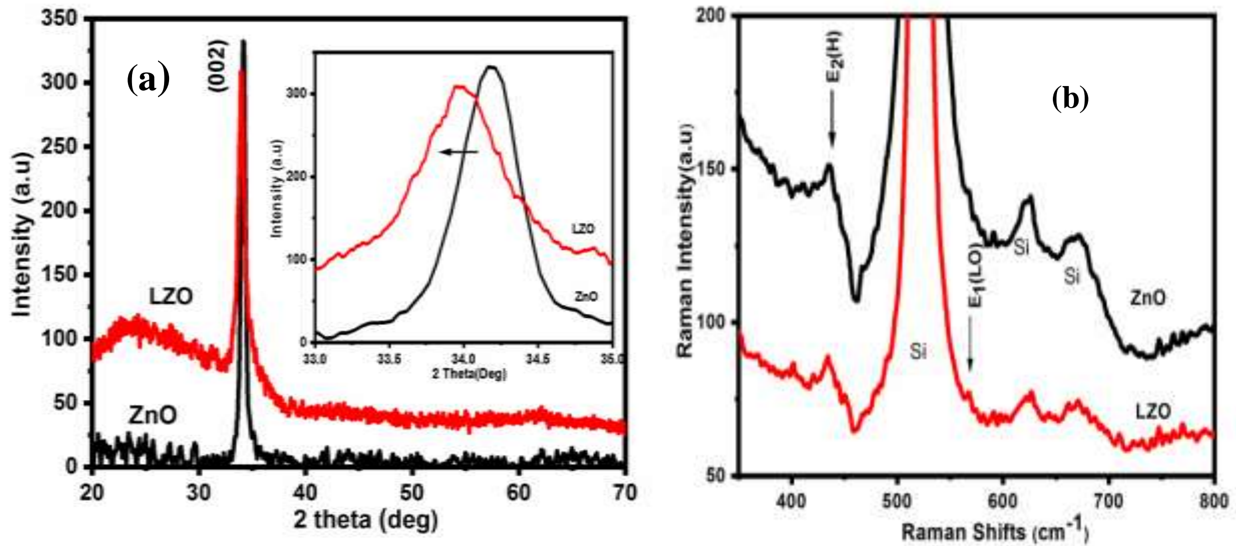

Figure.3.1. (a) XRD pattern of undoped (ZnO) and Li doped ZnO (LZO) thin films. Inset shows the shifting of diffraction peak due to Li doping and (b) Room temperature Raman spectra of undoped ZnO and LZO films

3.3.2. Morphological Properties

Nanocrystalline nature of the thin film is evident from the FESEM images (Figure.3.2 (a & b)). The FESEM images show uniform grains covering all over surfaces. Smaller grain size of LZO film (Figure.3.2 b) as compared to undoped ZnO film (Figure.3.2a) is concordant with the XRD data.

3.3.3. Compositional Analysis

The EDS spectra of undoped and lithium doped ZnO thin films are shown in Figure. 3.2 (c). The peaks corresponding to zinc and oxygen only are seen as the detection of Li is beyond the limit of EDS measurements due to its low atomic number.

The Figure.3.3 (a) illustrates the XPS survey spectrum, which shows the peaks corresponding to Li, Zn and O. The Li-1s peak (Figure. 3.3 (b) is observed at around 54.62 eV, which confirms the incorporation of Li-impurities in ZnO lattice. The XPS peaks at binding energies ~1021.5 eV and 1044.5 eV correspond to Zn $2p_{3/2}$ and Zn $2p_{1/2}$ respectively (Figure. 3.3

(c)). It can be seen that the spin–orbit splitting of 23 eV for Zn-$2p_{3/2}$ and Zn-$2p_{1/2}$ endorses that the Zn atoms are completely oxidized in both samples. Binding energies corresponding to Zn $2p_{3/2}$ and Zn $2p_{1/2}$ are found to shift to higher energies ($\Delta E \sim 1$ eV) in case of LZO films as compared to undoped ZnO. This shift to higher binding energy is associated with the decrease in kinetic energy of photoelectrons emitted from the Zn atoms due to the interaction with the electron cloud of Li atoms [192].

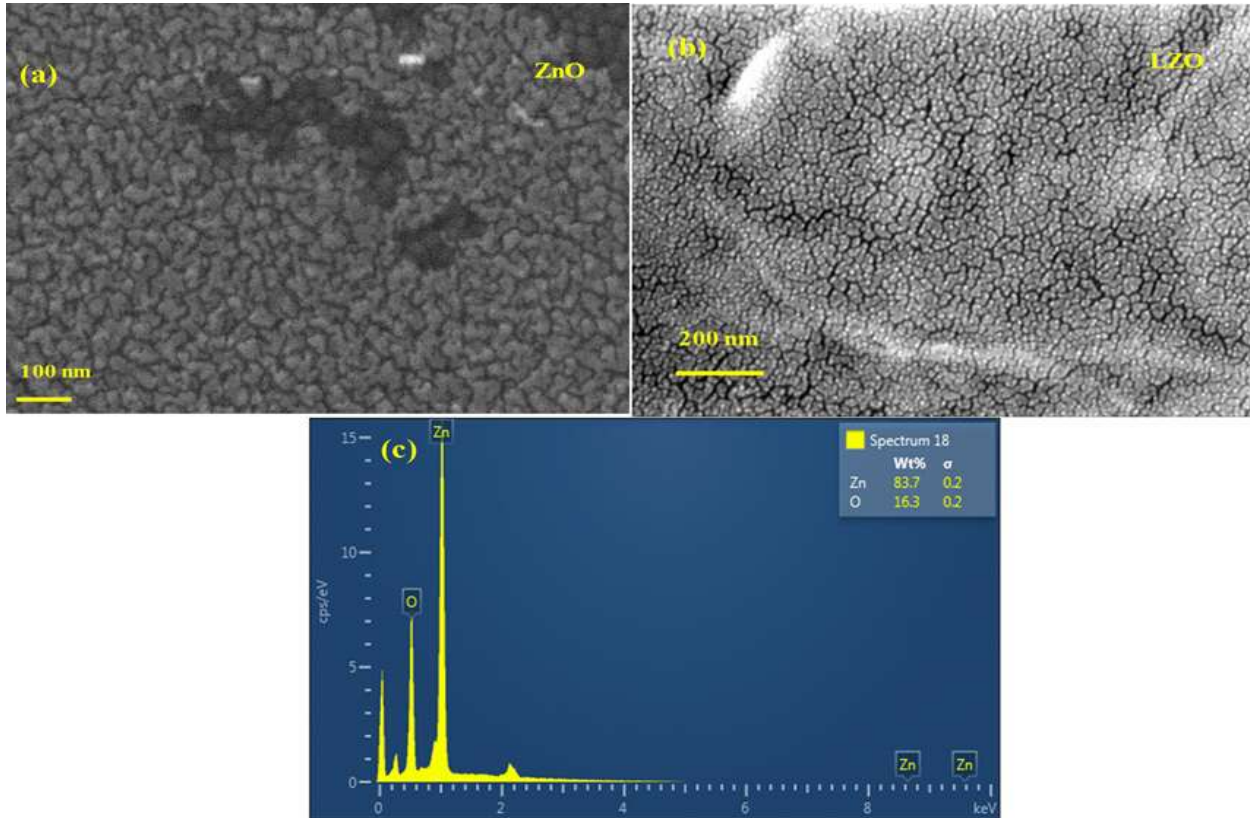

Figure.**3.2**.FESEM micrographs of (a) Undoped (ZnO) and (b) lithium doped zinc oxide thin films (LZO) (c) EDX spectrum.

Figure.3.3 (d) displays the O1s spectra of undoped and doped ZnO thin films, which could be deconvoluted to 3 sub-peaks (I, II and II) at 530.64, 531.5 and 532 eV, corresponding to different oxygen related species. These peaks represent (I) the lattice oxygen in the wurtzite structure (O-Zn or O-Li), (II) the oxygen vacancies (Ov) and (III) chemisorbed or dissociated oxygen or OH species on the surface of the ZnO thin films respectively [192-193].The area of the peak I is proportional to the amount of oxygen atoms in fully oxidized surrounding of the Zn atoms in tetrahedral symmetry. It can be noticed that area under peak I is smaller than that of

peak II (for LZO films), which could be attributed to the dominance of oxygen vacancies in doped films.

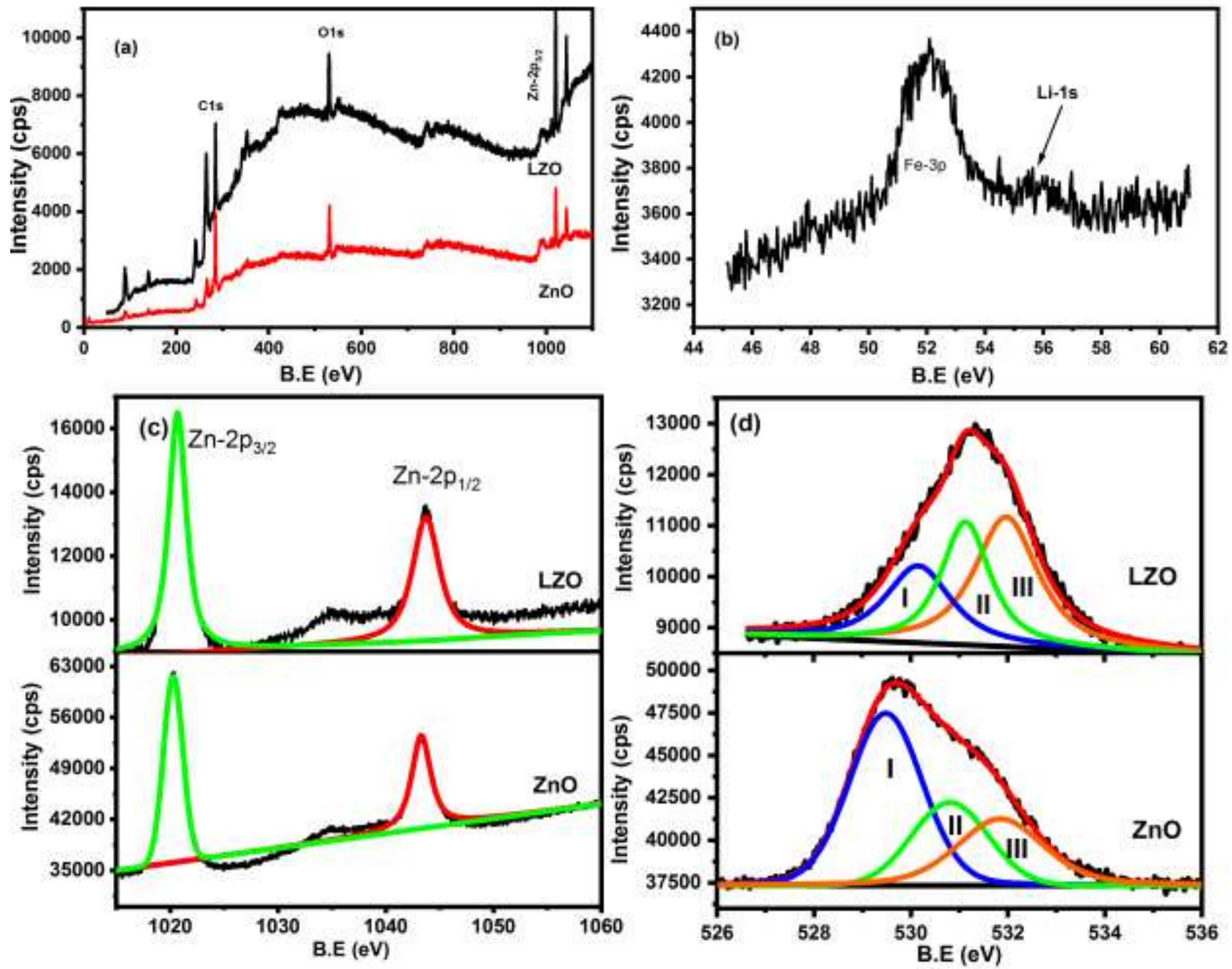

Figure.3.3 XPS spectra of undoped ZnO and LZO films: (a) Survey spectra of LZO films (b) high resolution selective spectra of Zn-2p (c) high resolution spectra of O-1s (d) high resolution selective spectra of Li-1s. Peak at 52.5 eV corresponds to Fe-3p from sample holder

3.3.4. Absorption and optical band gap

Figure.3.4 (a and b) shows the optical absorbance, transmission and reflectance spectra of ZnO and LZO thin films on glass substrate. There is a significant change in the amount of absorbance due to the incorporation of Li into ZnO lattice. The absorbance value and spectrum maximum of LZO are shifted towards lower wavelength region compared to undoped ZnO films due to the widening of band gap. The transmittance of all the films is over 95% in the visible region and decreases sharply near absorption edge; implying high crystallinity of undoped and Li

doped ZnO films. Analysis of optical absorption spectra is one of the most productive tools for determining optical band gap of the materials. From the spectral data, the absorption coefficient α is calculated using the relationship. The optical band gap Eg can be evaluated from the plot of $(\alpha h\nu)^2$ versus hν (Tauc plot).The inset of Figure. 3.4 (a) shows the Tauc plot for undoped and LZO films. The extrapolated band gap values for undoped and LZO films are found to be 3.20 and 3.37 eV respectively. Generally, the band gap of metal oxides is influenced by various factors such as morphology, carrier concentrations and defects due to oxygen vacancies, etc. In case of Li doped ZnO films, the Li ions located at interstitial sites of the ZnO lattice cause an increase in the donor electrons and the excess donor electrons cause the widening of optical band gap [194-195].

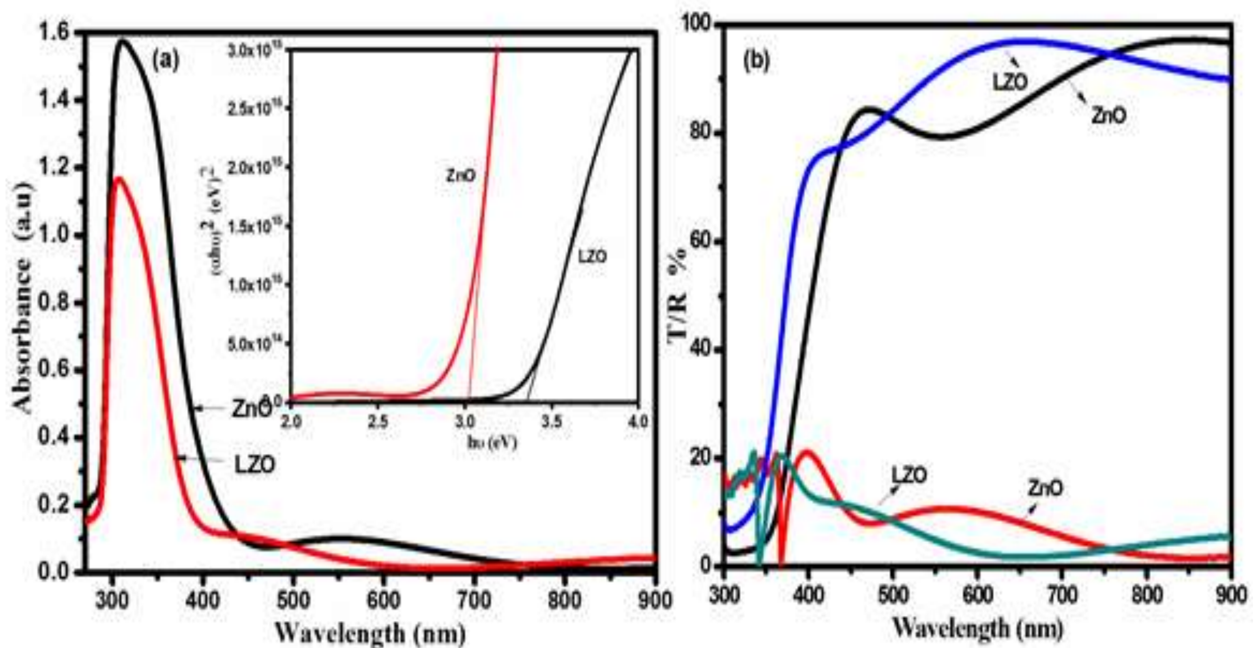

Figure.**3.4.** (a) Optical absorbance spectra and the inset shows the typical $(\alpha h\nu)^2$ vs (hν) plot (b) optical transmittance/Reflectance spectra of undoped and LZO thin films.

3.3.5. Photoluminescence Properties

Normally the PL spectra of ZnO based films shows two types of emission: near band emission (NBE) and defect level emission (DLE). The NBE emission which appears in UV range is attributed to the radiative recombination of holes in the valence band and electrons in the conduction band (excitonic recombination). DLE in visible region is associated with electron hole recombination at deep level present as defects such as oxygen vacancy or zinc interstitials.

PL spectra of undoped and lithium doped ZnO thin films (Figure.3.5 (a) and (b) show a broad peak centred at 383 nm and 381 nm respectively. The decrease in wavelength of band edge emission confirms the band gap widening in LZO films and the results are consistent with optical absorption measurements.

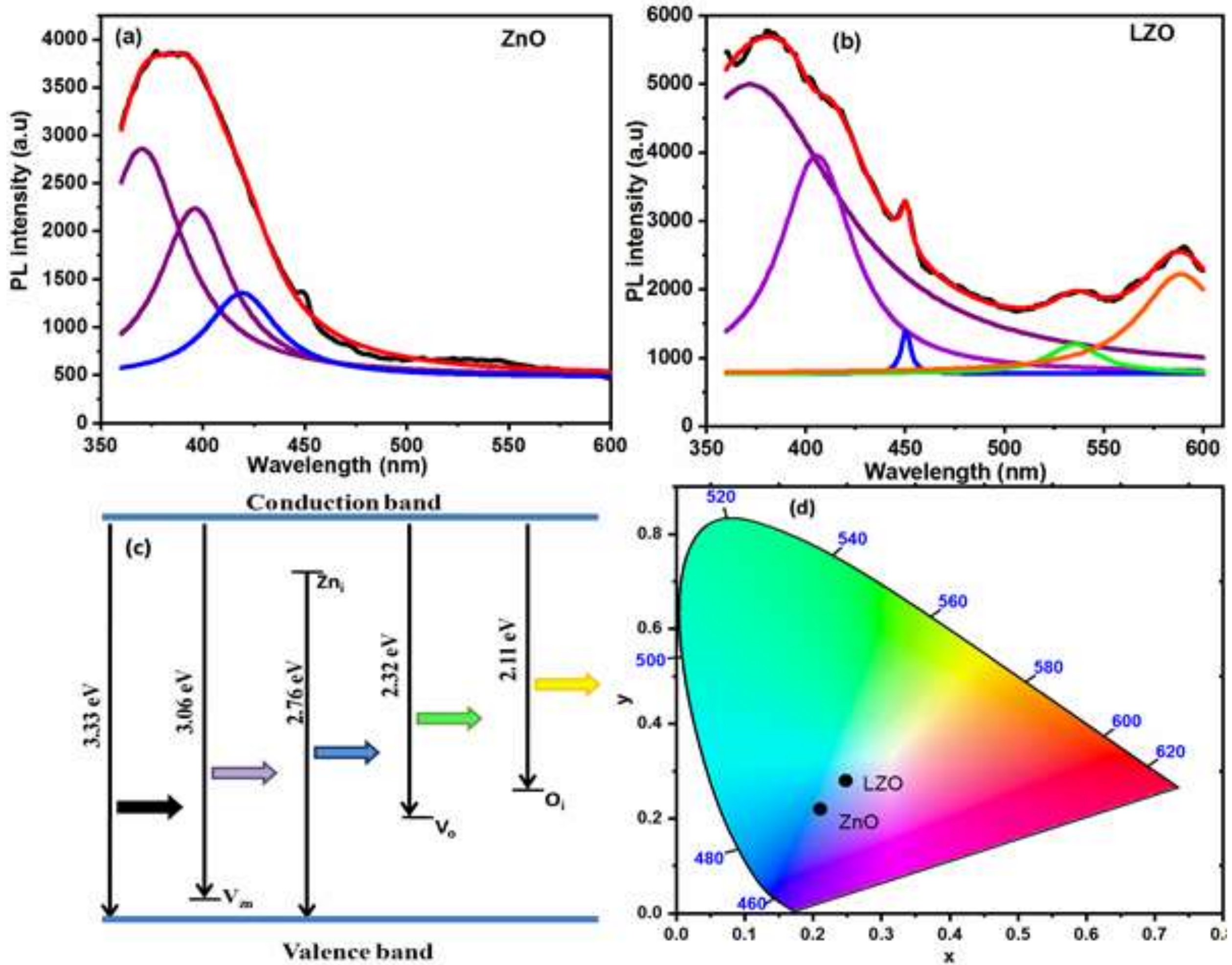

Figure.**3.5.** Room Temperature Photoluminescence spectra (black line) along with fitting (red line) and the Deconvoluted peaks in different colors for (a) undoped (ZnO) and (b) LZO films (c) Schematic energy level of defects state in band gap of Li doped ZnO films with possible emissions. (d) Chromaticity diagram undoped and LZO films.

PL spectra of undoped ZnO can be deconvoluted into three sub peaks – first one is near band emission (NBE) at ~ 370 nm which is attributed to the recombination of free excitons through an exciton – exciton collision process; the second and third peak at ~ 395 nm and ~420 nm respectively arise due to various native defects in ZnO films. In case of LZO, multiple peaks (deconvoluted) corresponding to 368, 405, 449, 534 and 587 nm are seen, which are

schematically represented in Figure.3.5 (c). The peak at ~368 nm is attributed to NBE (CB→VB); whereas the peaks at 405 nm and 449 nm (violet - blue emission) are attributed to zinc vacancies (V_{Zn}) or zinc interstitials related emissions (CB→V_{Zn} or Zn_i→VB). The broad peak at 534 nm (green emission) and peak at 587 nm (yellow emission) emerge from various defects, primarily due to oxygen vacancies (CB→V_o) and oxygen interstitials (CB→O_i) brought by the Li^+ incorporation into ZnO thin films . Because of high formation energy (~2.85 eV), Li ions cannot replace O (Li_o) in the crystal lattice but it can diffuse into the space between the lattices as interstitials [196-199]. As a result, Li ions can form interstitials defects in ZnO lattice, hence to maintain the charge balance of the lattice, intrinsic defects such as O_i and V_o are created and coexist in ZnO thin films [191]. The predominance of interstitials defects is also supported by the observation of increase of lattice parameters. Figure.3.5 (d) shows the CIE chromaticity diagram of undoped and Li doped ZnO samples. The CIE color coordinates for ZnO and LZO films correspond to (0.211, 0.218) and (0.248, 0.278) respectively. It is evident that the colour coordinates of ZnO appear near blue region, whereas LZO coordinates have shifted towards white light region, suggesting that LZO can be used as potential white light emitter.

3.4. Conclusion

Undoped and Li doped ZnO nanocrystalline thin films were grown successfully by RF magnetron sputtering using powder targets. The influences of Li incorporation on the microstructural and optical properties were investigated. Both undoped and doped ZnO films have a single phase wurtzite structure with strong orientation along c-axis, as confirmed by XRD and Raman studies. The incorporation of Li was confirmed using XPS analysis. A blue shift observed in the band gap energy of LZO might be due to the incorporation of Li into the ZnO lattice. Photoluminescence spectra exhibited multiple defect emissions in the visible region in addition to NBE in LZO, indicating that Li doped ZnO films might be useful for white light-emitting devices in optoelectronic applications.

CHAPTER 4

Group V Elements Doped ZnO Nanocrystalline Thin Films

4.1.Antimony doped ZnO nanocrystalline thin films (SZO)

4.1.1. Introduction

4.1.2. Material and Methods

4.1.3. Result and Discussion

4.1.3.1. Structural Properties

4.1.3.2. Morphological Properties

4.1.3.3. Compositional Analysis

4.1.3.4. Absorption and optical band gap

4.1.3.5. Photoluminescence Properties

4.1.4. Conclusion

4.2. Phosphorous doped ZnO nanocrystalline thin films (PZO)

4.2.1. Introduction

4.2.2. Material and Methods

4.2.3. Result and Discussion

4.2.3.1.Structural Properties

4.2.3.2.Morphological Properties

4.2.3.3.Compositional Analysis

4.2.3.4. Absorption and optical band gap

4.2.3.5.Photoluminescence Properties

4.2.4. Conclusion

This chapter is composed of 2 sections, which are designated to a material group of antimony and phosphorous doped-ZnO thin films and their characterization.

CHAPTER 4

Group V Elements Doped ZnO Nanocrystalline Thin Films

4.1. Antimony doped ZnO nanocrystalline thin films (SZO)

4.1.1. Introduction

ZnO has been recognized as a remarkable material for short wavelength optoelectronics devices due to its electronic and optical properties. High-quality p- and n-type ZnO thin films are essential for applications in such devices, including light emitting diodes and laser diodes. To realize the light-emitting devices, an important issue is the fabrication of p-type ZnO films with a high-hole concentration and a low resistance. However, it is difficult to obtain p-type ZnO films because of its self-compensation of shallow acceptors resulting from various naturaly occurring or spontaneously generated donor defects such as oxygen vacancies or interstitial zinc [181-184]. Although, p-type ZnO films by doping with N, As, P, and Li have been reported elsewhere, indistinct doping mechanism and conduction reliability are still the key issues that impede the development of all ZnO-based optoelectronic devices. Among these materials doping of antimony is special interest because it is expected to result in the p-type conduction by introducing the acceptor levels.

4.1.2. Material and Methods

Antimony doped (SZO) and undoped ZnO nano crystalline thin films were deposited on glass substrates and n type Si (111) substrate by R.F magnetron (powered at 13.56 MHz radio frequency) reactive sputtering system (Hind High Vaccum Co.P Ltd). A mixture of Sb_2O_3 purity, 99.99% and ZnO purity, 99.9% (May and Baker Ltd) powders with antimony doping content of 0,1,5, and 10 wt % were used for target preparation.

4.1.3. Result and Discussion

4.1.3.1. Structural Properties

Figure.4.1 (a). shows XRD patterns of nanocrystalline undoped and antimony doped ZnO (SZO) thin films deposited on glass substrates with different doping concentrations. It can be observed from the XRD patterns that a wurtzite structure and a strong (002) diffraction peak occur for undoped and 1% antimony doped ZnO thin films. It is also observed that these films grow along the (002) orientation with c-axis perpendicular to the substrate surface. The average

crystallite size SZO nanostructures, calculated using the Scherrer formula, decreases from 22-10 nm as the concentration of Sb increases. A reduction in crystallite size Sb doped ZnO is due to the ionic radius difference of antimony (0.092 nm) vs Zinc (0.074 nm) in the tetrahedral coordination [200]. The ionic radius of Sb is higher than that of Zn^{2+} which leads to reduction in the distance between Zn-O and Sb. Hence, the lattice structure can be distorted by Sb substitution. For 5% and 10% Sb doping concentration, the intensity of (002) diffraction peak disappeared and other peak at 37.05 ^{o} of (101) appeared. This is ascribed to more absorption of Sb atoms that causes increase in the density of Sb atoms in the interstitial sites; hence the insoluble Sb atoms are segregated at the grain boundaries and suppress the growth of thin films crystals.

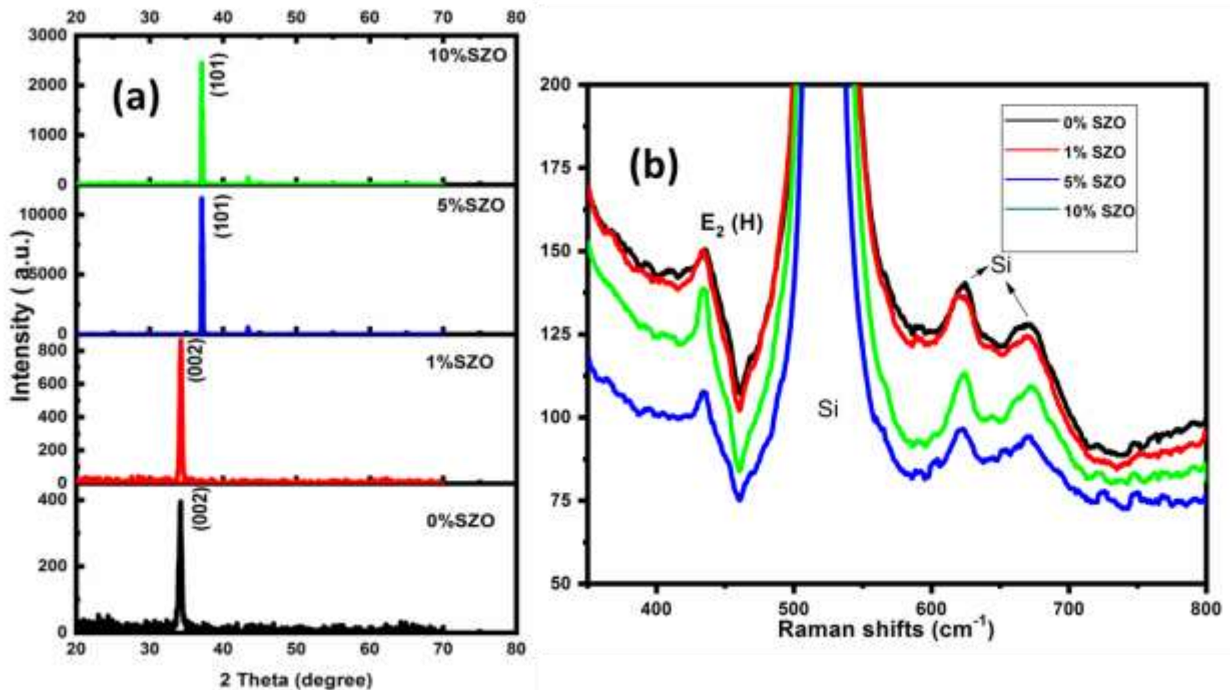

Figure.**4.1** (a) XRD pattern and (b) Raman spectra of undoped and SZO nanocrystalline thin films

Raman scattering was used to confirm the hexagonal wurtzite structure of ZnO thin films. It can be observed that E_2 (high) mode has the strongest intensity for all grown samples, which is the main Raman mode in the wurtzite crystal structure and confirms that all thin films deposited on Si substrates have a hexagonal wurtzite phase. In other words, Raman results indicate that the

Wurtzite structure of present thin films and the Sb ions have been doped into the lattice position of Zn ions.

4.1.3.2.Morphological Properties

The SEM images of doped samples (Figure.4.2 (a-d) specify that the samples were homogeneous with dopants (Sb) substituting Zn sites in ZnO and do not contain any other dopant dominating phases. The result also suggests that dopant is distributed with in ZnO lattice and not segregated or precipitated in the localized area.

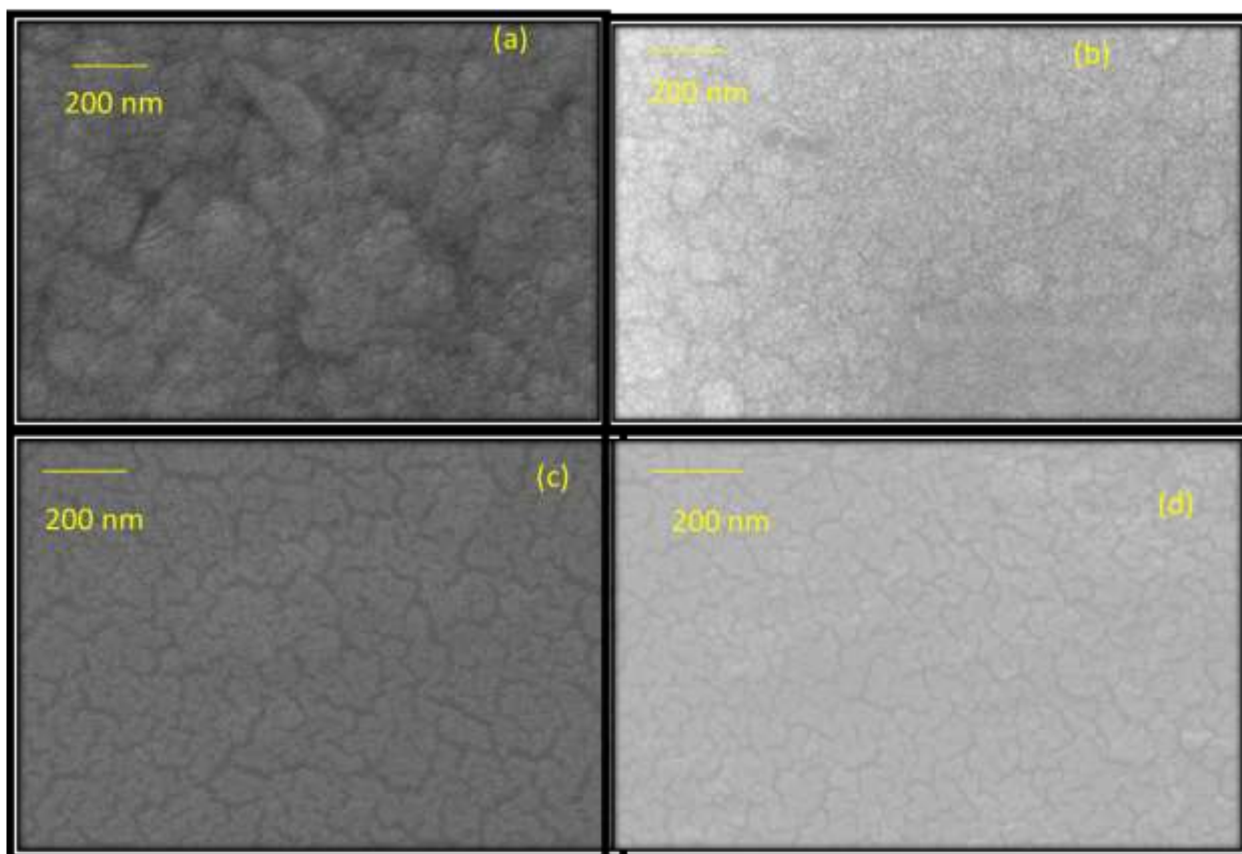

Figure.4.2 FESEM micrograph of (a) 0% SZO (b) 1% SZO (c) 5% SZO and (d) 10% SZO nanocrystalline thin films

4.1.3.3.Compositional Analysis

Figure.4.3 (a & b) shows the typical EDS spectra for 0% and 10% Sb doped ZnO thin films deposited on glass substrate. The same EDS pattern is observed for all samples with varying zinc and oxygen atomic ratios as per stoichiometric of the samples. There are no peaks observed related to the elements other than Zn ,O and Sb in the EDS spectra, which reveal the pure phase formation of ZnO thin films and are consistent with the XRD results.

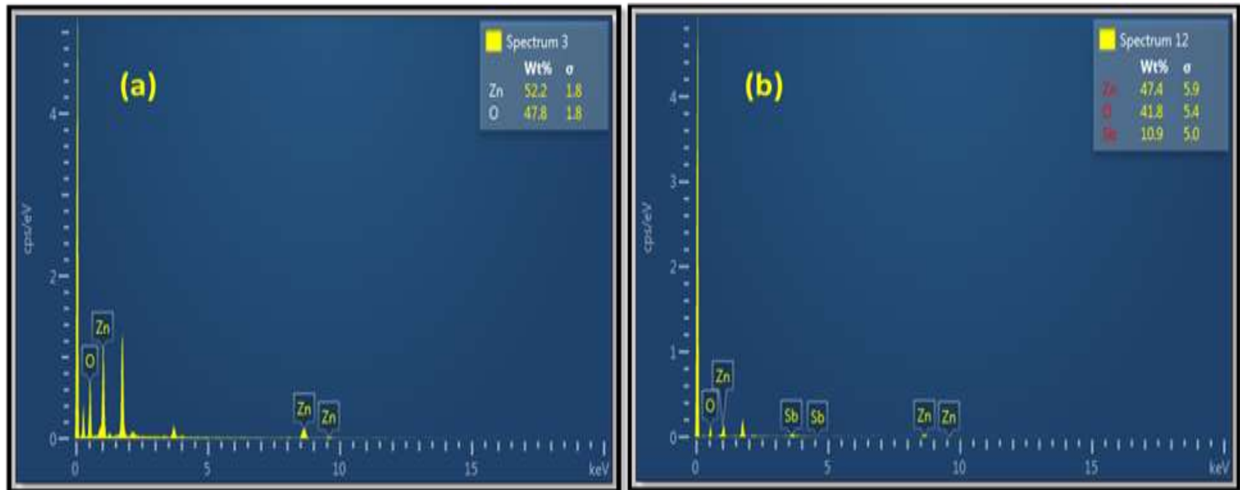

Figure.4.3. EDS spectra of (a) undoped and (b) 10 wt% SZO nanocrystalline thin films

The Sb 3d peak spectra, O 1s spectra, Zn 2p spectra and survey spectra are shown in Figure.4.4 (a-e). From the survey spectra it is confirmed presence of Zn, O and Sb in undoped and SZO films. XPS spectra of the characteristic peak of Sb $3d_{3/2}$ at 539.84 eV, confirming the presence of Sb elements in ZnO films as dopants (Figure.4.4 (a)). In principle, Sb ions could have two possible locations in ZnO lattice, substitutional and interstitial. In the substitutional case, Sb ions would either substitute Zn (Sb_{Zn}) or oxygen (Sb_O). However, isolated Sb_{Zn} in SZO would behave as donor impurity and Sb_O work like a deep acceptor; and in both the cases it was impossible to realize p-type behavior in SZO at room temperature. In the interstitial case, Sb ions were supposed to occupy interstitial positions in ZnO lattice, and this yielded deep acceptor states and thereby could not contribute to p-type conduction [200]. The peaks of Zn $2p_{3/2}$ and Zn $2p_{1/2}$ spectra were observed to be nearly centered at binding energy values of 1022.44 eV and 1045.61 eV, respectively, which (Figure.4.3 (c)) indicate that Zn is only in oxidized state. The binding energy difference between these peaks was calculated to be 23.17 eV, which was a typical value of ZnO [201].

The core level XPS spectra related to O1s and Sb $3d_{5/2}$ overlapped. However, Sb 3d peak overlapped with O1s, further clarification was required thus the narrow scan XPS spectra of Sb 3d were taken as shown in Figure.4.4 (e). The Figure shows a prominent peak at 529.64 eV, attributed to Sb atoms bonded with O atoms in the ZnO lattice. The absence of metallic Sb in XPS spectra reveals the proper incorporation of the dopants in to the ZnO lattice; indicate the formation of an (Sb_{Zn}-$2V_{zn}$) acceptor complex in the SZO films. The Sb atom replaces one Zn

atom and it creates two Zn vacancies to become stable in lattice. The formation of acceptor complex can be described as follows [202].

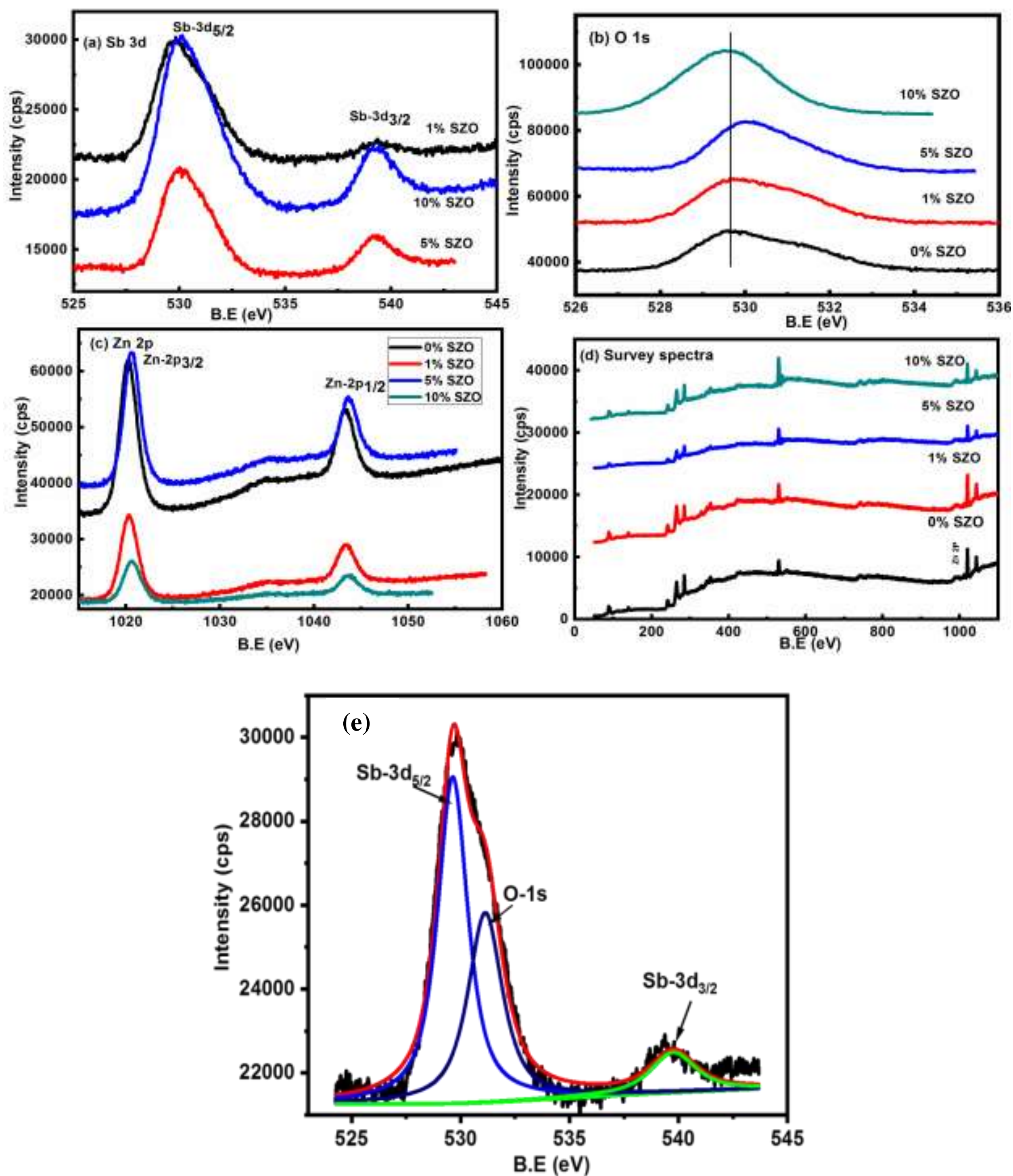

Figure.4.4 The chemical state of (a) Sb3d (b) O1s (c) Zn 2p (d) survey spectra SZO nanocrystalline thin films and (e) The deconvoluted chemical state of Sb in 1% SZO films for Sb 3d $_{5/2}$ state.

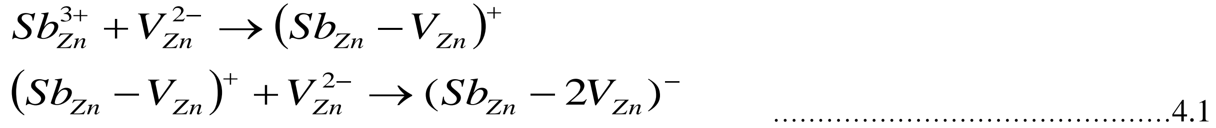

$$Sb_{Zn}^{3+} + V_{Zn}^{2-} \rightarrow \left(Sb_{Zn} - V_{Zn}\right)^{+}$$
$$\left(Sb_{Zn} - V_{Zn}\right)^{+} + V_{Zn}^{2-} \rightarrow (Sb_{Zn} - 2V_{Zn})^{-} \qquad \text{...4.1}$$

The negative charge possessing acceptor complex resultantly induces the Zn 2P peaks shift for SZO films [203]. It confirms the Sb dopants are successfully incorporated in to the ZnO lattice.

4.1.3.4. Absorption and optical band gap

The absorbance and transmittance spectra of SZO thin films are shown in Figure.4.5 (a & b). It is found that, all the films have the transmittance above 95% in the visible region and sharp absorption edge in the UV region. This indicates that the Sb dopant do not affect the transmittance of the film. The sharp decrease in the transmission near UV region was observed due to the band gap absorption. Good transmittance in the visible region reveals that a film has less defects and better crystallinity. It is observed that the absorption edge of Sb doped ZnO thin films shifts to lower wavelength region when compared with undoped ZnO thin films. It is found that Eg values slightly increased from 3.24 to 3.34 eV as the concentration of dopant increased from 0 to 10 wt%. The band gap broadening on doping makes the film more transparent to solar radiation making it suitable for transparent conducting oxide applications

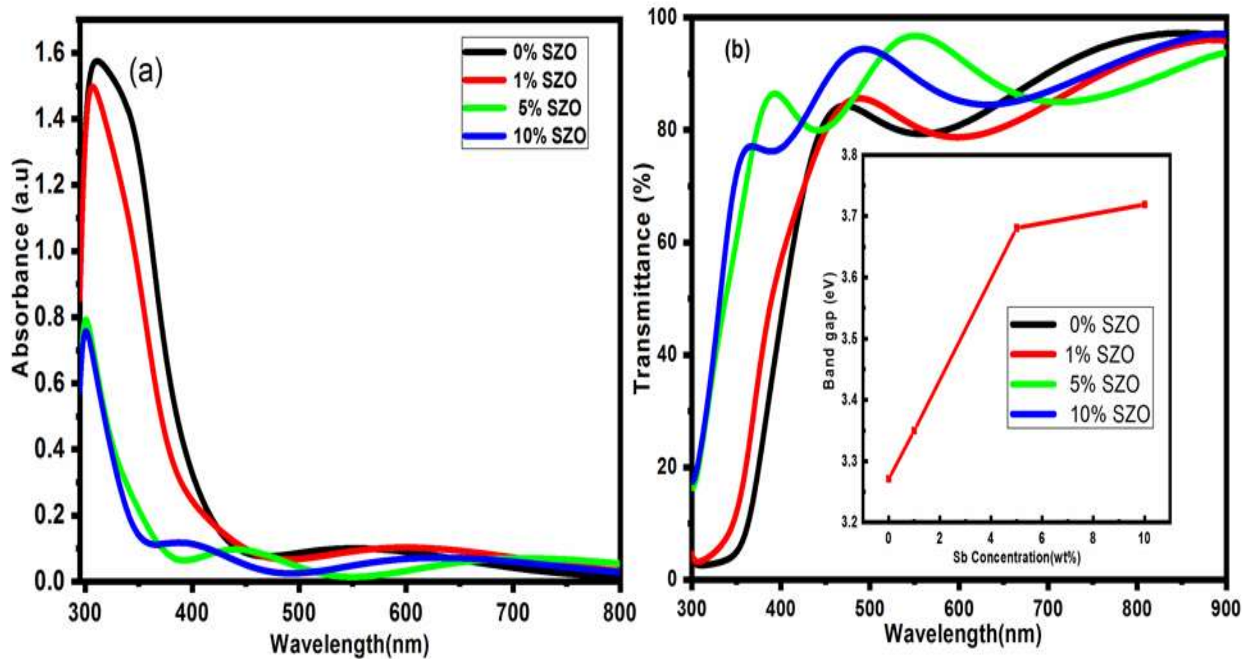

Figure.4.5 (a) Absorbance and (b) transmittance spectra of undoped and SZO thin films. The inset shows variation of the optical band gap with doping content.

4.1.3.5. Photoluminescence Properties

Figure.4.6 (a) shows the photoluminescence spectra of undoped ZnO and Sb doped ZnO thin films. The visible emission from ZnO thin films may be due to the defect, particularly the oxygen vacancy arising from the oxygen deficiency and both O and Zn interstitials. The UV emission at 389 nm can be attributed to the near band edge (NBE) emission of ZnO and originated by the recombination of free exciton transition from the localized level below the conduction band to the valance band. A blue luminescence peak centered at 420 nm in visible region is observed for all the samples (inset of Figure 4.6 (a)). The blue emission is caused by intrinsic defects and donor-acceptor pair recombination. It is also found from PL measurement that the peak of NBE emission of ZnO thin films has a blue-shift to higher energy. According to the structural characteristics of ZnO, blue-shift in the PL spectra may be attributed to the decrease in defects and structural discrepancy. In case of heavily doped ZnO thin films, the donor electrons occupy states at the bottom of the conduction band. The blue-shift in the UV emission is ascribed to the quantum confinement effect which state that the band gap energy of a semiconductor increases with decrease in crystal size [204].

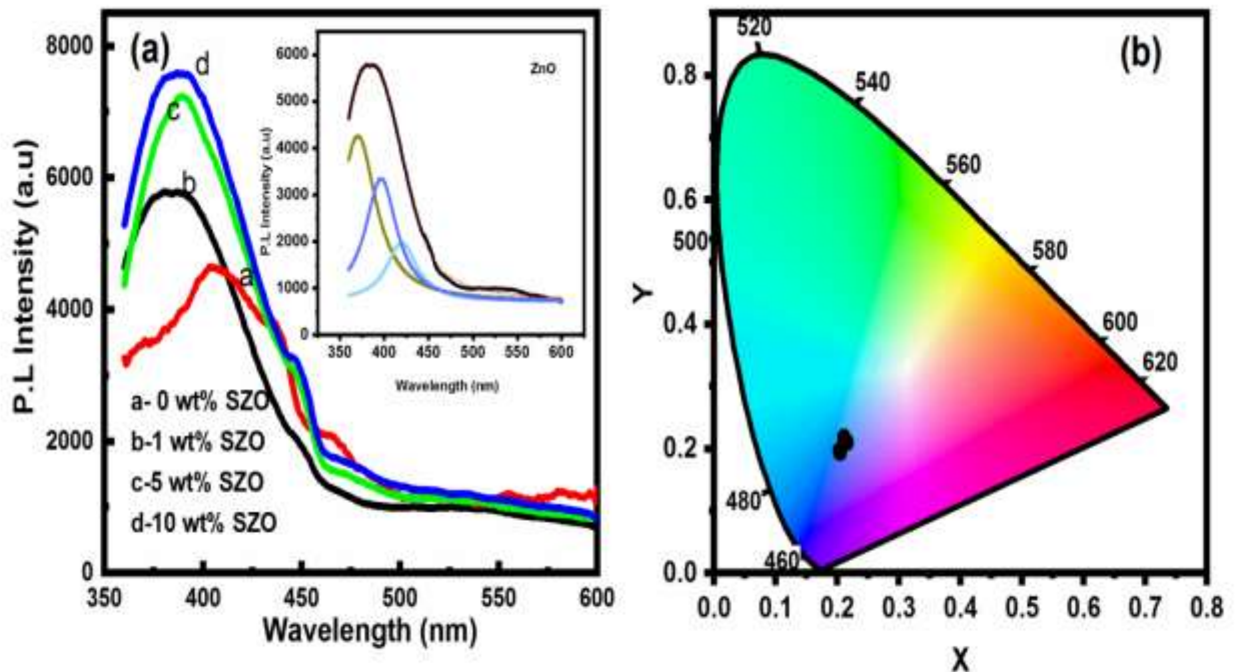

Figure.**4.6** (a) Room temperature PL spectra of undoped and SZO thin films (inset shows deconvoluted spectra) (b) chromaticity diagram of SZO films based on PL data.

The CIE colour coordinates measured from the photoluminescence emission of doped ZnO by varying the Sb dopant concentration are shown in Figure.4.6 (b). For the case of the Sb-doped ZnO thin films with Sb dopant concentration of 0 wt%, 1 wt%, 5 wt% and 10 wt%, the CIE coordinates are (0.211, 0.218), (0.216, 0.210), (0.204, 0.194) and (0.204, 0.197) respectively and these show that the colors are in blue regions.

4.1.4. Conclusion

Sb doped ZnO thin films have been deposited using RF sputtering technique. The effect of Sb doping on the structural, optical and electrical properties of ZnO thin films has been investigated. XRD analysis reveals that Sb doped ZnO thin films exhibit hexagonal wurtzite structure with preferred orientation. XPS analysis results clearly shows that the Sb element has been doped in to the ZnO lattice and no metallic Sb as well as Zn exists in the SZO films. PL results have shown and confirmed that for SZO samples exhibit UV emission peak accompanied by a peaks in the blue region. Thus these films are useful for luminescent thin film applications, particularly where blue emission is required.

4.2. Phosphorous doped ZnO nanocrystalline thin films (PZO)

4.2.1. Introduction

Zinc Oxide is a well-known II-VI semiconductor due to its fundamental and technological importance. It is a wide band gap semiconductor (~ 3.37 eV) with a high exciton binding energy of 60 meV, has excellent chemical stability, is abundant in nature and non-toxic [205-206]. It has a wide range of applications like solar cells, luminescent devices, laser diodes, chemical sensors, surface acoustic wave devices, and microelectronics etc. The material properties of the metal oxide films can be tuned by controlling the deviation from stoichiometry using suitable doping elements. ZnO thin films can be doped with a variety of impurities to meet the demands of these applications. Specifically, for transparent electrodes, elements such as Al, Ga, and In (P and As) atoms are incorporated to increase electron (hole) carrier density [207-208]. To enhance absorption of visible light, the dopants are chosen such that they create defect levels within the band gap or shift band-edge positions, thereby narrowing the optical gap [205-206]. In sensor and catalyst applications, transition metals are used to increase active sites that accelerate chemical reactions [209-210]. Lastly, the magnetic impurities are incorporated to use ZnO as the spin-transport layer in spintronic devices [211].

4.2.2. Material and Methods

$Zn_{(1-x)}P_xO$ (x= 0, 0.01, 0.03 and 0.05) thin films were deposited by RF magnetron sputtering on glass substrates in sputter-up configuration using powder targets. High purity ZnO and P_2O_5 powders were used to prepare the targets.

4.2.3. Result and Discussion

4.2.3.1. Structural Properties

Figure.4.7.(a) shows the X-ray diffraction of PZO thin films deposited on glass substrate with different P concentration. The XRD measurements show that both undoped and P-doped ZnO have hexagonal wurtzite structure with (002) preferential orientation. The intensity of (002) orientation decreases with the concentration of P. Some additional peaks are observed along (100), (110) and (101) orientations for 5% PZO films. The peak at 20.9^o for 3% and 5% PZO films can be attributed to the un-dissociated zinc phosphate hydrate ($Zn_3(PO_4)_2.4H_2O$) by the RF plasma during sputter deposition. The (002) peak of the PZO films shifts towards higher angle up to 3%, while for 5% (Figure.4.7.b), it shifts towards lower angle. The shift towards higher angle

indicates a decrease in lattice constant due to the incorporation of the P into ZnO lattice to form antisite Pzn [208]. The lattice constant of the c-axis increases for 5% PZO film compared to other concentration, which could be due to the incorporation of P into O site of ZnO lattice or the formation of Zn-P bond. The crystallite size (D), lattice constant (c), dislocation density (δ) and interplanar spacing (d) are calculated along (002) orientation and tabulated in Table.4.1.

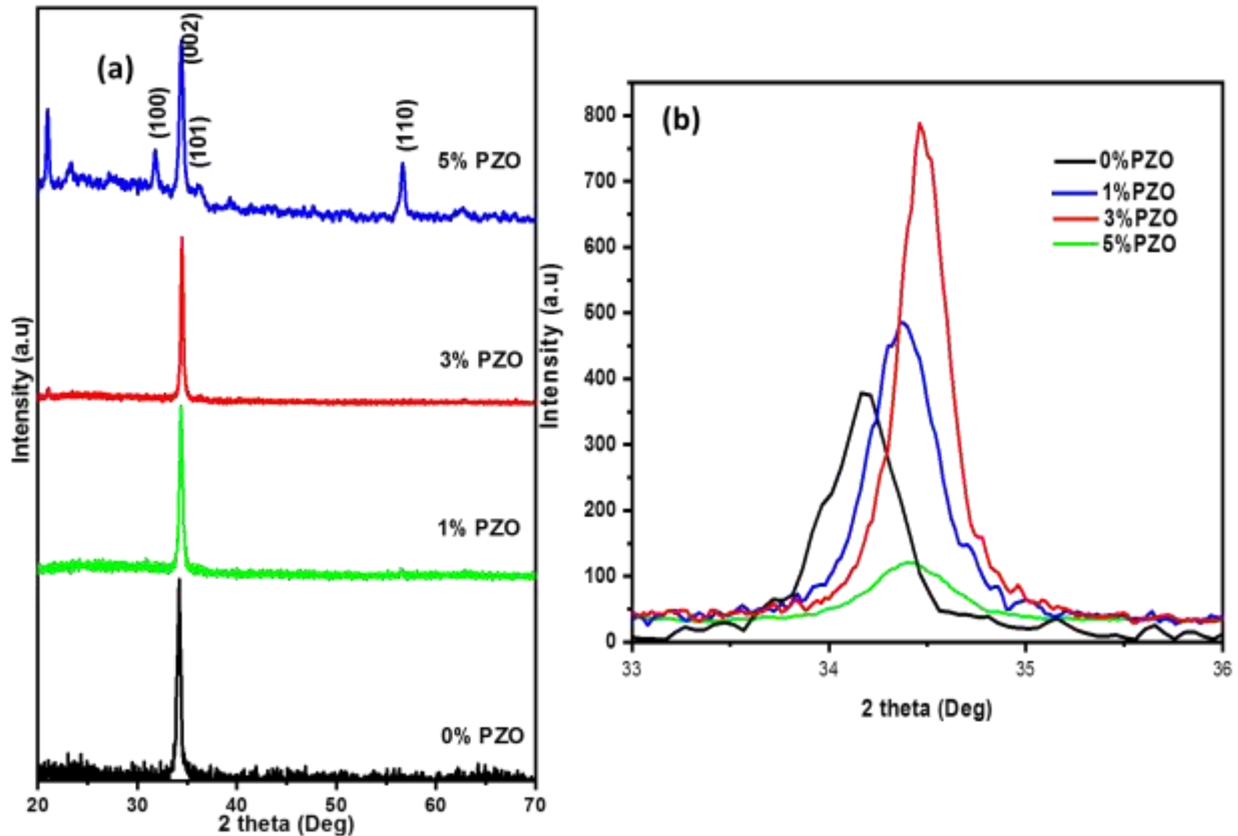

Figure 4.7 (a) XRD patterns of PZO thin films and (b) shifting of diffraction angle of (002) plane of PZO thin films.

4.2.3.2.Morphological Properties

The surface morphology of the deposited film is investigated using FESEM. Figure.4.8. (a) 0% (b) 1% (c) 3% and (d) 5% shows the micrographs of films grown with various phosphorous content. As shown in Figure.4.8, the smooth surface is composed of dense grain with uniform dimension.

Table.4.1. Structural parameters of PZO thin films

Sample	2θ (Deg)	D (nm)	d (nm)	c (nm)	Δ 10^{15}
0% PZO	34.178	22	0.262	0.524	2.07
1% PZO	34.377	22.5	0.261	0.521	1.975
3% PZO	34.478	30.5	0.259	0.519	1.075
5% PZO	34.413	20.6	0.261	0.521	2.37

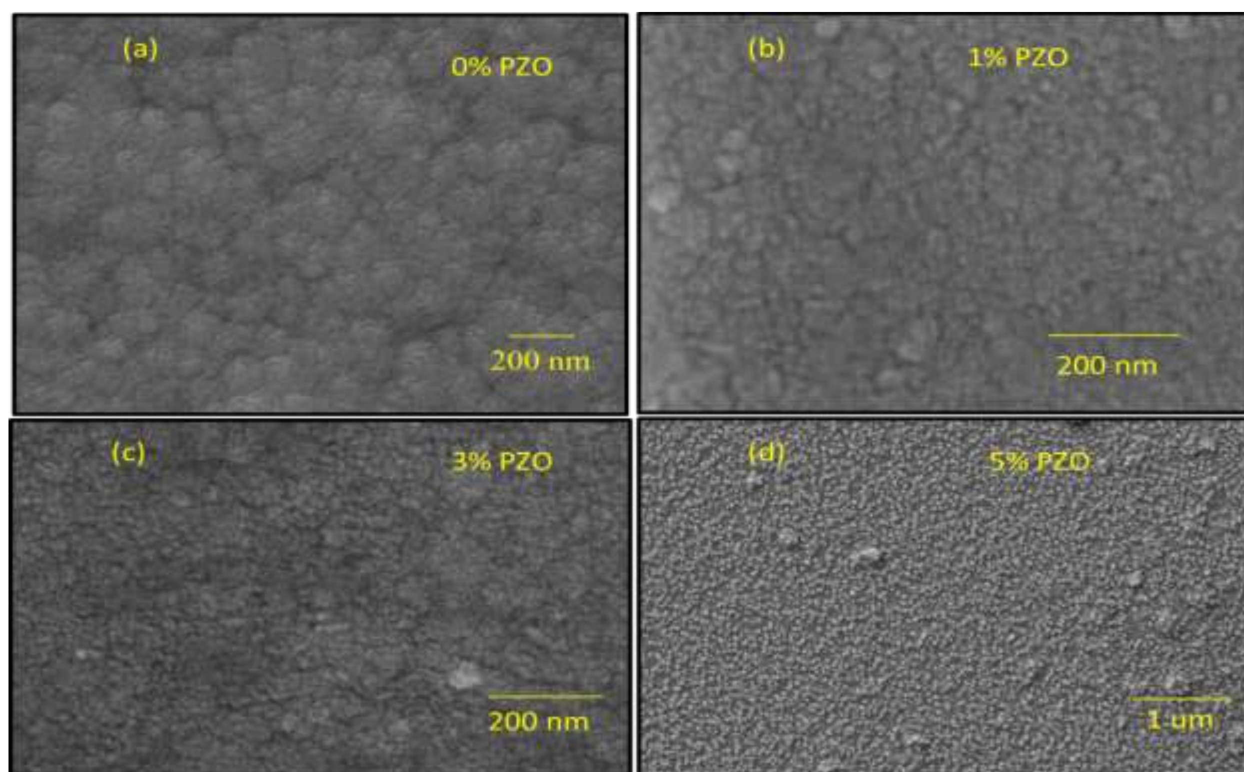

Figure.4.8 FESEM micrograph of (a) 0% (b) 1% (c) 3% and (d) 5% PZO thin films

4.2.3.3. Compositional Analysis

The film stoichiometry and defects analysis of the PZO film are carried out by XPS measurements. Figure.4.9 (a) shows XPS spectra of O1s core level of PZO thin films. The O1s spectra is fitted in to 3 distinct Gaussian curves centred at binding energy 529.5±0.4 eV, 530.5± 0.5 eV and 531.7 ± 0.2.eV. The low energy peak is attributed to oxygen atom at regular lattice

site (O_L). The medium energy peak is associated with oxygen atoms in oxygen-deficient region (O_v) with in ZnO lattice and the highest energy peak corresponds to interstitial oxygen atoms (Oi) or surface oxygen in the form of OH groups. The area of peak corresponding to Oi is higher than that of Ov peak for doped ZnO thin film. This in turn justifies the presence of yellow emission peak (587 nm) in addition to bluish – green emission peak in the PL spectra corresponding to oxygen interstitials and oxygen vacancy respectively in PZO films. Figure.4.9 (b) shows the Zn2p level spectra of PZO film. $Zn2p_{3/2}$ and $Zn2p_{1/2}$ peaks are nearly centred at B.E. values of 1043 ± 0.5 eV and 1020.4 ± 0.4 eV respectively, corresponding to Zn atoms at lattice site in PZO. The binding energy difference between $2p_{3/2}$ and $2p_{1/2}$ is calculated to be ~23 eV which is the typical characteristics value for ZnO. P related peaks at 131 eV and 133 eV (2p) (Figure.4.9 (c)) are observed which confirm that P has been incorporated in to the ZnO lattice and bonded with Zn/O to occupy oxygen/Zinc [212]. This is consistent with XRD results.

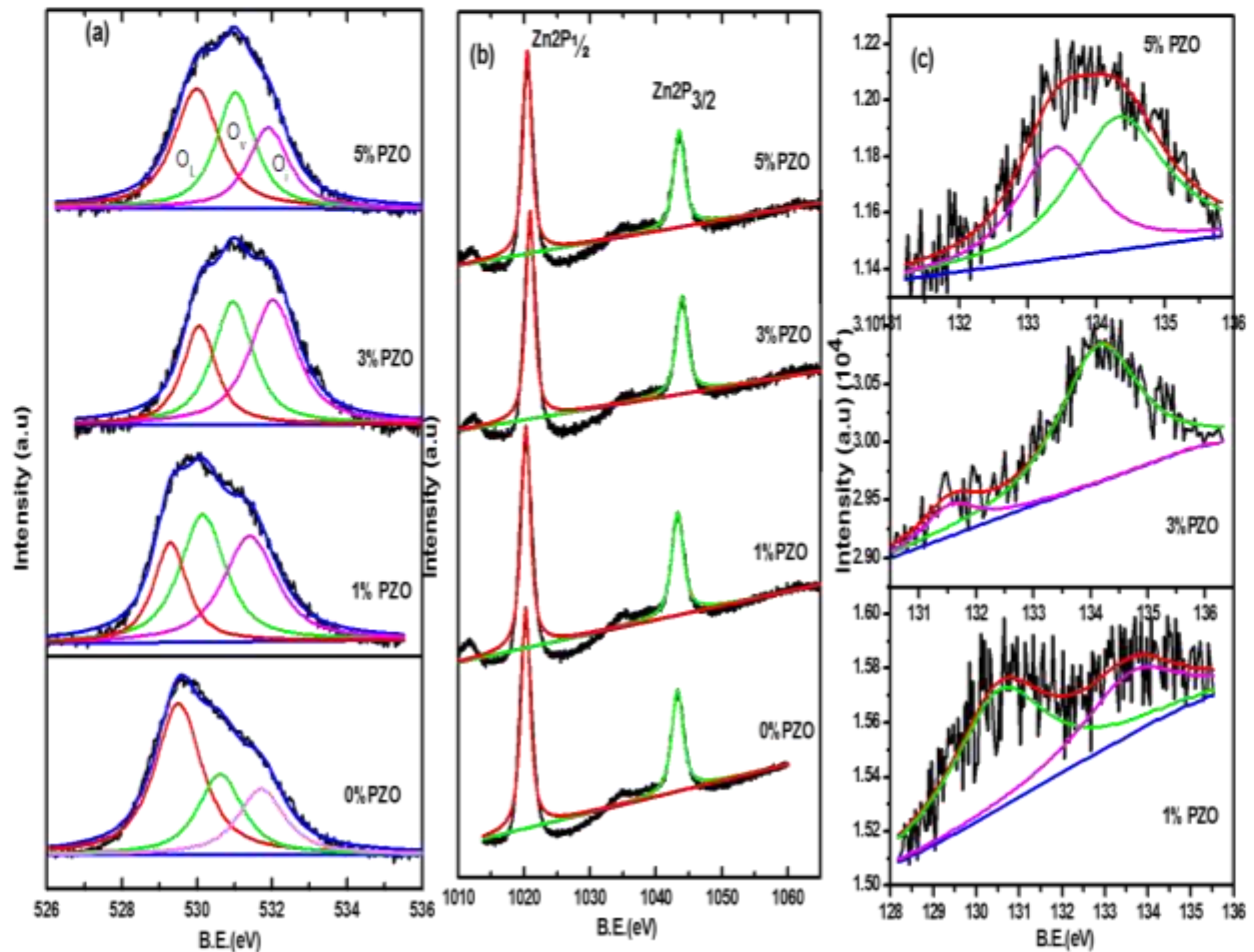

Figure 4.9 (a) Deconvoluted O1s spectra (b) Zn2p spectra and (c) 2p spectra of PZO thin films

4.2.3.4. Absorption and optical band gap

Figure.4.10.(a) shows the absorbance spectra of PZO thin films recorded in the wavelength region of 300 - 800 nm. It can be seen that the absorbance increases with the doping level which is due to the defect formation leading to an increasing band gap value. The transmittance spectrum of PZO thin films is illustrated in Figure.4.10. (b). The transmittance of all film are over 90% in the visible region and the decreases sharply near absorption edge implying high crystallinity of the PZO films. The variations $(\alpha h\upsilon)^2$-vs hυ in the fundamental absorption region are plotted in the inset of Figure.4.10.(a). The optical band gap can be evaluated by extrapolation of the linear part of $(\alpha h\upsilon)^2$ to zero. The computed optical band gaps of PZO thin films are 3.19 eV, 3.25 eV, 3.28 eV and 3.317 eV respectively. As shown in the inset of Figure.4.10 (b), band gap increases with P doping content, which is ascribed to the lattice distortion due the substitution of P on Zn site.

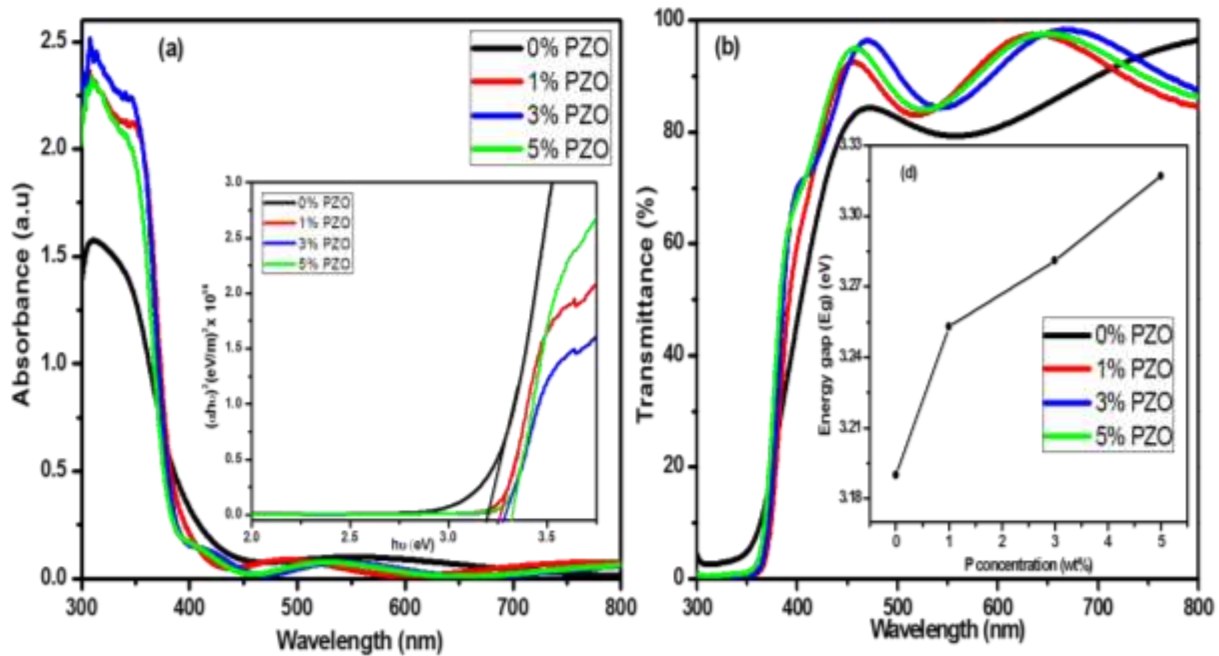

Figure.4.10 (a) Absorbance spectra (Inset shows the band gap) and (b) Transmittance spectra (Inset shows the variation of band gap with P concentration) of PZO thin films

4.2.3.5. Photoluminescence Properties

Photoluminescence spectra of PZO films at an excitation wavelength of 325 nm are shown in Figure.4.11 (a). PL spectra of undoped ZnO include a peak for direct band gap emission at about 390 nm in the UV region and two peaks at 420 nm and 487 nm in visible

region. All P doped ZnO films exhibit peaks at 415 nm and 449 nm, which could be attributed to Zn vacancy and interstitial respectively (blue region). A peak at about 530 nm is present in all films, which might be associated to oxygen vacancies or interstitials (green region). In addition, all doped films showed PL emission band around 587 nm, which could be assigned to the enhanced oxygen vacancies in doped films. It is observed that at doping, defect related emissions in the yellow region become more intense. The CIE colour coordinates measured from the photoluminescence emission of PZO thin films by varying the P content are shown in Figure.4.11(b). The CIE coordinates are (0.181, 0.145), (0.253,0.279), (0.278, 0.322) and (0.266, 0.298) for 0 wt%, 1 wt%, 3 wt% and 5 wt% respectively, and these value suggest that the tuning of blue emission to white light emission is possible on the addition of suitable P content.

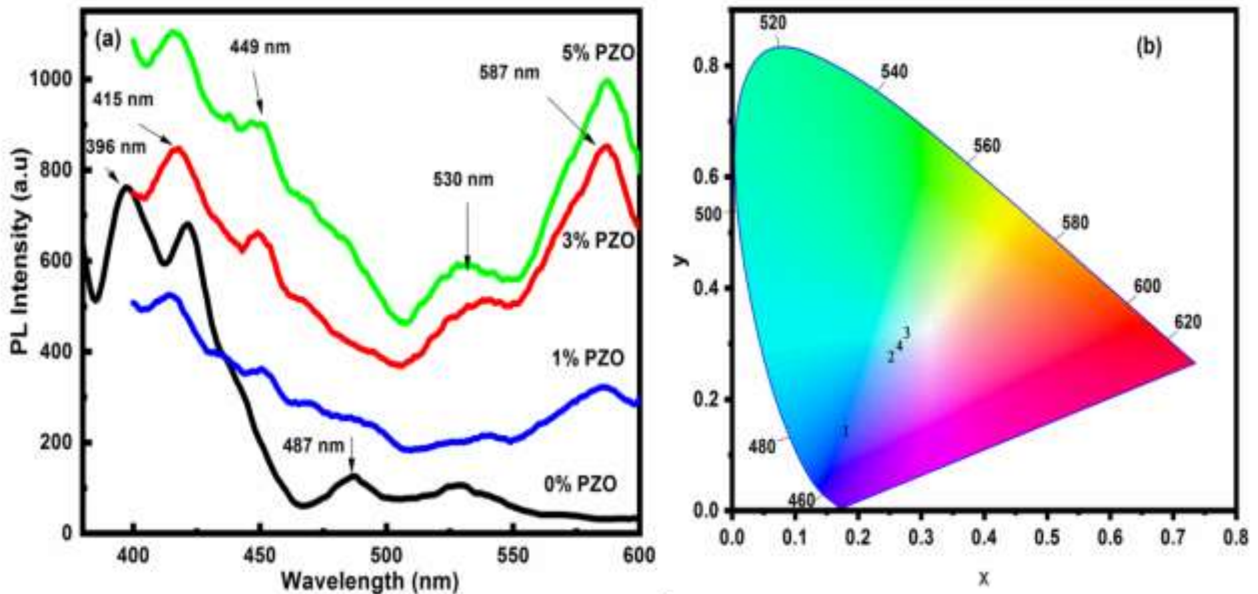

Figure. **4.11**.(a) Room temperature PL spectra and (b) CIE diagram of (1) 0 wt% (2) 1 wt% (3) 3 wt% (4) 5 wt% PZO thin films at an excitation wavelength of 325 nm

4.2.4. Conclusion

Phosphorous doped ZnO nanocrystalline thin films were grown on glass substrate by RF magnetron sputtering using powder targets. XRD patterns showed that all the films were preferentially oriented along the c-axis with a strong Bragg reflection corresponding to (002) orientation. XPS demonstrated the substitution of P in ZnO lattice. PL and XPS analysis confirmed the signatures of oxygen interstitials and vacancies defects in PZO films. All the films exhibited >90% optical transmittance in the visible range. These studies provide a pathway for tuning the material properties of ZnO based devices to achieve the desired performance.

CHAPTER 5

Group III elements doped ZnO nanocrystalline thin films (Indium, Gallium and In and Ga codoped)

5.1. Indium doped ZnO nanocrystalline thin films (IZO)

5.1.1. Introduction

5.1.2. Materials and Methods

5.1.3. Result and Discussion

5.1.3.1. Structural Properties

5.1.3.2. Morphological Properties

5.1.3.3. Compositional Analysis

5.1.3.4. Absorption and optical band gap

5.1.3.5. Photoluminescence Properties

5.1.3.6. Homojunction Devices

5.1.3.7. Gas sensing measurements

5.1.4. Conclusion

5.2. Gallium doped ZnO nanocrystalline thin films (GZO)

5.2.1. Introduction

5.2.2. Materials and Methods

5.2.3. Result and Discussion

5.2.3.1. Structural Properties

5.2.3.2. Morphological Properties

5.2.3.3. Compositional Analysis

5.2.3.4. Absorption and optical band gap

5.2.3.5. Photoluminescence Properties

5.2.3.6. Homojunction Devices

5.2.4. Conclusion

5.3. Indium and Gallium codoped ZnO nanocrystalline thin films (IGZO)

5.3.1. Introduction

5.3.2. Materials and Methods

5.3.3. Result and Discussion

5.3.3.1. Structural Properties

5.3.3.2. Morphological Properties

5.3.3.3. Compositional Analysis

5.3.3.4. Absorption and optical band gap

5.3.3.5. Photoluminescence Properties

5.3.4. Conclusion

In this chapter we analyses, indium doped (IZO), gallium doped (GZO) and indium and gallium codoped zinc oxide (IGZO) thin films. The effect of varying dopant concentrations of IZO and GZO was analyzed and the best film conditions were then used to produce co-doped IGZO films. All films were investigated focusing on the growth behavior and luminescent properties

CHAPTER 5

Group III elements doped ZnO nanocrystalline thin films (Indium, Gallium and In and Ga codoped)

5.1. Indium doped ZnO nanocrystalline thin films (IZO)

5.1.1. Introduction

Among the wide band gap II-VI compound semiconducting oxides, ZnO is one of the most desirable and special materials used in a variety of applications such as light emitting diode, photo detectors, gas sensors, piezoelectric devices, transparent conducting oxide layers in solar cell, varistors and electroluminescence (EL) devices [213-217]. Inspite of years of study and recent progress in research on ZnO properties, there persist controversies related to the origin of green emission, the nature of the inherent shallow donors, native defects and reproducible p-type doping etc.[218-219]. In controlling the electrical and optical properties, the vital role of the defects in semiconductor materials has been well defined. In particular, there is need for understanding of defects in order to achieve reproducible, high quality n-type and p-type ZnO that are needed for device applications.

It is well known that doping in ZnO with suitable impurities can improve the electrical and optical properties. While p type doping remains a challenging task in ZnO, it is equally important to carry out n-type doping in ZnO with precise carrier concentrations, high crystallinity and easy synthesis are necessary for optoelectronic applications. Various dopants from group-III elements such as Ga, Al, In and transition metals such as Fe and Mn and rare earth elements such as Er and Eu were widely used depending on the application [220-223]. Among the III group elements, indium is considered as one of the most effective dopant because of the easier process controllability, lower reactivity and greater resistance towards oxidation [224]. The changes taking place after doping of ZnO by In atoms, may be due to either substitution of a Zn atom by an In atom in the lattice or to the migration of In atoms to a non-crystalline region of the grain boundaries, creating links between In-O. In case when In^{3+} ion substitutes Zn^{2+} ion, a free electron is expected to be present for each substitution of In atom resulting in an increase in carrier concentration and hence altering properties of ZnO with increase in In doping. Additional defects created due to difference in size of In ion (0.080 nm) and Zn (0.074 nm) may also contribute towards change in properties due to doping.

5.1.2. Materials and Methods

Indium doped ZnO (IZO) and undoped ZnO films were fabricated on glass and p type Si (100) substrate by RF magnetron sputtering using a powder target under O_2 and Ar ambient. For fabrication of homojunction device, Sb doped films were prepared in a method similar to In doped film using Sb_2O_3 powder (99.99%, May and Baker Ltd) and ZnO powder.

For the fabrication of homojunction devices, initially 1wt% antimony doped ZnO (SZO) film was grown on a pre-cleaned indium tin oxide (ITO) substrate by RF magnetron sputtering using the same process parameters. Afterwards, indium doped (1%, 5% and 10%) ZnO film was grown over the SZO film. The schematic diagram of the fabricated homojunction device using the SZO and IZO films is shown in Figure.5.1. In this device, thickness of the SZO and IZO films was ~100 nm and 60 nm, respectively. For studying I-V characteristics, top contacts were made on IZO films, by thermally evaporating Titanium (10 nm) and gold (30 nm). To reduce contact resistance, rapid thermal annealing was carried out at 400°C for 3 minute in high purity oxygen ambient. ITO was used as the rear (second) contact. I-V measurements on the fabricated device were carried out using Keithley meter cum voltage source 6487.The ohmic nature of contact electrodes was confirmed prior to the I-V measurements.

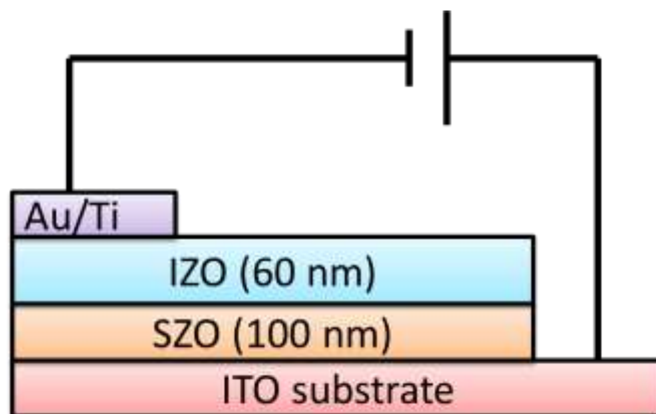

Figure 5.1 Schematic diagram of homojunction device configuration

5.1.3. Result and Discussion

5.1.3.1.Structural Properties

Figure.5.2 (i) shows the XRD patterns of undoped and indium incorporated ZnO thin films (on glass substrates).It is clearly evident from the XRD spectra that both films exhibit a preferred orientation along (002) plane corresponding to hexagonal wurtzite structure. Among all

the films, undoped ZnO (0% IZO) film exhibits highest crystallinity. With increase in In doping till 5wt %, additional peaks corresponding to (100) and (101) planes are observed. For 10% IZO films multiple peaks at different orientations corresponding to (100), (002), (101), (102) and (110) planes are seen. In addition, the intensity and full width at half maximum of (002) peak is observed to decrease and increase, respectively. It is observed that growth of c-axis oriented films is hindered with increase in indium concentration. This could be attributed to stress developed due to the difference in size of Zn^{2+} and In^{3+}ions [225].The slight broadening and shift in peak position of (002) plane, towards a lower angle after In doping, could be due to distortion in ZnO lattice, caused by accommodation In^{3+} ion in place of Zn^{2+}ion. No indium related phase is seen in the XRD patterns, suggesting that In substitutes Zn in the hexagonal lattice or In segregates to non-crystalline region in the grain boundary and forms In–O bond [226-227].Table.5.1 tabulates the structural parameters of IZO films including crystallite size, 'd' spacing etc., which are calculated from the respective XRD pattern.

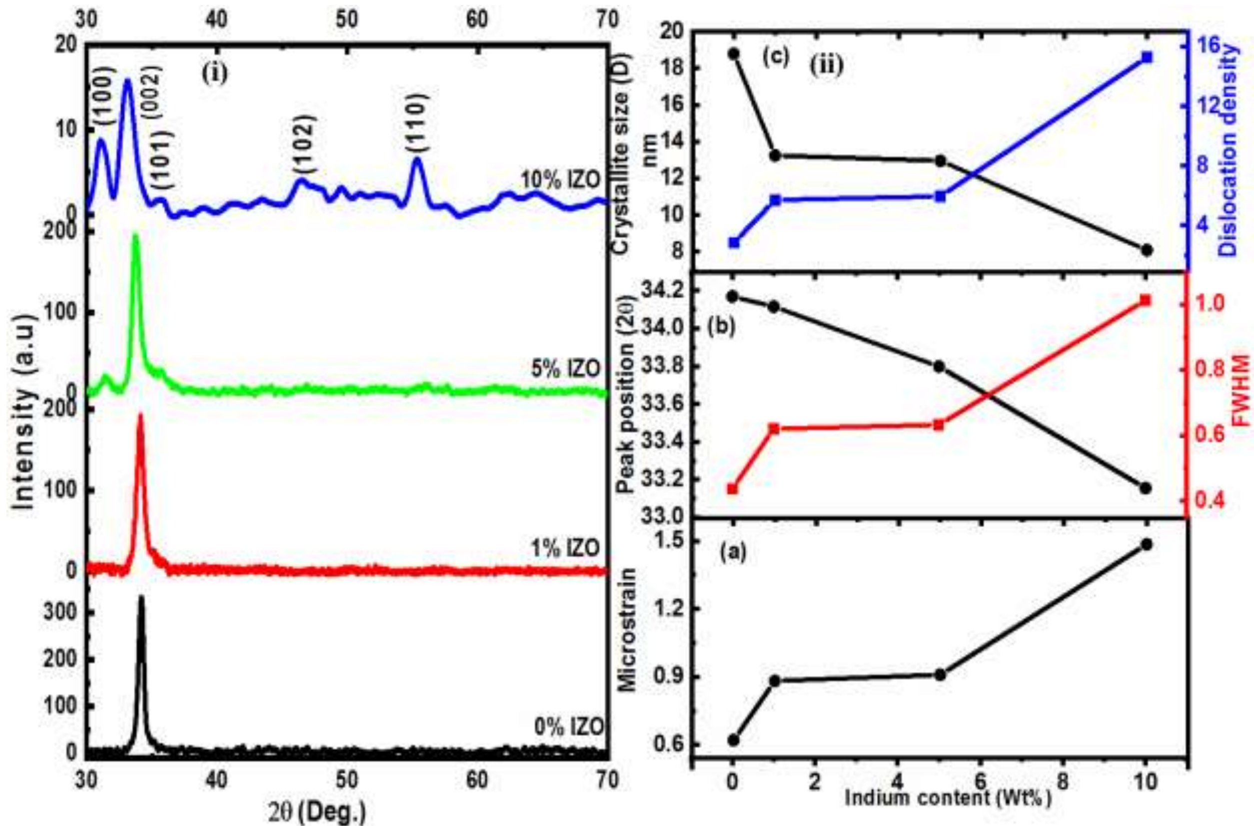

Figure 5.2 (i) XRD pattern of IZO thin films at various indium contents and (ii) Variation of (a) Micro strain (b) peak position and FWHM (c) Crystallite size and Dislocation density and with various indium content of ZnO films.

It is observed from Table.5.1.that the crystallite size of ZnO decreases from ~19 nm to 8 nm as the In content increases from 0 wt% to 10 wt%. Figure.5.2 (b) shows the effect of indium doping on (002) peak position and FWHM which are found to change systematically with doping concentration. Associated increases in lattice strain and dislocation density are also seen with In incorporation (Figure.5.2).Table.5.2.summarizes the dislocation density, strain across c axis and micro strain of IZO films at various dopant concentrations. The lattice strain (ε) is mostly due to the mismatch between the polycrystalline film and the glass substrate. The increase of strain with doping concentration may be attributed to the shifting of preferred orientation. It means that the doping creates crystal defects and charge imbalance around the dopants.

The dislocation density (δ) gives the number of dislocation lines per unit volume present in the synthesized films. It is seen from the Table 5.2.that δ has increased by an order with In doping. It is evident from the XRD, that the crystallite size decreases with In doping, resulting in nano grains with large number of grain boundaries and reduction in spacing between them. This could be mainly responsible for manifold increase in δ as well as ε.

Table.5.1. Values of 2 theta values, FWHM, crystallite size D,'d'spacing and lattice parameters of IZO films at various dopant concentrations

Indium content (wt %)	Plane	2θ (deg)	FWHM (β) (deg)	Crystallite size D (nm)	d (nm)	Lattice parameters		
						a(nm)	c(nm)	c/a
0%	(002)	34.169	0.4369	18.8	0.2622	0.3027	0.5243	1.7321
1%	(002)	34.115	0.6203	13.243	0.2626	0.3032	0.5252	1.7322
5%	(002)	33.799	0.6329	12.966	0.2649	0.3059	0.5299	1.7322
10%	(002)	33.155	1.0128	8.089	0.2699	0.3117	0.5399	1.7321

Table.5.2.Values of dislocation density, strain along c axis and micro strain of IZO films at various dopant concentrations

Indium content	Plane	Dislocation density δ (line/m^2) x 10^{15}	Strain along 'c' axis (%)	Micro strain Ɛ (x 10^{-2})
0%	(002)	2.829	0.699	0.6205
1%	(002)	5.702	0.872	0.8824
5%	(002)	5.948	1.775	0.9094
10%	(002)	15.28	3.695	1.485

The Raman spectrum is an essential and versatile diagnostic tool in order to study the crystallization, structural disorder and defects in micro/nanostructures of semiconducting

materials. Figure.5.3 shows the Raman spectra of undoped and IZO thin films deposited on Silicon substrate. The E_2 high mode (433 cm^{-1}) is well defined in all films, which is the characteristics peak of wurtzite structure of ZnO. Well defined E_2 peak reveals good crystallinity of IZO films. Raman spectra of doped films exhibit measurable peak shifts from undoped ZnO. The peaks at 303 $cm^{-1}$and 522 cm^{-1} originate from the underlying Si substrate peaks. No Raman peak related to In_2O_3 is seen in the spectra of IZO films, indicating the absence of secondary phase in films, which is consistent with the XRD results.

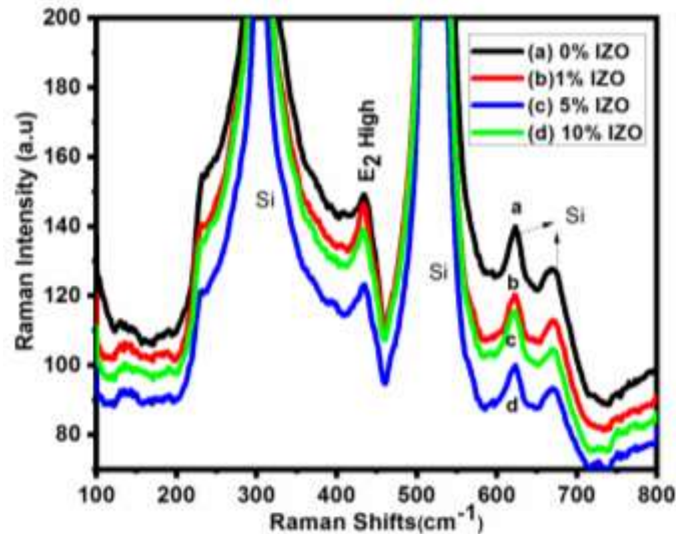

Figure.**5.3** Raman spectra of undoped and indium doped ZnO thin films.

5.1.3.2. Morphological Properties

FESEM images of the IZO films are shown in Figure.5.4 (a-d). All the films have crystalline microstructure of nanometer order with uniform and dense distribution. In concentration has great influence on the morphology and grain size of IZO films. Undoped ZnO films show uniform, nanoflower like structures. 1% IZO films exhibit distinct nanorod like granular structures, which become smoother and more compact with increasing indium concentrations. A decrease in grain size with doping is clearly seen in micrographs in accordance with the XRD results. Three-dimensional AFM pictures of indium doped ZnO samples and their two-dimensional projections are given in Figure.5.5. These micrographs illustrate that the deposited films have well defined grains with uniform and smooth surface. The films comprise of slightly elongated crystallites, with a tendency for the In-doped material to exhibit smaller grains.

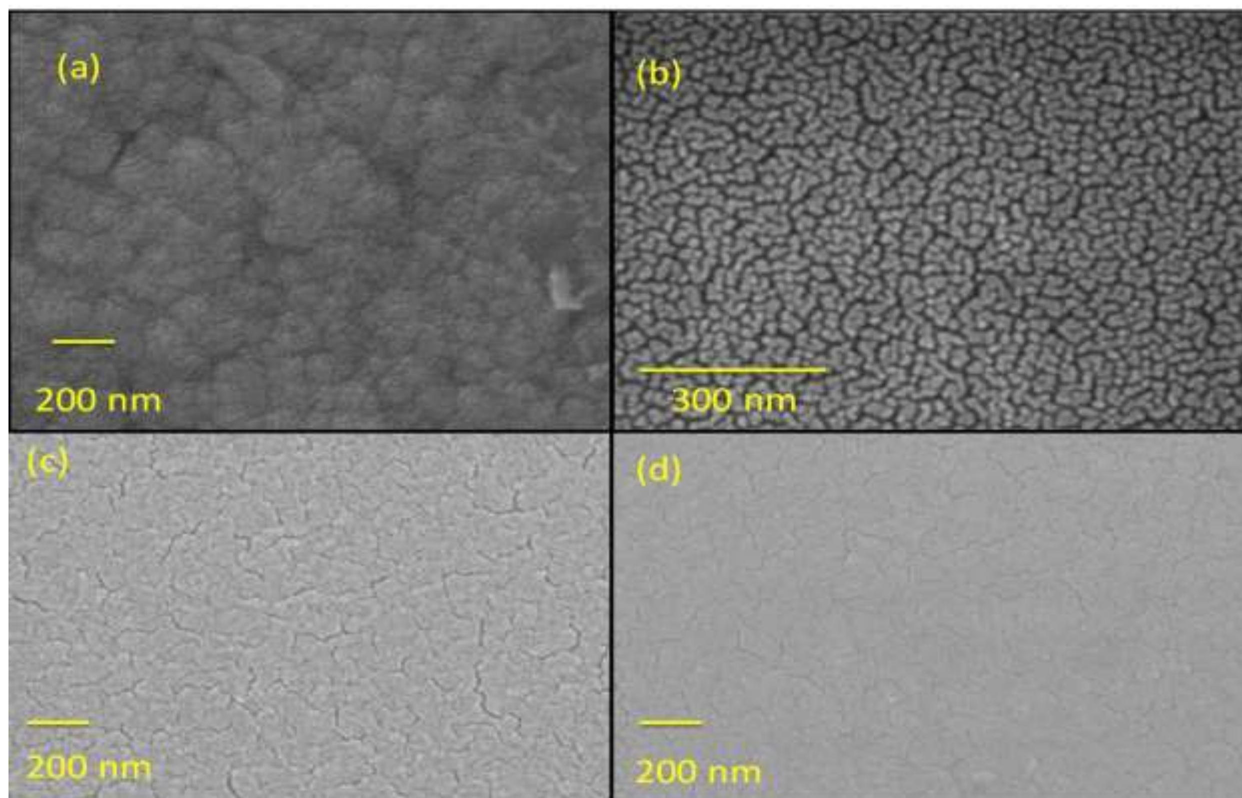

Figure.5.4 FESEM Micrograph of (a) 0wt% (b) 1wt% (c) 5wt% and (d) 10wt% indium doped ZnO thin films

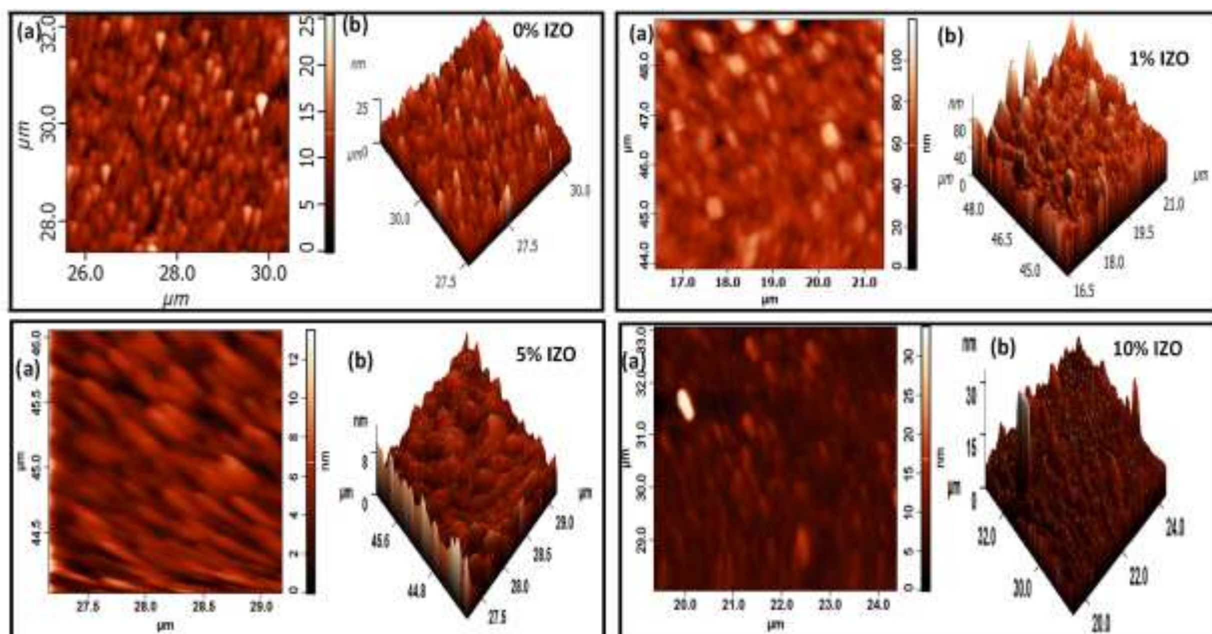

Figure 5.5 (a) 2D and (b) 3D Atomic force Microscope (AFM) images of ZnO thin films doped: 0%, 1%, 5%, and 10% of Indium.

5.1.3.3. Compositional Analysis

The amount of indium contained in the ZnO thin films can be semi-quantitatively analyzed by using the energy dispersive spectrometer (EDS). Figure.5.6 (a-d) illustrates the EDS spectra of undoped and IZO thin films. The elemental bulk compositions of IZO thin films analyzed from EDS technique is shown as insets. The EDS analysis of undoped and indium doped ZnO thin films confirms the presence of Indium in the ZnO films. No other metallic impurities are detected, indicating phase purity of the films, which support XRD results.

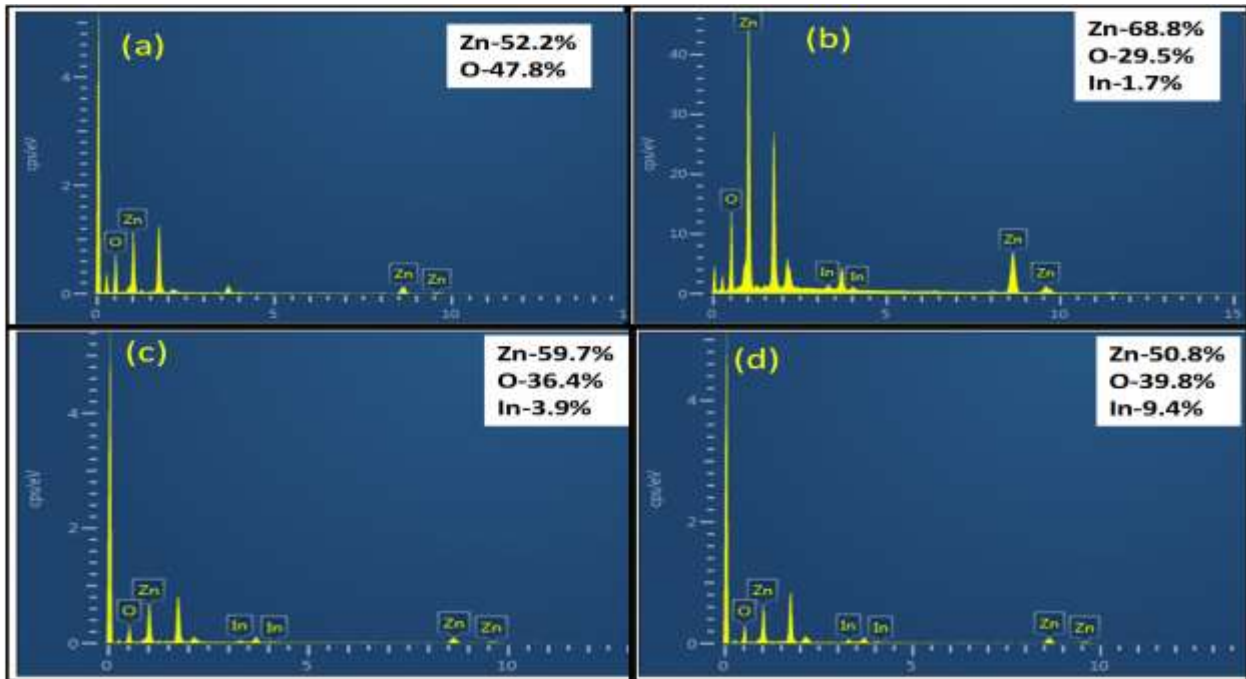

Figure.5.6 (a) 0wt% (b) 1wt% (c) 5wt% and (d) 10wt% shows EDS spectra of undoped and indium doped ZnO thin films and the inset shows the elemental composition of films.

In order to confirm the composition and quality of undoped and indium doped ZnO films, high resolution X-ray photoelectron spectroscopic analysis has been performed. The binding energy obtained in the XPS analysis is corrected for the sample charging by referring the C 1s at 284.6 eV. Figure.5.7 (a-d) shows XPS spectra of survey, Zn, O and In regions for undoped and IZO films deposited on the glass substrate. In the survey spectra of undoped and IZO films (Figure.5.7 (a)) the peaks corresponding to O1s, C1s, Zn 2p and In 3d (for IZO films) are clearly seen. Figure.5.7 (b) shows peaks at ~452.8 eV and ~445.2 eV corresponding to the electronic states of In $3d_{3/2}$ and In $3d_{5/2}$, respectively, confirming the presence of indium in the IZO films.

The energy difference (about 7.5 eV) between the two In peaks indicates that In is in +3 oxidation state and substituted into the lattice [228]. The $In3d_{5/2}$ peak at about 445.2 eV corresponds to the In-In bond. As the indium content increases, the intensity of indium peaks also increases indicating more substitution of indium atoms into ZnO lattice. It is also observed that the B.E corresponding to the In 3d peaks shows a shift (towards low B.E) in comparison to the standard value of In, which may be caused by electron transfer from ZnO to In due to the strong electronic interaction between In and oxide.

Table.5.3. Relative surface composition Zn:O:In as calculated from the XPS

Material	Compositional Ratio (Zn: O: In)		
	Zn	O	In
ZnO	1	0.93	0
1% IZO	1	1.20	0.14
5% IZO	1	1.36	0.24
10% IZO	1	1.94	0.46

Figure.5.7 (c) shows two strong peaks at ~1021.3 eV and ~1044.4 eV typical to that of Zn $2p_{3/2}$ and Zn $2p_{1/2}$ respectively, confirming that zinc is present in Zn^{2+} state in all the films. The Zn $2p_{3/2}$ peak of ZnO located at ~1021.3 eV is characteristics of the wurtzite ZnO. The energy difference between the two Zn 2p peaks is ~23.1 eV, and two In 3d peaks is~ 7.5 eV which agree well with standard value of 23 eV and 7.45 eV, respectively [229-230].

Figure.5.7 (d) gives O 1s spectrum showing a broad asymmetric peak, which can be deconvoluted in to three regions viz. I, II and III with peak binding energies at ~530.5 eV, ~531.9 and ~533.0 eV respectively. The peaks corresponding to I and II are accredited to the oxygen ions in the completely oxidized surrounding (i.e., Zn-O and O-In bonding) and oxygen-vacant regions. Peak III is related to the hydrated oxide species (i.e. H_2O and CO_3 bonds) on the film surface. [231-232]. The relative surface composition Zn:O:In has been calculated from the XPS and the result are tabulated in table.5.3. In conclusion, XPS study provides evidence of the successful addition of In into ZnO films. The amount of Indium as well as Oxygen content is found to increase with increase in Indium concentration. The XPS spectrum does not show any peak corresponding to any other elements or impurity

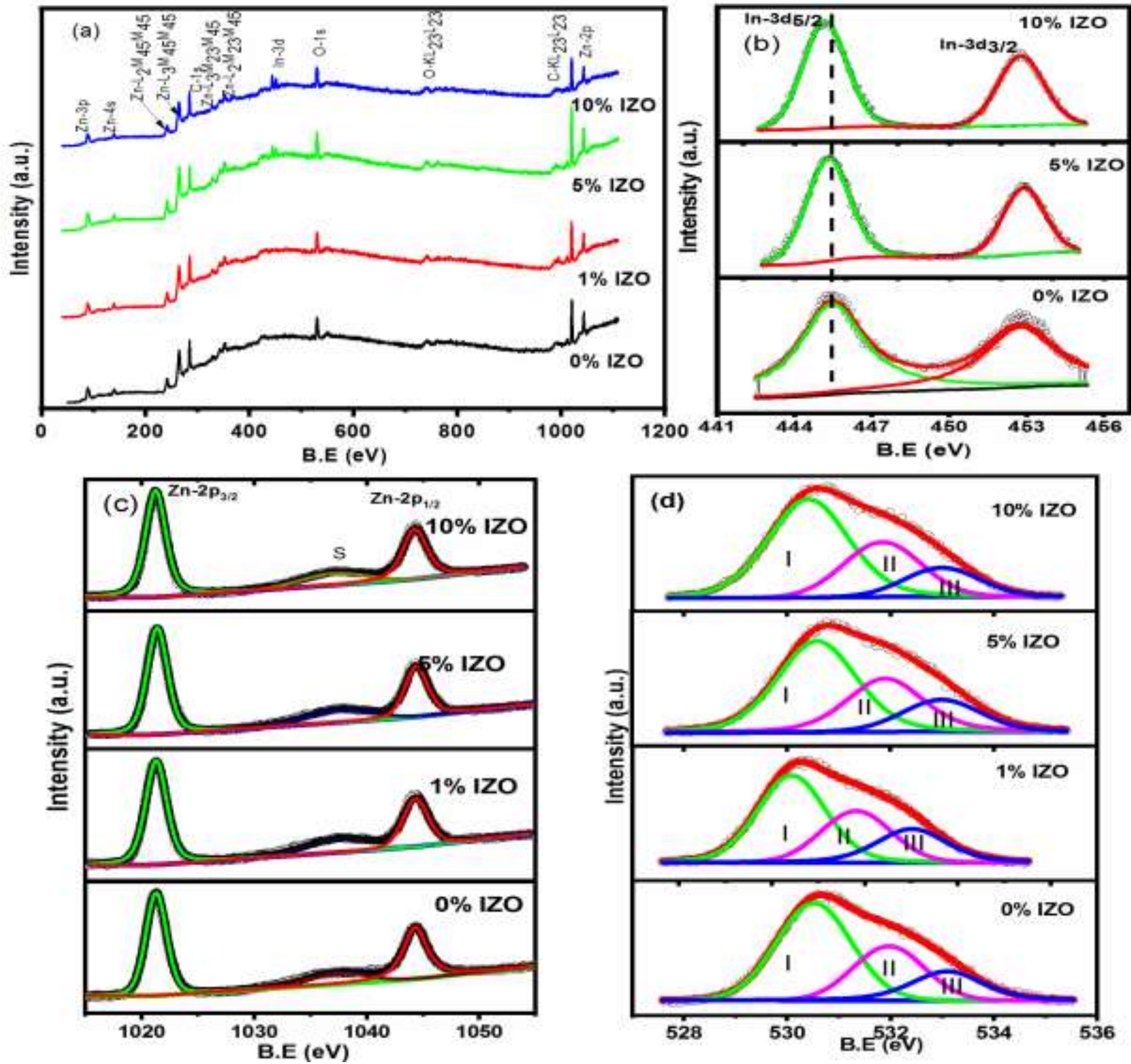

Figure.5.7 Deconvoluted high resolution XPS spectra (a) Survey spectra (b) Zn 2P region (c) O 1s region and (d) In 3d region of indium doped Zinc oxide thin film.

5.1.3.4. Absorption and optical band gap

The influence of Indium on the optical properties of IZO thin films has been studied by UV-Vis spectrometry. All the absorbance and transmission curves are corrected for glass substrate. Figure.5.8 (a) depicts the absorbance spectra of IZO films. It is seen that there is high absorption in the ultra violet range and almost no optical absorption in the visible region. Strong absorption in the ultra violet region is related to the band edge absorption that occurs due to the transfer of electrons from valence band to the conduction band, and can be used to calculate the

energy gap of the ZnO. The optical transmission and reflectance spectra in the wavelength range 300 - 900 nm for the IZO thin films with various indium contents are shown in Figure.5.8 (b). All films show 90% transmittance in the visible region. This high transmittance of the films is the direct consequence of the wide band gap nature of the films. There is a sharp absorption region at around 380 nm for all IZO films. The fringes related with interference effects endorse the optical homogeneity and the high surface quality of the ZnO thin films.

Figure.5.8(c) shows typical variation of $(\alpha h\nu)^2$ vs. hν graph for ZnO films with various indium content. The optical energy gap decreases from 3.233 eV for undoped ZnO to 3.095 eV for 10% IZO (red shift) as shown in Figure.5.8 (d). The decrease in optical band gap could be due to the influence of various factors such as grain size, structural parameters, carrier concentration, or by deviation from stoichiometry of the film and lattice strain [233]. Compared to doped ZnO, undoped ZnO has a larger band gap, indicating an increase in carrier concentration. In present work, Eg value decreases as the concentration of indium increases, which can be regarded due to the shrinkage effect of band gap or Moss–Burstein effect. More importantly, the narrowing of band gap energy is probably due to the presence of In impurities in Zn lattice, facilitating the formation of new recombination centers with lower energy state near conduction band which is further investigated by photoluminescence spectroscopy. The optical parameters like absorption coefficients, refractive index, and extinction coefficient of IZO films are calculated at the wavelength 540 nm and are tabulated in the Table 5.4. It is evident from Table 5.4 that the In doping can improve the extinction coefficient and refractive index. The increase in refractive index with In doping is accredited to the increase in polarisability due to the lager atomic radius of In as compared to Zn atom.

Table.5.4. The optical parameters values IZO thin films

Indium content (%)	Absorption coefficients (α)	Refractive index (n)	Extinction coefficient (k)	Optical band gap (Eg), eV
0	3.797×10^6	1.40	0.1632	3.233
1	9.849×10^5	1.213	0.0423	3.183
5	8.771×10^6	1.385	0.3771	3.139
10	7.728×10^6	1.438	0.3323	3.095

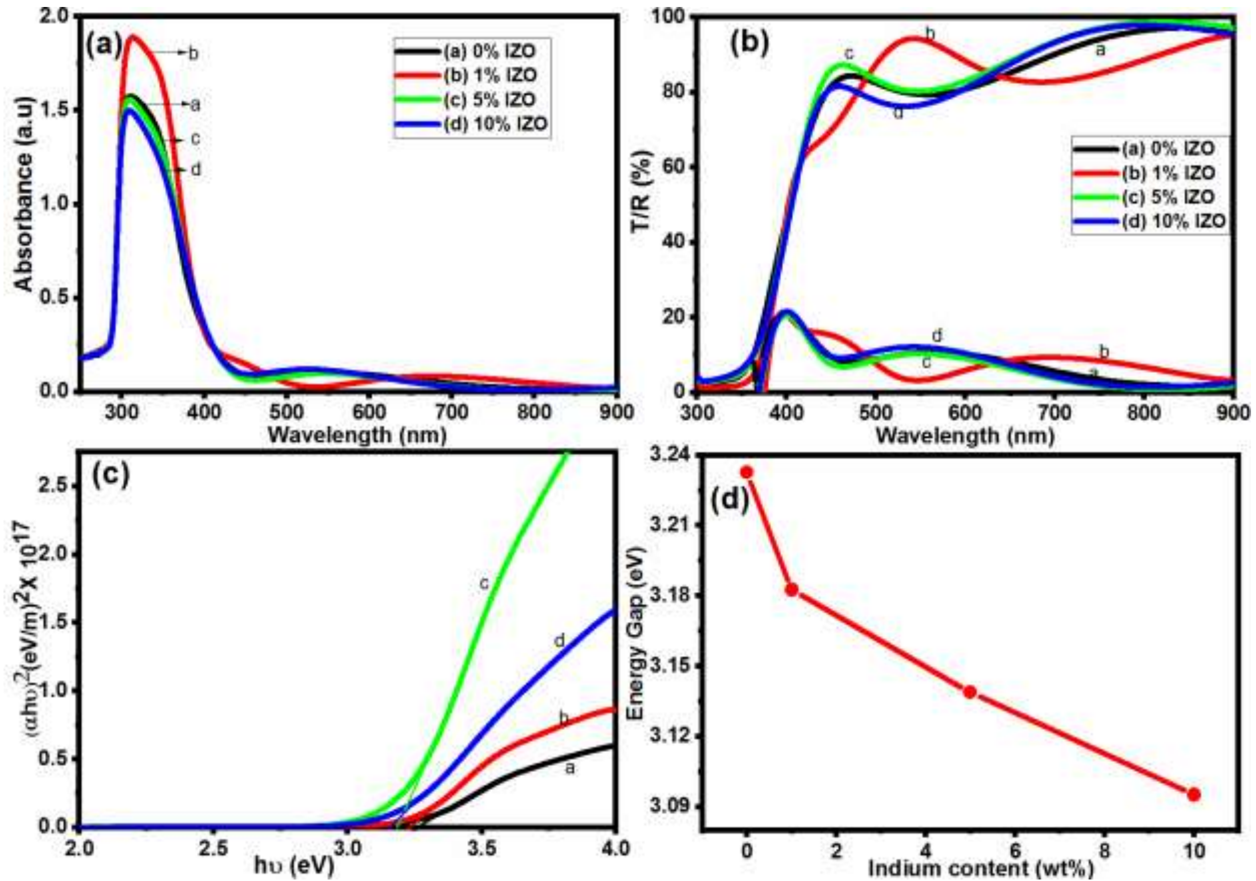

Figure.5.8 (a) Optical absorbance spectra (b) Optical Transmittance/Reflectance spectra (c) Variation of $(\alpha h\nu)^2$vs hν curve and (d) Variation of band gap with concentration of IZO films.

5.1.3.5. Photoluminescence Properties

Figure.5.9 (a-d) shows the deconvoluted room temperature photoluminescence spectra of the IZO films recorded using excitation wavelength of 325 nm. In order to identify the defect emission, higher excitation energy (3.81 eV) is chosen as compared to the band-gap energy of ZnO (3.37 eV). The spectra of undoped ZnO consist of broad peak centered at 390 nm in the UV region, which indicates high crystalline quality and low defect concentration. The deconvoluted spectra of ZnO show peaks at 375 nm, 400 nm and 435 nm respectively. The peak at 375 nm is the near band edge (NBE) emission and the peak at 400 nm is associated to the transition from conduction band to V_{Zn}.; whereas the other peak at 435 nm is attributed to zinc vacancy (V_{Zn}) related emission. The deconvoluted PL spectra of IZO films are shown in Figure 5.9. (b-d). The entire IZO films show high intense peak centered at ~ 420 nm and 590 nm corresponding to violet-green emission. In addition, peaks are observed at 449 nm, 470 nm, and 540 nm in all indium doped films. PL intensity decreases with increasing doping level of indium. The peak

position of NBE emission slightly shift to lower energy and this phenomenon of red shift can be attributed to the narrowing of the optical band gap due to the Burstein- Mass effect. This shift in peak position (UV) can also be explained by the different chemical surrounding of the oxygen vacancies resulted by the inclusion of indium ions in to the crystalline structure of ZnO [234]. Similar results were reported by Bae et al. who suggested that high doping effect causes the decrease of band gap and the energy broadening of valence band states [235]. As the doped elements enter into the ZnO lattices, additional band edge states form at the doped sites, with a reduction of band gap. The incomplete oxidation of oxide compound semiconductors leads to the production of oxygen vacancy defects [236]. The radiative transition peak at 485 nm is due to the intrinsic defect in ZnO, and also due to the transition from the conduction band to deep levels induced by indium doping.

The origin of blue-green emission in ZnO films is still in controversy. Generally oxygen vacancies such as neutralized oxygen vacancy (V_o*), single ionized oxygen vacancy (V_o^+) and doubly ionized oxygen vacancy (V_o^{++}) are considered as green emission centers. Beside the oxygen vacancies, oxygen antisite (Ozn) can also give rise to green emission. Other defects such as; Zinc interstitials (Zn_i), zinc vacancy (V_{zn}), singly (Zn_i^+) and doubly ionized interstitials (Zn_i^{++}) are responsible for blue emission [60,199]. The green band observed at 520 nm can be related to recombination of electron, in the singly ionized oxygen vacancies, with photo excited holes, in the valence band, as the energy gap is of the order of 3.6 eV. Nevertheless, transition from conduction band to O_{zn} or presence of V_o^+ level could also contribute to the green emission at 537 nm. The blue emission at 420 nm corresponds to the jumping of electrons from conduction band to oxygen interstitials (O_i). Yellow band at 565 nm can be due to the recombination of electrons with deeply trapped holes in the oxygen interstitials.

The emission at 589 nm may be due to the movement of electrons from conduction band to oxygen interstitials. In addition, there is a systematic change in the intensity of the peak at 589 nm with In doping, which could be attributed to the presence of non-radiative traps and defect centers resulting from structural disorders. Indium doping reduces the oxygen vacancies while increasing oxygen interstitials which results in enhancement in orange emission. XRD spectra, FESEM studies and optical properties along with photoluminescence spectra suggest that addition of dopant in ZnO with suitable higher valence impurities degrades the crystallization. Also doping enhances the extent of defects which can be tuned for light emitting applications.

Based on the PL studies, the schematic energy band diagram with possible radiative transition is represented in Figure5.10 (a). The small peaks around ~375 nm and ~400 nm are due to the band to band transition of ZnO and transition from the conduction band to zinc vacancy (V_{zn}) respectively. The peak at 435 nm is attributed to the transition from zinc interstitials Zn_i to V_{zn}. The peaks centered at 542 nm and 589 nm are regarded as the transition from Zni to oxygen interstitials and from conduction band to Oi respectively.

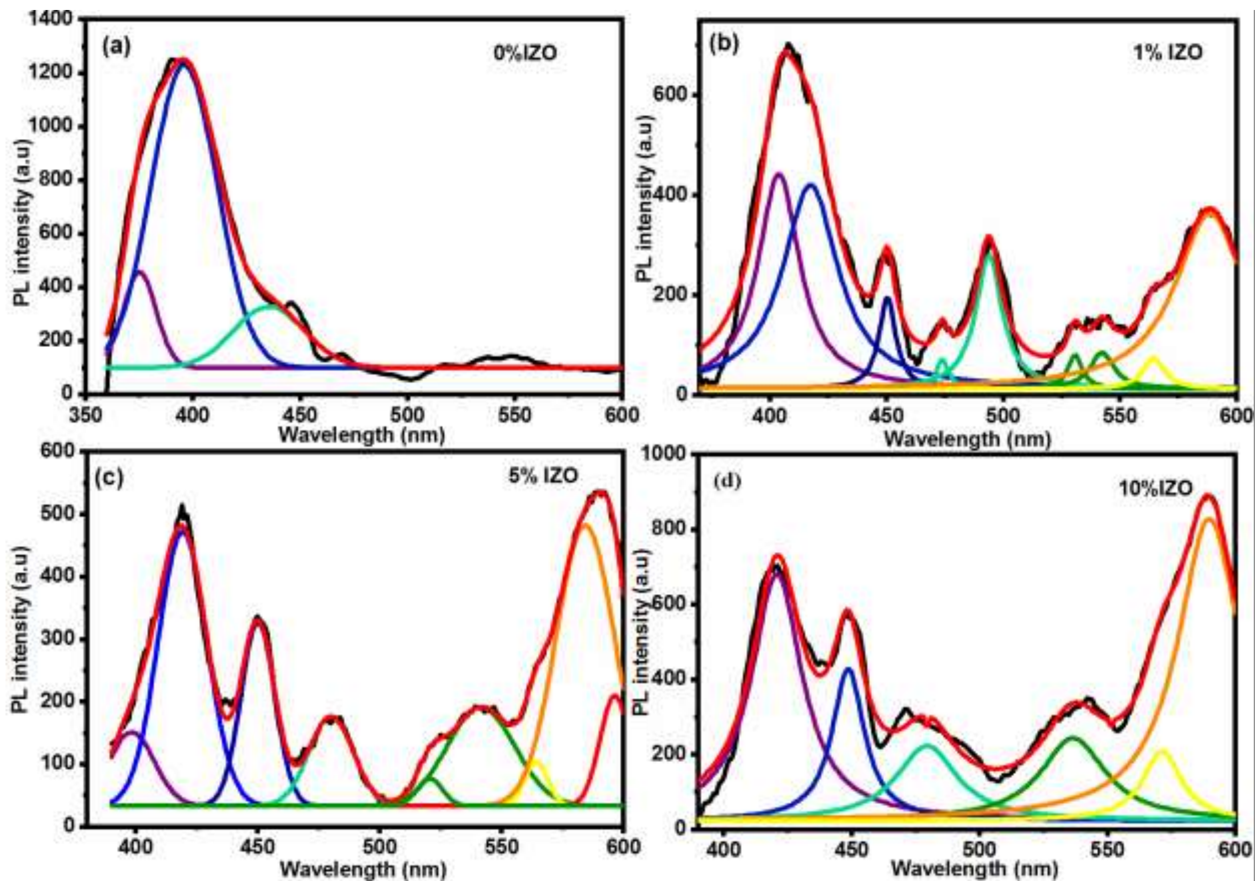

Figure.**5.9** (a-d) Deconvoluted room temperature Photoluminescence spectra of IZO thin films

The CIE (Commission International del'Eclairage) color coordinates measured from PL emission of undoped and indium doped ZnO thin films are shown in Figure.10(b).It is worth noting that undoped ZnO has CIE values of x = 0.21 and y = 0.19, confirming the blue emission. The CIE coordinates for 1%, 5% and 10% IZO thin films are (0.28, 0.29), (0.31, 0.32) and (0.33, 0.32) respectively. From the chromaticity diagram, it can be seen that the color coordinates traverse a wide range from blue to white light region with In doping. The results show that the tuning of the white light emission is possible by optimizing the In concentration in ZnO films. It

can be concluded that the deposition parameters and dopant concentrations make it feasible to have combination of process-induced defects (both due to dopant and the host) responsible for the observed visible light emission.

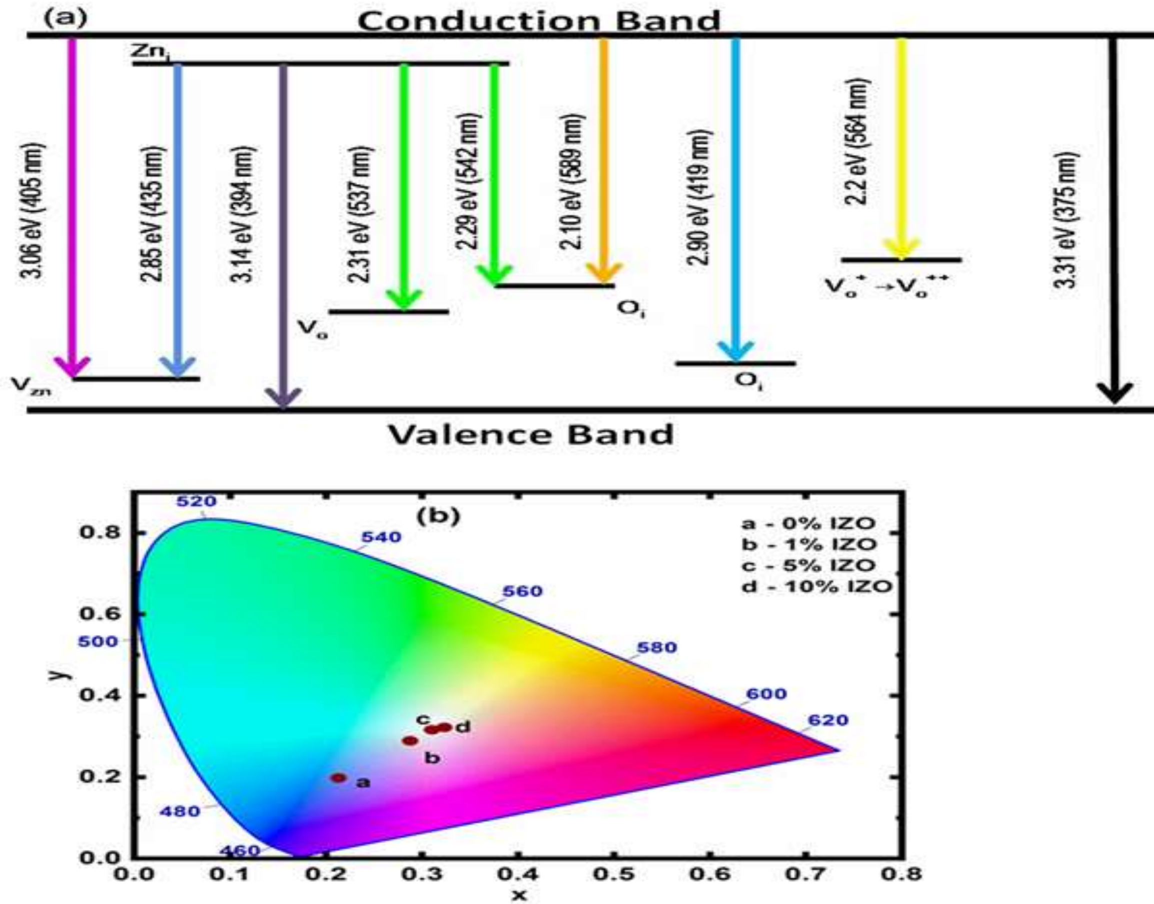

Figure 5.10 (a) The schematic energy band diagram of IZO film with possible radiative transition and (b) The CIE diagram of IZO film with different concentration

5.1.3.6. Homojunction Devices

Figure. 5.11 (a) shows the I-V characteristics of the IZO/SZO structure and Figure.5.11 (c) show the schematic band diagram of IZO/SZO homojunction structure. It is observed that ZnO homojunction exhibits a typical p-n junction rectifying behavior with turn on voltage of 1.87 V, 3.16 V and 3.54 V for 1%, 5% and 10% IZO/SZO respectively. These measurements suggest that the rectifying behavior of the prepared p-n homojunction is the behavior of the junction formed between IZO layer and SZO layer. The ideality factor n derived from the three curves are ~11.78, ~15.58 and ~18.67 for 1%, 5% and 10% IZO respectively The ideality factors

of these homojunction are higher than those of a standard homojunction (n = 1-2). The high values of measured ideality factor in homojunction may be due to an active contribution from the defect-assisted tunneling with electron- hole recombination and by interface states across the metal and thin oxide semiconductor [237].

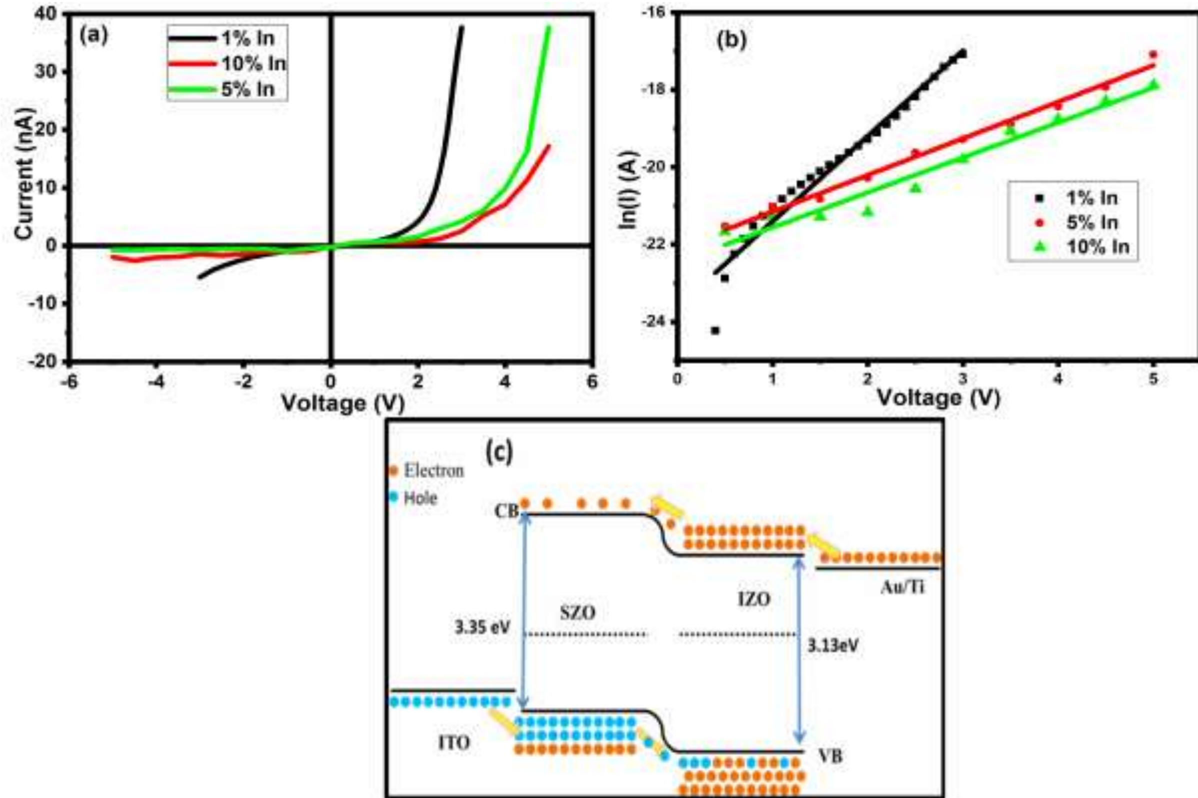

Figure.**5.11** (a) I-V characteristic curve, (b) ln(I)-V characteristics curve with different IZO content and (c) schematic band diagram of the IZO/SZO homojunction structure

5.1.3.7. Gas sensing measurements

Hydrogen sulfide (H_2S), as the typical representation of sulfide, is a harmful, corrosive, flammable and toxic acidic gas and widely used in various industries. Even at low concentrations it can cause hypoxia and seriously threatens the safety of human. According to the US scientific advisory board on toxic air pollutants, the acceptable concentration of H_2S in the environment is less than 83 ppm. Therefore, it is necessary to fabricate gas sensors which can detect ppm level H_2S in time to reduce the environmental pollution and harm to human.

The gas sensing properties of IZO films were studied in a static gas sensing set up shown in Figure.5.12 (a). Gas sensors were fabricated by thermal evaporation of gold to form inter-digitized electrodes on top surface of the films, using a shadow mask with 0.5 mm electrode

width and 100 μm separations between the electrodes (Figure.5.12 (b)). Then the gas sensors were mounted in a stainless steel test chamber of volume 250 cm^3, equipped with temperature control circuit. The required temperature was tuned using a Pt wire based heater attached to the back side of the film. The sensor resistance was stabilized at each operating temperature for about 30 minutes prior to test gas exposure. The desired concentration of the commercially available gas was injected inside the chamber using a tight syringe. The response curves were measured by applying fixed bias across the electrodes and the variation in the resistance of the film was monitored and recorded using software, and the recovery of the sensor was achieved by opening the chamber to the atmosphere. The gas response, S, is defined as the ratio R_a/R_g for reducing gases (H_2S), where R_a is the electrical resistance of the sensor in dry air and R_g its electrical resistance at the fixed reducing gas concentration.

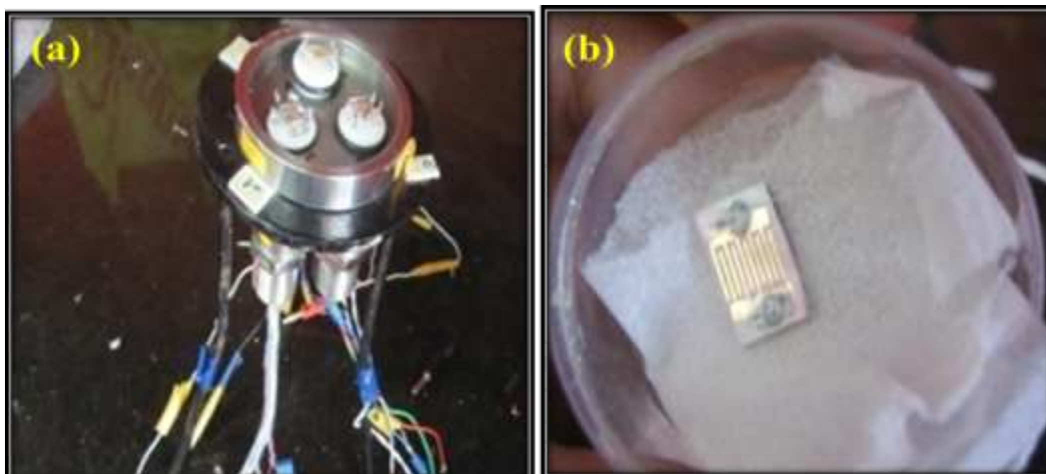

Figure.5.12 (a) Static gas sensing set up and (b) Inter-digited IZO gas sensor

Figure.5.13 shows sensitivity plot corresponds to (a) 10 wt% IZO sensor towards different gas concentration at 250°C, (b) IZO sensor at different temperature, (c) variation with indium content & (d) IZO sensor at different gas concentrations respectively. The gas sensing properties of the IZO sensor were measured at different temperatures as a function of H_2S concentration up to 50 ppm. The response and recovery characteristics of 10 wt% IZO at 250°C are shown in Figure.5.13 (a) for different concentrations of H_2S. It can be seen that the response increases rapidly and reaches its equilibrium. Once the chamber is removed, the response decreases quickly to the baseline.

In order to determine the optimum operating temperature for the H_2S gas sensor, a systematic study of temperature effects on gas sensing properties of IZO sensors is performed.

The response of all sensors initially increases with the temperature, attain maximum at 250°C and then decreases as shown in Figure.5.13 (b). All the films showed high sensitivity and response at 250 °C and this temperature is considered as optimum operating temperature. The mechanism of sensor response of a reducing gases like H_2S, depends on the interaction between adsorption desorption rates of H_2S and the surface reactivity of H_2S adsorbed with the adsorbed oxygen. The increase in operating temperature improves H_2S adsorption to a certain extent, thus rate of reaction on IZO surface leads to an enhancement in gas response. At high temperature, the desorption rate increase on the IZO surface, hence gas response is reduced. At low temperature electrons do not get sufficient thermal energy to interact with adsorbed oxygen species, thus sensitivity reduced at low temperature. Oxygen vacancies and defects in ZnO lattice play an important role in improving the sensitivity, because it acts as adsorption sites for oxygen and H_2S gases. The PL and XPS performed on sensors and it is revealed that as indium content increases the more defects and oxygen vacancies are created. These vacancies and defects created due to the incorporation of In in the sensor act as additional sites for gas adsorption, thus sensitivity enhanced for IZO sensors.

The sensor responses are studied for different concentration of H_2S gas for different indium doping content as shown in Figure.5.13 (c). The 10wt% IZO shows the maximum sensitivity and fast response among all the sensors, suggesting that it is the optimum doping concentration. It is seen that from Figure.5.13 (d) the sensitivity of the IZO sensor increased linearly with increase in H_2S concentration.

A decrease in resistance of the sensor under H_2S exposure was observed, which can be explained by its reaction with chemisorbed oxygen.

$$H_2S_{(g)} + O^-_{2\,(g)} \leftrightarrow H_2S_{ads} + O_{2(g)} + \bar{e} \quad \ldots\ldots 5.1$$

$$3H_2S + 3O_2^- \leftrightarrow 2SO_2 + 2H_2O + 3\bar{e} \quad \ldots\ldots 5.2$$

According to the reaction (5.1), addition of gases increases number of electron, which moves towards sensing layer and thereby decreasing the resistance of sensors. Another possible reaction mechanism, which affects the conductivity of sensor, is the chemical conversion of ZnO with H_2S [222]. The formation of ZnS on the surface of ZnO on exposure to H_2S gas at a temperature above 300°C and XPS studied reveals that above 300°C, H_2S decomposes to form Zn-S bond in ZnO. Which causes the formation of shallow donor level and causes increase in conductivity was reported by Kim et al [238].

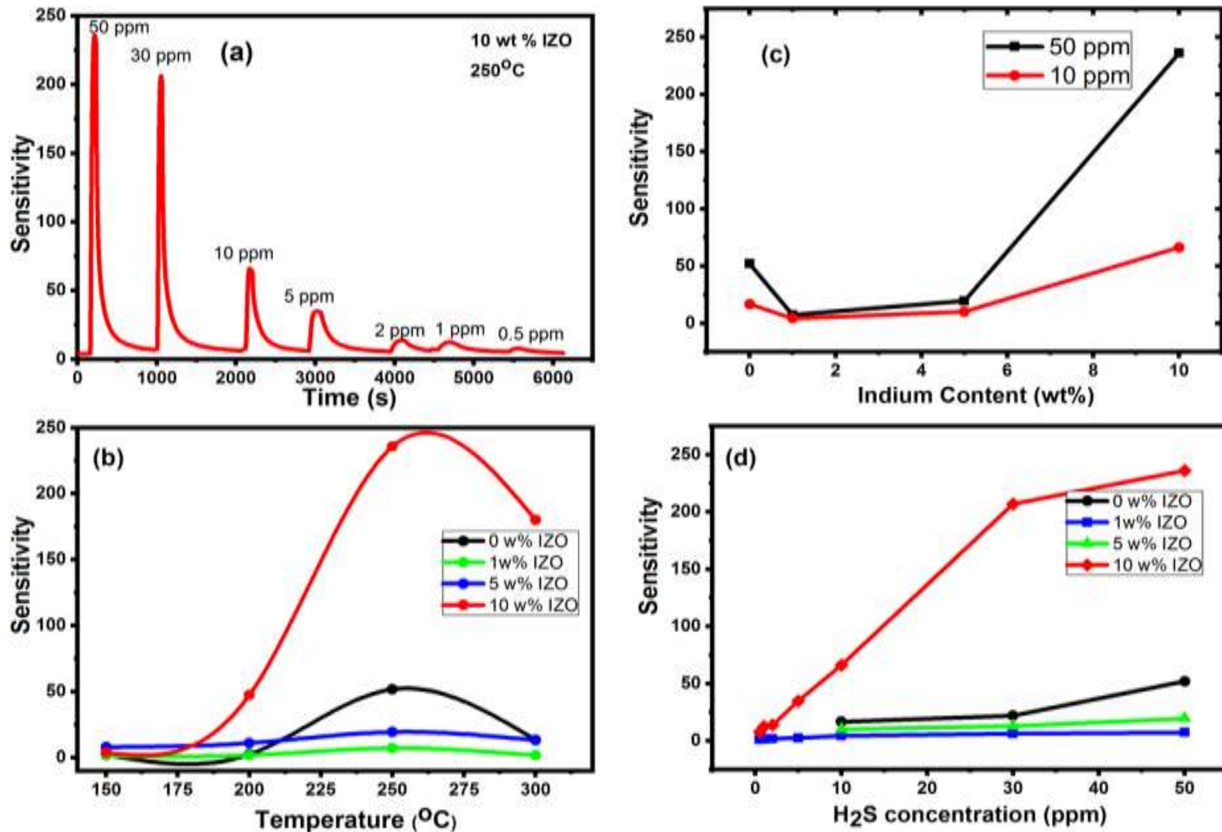

Figure.**5.13**. Variation in response of (a) 10 wt% IZO sensor towards different gas concentration at 250°C (b) IZO sensors at different temperature for 50 ppm H_2S gas, (c) IZO sensor with indium content & (d) IZO sensor at different gas concentrations.

The response and recovery time of 10 wt% IZO at 250°C are shown in Figure.5.14 (a) for different concentrations of H_2S. The response and recovery time of IZO films with different doping content indium for 50ppm H_2S exposure are shown in Figure.5.14 (b). It is evident from the Figure that the response and recovery times are varying with concentration and indium content. Among all the films, the response and recovery of 10 wt% IZO is the fastest for 50 ppm at 250 °C. Selectivity is an important parameter for sensors to differentiate between different types of interfering gases. To determine the selectivity, cross response of IZO films is tested by exposing the sensor to various gases at an operating temperature of 250°C and the result are shown in Figure.2.14. As can be seen from Figure, the sensor shows negligible response to other gases and a highest response for H_2S, indicating excellent selectivity.

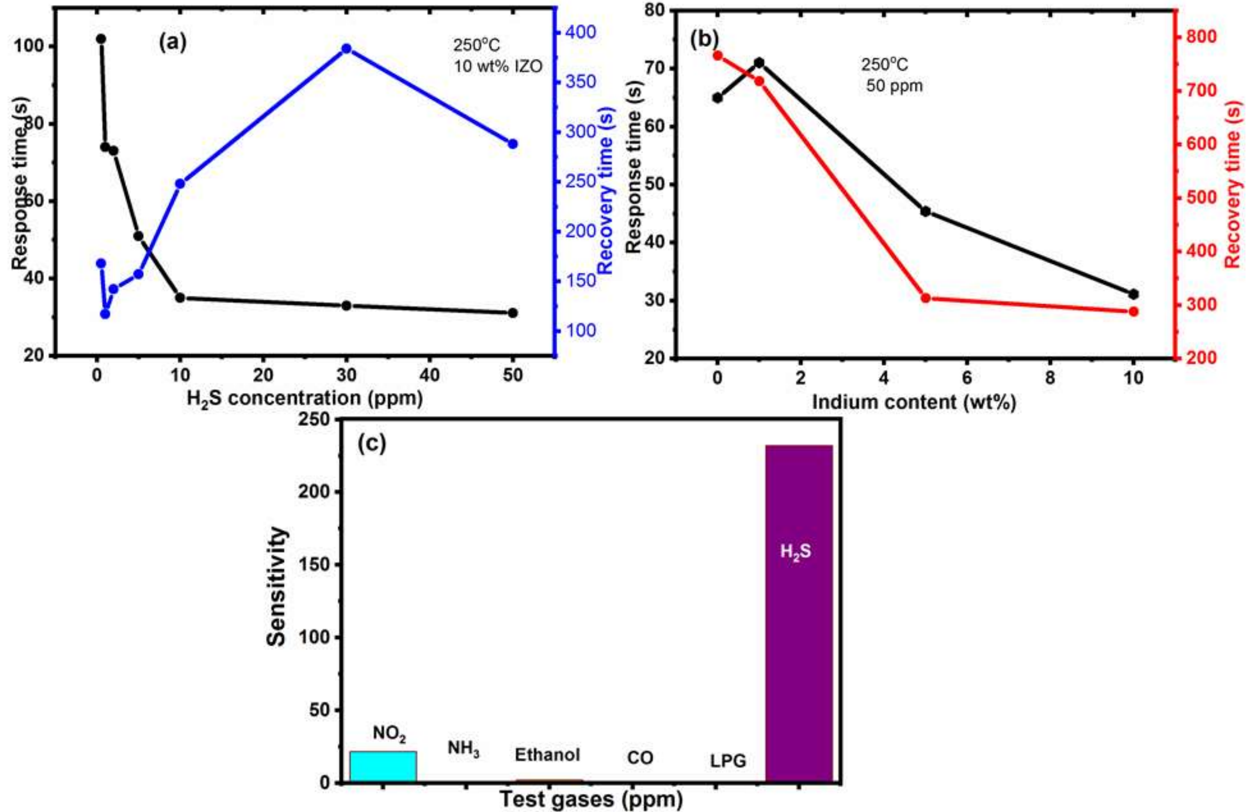

Figure.**5.14** Response and recovery time of 10 wt% IZO sensor (a) with gas concentration (b) with indium content and (c) Relative response of 10wt% IZO sensor for various gases at 250°C

5.1.4. Conclusion

In summary, Indium doped nanocrystalline ZnO films were grown by RF sputtering using home-made powder targets. The dependence of the structural and morphological properties of IZO films, on their doping content was studied. All the films were highly crystalline with standard hexagonal wurtzite structure and exhibited a preferred orientation along the c-axis. The intensity of (002) peak tended to decrease with the indium content. The XRD spectra revealed that In atoms substituted Zn in the hexagonal lattice. The presence of In, Zn and O was confirmed by EDS and XPS analysis. PL emission across the visible light region of IZO films was attributed to a range of structural defects, such as oxygen vacancies, oxygen interstitials, zinc interstitials and zinc vacancies formed during indium doping. PL results suggested that by controlling the doping amount it was possible to achieve white light emission. The average transmittance of IZO films in the visible region was above 90% and the band gap decreased with doping content. Homojunction devices fabricated with IZO/SZO bilayers showed rectifying type

I-V characteristics with knee voltage of 1.87 V, 3.16 V and 3.54 V for 1%, 5% and 10% IZO/SZO respectively.

Gas sensing studies revealed that the sensor response was strongly affected by the operating temperature and concentration of indium. Among the all fabricated gas sensors, 10 wt% shows the highest sensitivity for H_2S at an operating temperature of 250°C. The 10 wt% sensor showed high selectivity to H_2S with fast response and recovery characteristics and this doping level considered to be optimum for sensing H_2S. The above results suggest that IZO has the potential for use in practical applications such as white light source, LED devices and H_2S gas sensors.

5.2. Gallium doped ZnO nanocrystalline thin films (GZO)

5.2.1. Introduction

Now days, multilayer thin films are intensively used for designing of various optoelectronic devices. To improve n type conduction Ga, Al, and In elements from group III are suitable dopants for the ZnO. Of these, Ga is less reactive and more resistant to oxidation than Al [239]. Recently, the Ga doped ZnO thin film has drawn special attention as Ga seems to behave as perfect substitutional dopants for Zn. Moreover, Ga has a similar ionic (0.62 Å) and covalent radius (1.26 Å) to Zn (0.74 Å and 1.31 Å), respectively, which is in contrast to In (0.81 Å, 1.44 Å) and Al (0.5 Å, 1.26 Å) [239-240].

5.2.2. Materials and Methods

A powder target of the mixed powder of high purity ZnO and Ga_2O_3 acted as the sputtering source material. The Ga doped ($Zn_{1-x}Ga_xO$, x=1, 3, 5 and 10%) (GZO) thin films were deposited using 13.56 MHz RF magnetron sputtering on various substrates like glass, Si and ITO. The homojunction was fabricated on ITO substrate with first layer as SZO and second layer as GZO with same condition as mentioned above. Finally a 60 nm Au and Pt 10 nm was deposited on GZO films by thermal evaporation with masking for contacts. Here Au/Ti act as anode electrode and ITO was used as the cathode. A mask was designed using SS sheet such that the active area of each electrode is 0.2 mm^2. I-V characteristics measurements were performed by placing directly to the Pt wire attached to the probe station. One end of Pt wire was used in contact with anode and other end with the ITO substrate. The fabricated devices were subjected to RTA to activate the layer in air for 5 minutes in temperature of 400°C. A schematic diagram of the GZO/SZO homojunction device is shown in Figure.5.15.

5.2.3. Result and Discussion

5.2.3.1. Structural Properties

Figure.5.16 shows the XRD pattern of GZO films fabricated on glass substrate. The strong (002) peaks in all of the films indicate that films has a c-axis preferred orientation with hexagonal structure. Despite the existence of (002) peak in all the films, the relative intensities of the peak are tend to decreases with increase in Ga concentration. The absence of any additional peaks for Ga_2O_3 confirmed the purity of ZnO, which is important for the device fabrication. The absence of gallium oxide peaks in XRD pattern states that Ga^{3+} ions are substituted in to the Zn^{2+}

sites. The intensity of (002) peak is found to decrease with the concentration of Ga, indicating a decrease in crystallinity. This designate that increasing the doping concentration, deteriorates the crystallinity of the film as a result of stress formed due to the difference in ionic size between zinc and Ga dopants and the segregation of dopants in grain boundaries. In addition, as the amount of Ga concentration increases, the angle of (002) peak is gradually shifted to lower angle. This shift to lower angle could be attributed to stress in thin films, which causes increase in inter planar distance of the lattice. From the Figure 5.16, it is also observed that above a doping level of 5%, an additional peak at 36.2 corresponding to (101) plane is observed along with (002) peak, indicating mis-orientation from the c-axis. This means that an extra phase with in ZnO films starts to develop along with hexagonal wurtzite phase beyond certain doping level due to segregate Ga atoms either at interstitials site or substitutional sites. The crystallite size was calculated by using the Debye Scherer's formula and is tabulated in Table.5.5.The variation in crystallite size of GZO thin films could be occurred due to the inclusion of Ga into ZnO lattice with higher ionic radii and crystallographic defects and shown in Figure.5.16.

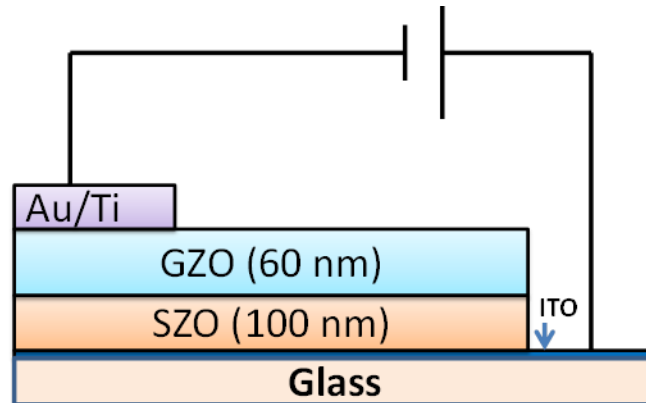

Figure.5.15 Schematic diagram of homojunction device fabricated using GZO and SZO layers

The variation in the lattice parameters, unit cell volume, crystallite size, bond length (L) and structural parameters of the films are given in the table.5.5. From the table it is clear that as lattice constant increases for GZO films compared with pure ZnO films. The change in lattice parameters is attributed to size discrepancy of dopants and Zinc. It is found that volume of unit cell increases with increasing Ga content and it may be due to increasing in the lattice parameters "a" and "c".

When dopant atoms are introduced, there is a change in the electronic bonding between the nearest two atoms which affect the Zn-O bond length. The calculated values of Zn-O bond

length increases from 1.77 Å to 1.794 Å as Ga concentration increases from 0%-10% for GZO films. The dislocation density in the present case is found to increases with Ga concentrations. Structural analysis of thin films reveals that the diffraction angle and the corresponding'd' values of the lattice spacing of the thin films slightly changed with variation in Ga content. Changes give the evidences of stress and strain in the GZO thin films.

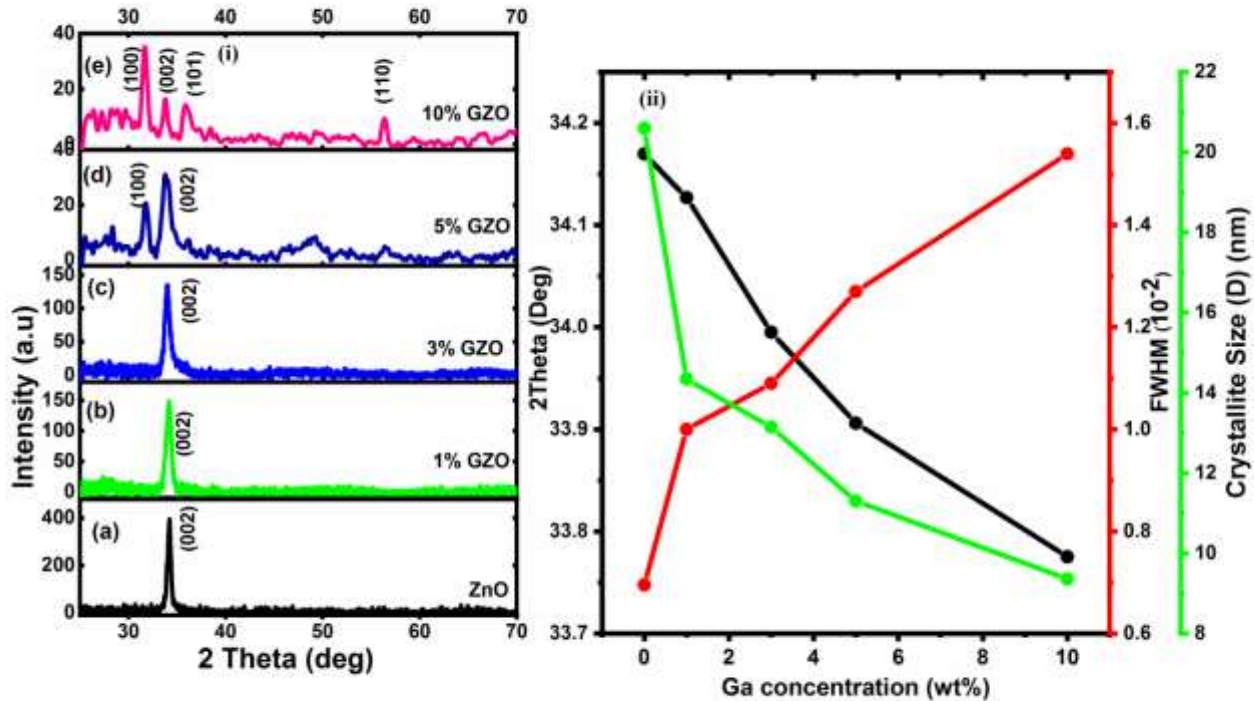

Figure.5.16. (i) X-ray diffraction patterns of the (a) undoped ZnO (b-e) GZO nanocrystalline thin films. (ii) Variation of crystallite size, FWHM, and 2theta with Ga concentration of GZO nanocrystalline thin films.

Figure.5.17 shows the Raman spectra of the GZO samples. For all spectra, a prominent peak at 438 cm^{-1} and 578 cm^{-1} were observed. These lines were assigned to ZnO E_2 (high) and A1 longitudinal optical (LO) mode respectively. The shift from 437 cm^{-1} to 433.26 cm^{-1} of E_2 (high) was caused by the tensile strain in the films which was in good agreement with the XRD result. The A_1 (LO) mode was caused by the defects of O-vacancy and Zn interstitial. The increase of the A_1 (LO) intensity for ZnO thin film implied the increase of defects (O- vacancy and Zn interstitial) in this film which is consistent with the PL result.

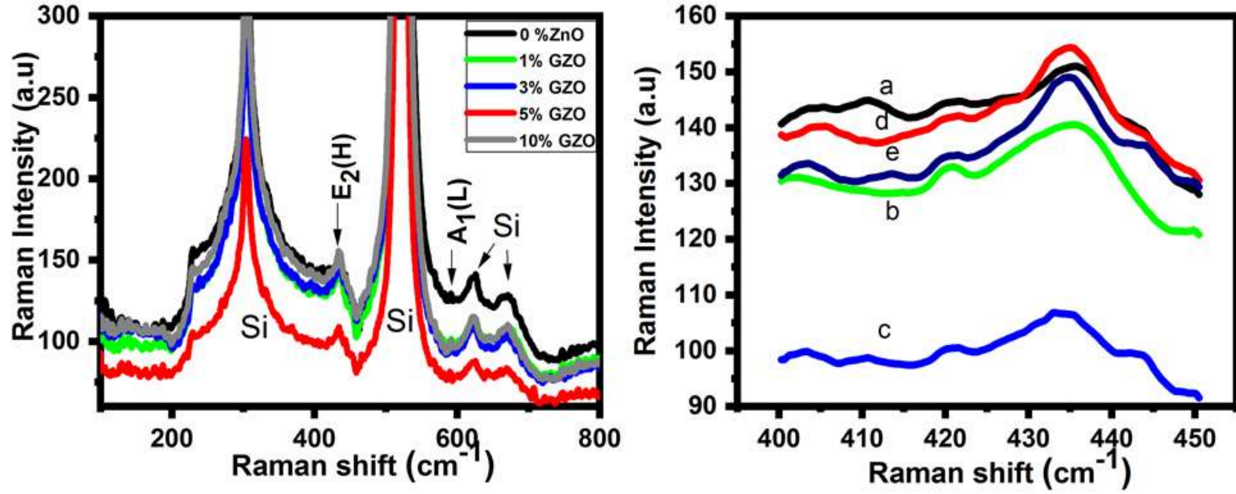

Figure.5.17.(a) Raman spectrum and (b) shows the shift in E_2 high peak of undoped and doped ZnO thin films

Table: 5.5. Variation in lattice parameters, unit cell volume, Zn-O bond length, crystallite size and grain size of ZnO and GZO nanocrystalline thin films.

Sample	Lattice parameters			Volume of unit cell $(A^0)^3$	Zn-O bond length (A^0)	Crystallite Size (D) nm	Average Grain size by FESEM(nm)
	a (A^0)	c (A^0)	c/a				
ZnO	3.027	5.244	1.732	41.61	1.771	20.6	~20
1%GZO	3.031	5.25	1.732	41.77	1.776	14.34	˜13
3%GZO	3.043	5.27	1.732	42.26	1.783	13.15	~11
5%GZO	3.051	5.284	1.732	42.59	1.786	11.3	~10
10%GZO	3.062	5.304	1.732	43.066	1.794	9.36	~7

Table:5.6 Structural parameters of ZnO and GZO nanocrystalline thin films

Sample	Plane	FWHM β (deg)	2θ (deg)	$d(A^0)$	$\delta x10^{-3}$ (nm^{-2})	ε $x10^{-2}$
ZnO	(002)	0.00695	34.17	2.622	2.356	1.662
1%GZO	(002)	0.01	34.13	2.625	4.863	2.39
3%GZO	(002)	0.0109	33.99	2.635	5.783	2.61
5%GZO	(002)	0.0127	33.91	2.642	7.831	3.04
10%GZO	(002)	0.0154	33.78	2.652	11.414	3.68

5.2.3.2.Morphological Properties

The Figure.5.18 (a-e) shows the surface morphology of GZO thin films with different Ga concentration. The microstructure shows homogeneous dense grains and density of the structure

was increased with increasing dopants content. The GZO films show a surface morphology of small and large grains. The average grain size estimated from FESEM studies for ZnO samples has been found to be~ 20 nm which decreases to~ 7 nm after doping, supporting the result of XRD.

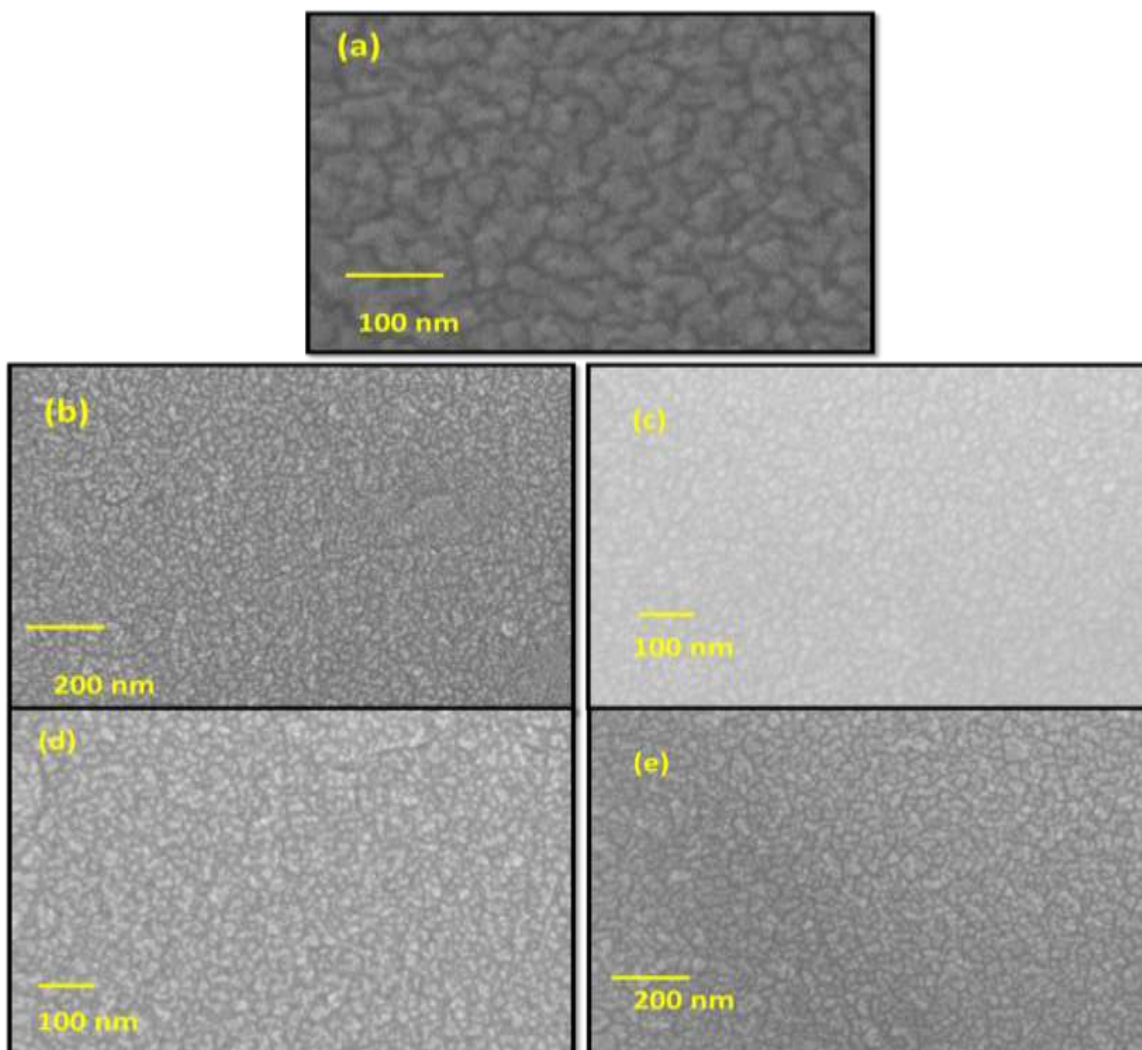

Figure.5.18. FESEM images of (a) undoped ZnO and (b-e) GZO ((b) 1% (c) 3% (d) 5% and (e) 10%)) nanocrystalline thin films

The AFM images are obtained in contact mode taken over a scale of 5 x5 μm^2. From the Figure.5.19. (a-c), it is observed that the particles on the surface of all the films are regular in nature. The occurrence of columnar growth is evident from the AFM images as expected in the case of highly c-axis oriented sputtered ZnO films. All the films are crystalline in nature with grains and grain boundaries and it is clear that grain size decreases with doping.

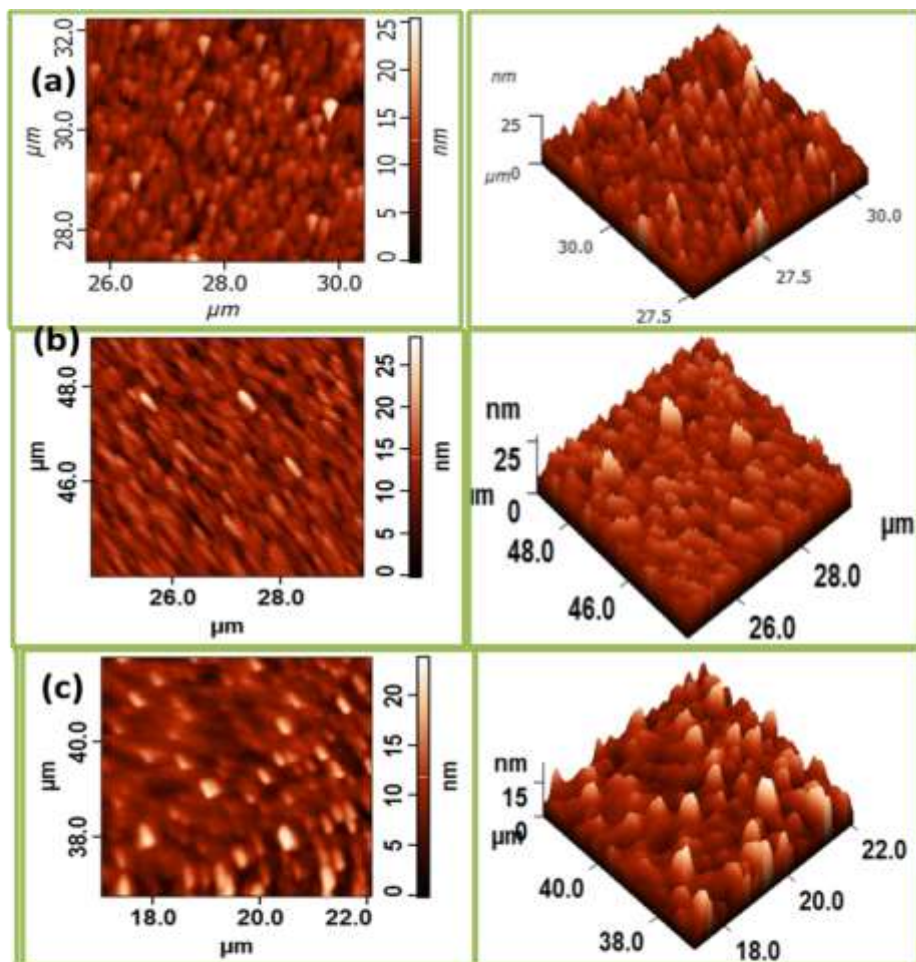

Figure.**5.19**. AFM 2D and 3D images of (a) undoped ZnO (b) 1% GZO and (c) 5% GZO) nanocrystalline thin films

5.2.3.3. Compositional Analysis

In order to determine the elemental composition of the doped samples EDS measurements was carried out. Typical EDS spectra of doped ZnO films are shown in Figure.5.20. (a-e). It can be seen in Figure, all EDS spectra consist of Zn, O and Ga peaks. The elemental composition of undoped and doped ZnO films determined by EDS analysis are given in inset of the Figure.5.20. No additional elements were observed in the EDS spectra, confirming the pure phase of films, which is consistent with XRD results.

The XPS spectra of the doped films show that the binding energy of each constituent elements was positioned at 19.75 ± 0.2 eV (Ga 3d), 1020 ± 0.5 eV (Zn $2p_{3/2}$) and 530.9 eV (O1s) as calibrated to 285.43 eV (C1s). The full scan spectra of SZO, GZO and pure ZnO exhibited peaks exclusively related to Zn, O and Ga, confirming the chemical purity of the film as shown

in Figure.5.21 (a). The chemical states of Ga in GZO films are investigated by XPS peaks for Ga 3d states as shown in Figure.5.21 (b) .The binding energy of the Ga 3d peaks around 19.75 ± 0.2 eV indicates that oxidation state of Ga in the ZnO lattice is close to +3, implying donor behavior of Ga in the GZO thin film. The Ga 3d peak can be deconvoluted into a peak which is assigned to Ga $3d_{5/2}$(19.75 ± 0.2 eV) state, indicate Ga-O bonds [241].

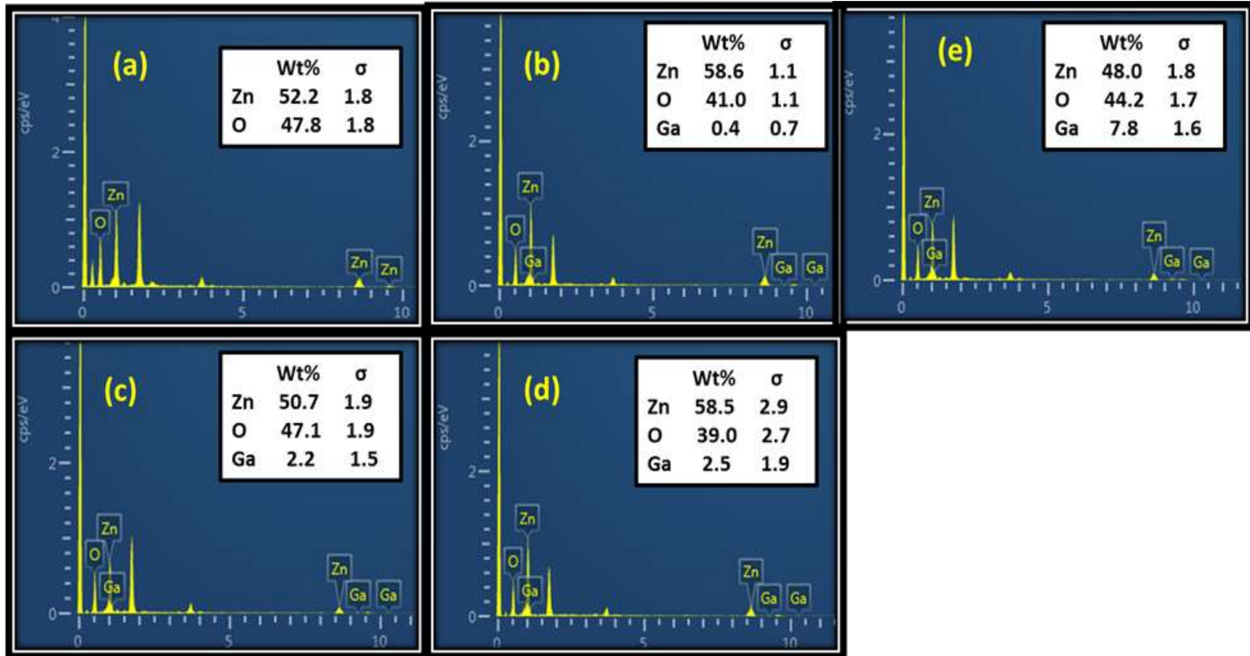

Figure.5.20. EDS spectra of (a) undoped ZnO (b) 1% (c) 3% (d) 5% and (e) 10% GZO nanocrystalline thin films

Figure.5.22 (a-e) exhibits the high resolution XPS spectra of Zn 2p states with double peak characterization of doped ZnO thin films The deposited thin films show two peaks located at 1020 ± 0.5 eV (Zn $2p_{3/2}$) and 1043 ± 0.7 eV (Zn $2p_{1/2}$) for Zn 2P states. The energy separation between these two peaks is 22.9 eV, which are in agreement with the reported values of ZnO [151, 242]. However there is a small shift towards higher binding energy of Zn 2p states for Ga doped films, and is attributed to presence of Zn-Ga bonds in GZO films. Due to the higher electronegativity of Ga (χ = 1.81) than that of Zn (χ = 1.65), the valence electron density of Zn in Zn–O– Ga bond became smaller than that in the Zn– O– Zn bond in the undoped sample. As a consequence, the screening effect of the Zn is reduced and the binding energy of Zn 2p increased in the doped samples [242-243].

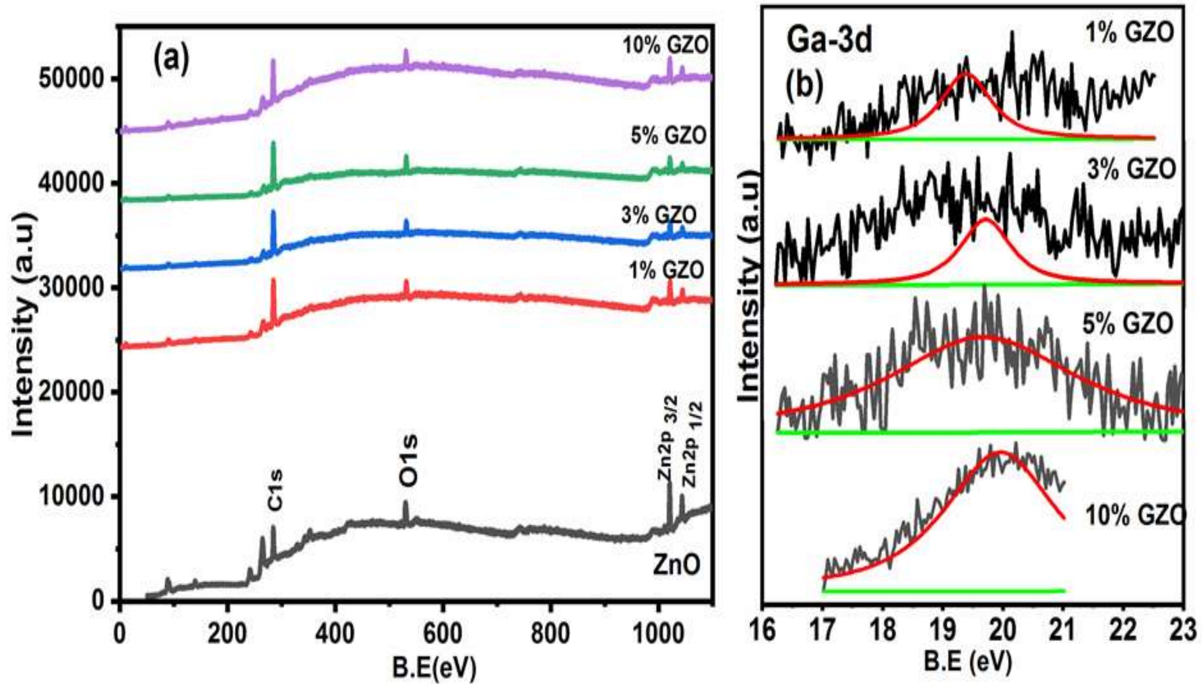

Figure.**5.21**.High resolution XPS (a) survey scan spectra of ZnO nanocrystalline thin films (b) the chemical state of Ga in GZO films for Ga $3d_{5/2}$ states .

The XPS spectra of O1s core level states of ZnO and GZO thin films are illustrated in the Figure.5.23 (a-e). It is observed that O1s peak is asymmetric in nature and can be deconvoluted in to 3 components which situated at ~ 531 eV, ~532 eV and ~533 eV (noted as I, II and II). The region I and II relate O^{2-} ionic bonds. The low energy (region-I) attributed to presence of O^{2-} of hexagonal wurtzite ZnO lattice points, whereas region II are related to oxygen vacancies (V_o) in the lattice [244]. Therefore the changes in the relative intensity ratio between I and II were related to the variations in the concentration of oxygen vacancies in the lattice. The ratio has been found to increase from 0.889 to 1.169 for GZO film with Ga, which identifies the formation of a considerable amount of oxygen vacancies in GZO lattice. The highest energy region is referred to Zn^{2+} bonding to hydroxyl group (OH) or adsorbed oxygen in the lattice [244]. As shown in Figure.5.23, the O1s peaks of the GZO samples slightly shifted toward a higher binding energy compared to those of the undoped ZnO sample. These shifts were also due to the higher electronegativity of Ga than that of Zn. Thus XPS analysis shows the evidence of defects variation in the undoped and doped films which result in the various emissions in the visible region.

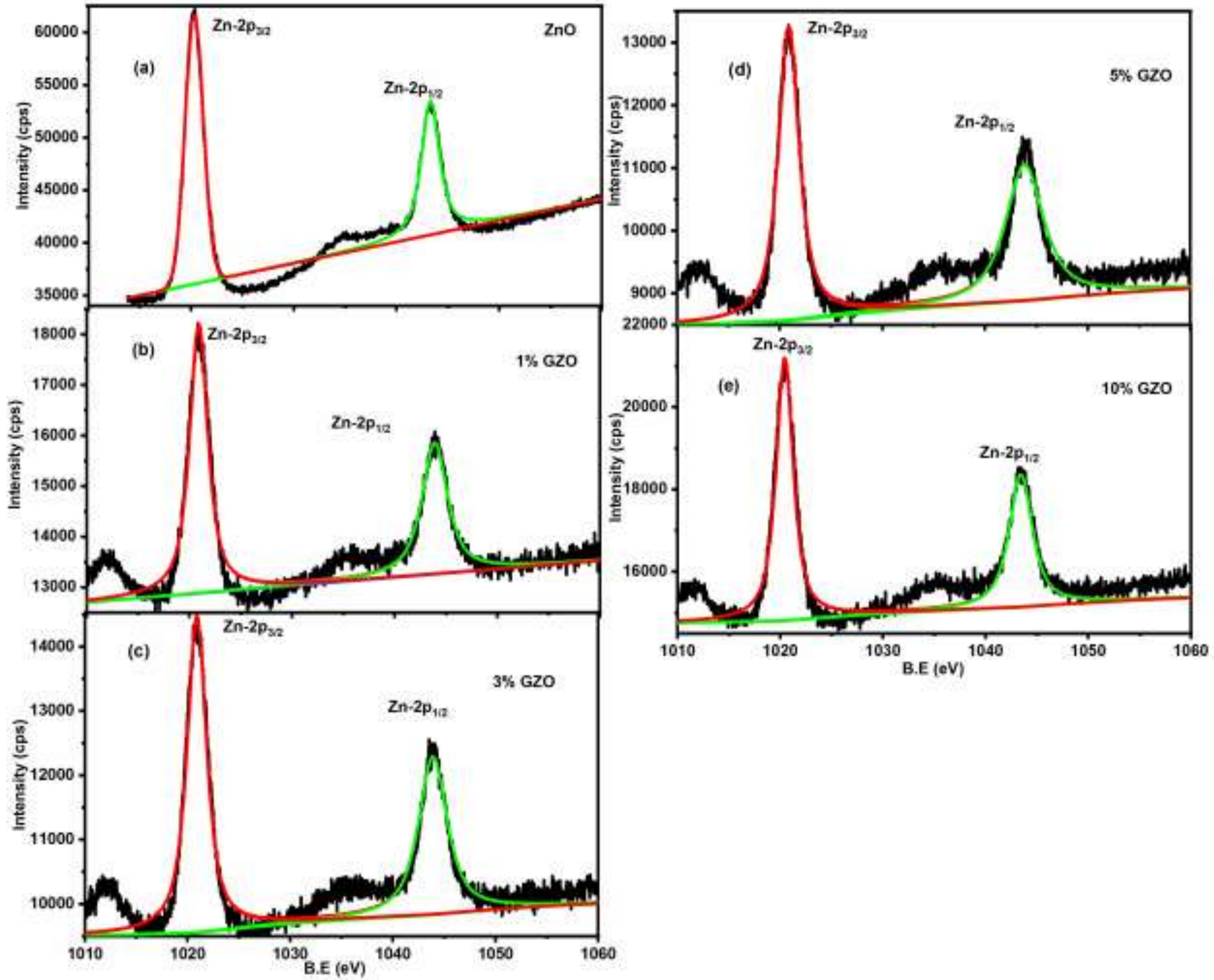

Figure.5.22. Deconvoluted High resolution XPS spectra for core level Zn 2P of (a) undoped ZnO (b) 1% (c) 3% (d) 5% and (e) 10% GZO nanocrystalline thin films

5.2.3.4. Absorption and optical band gap

The knowledge of optical constants of material is of great interest in the design analyses to be used in optoelectronics. Optical absorbnce and transmission spectra of ZnO, SZO and GZO thin films are depicted in Figure.5.24. (a & b). The average transparency in the visible region was around 90%. The well-developed interference pattern and high transparency is associated with structural homogeneity and crystallinity. All sample exhibit increased transmission in the visible region which is essential for potential applications in transparent optoelectronic devices. The increase in transparency of the GZO films after doping was due to formation of c-axis oriented grains that grow perpendicular to the substrate while decrease in transmittance at higher doping due to the increased scattering of photons by deflects formed due to doping.

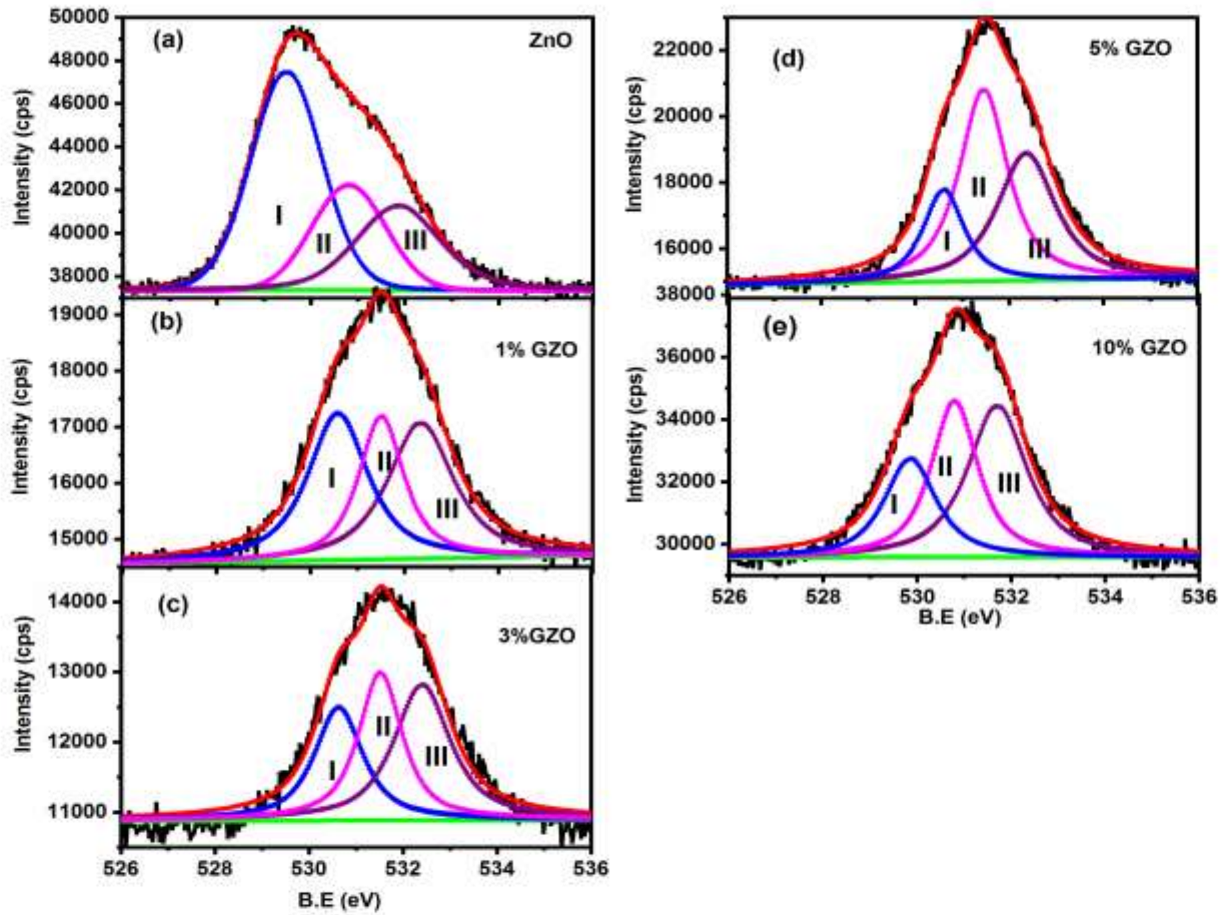

Figure.5.23. The O1s core level peaks of (a) undoped ZnO (b) 1% (c) 3% (d) 5% and (e) 10% GZO nanocrystalline thin films

It is observed that the absorption coefficient was maxima in the ultraviolet region compared with visible region. The absorption edge and absorption coefficients changes with doping concentration. The optical band gap energy of GZO films increased with increasing Ga content shown in the inset of Figure.5.24.(b). The increase in optical band gap is in agreement with absorption edge shift to UV region and also believed to be due to Burstein mass effect.

5.2.3.5. Photoluminescence Properties

Room temperature PL spectra of pure and doped thin films were measured using xenon lamp of 325 nm as excitation source is shown in Figure.5.25.(a-e). The PL spectra of films consists of the UV emission originated from the excitonic recombination corresponding to the near band emission of ZnO, while the defect level emission in the violet, blue, green and yellow regions are due to the recombination of photo generated holes with various structural defects

such as oxygen vacancies, Zn interstitials, zinc vacancies, oxygen antisite etc [245-246]. The band to band excitation (NBE) of ZnO promotes electron from the valence band to conduction band, leaving holes in the valence band. The holes migrate from the valence band to deep levels and recombination occurs between electron from either the conduction band or shallow donor levels and trapped holes on deep levels. The PL emission spectra of GZO films are broad centred on violet region and it can be deconvoluted in to different bands which were red shifted in GZO thin film. With increase in Ga concentration, the low-energy shift of NBE emission peak is observed. This effect is caused by the following facts: (i) the band gap of GZO is higher than that of ZnO; (ii) the sp–d spin exchange interaction, and (iii) the Burstein-Moss effect [247]. The peak intensity at 375 nm is gradually increased for GZO films, which ascribed to the greater amount of photo carrier recombination in the NBE due to the doping.

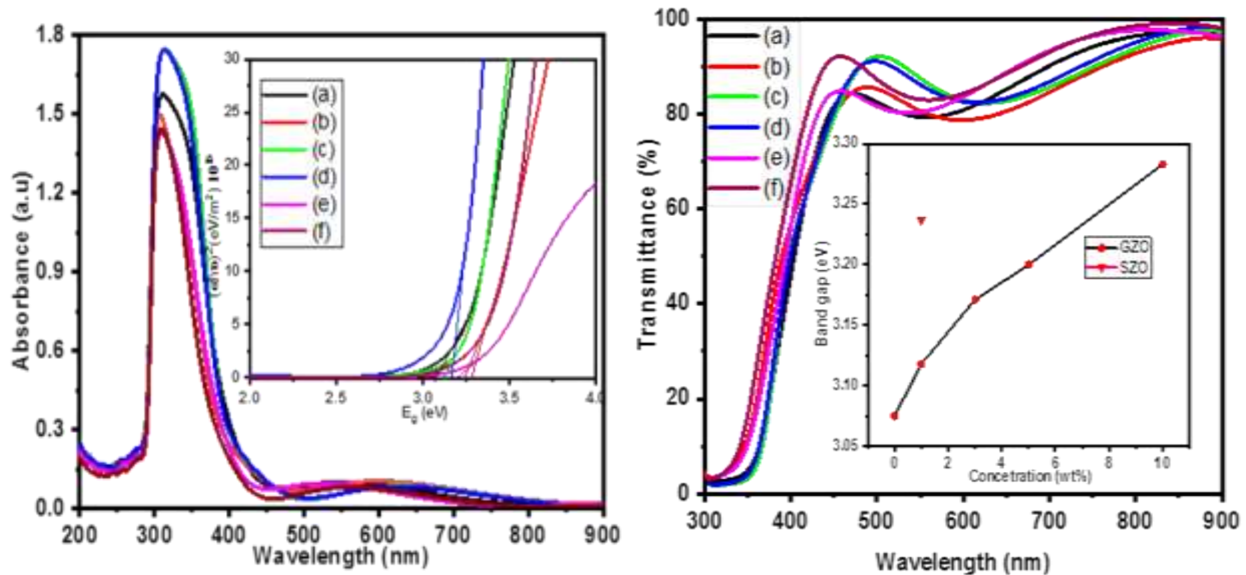

Figure.5.24. (a) Absorbance spectra and the inset shows the tauc's plot and (b) Optical transmittance and inset shows the band gap variation with concentration of dopants spectra of ZnO thin films

The appearance of PL emission within 425 - 430 nm (violet emission) and 450 - 460 nm (blue emission) were characterized due to presence of zinc interstitial (Zn_i) and single ionized zinc vacancies in the films. [246]. Also, the formation of antisite oxygen would responsible for the emission appeared at 485 nm and its origin might be the recombination of electrons between the antisite oxygen and the conduction band. The violet luminescence at 419 nm is due to radiative defects related to the interface traps existing at the grain boundaries and emitted from

the radiative transition between this level and the valence band and also attributed to the Zn vacancies [245]. The peak centered at 406 nm is the origin of the violet emission is ascribed to an electron transition from shallow donor level of the natural zinc interstitials to the top level of the valence band [248]. Focusing on the green emission, different kinds of luminescent centers have been responsible for the green emission such oxygen vacancies, oxygen interstitials, oxygen antisite etc. A prominent emission was observed at 530 nm is due to neutral oxygen vacancy formed in the film. The green emission resulted from the recombination of electron with the holes trapped in singly ionized oxygen vacancies which are commonly made in oxygen deficient condition. The yellow emission band is at 570 nm due to the presence of interstitials oxygen vacancies [246]. It is also observed that with the increase of Ga concentration, the orange emission peaks become dominant; it is due to increase the concentration of interstitials oxygen in the GZO film.

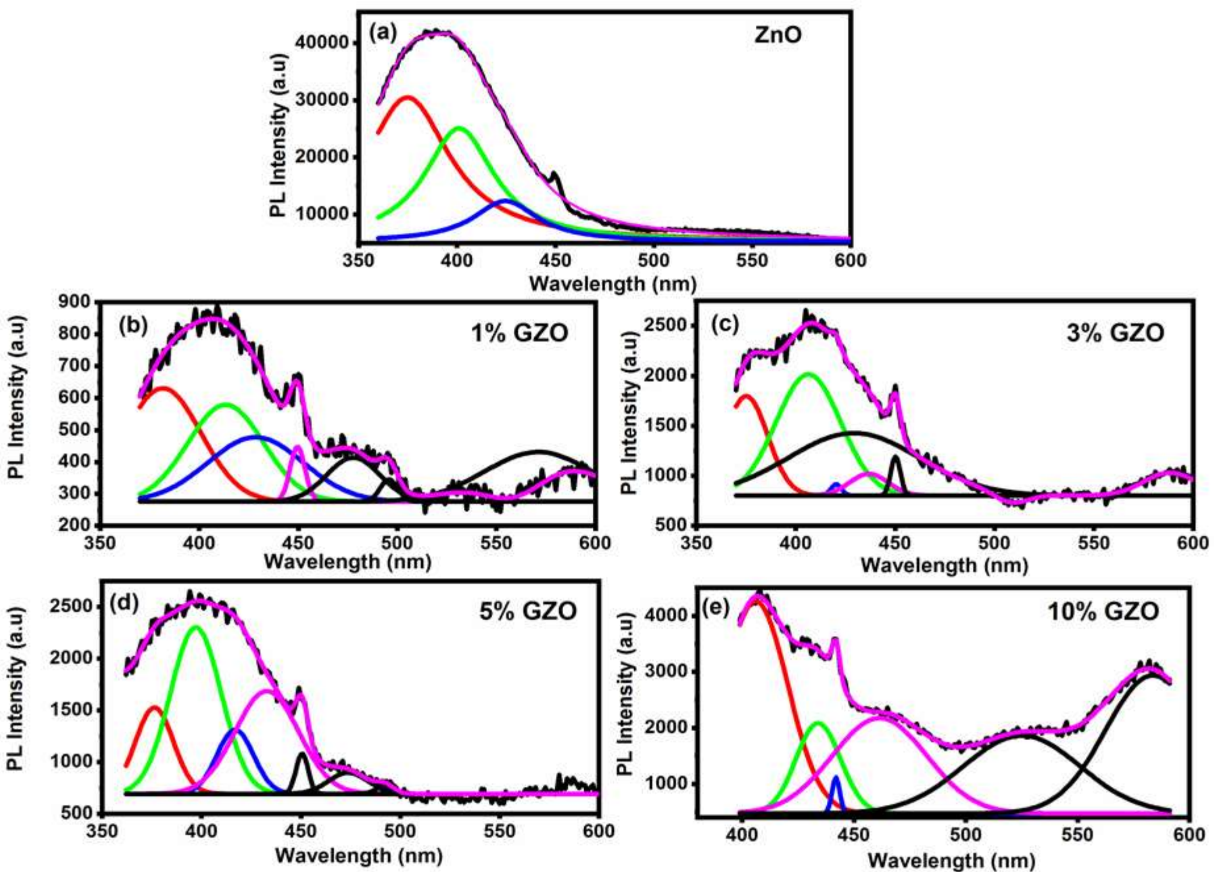

Figure.5.25.Room temperature Photoluminescence spectra of (a) undoped ZnO (b)1% GZO (c) 3% GZO (d) 5% GZO and (e) 10% GZO nanocrystalline thin films

To investigate the origin of the emission band diagrams of the films with possible radiative transition are shown schematically in Figure.5.26. (a) The small peak at 378 nm is assigned to the band- band transition as supported by the NBE in the PL spectra. The dominant peak at 400 nm is considered to be result of the transition from a zinc interstitials Zn_i to a valence band. The energy levels corresponding to the Zni native defects are located below the conduction band, which originates electron for non-radiative relaxation from the conduction band rather than a band – band transition. The other peak at 590 nm in the visible region is attributed to the transition from Zn_i to an oxygen vacancy (O_i). Figure.5.26.(b) Illustrate the CIE (International commission on illumination) chromaticity diagram of pure, SZO and GZO films for different Ga concentrations. CIE parameters such as colour coordinate (x, y) were calculated to characterize the colour emission. It can be seen that the colour coordinates traverse with the Ga content. The result shows that the tuning of the visible emission is possible by the change of the Ga concentration in ZnO host.

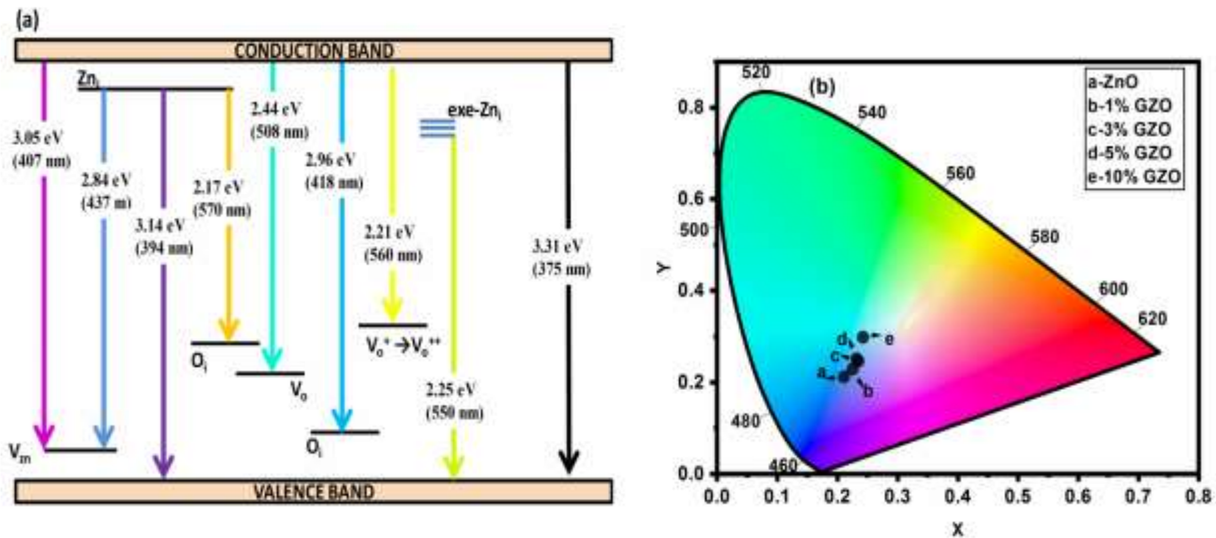

Figure.5.26 (a) Energy level diagram showing some of the principal defect levels in ZnO thin films and (b) Chromaticity diagram undoped and doped ZnO thin films in the visible spectral range

5.2.3.6. Homojunction Devices

Figure.5.27.(a) shows the current-voltage (I-V) characteristics of the GZO/SZO ZnO homojunction diodes fabricated by RF sputtering on ITO substrate. The measured low current for the applied voltage might be due to high resistance of metal-semiconductor contacts. The I-V curve of homojunction showing typical diode characteristics with good rectification. The p-n

homojunction diode with low turn on voltage of approximately 1.29 V,1.65 V, and 1.72 V for 1% GZO, 5% GZO and 10% GZO respectively, which showed enhanced rectifying behavior with increasing Ga concentration. The initial turn on voltage is approximate to the band gap of ZnO, corresponds to injection of electron into the SZO from GZO. The substitution of Sb in to ZnO contributes acceptor characteristics. The electron in the outer shell (d) of Sb states appears near Fermi level. The bonding states have a higher energy level and are very close to the conduction band, and the electron in this state have higher probability of jumping to the conduction band, resulting in the increase of conductivity, which cause the increase of the turn on voltage of homojunction.

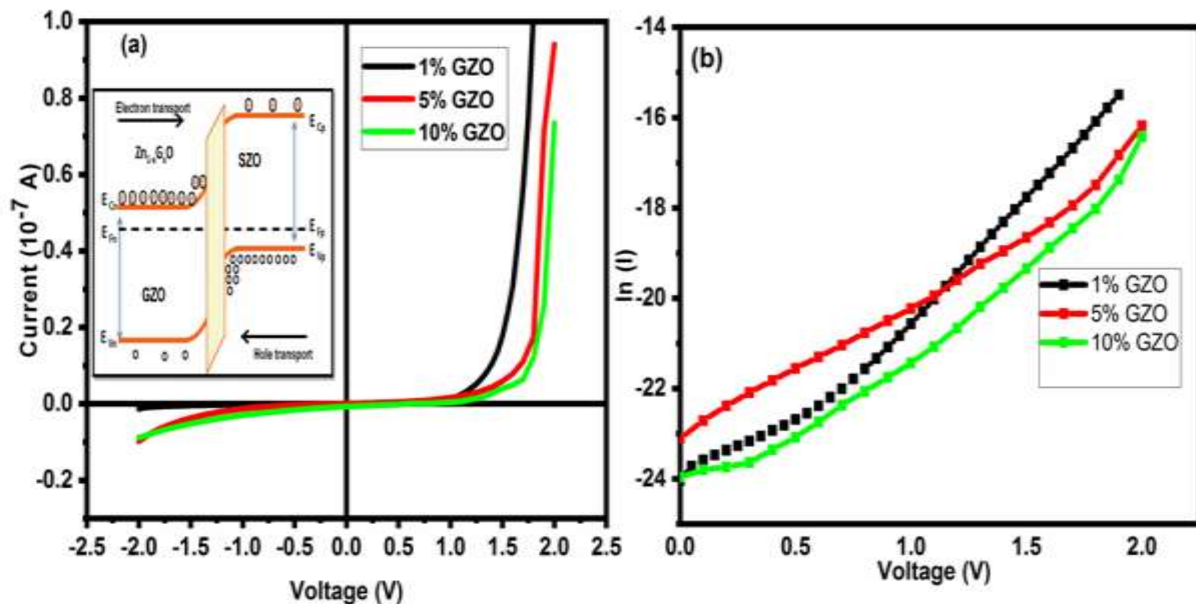

Figure.**5.27** (a) Current-Voltage characteristics curve and (b) Ln(I) vs Voltage graph of GZO/SZO homojunction diode with Ga content and the inset shows the band diagram of GZO/SZO structure

According to the Sah-Noyce-Shockley theory, the value of the ideality factor of a diode is about 1-2 at low or high voltage. The ideality factor n can be estimated as 8.5, 8.7 and 9.65 for 1%, 5% and 10% GZO/SZO respectively. High ideality factor (n>2) in wide band gap semiconductor like ZnO are usually reported. This high ideality factor suggests that the I−V characteristic is not limited by thermionic emission of the normal p−n junction. It may also be due to several effects: (i) interface states at a thin oxide between the metal and the

semiconductor; (ii) deep-level-assisted tunneling in highly doped semiconductors and (iii) generation/recombination currents within the space-charge region [249-250].

5.2.4. Conclusion

All thin films showed pronounced c-axis orientation resulting in a strong (002) peak corresponding to hexagonal wurtzite structure. The transmittance of ZnO and GZO films was higher than 90% in the visible region, and the optical band gap of film became wider with increasing Ga content, because of the Burstein-Moss effect. The photoluminescence showed that the doping with ZnO altered the band emission due to zinc vacancies, oxygen vacancies and surface defects. In addition to increasing oxygen vacancies in neutral (V_o) and ionized (V_o^+) states, a number of other effects are generates, which include Zn interstitials (Zn_i), neutral ionized Zn vacancy(V_{zn}) and oxygen antisite (O_{zn}) as the dynamic acceptor defects which act as the defect origins of different visible PL components classified in the UV- violet, violet- blue and green-yellow regions. UV luminescence and visible emission of the GZO films are extremely useful for many optoelectronic devices along with TCO layers.

5.3. Indium and Gallium codoped ZnO nanocrystalline thin films (IGZO)

5.3.1. Introduction

Doping of ZnO with suitable dopants is a well-known method for achieving the desired material properties. The idea of co-doping is not new. Co-doping allows the benefits of two dopants to be exploited simultaneously. The strengths of one dopant can compensate for the weaknesses of another. Many dopants have been used to improve the physical properties of ZnO. The most common of these are the group 13 elements such as aluminium, gallium, indium, etc. Some related studies based on Al and Ga co-doped ZnO nanostructures via a sol–gel route to modify their electrical and sensing properties have been carried out by Hayder et al [251]. While Benhaliliba et al [252] synthesized ZnO thin films which were doped separately with Al and In and these films exhibited good electrical conductivity and high optical transmittance in the visible region. These trivalent elements by replacing the Zn atom in the parent crystal structure modify the ZnO lattice and reveal improved properties. And also these dopants are introduced as substitutional defects on zinc sites. The fact that the radius of 4-coordinate Ga^{3+} (0.62 Å) and that of In^{3+} (0.81 Å) is closer to that of 4-coordinate Zn^{2+} (0.74 Å), make it useful as a codopant for ZnO structures [239].

5.3.2. Materials and Methods

Thin films of pristine ZnO, ZnO with In ($Zn_{0.99}In_{0.01}O$) (IZO) and Ga ($Zn_{0.99}Ga_{0.01}O$) (GZO) as a single dopant and indium and gallium ($Zn_{0.98}In_{0.01}Ga_{0.01}O$) (IGZO) as co-dopants were deposited on glass substrates using RF magnetron sputtering using powder targets. Sputter targets were prepared using a mixture of high purity ZnO powder and the desired amount of high purity In_2O_3 and Ga_2O_3 powders.

5.3.3. Result and Discussion

5.3.3.1. Structural Properties

The XRD patterns of pristine, single-doped (IZO and GZO) and co-doped (IGZO) ZnO thin films have only one strong (002) peak indicating that all films have a well-developed wurtzite structure and a good c-axis orientation perpendicular to the substrate (Figure.5.28). No other peaks belonging to either gallium or indium phases are observed in the spectra, suggesting that both Ga and In are incorporated well into the ZnO lattice. It is observed that the doped-film

shows a slight shift towards a lower angle compared to pristine ZnO, which can be attributed to the difference in the ionic radius of In^{3+} , Ga^{3+} and Zn^{2+} respectively. Also different shift directions of the (002) peak indicate different alternations of interplanar distances.

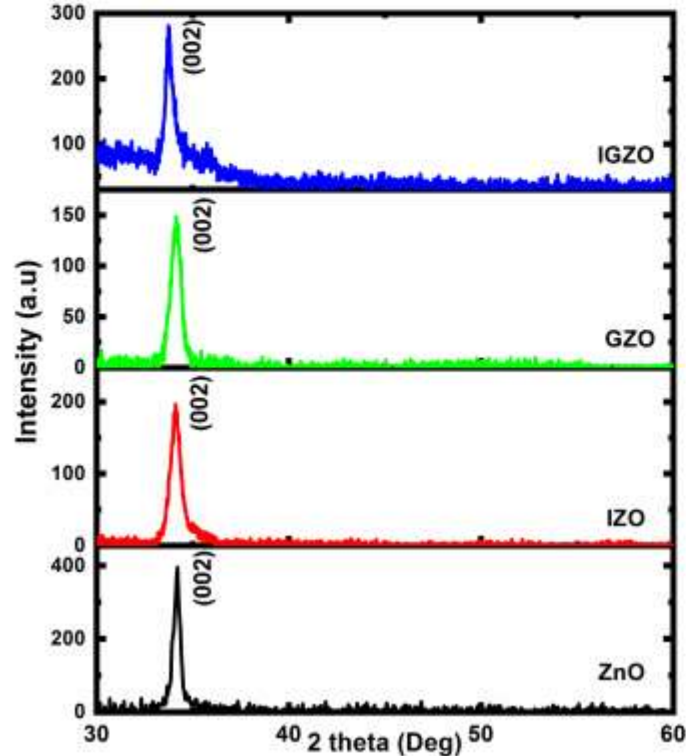

Figure 5.28. X-ray Diffraction pattern of pristine ZnO, IZO, GZO and IGZO nanocrystalline thin films

The values of lattice parameters (a and c) were estimated to be 0.302 nm and 0.5248 nm, respectively with c/a ratio of 1.732. The grain size and lattice parameters, dislocation density and strain developed in the film are tabulated in table 5.7. It can be observed that the crystallite size of single and co-doped ZnO decreases from 177 to 109 Å. This could be attributed to the presence of a small strain and dislocations in the ZnO films due to the difference in the ionic radius of In and Ga dopants. The data reveal that the presence of In and Ga ions in ZnO prevents the growth of crystal grains. The calculated crystal defect parameters like microstrain and dislocation density indicate an increasing trend with doping while the crystallite size decreases due to the replacement of Zn^{2+} by In^{3+} and Ga^{3+}. In the case of IGZO, it is possible that the simultaneous incorporation of both dopants in the lattice structure is leading to a compensation effect, and the difference in the size of the two dopants helps in reducing some of the crystal strain, in turn allowing greater dopant incorporation in the ZnO structure.

Table 5.7. Lattice parameters of single and codoped ZnO thin films calculated along (002) orientation

Sample	2θ	FWHM	D(nm)	Dislocation density $\delta \times 10^{15}$	a nm	C nm	d nm	c/a	Strain (10^{-3})
ZnO	34.17	0.469	17.709	3.189	0.3026 ±0.0004	0.5241 ±0.0008	0.2621 ±0.0004	1.732	1.957
IZO	34.12	0.729	11.394	7.703	0.3031 ±0.0002	0.5249 ±0.0004	0.2625 ±0.0002	1.732	3.042
GZO	34.13	0.676	12.293	6.617	0.3029 ±0.0003	0.5248 ±0.0005	0.2624 ±0.0003	1.732	2.82
IGZO	33.81	0.759	10.925	8.378	0.3057 ±0.0006	0.5295 ±0.0007	0.2648 ±0.0008	1.732	3.173

Figure.5.29 (a) shows the Raman spectra of single and codoped ZnO thin films. The Raman lines around 437 cm^{-1} are observed for all the thin films, which is assigned to E_2 (high) mode. This mode is assigned to the vibration of oxygen sub lattice and is the characteristics peak of hexagonal wurtzite phase of ZnO films. In doped films, the E2 (high) mode is slightly blue shifted from 437 cm^{-1} to 436.4 cm^{-1}, caused by the tensile strain in the films which is in good agreement with the XRD result. A weak peak at 589 cm^{-1} (Figure.5.29. (b)) corresponds to A_1 (LO) mode and may be caused by the defects such as O-vacancy and Zn interstitial and their complexes, which is consistent with the PL and XPS results.

5.3.3.2. Morphological Properties

Figure 5.30 shows the FESEM images of pristine and codoped-ZnO films. All the films have a dense, uniform, smooth and crack free microstructure. The morphology of ZnO and GZO has a granular structure while that of IZO shows a cornlike structure. The grain size of the IGZO thin films is smaller than that of ZnO which is attributed to the various relationships between the nucleation, growth and activation energy of the thin films. Owing to the close ionic radius disparity between Ga^{3+} and In^{3+}, the compression in the volume caused by gallium to the ZnO lattice is effectively compensated and counteracted by the tension in the lattice caused by indium such that there will be less strain imposed in the lattice and fewer dislocations will be formed [253]. As a result, IGZO films have a better surface morphology than other films.

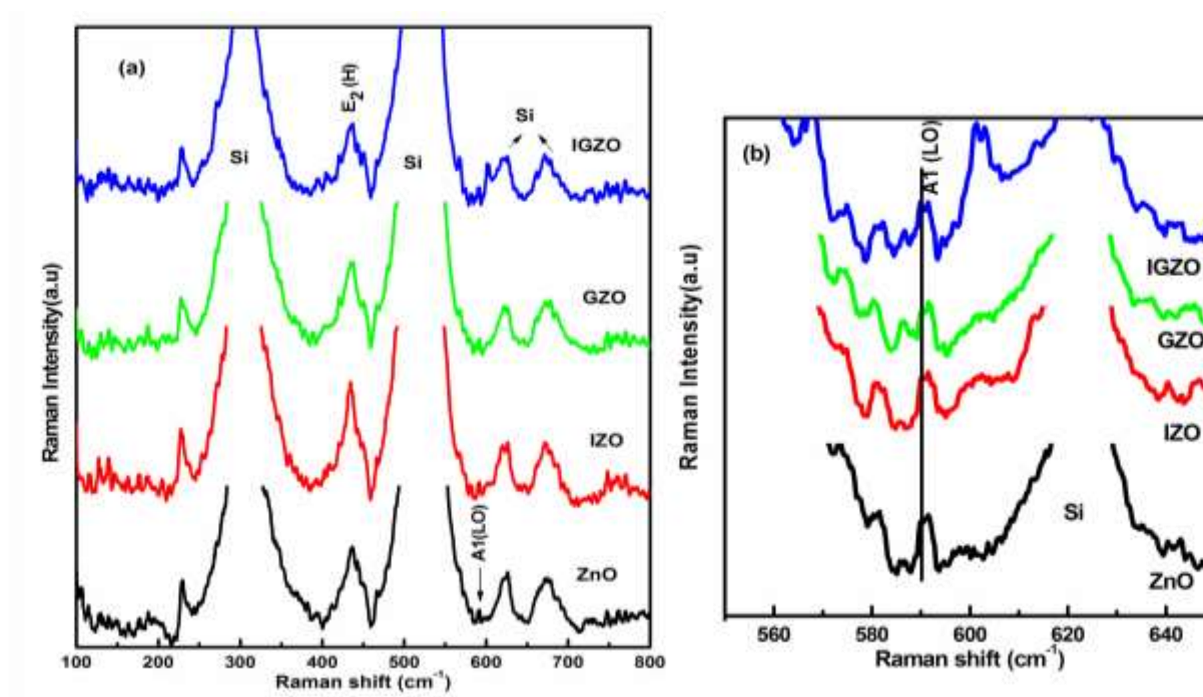

Figure.5.29. (a) Raman spectra ((b) enlarged view) of single and codoped ZnO thin films

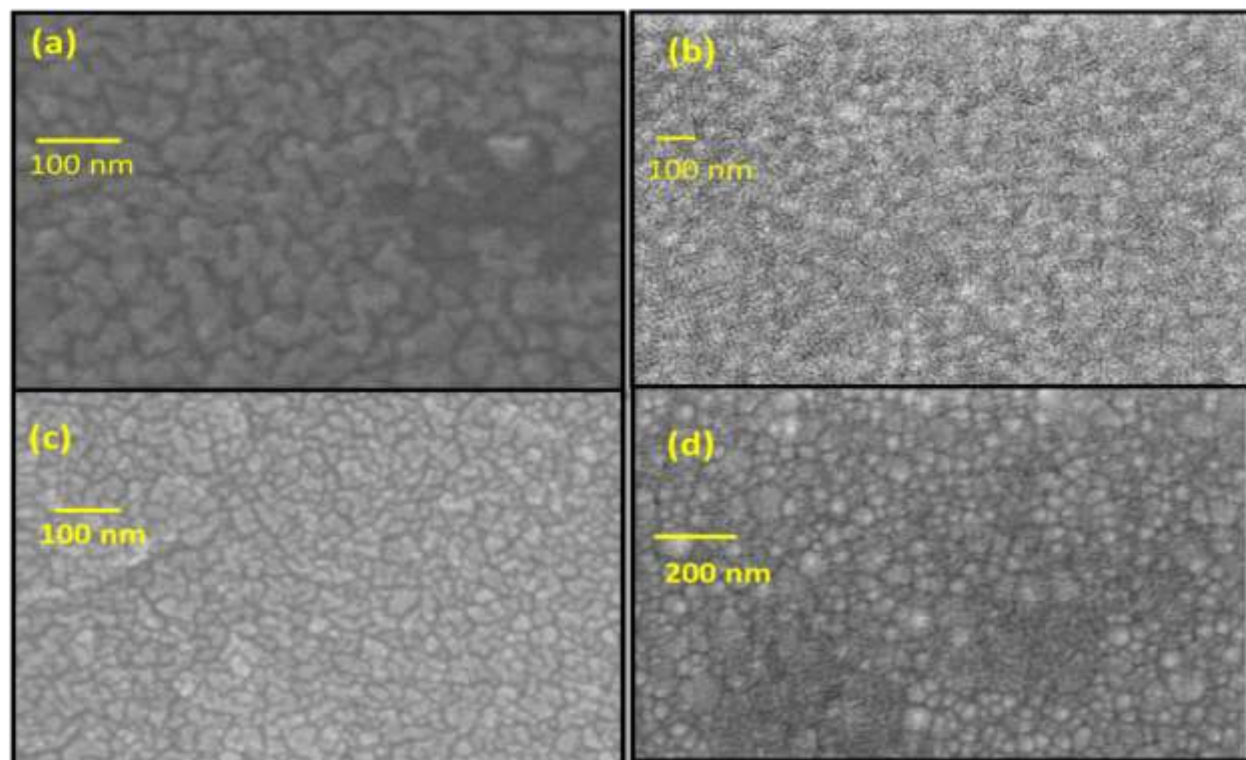

Figure 5.30. FESEM micrograph of (a) ZnO (b) IZO (c) GZO and (d) IGZO nanocrystalline thin films

5.3.3.3. Compositional Analysis

The weight % of all elements of the thin films is studied with the help of EDS and summarized in Table.5.8. The associated spectra obtained by EDS studies of all films are shown in Figure.5.31 (a-d). EDS studies confirm the presence of doped elements such as In, Ga, in ZnO. The amounts of doped element are found to be less than the actual amount of target composition.

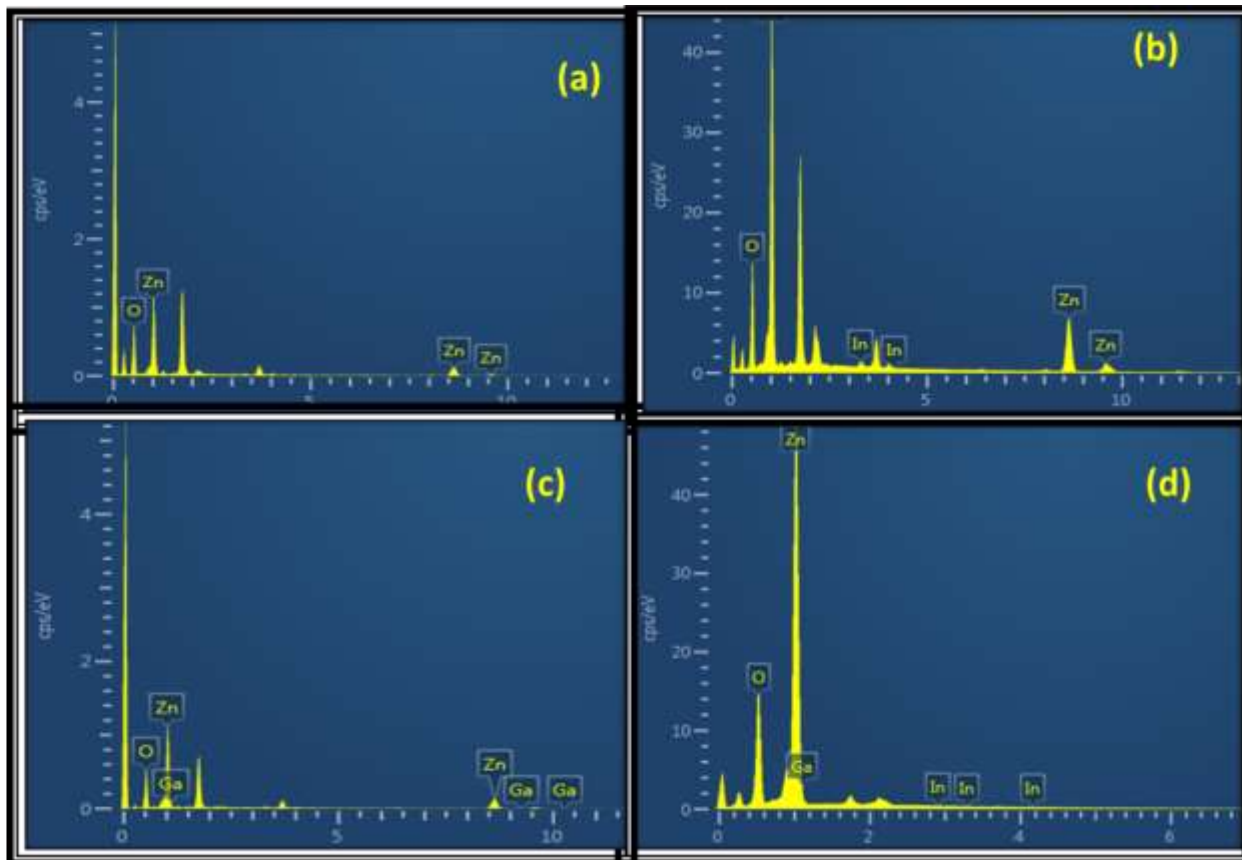

Figure.**5.31**. EDS spectra of (a) ZnO (b) IZO (c) GZO (d) IGZO nanocrystalline thin films

Table 5.8. Compositional ratio of ZnO, IZO, GZO and IGZO thin films from EDS

Sample	Zn (wt%)	O (wt%)	In (wt%)	Ga (wt%)	Total %
ZnO	52.2	47.8	-	-	100
IZO	68.8	29.5	1.7	-	100
GZO	58.6	41	-	0.4	100
IGZO	81.4	18	0.4	0.2	100

In order to understand the oxidation states of the deposited thin films, XPS analyses are performed and shown in Figure.5.32 and 5.33. The spectra are corrected using the C 1s line from adventitious aliphatic carbon (285 eV). It is seen that the O 1s and Zn 2p peaks of the doped ZnO thin films (Figure.5.32 (a) and (b)) shift towards higher binding energies compared to pristine ZnO thin films. This attributed to the formation of stronger bonds between the dopants (In & Ga) and oxygen in doped thin films compared to those between Zn and oxygen in the pristine ZnO.

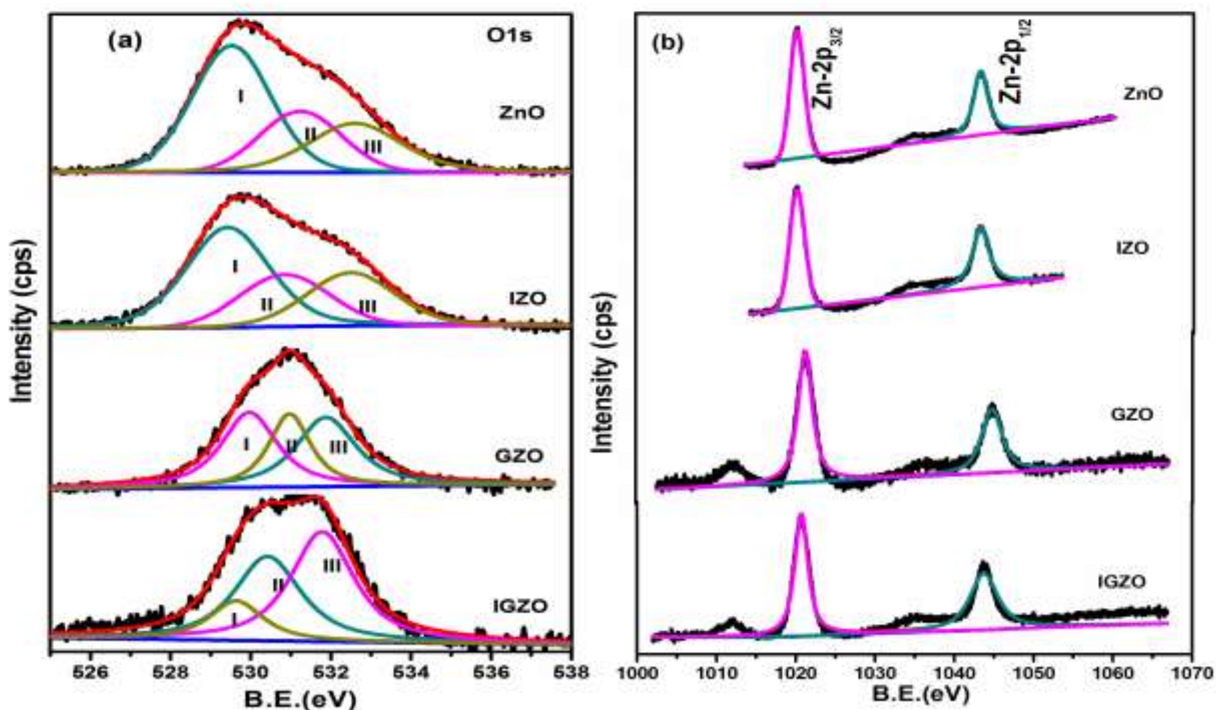

Figure.5.32. XPS (a) Deconvoluted O1s spectra and (b) Zn 2p spectra of ZnO, IZO, GZO and IGZO thin films

The binding energy of the zinc $2p_{3/2}$ and $2p_{1/2}$ peaks (Figure.5.32 (b)) of all the films are consistently found to be 1020.2 ±0.2 eV and 1043.2 ±0.2 eV respectively which can be attributed to the Zn^{2+} in ZnO. O1s spectra of all the films can be deconvoluted into 3 distinct sub peaks (I, II and III) using Gaussian fitting (Figure. 5.32 (a)). Among them, the low energy (region I) peak (529.4 ± 0.2 eV) originates from O^{2-} ions forming bonds with the metal cations (Zn^{2+},In^{3+} and Ga^{3+}) in the lattice. The medium energy region II (530.4 ± 0.5 eV) components are associated with O^{2-} ions near the oxygen deficient regions within the ZnO lattice and region III (532.01± 0.5 eV) is due to the presence of loosely bound oxygen on the film surface belonging to a specific ratio such as CO_3, adsorbed H_2O or adsorbed oxygen [254-256]. The In 3d and Ga 3d peaks are

clearly seen from the XPS survey spectrum of IZO, GZO and IGZO thin films, indicating that In and Ga have indeed blended into the ZnO lattice. The gallium $3d_{5/2}$ peaks of GZO (Figure.5.33 (b)) and IGZO films (Figure.5.33 (c)) have binding energy (B.E) of 20.33 eV and 20.31 eV respectively, which is due to Ga^{3+}. Similarly, the indium $3d_{5/2}$ and $3d_{3/2}$ peaks of IZO (Figure.5.33 (a)) and IGZO (Figure.5.33 (d)) have B.E of 444.4 eV & 451.5 eV and 444.9 eV & 452.29 eV respectively, which is due to In^{3+}.

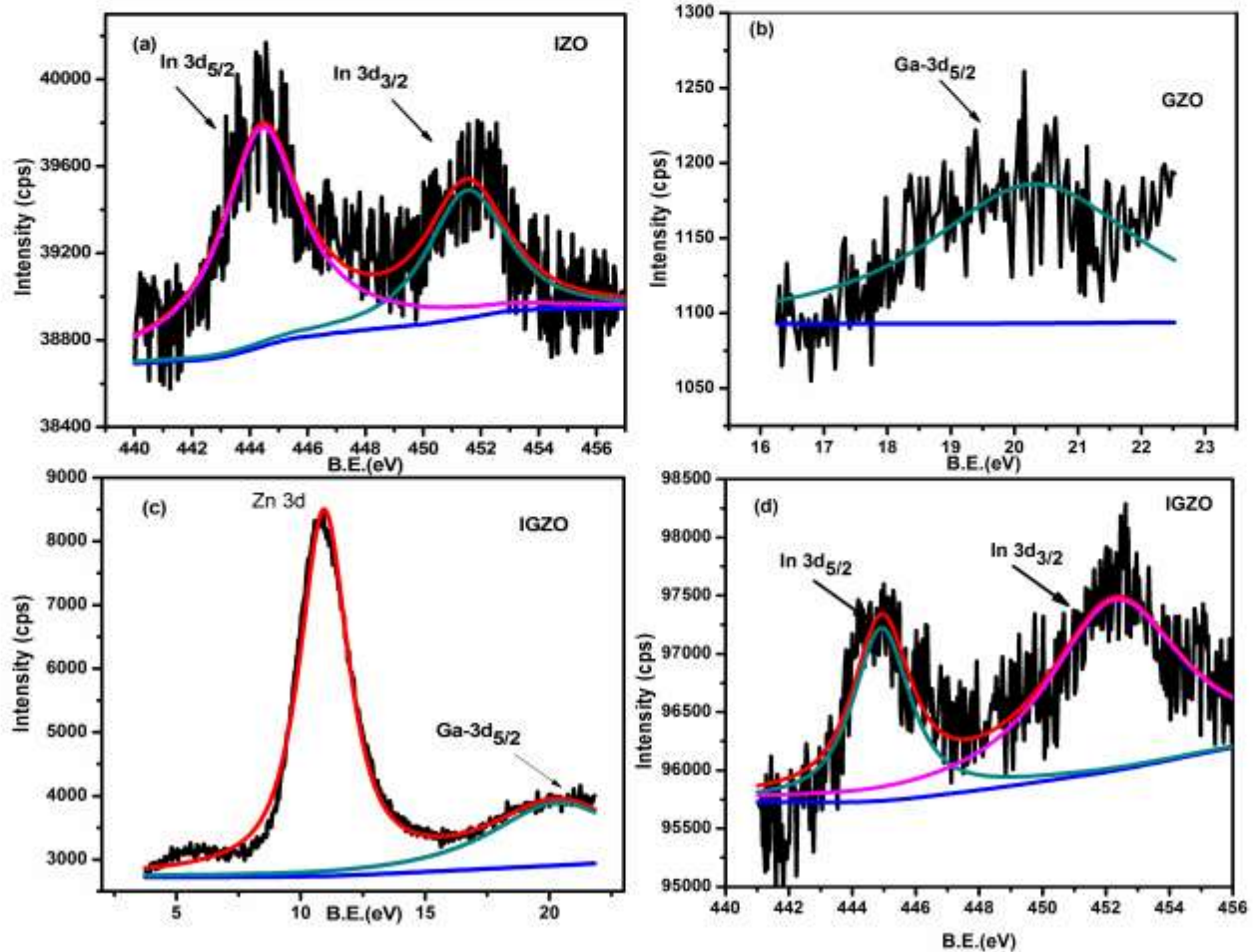

Figure.5.33 XPS spectra of (a) In 3d in IZO, (b) Ga $3d_{5/2}$ in GZO and (b & c) In 3d and Ga $3d_{5/2}$ in IGZO thin films

5.3.3.4. Absorption and optical band gap

Optical absorbance spectra of ZnO, IZO, GZO and IGZO thin films are shown in Figure.5.34 (a). The well distinguishable peak in the UV range of absorbance spectrum may be due to the exciton band of ZnO. The optical transmittance spectra of deposited films are shown in Figure.5.34 (b). All de-posited films exhibit an average transmittance of > 90% in visible

region and sharp cut off between 360 and 375 nm. The transmittance at 540 nm of ZnO, IZO, GZO and IGZO films are found to be 80%, 95%, 89% and 83% respectively. Among all the films, IZO shows the highest transmittance. It is evident that doping affects the transmittance of the films only marginally. This may be due to the formation of grainy surface leading to the large scattering loss. The absorption edge of the IGZO film is shifted towards lower wavelength. This shift is responsible for the improved transmittance in the lower wavelength region as compared to that of the pristine ZnO thin films. An interference fringe can be observed in each spectrum, indicating that the deposited films have a very smooth and homogeneous surface.

The optical band gap of the films is found to be dependent on the doping. The band gap of IZO (3.20 ± 0.02 eV) and IGZO (3.16 ± 0.04 eV) films decreases (red shift) whereas for GZO films (3.31 ± 0.03 eV) it increases (blue shift) as compared with that of ZnO (3.24 ± 0 .01 eV). This variation could be due to the increase in carrier concentration, known as Burstein-Moss effect.

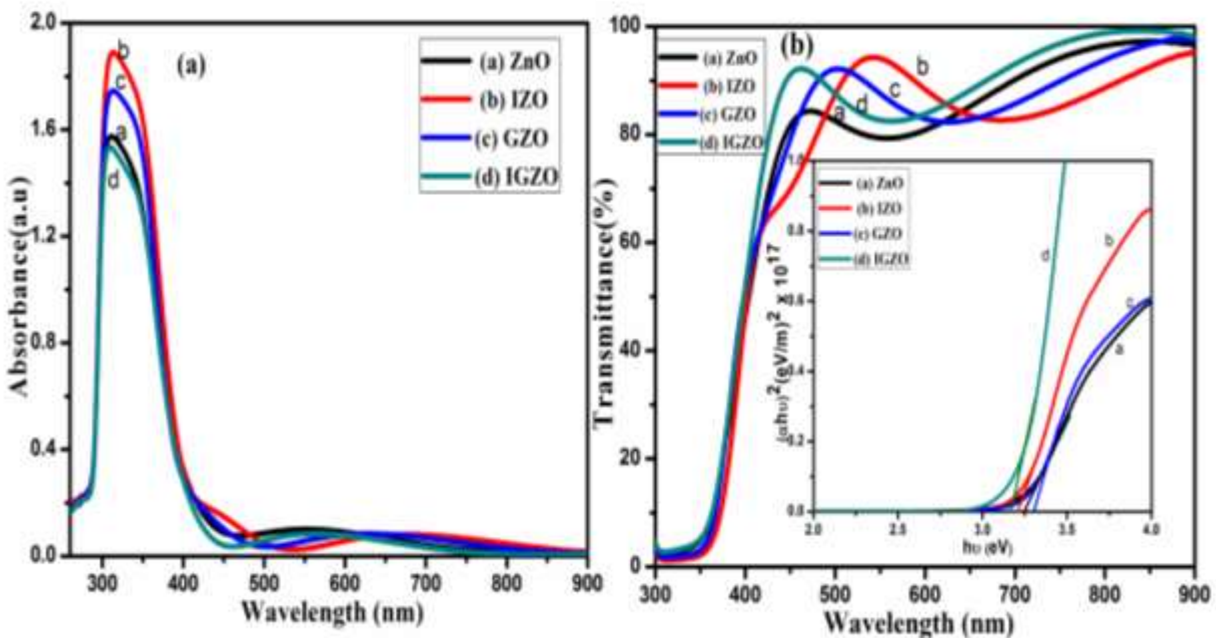

Figure.**5.34** UV-visible (a) Absorbance spectra (b) Transmittance spectra in the wavelength range 300-900 nm and inset shows the plot of $(\alpha h\nu)^2$ vs hν of the pristine, single and co doped ZnO thin films

5.3.3.5. Photoluminescence Properties

Figure.5.35 (a-d) illustrates the room temperature PL spectra of pristine and doped ZnO thin films for an excitation wave-length of 325 nm. The spectral peak of all the samples is broad

in the range 350-600nm. This broad visible band is associated with deep level emissions (DLEs) due to intrinsic point defects and defect complexes in the film structure. The fitted PL spectra of IZO (Figure.5.35 (b)) and GZO (Figure.5.35. (c)) consist of several peaks. The orange-red emission is attributed to the deep interstitial oxygen (Oi) states inside the IZO structures. The yellowish-green emission is attributed to transition from the bottom of the conduction of IZO and GZO structure to the Oi states, and the green emission is recognized as the V_O defects in the both structures [254]. The intensity of the orange-red emission is enhanced after indium doping, implying that the density of Oi states is increased in IZO film.

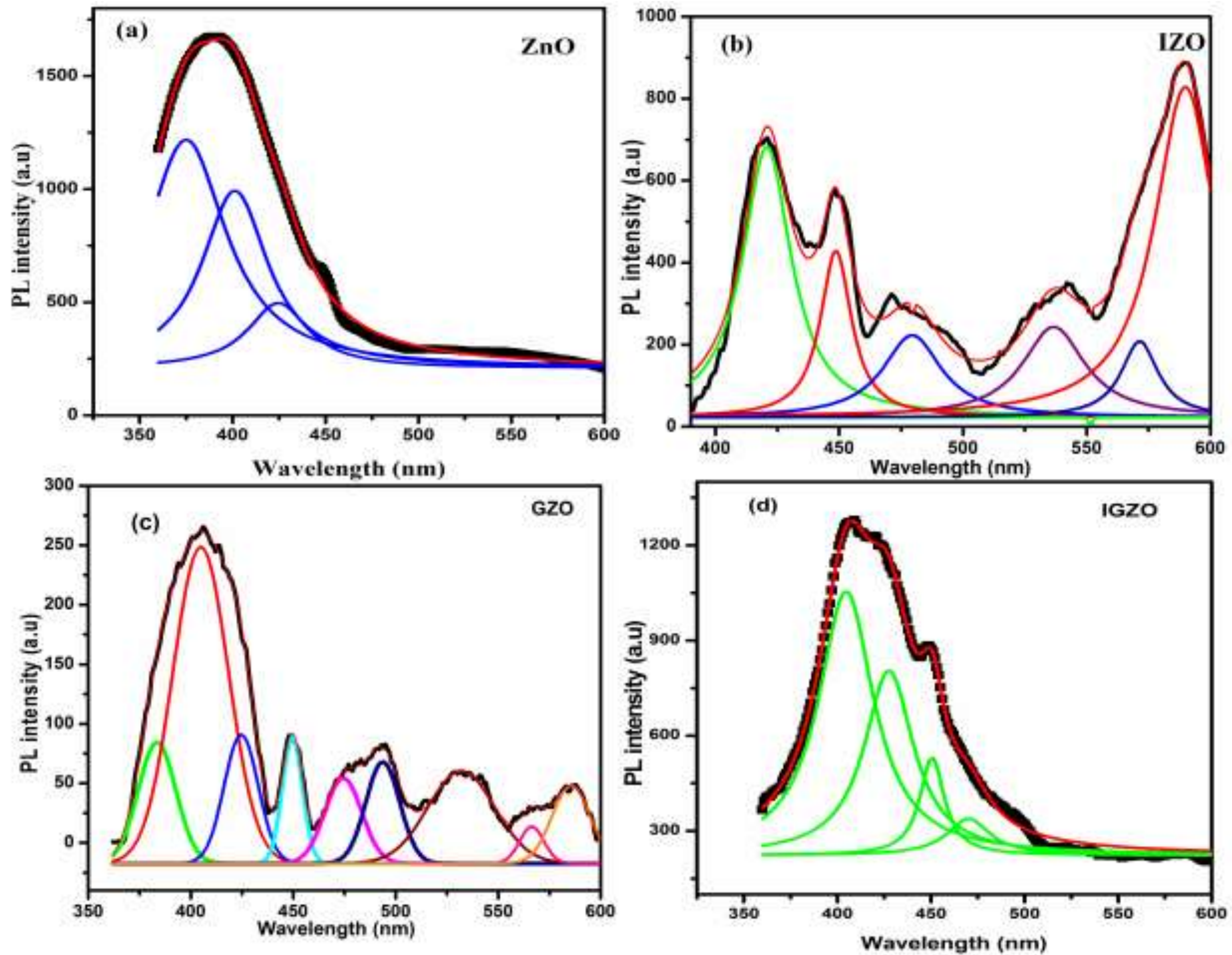

Figure.5.35. Deconvoluted room temperature photoluminescence spectra of (a) ZnO (b) IZO (c) GZO and (d) IGZO thin films.

All the films exhibit the UV peak, which is associated with free exciton-exciton collision process and attributed to the near band edge emission (NBE). Pristine ZnO thin film exhibits an emission band ranging from 360 nm to 450 nm with peak centered at 375 nm (Figure.5.35 (a)).

For IGZO, (Figure.5.35 (d)) emission band (ranging from 375 nm to 520 nm) is slightly shifted towards visible region due to incorporation of dopants with peak centered at 420nm. The PL spectra of IGZO thin films contain multiple peaks between 420 to 480 nm.These violet – blue and blue emissions are attributed to zinc interstitials (Zni) and zinc vacancy (Vzn), respectively, explaining the change in emission during doping [257-258]. From the PL characteristics, it is clearly evident co-doped IGZO material is a potential candidate for use in down converting LEDs.

5.3.4. Conclusion

Pristine, single (In, Ga) and codoped ZnO thin films were deposited on glass substrates by RF magnetron sputtering. All the thin films exhibited typical wurtzite structure with a strong (002) preferred orientation. XPS analysis confirmed the presence of the oxidized dopants in each film. The tensile strain in the films that caused the Raman lines shift was in good agreement with that obtained from the XRD result. The peak attributed to the oxygen vacancy defect in Raman spectra is consistent with that observed from PL spectra and XPS. Among doped films, IGZO film showed better morphology, crystallinity and PL emission. All the films had very high optical transmittance of the order of 95% in the visible range. The excellent optical properties reveal a great promise for the proposed thin films with applications in various optoelectronic devices.

CHAPTER 6

Solution processed Zinc Oxide nanostructures as NO_2 gas sensor

6.1. Introduction

6.2. Material and Methods

6.2.1. Synthesis of ZnO nanostructures: Hydrothermal method

6.2.2. Deposition of ZnO thin films: sol-gel methods

6.2.3. Fabrication of gas sensors

6.3. Result and Discussion

6.3.1. Structural Properties

6.3.2. Morphological Properties

6.3.3. Compositional Analysis

6.3.4. Photoluminescence Properties

6.3.5. Gas sensing Measurements

6.4. Conclusion

In this chapter we discussed about synthesis of solution processed Zinc oxide nanostructures and their application as NO_2 gas sensors.

CHAPTER 6

Solution processed Zinc Oxide nanostructures as NO_2 gas sensor

6.1. Introduction

Among the various types of sensors, gas sensors have attracted considerable attention due to their role in monitoring of the atmosphere environment and in human health for medical diagnosis, as well as in the detection of pollutants and toxic gases such as NO_2, NH_3, CO and SO_2 [164]. Among these NO_2, is the most common air pollutant produced by fossil-fuel combustion and vehicle emission. In addition to environmental problems, NO_2 causes skin damage even on very small amounts of exposure and critical respiratory disorder when exposed to about 50 ppm [259]. Therefore it is necessary to develop an improved gas sensor using various techniques and materials for detecting traces of NO_2.

Owing to their remarkable sensing properties as well as simple sensing mechanism relying on changes in resistivity; metal oxide semiconductor based gas sensors have been widely investigated. Among the metal oxides, ZnO can be easily synthesized as nanomaterials such as nanobelts, nanorods and nanowires using low temperature solution process [139]. These ZnO nanomaterials have already been applied to sensing of various gases including hydrogen, NO_2, NH_3, CO and ethanol due to their excellent properties, environmental stability, low cost, non toxic, easy synthesis and large specific surface area [160]. Despite of these advantages, ZnO based gas sensors generally operate at high temperatures, and their sensing performances still need to be improved in terms of response, saturation behavior, characteristics time, recovery and selectivity. Because most of the conventional ZnO based gas sensors generally have cross-sensitivity to various gases, it is necessary to develop highly selective sensors with improved gas response. Many efforts have been developed to synthesizing nanostructured ZnO with different morphologies using various physical and chemical approaches. Amongst these approaches the chemical synthesis route stands as a promising method because of its simplicity, low cost, low temperature and large mass production. Out of the various chemical routes, sol-gel and hydrothermal are well established method that has been moved to be the best due to its low temperature and low cost. In this study, ZnO thin films, nanorods were fabricated by the sol-gel method and hydrothermal method. Moreover the fabrication samples were exposed to NO_2 in a concentration range between 3 ppm to 10 ppm at various temperatures.

6.2. Material and Methods

6.2.1. Synthesis of ZnO nanostructures: Hydrothermal method

Zinc acetate dehydrate ($Zn(CH_3COO)_2.2H_2O$), Sodium hydroxide (NaOH) and isopropanol where used for ZnO seed layer synthesis. Zinc acetate dehydrates of 0.01M concentration was dissolved in isoproponal and 0.02M sodium hydroxide was dissolved separately in isoproponal. NaOH solution was drop wise added on to Zinc acetate solution under stirring at 90 ^{o}C for 2 hrs. Then the solution was spin coated on pre cleaned glass substrate. Prior to the film deposition the substrate were ultrasonically cleaned with acetone, isoproponal and DI water for 10 minutes respectively.

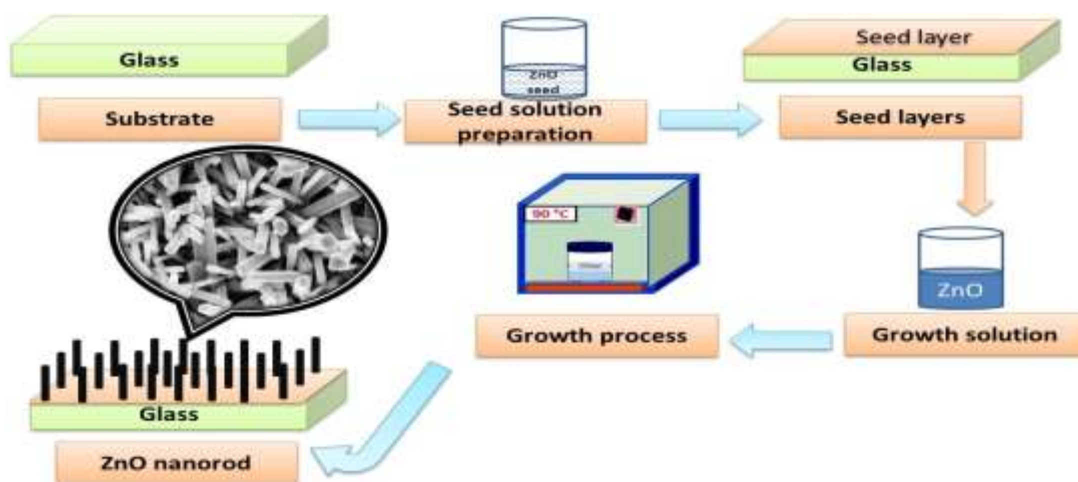

Figure.6.1 Schematic diagram of deposition of Zinc oxide nanorods by hydrothermal method

Zinc nitrate hexahydrtae ($Zn(NO_3)_2.6H_2O$ and Hexamethylenetetraamine (HMTA) were used for hydrothermal growth of ZnO nanorods on the seeded substrate (named Z1). 0.025M equimolar aqueous solutions of Zinc nitrate hexahydrtae and HMTA were prepared using DI water separately and then mixed together. HMTA also known as methenamine or hexamine is water soluble, non-toxic terta dentate cyclic tertiary amine. The seeded microscopic glass slide was immediately put into the solution mixture with the substrate facing the bottom surface of the beaker. The complex solution was then heat slowly up to 90 ^{o}C over a period of 3 hrs. During this appearance of complex solution changed from clear to cloudy confirming the reaction taking place. During the deposition the reaction mixture in the beaker was kept at 90 ^{o}C. After 3 hrs the substrate were removed from the solution and rinsed thoroughly with DI water and dried under

air. The grown samples were given heat treatment of 300 ^oC for one hr in muffle furnace for removing any organic deposits from the bath solution.

6.2.2. Deposition of ZnO thin films : sol-gel methods

Zinc oxide thin films were deposited onto glass substrate by the sol-gel method using spin coating techniques (sample name Z 2). Figure.6.2 (a) shows the flow chart of technique of the preparation and (b) shows the schematic diagram of the procedure. Zinc acetate dehydrate (0.5M) was used as a starting material. Isopropanol and monoethanolamine (C_6H_7NO, MEA) were used as a solvent and stabilizer respectively. The molar ratio of MEA to Zinc acetate dehydrate was maintained at 1:1. The obtained solution was stirred at 60°C for 2 h to yield clear and homogenous solution. Then the solution was kept for 24 hrs for aging, which was then served as coating solution. The coating solution was dropped into glass substrate, which was rotated at 3000 rpm for 30 s. After the spin coating, the film was dried at 100°C for 10 minute in an oven to evaporate the solvent and to remove organic residuals. This coating/drying procedure was repeated for 5 times before the film was inserted into muffle furnace and annealed at 500°C in air for 1 h. This coating process was performed for all the films.

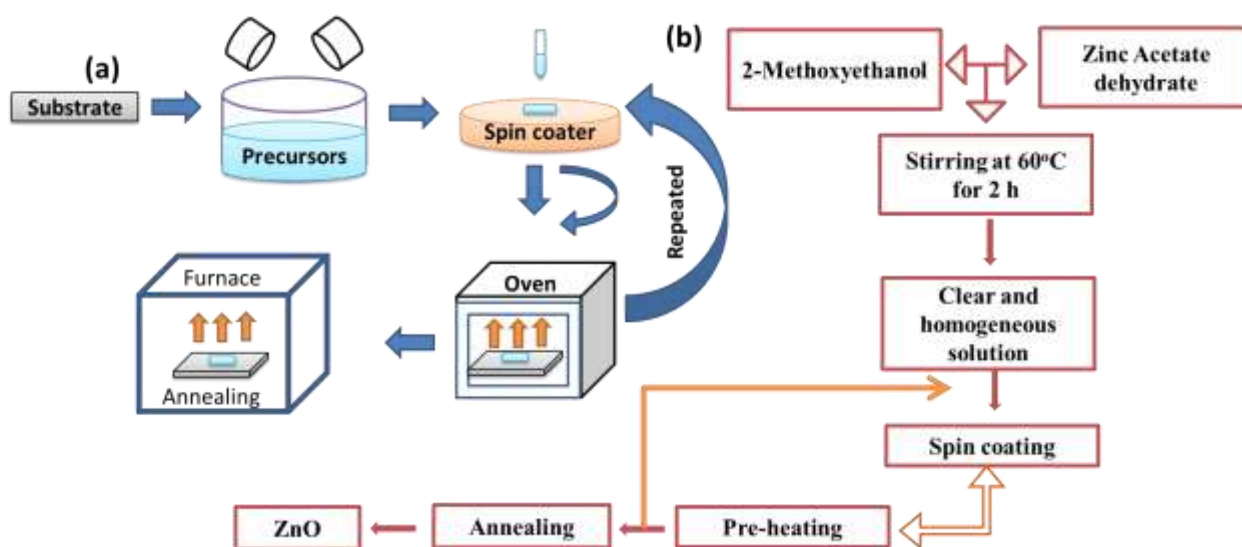

Figure.6.2 (a) schematic diagram and (b) flow chart showing the steps for depositing ZnO thin films

6.2.3. Fabrication of gas sensors

Gas sensors were fabricated by thermal evaporation of gold to form inter-digitized electrodes on top surface of the films, using a shadow mask with 0.5 mm electrode width and

200 μm separation between the electrodes. The fabricated sensors were annealed at 300°C for one hr before gas sensing measurements to ensure the uniformity and stability of the devices. The response of sensor for different gases was recorded in a static gas sensing set-up as shown in Figure.6.3. (a) with a heating stage. Heating stage temperature was precisely controlled by a PID programmer/ controller which are shown in Figure.6.3 (b). The set up consists of an airtight stainless steel chamber (1L) with provision of gas inlet and outlet. The sensor was placed in chamber and connected to parameter analyzer, to measure response. The sensor resistance was stabilized at each operating temperature for about 30 minutes prior to test gas exposure.NO_2 was injected into chamber through scaled syringe, prefilled with air at atmosphere pressure. I-V characteristics were recorded with different concentration (3-10 ppm). Then the sensor was exposed to air through outlet valve for recovery. Electrical connections from the sensor are taken with the help of two copper strips bonded to the sensor with silver paste. The sensing capability of the sensor is characterized at different operating temperature with precisely controlled heater inside the system to find out optimum working temperature. The response of the sensor was studied at different operating temperature in the range RT -300°C for various concentration of NO_2.

Figure.**6.3** Photograph of (a) gas sensing chamber and (b) PID controller

6.3. Result and Discussion

6.3.1. Structural Properties

Figure 6.4 (a-b) shows the x-ray diffraction spectra of ZnO films deposited on substrate by different techniques. Both of the films showed polycrystalline nature, with (100), (002), (101),

(102), (110), (103) and (112) peaks of hexagonal ZnO at 31.87°, 34.58°, 36.42°, 47.73°, 56.78°, 63.06° and 68.11° respectively. Both the films contains major phase of ZnO at the plane (101) for 2θ = 36.42°. By Debye Scherrer formula, the crystallite size found was 50 nm and 193 nm for Z1 and Z2 samples along (101).

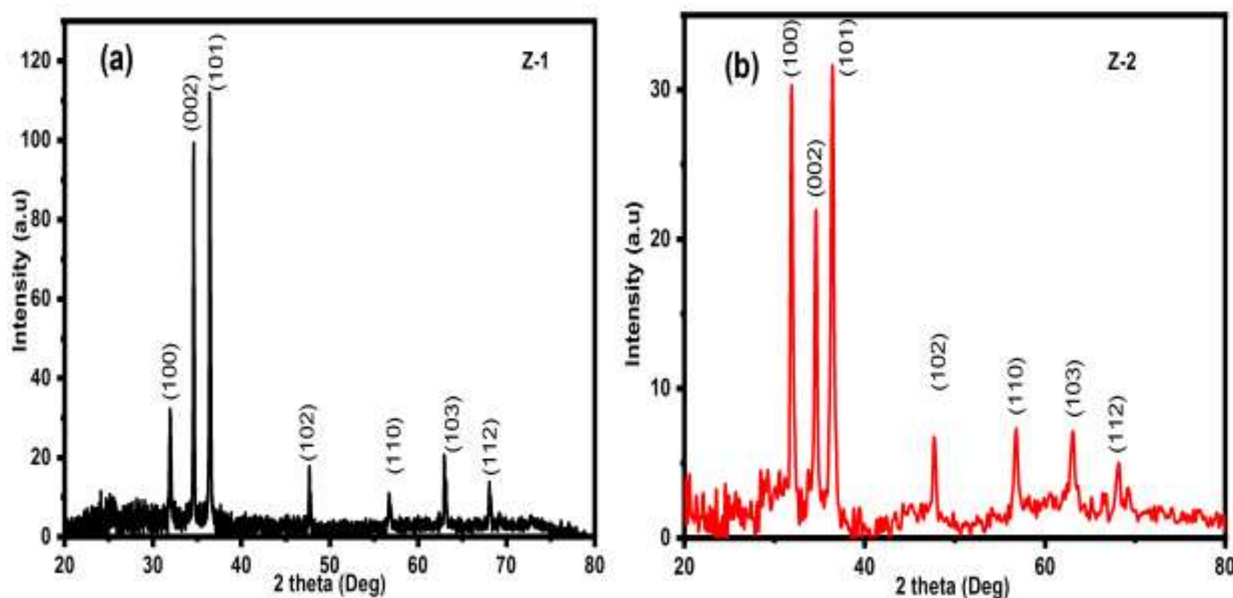

Figure.6.4. XRD pattern of ZnO samples prepared by (a) hydrothermal and (b) Sol–gel techniques

The Raman spectrum of Z1 and Z2 film annealed at a temperature of 400 °C is shown in Figure.6.5. The characteristic mode of ZnO wurtzite phase at around 433 cm^{-1} and 437 cm^{-1} are observed for both films. Other than the characteristic mode of ZnO, few second order modes are also observed in Z2. The modes at 227 and 274 cm^{-1} are related to B_1 (high) and B_2 (low) phonon mode frequencies. The A_1 (LO) mode at 574 cm^{-1} originates from defects such as oxygen vacancies and Zn interstitials which is absent in Z2 samples. [260]. The weak peak at 334 cm^{-1} was attributed to second order Raman processes [261].The additional vibrational mode present at 675 and 757 cm^{-1} can be attributed to defects such as zinc interstitials, anti-site oxygen etc for Z2 sample.

6.3.2. Morphological Properties

Figure.6.6 (a-b) shows the surface morphology of ZnO semiconductors obtained using different techniques. It can be seen from the micrographs of the films that, the films covered the surface homogenously and the smooth surfaces was observed without any cracks. The microfiber

structured grains was observed for Z2 films. The low magnification images of Z1 indicated that the products obtained are quasi-aligned hexagonal-shaped nanorods grown in high density on the whole substrate surface. The well faceted side surfaces and perfect hexagonal end planes of the ZnO nanorods are shown in the inset of Figure.6.6 (a). Due to the well defined side surface, hexagonal end planes, and straight shape throughout their lengths, the obtained nanorods exhibit a good crystal quality.

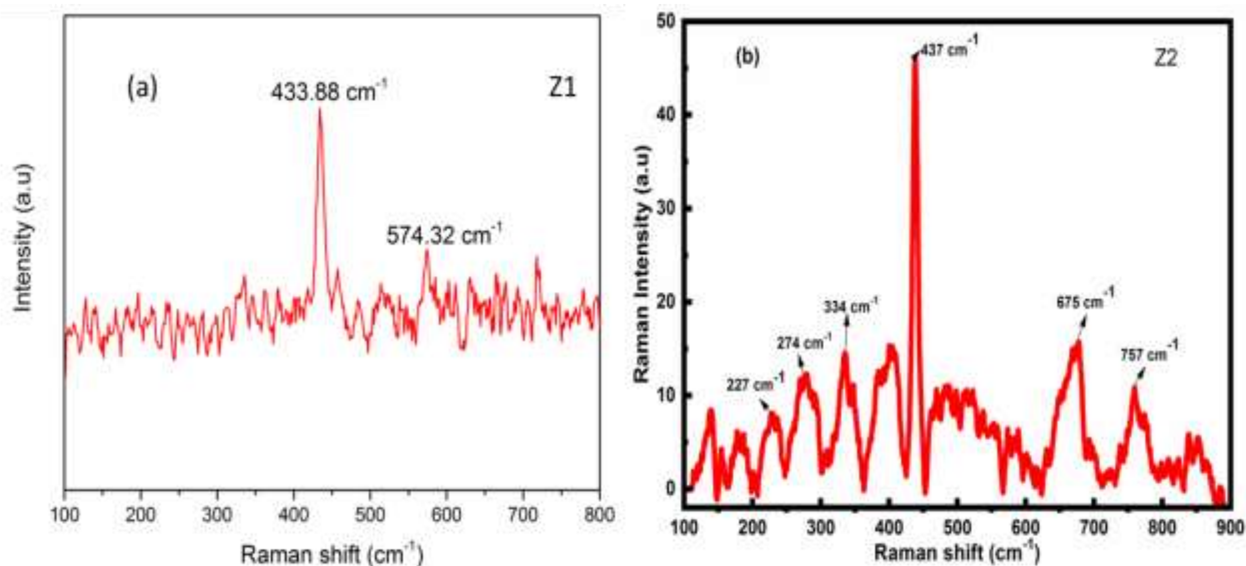

Figure.**6.5**. Raman spectra of (a) Z1 (b) Z2 thin films

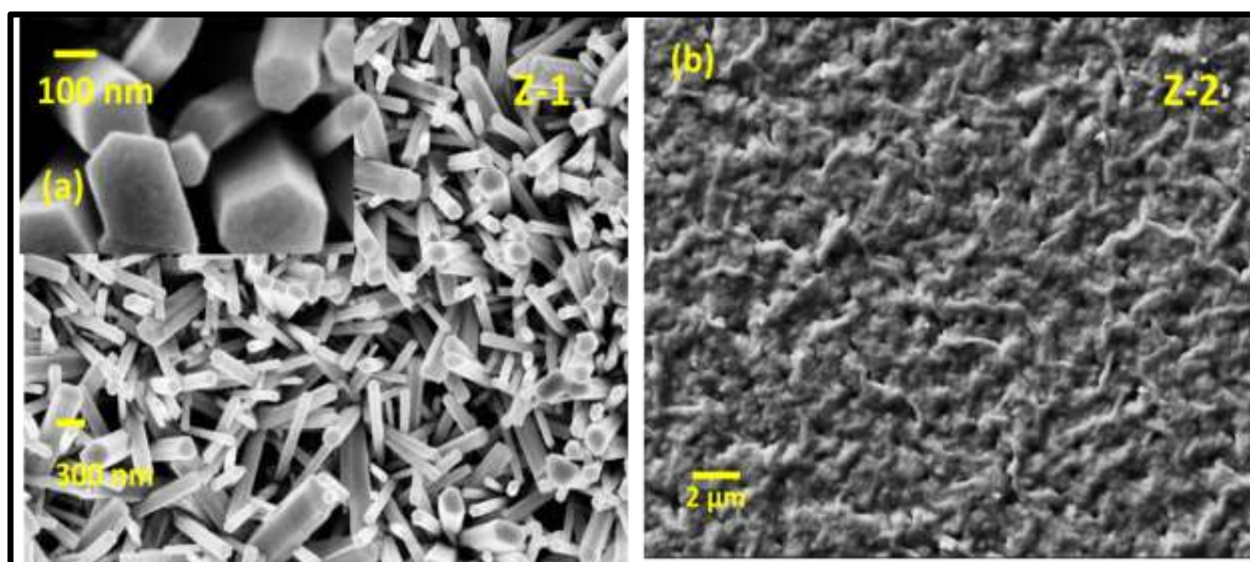

Figure.**6.6**. SEM micrographs (a) Z1 nanorod (inset shows the enlarged view of hexagonal shaped nanorod) and (b) Z2 thin films

6.3.3. Compositional Analysis

Figure.6.7 (a & b) shows the typical EDS spectrum of the ZnO nanorods and film, which reveals that the synthesized products are composed only of zinc and oxygen.Figure.6.8 (a) & (b) shows the XPS survey spectra of Z1 and Z2 samples and it confirms the purity of prepared samples. The presence of oxygen is confirmed by main peak which located at 529 eV, is ascribed to O^{2-} ion in the ZnO lattice.

The asymmetric O 1s peak in the surface was deconvoluted with resolved peaks at 529.6, 530.4 and 531.7 eV respectively for the sample as shown in Figure 6.9 (a). The peak at 529.6 eV (region I) is attributed to the O^{2-} ions on the wurtzite structure of the hexagonal Zn^{2+} ion lattice. Therefore; the lower energy peak of oxygen spectrum is attributed to Zn-O bonds. The component of binding energy centered at 530.4 eV (region-II) is associated with the O^{2-} ions that are in oxygen deficient regions within the ZnO lattice. The higher binding energy region III (531.7 eV) is usually attributed to chemisorbed or dissociated oxygen or hydroxyl (OH^-) species on the surface of the ZnO thin film [262]. As a result, changes in the intensity of this component may be in connection with the variation in the concentration of the oxygen vacancies. As seen in Figure.6.9 (b), the obtained binding energies at 1021 eV and 1044 eV corresponds to Zn $2p_{3/2}$ and Zn $2p_{1/2}$ peaks respectively, confirm the presensce of Zn in the samples.

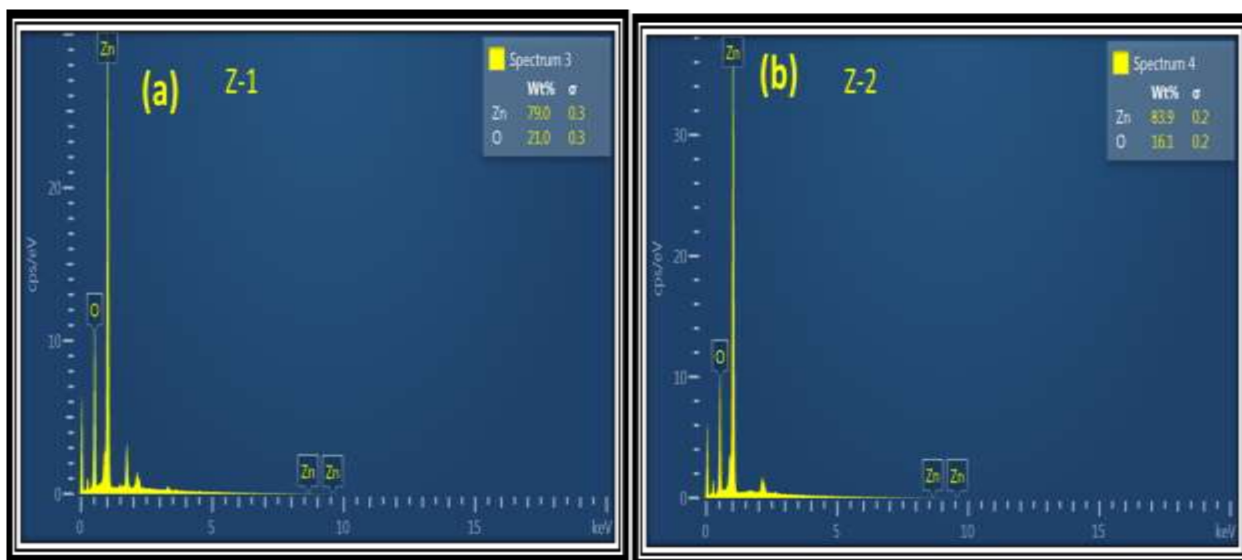

Figure.6.7. EDS spectra of (a) Z1 nanorod and (b) Z2 thin films , inset shows the composition of Zn and O present in the samples.

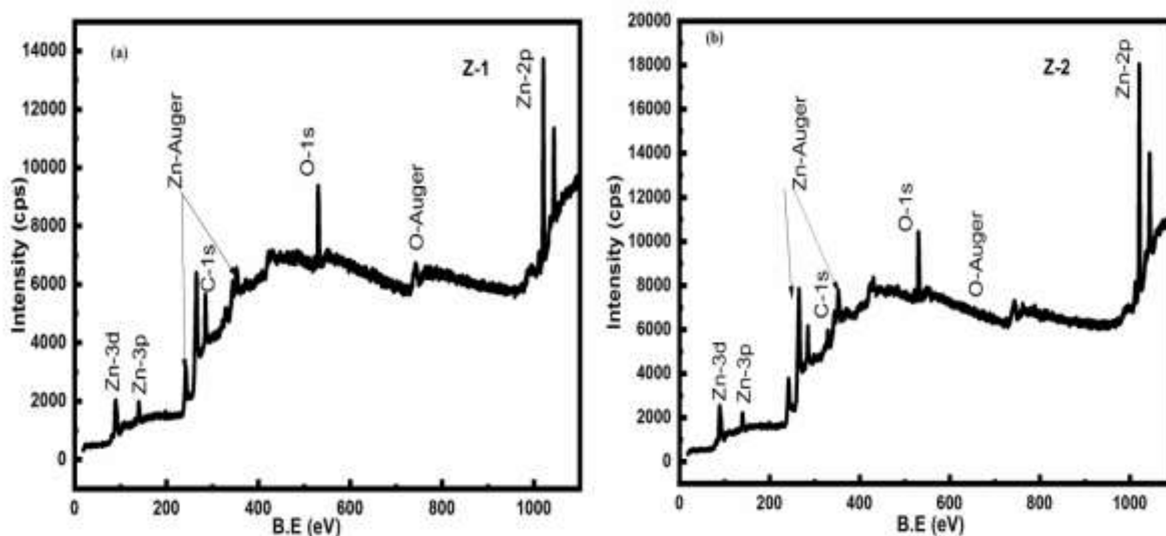

Figure.**6.8** The XPS survey spectra of (a) Z1 and (b) Z2 samples

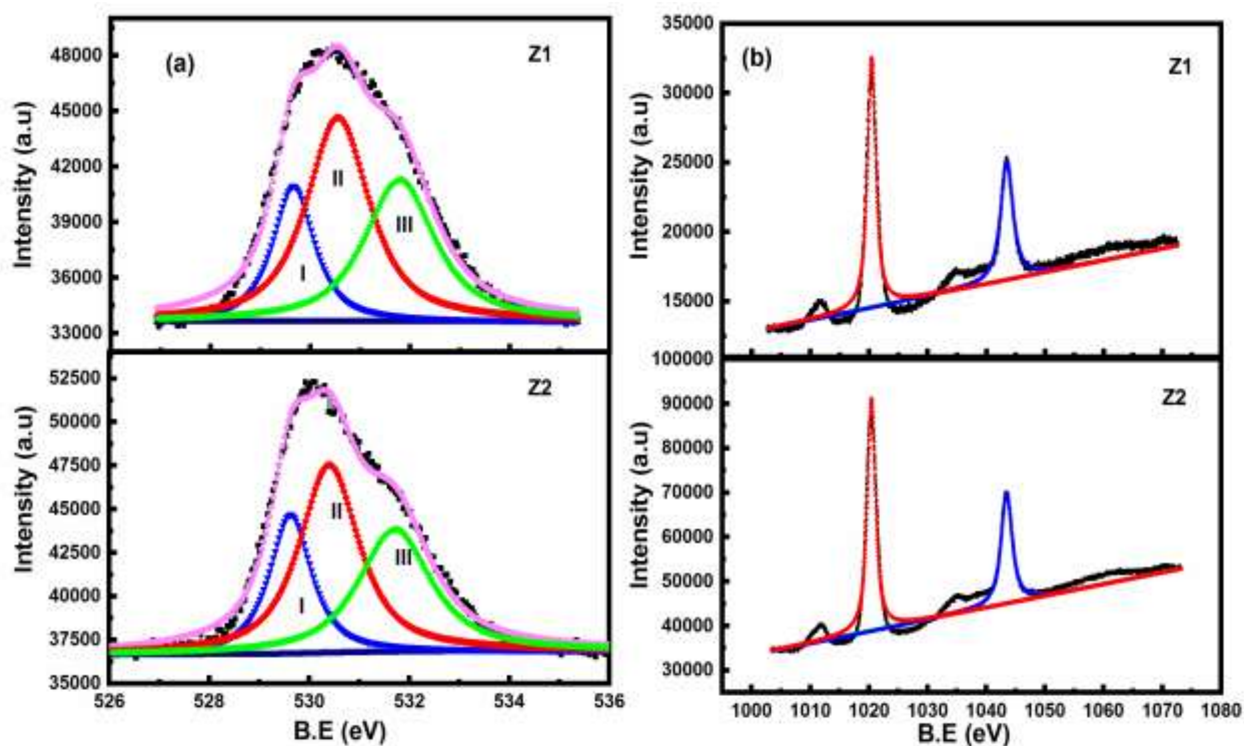

Figure.**6.9** XPS images of (a) Deconvoluted O1s spectra and (b) Zn2p spectra of Z1 and Z2 thin films.

6.3.4. Photoluminescence Properties

Figure 6.10 (a) and (b) shows the PL spectra of formed ZnO thin film and nanorod by sol gel and hydrothermal technique upon 325 nm excitation. The PL spectra of samples show UV

emission peak (388-391 nm), violet emission (412 - 414 nm), blue emission (444 - 491 nm) and green emission (521 nm) respectively. The UV emission was due to near band edge emission of wide band gap of ZnO due to annihilation of excitation. The violet and blue band emission was due to the surface defects in ZnO such as Zinc vacancies and zinc interstitials and green emission was due to the intrinsic defects due to oxygen vacancies and oxygen interstitials [263].

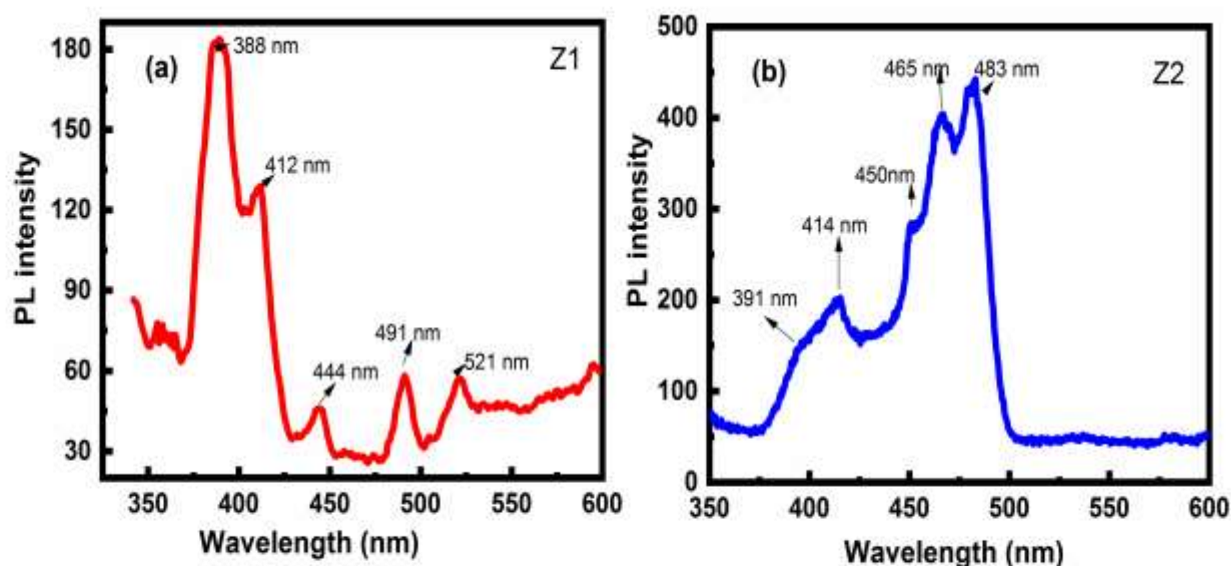

Figure.6.10 Room temperature PL spectra of (a) Z1 and (b) Z2 samples excited at a wavelength of 325 nm.

6.3.5. Gas sensing Measurements

The gas sensing properties of ZnO samples were studied at various temperatures ranging from RT-300 ^{0}C as a function of NO_2 concentration up to 10 ppm. It is well known that sensitivity of a semiconductor metal oxide gas sensor is highly influenced by its operating temperature, gas diffusion activities along with effective surface area. Therefore, to determine the optimum working temperature of the sensor performed gas sensing of all ZnO samples for different operating temperature at a different gas concentration. Figures.6.11 (a-f)) and Figure 6.12 (a-f), correspond to sensitivity plots of ZnO (Z1 and Z2) samples on exposure of NO_2 gas at different temperature & different concentrations. The both samples showed high sensitivity and response kinetics at 200 °C.

Figures 6.11 (a) and 6.12 (a) shows response of Z1 and Z2 sample towards different concentration at 200°C. It is seen that the sensitivity of the sensor increased linearly with increase in NO_2 concentration (Figure.6.11 (d) & 6.12 (d)). Figure.6.11 (d) shows the variation

of gas sensitivity against operating temperature at constant gas concentration (10 ppm). The gas sensitivity of the samples first increases and then decreases with increasing the operating temperature from 100^oC to 300^oC. An increase in temperature, improves the amount of chemisorbed NO_2 and the progress of the adsorption and surface tension to overcome the activation energy barrier; consequently it increase the gas sensitivity [264]. Beyond 200^oC gas sensitivity is reduced, it may due to the harmonization effect (the decrease in the amount of NO_2 that was adsorbed on the ZnO surface) and conversion of NO_2 to NO gas [265].

Gas sensing mechanism

ZnO is an n type semiconductor because the amount of free electron is higher than that of trapped electron. In air, molecular oxygen abstract electron from the conduction band of ZnO and become chemisorbed on the surface and also on the grain boundaries in the form of O_2^-, O^- or O^{2-} species depending on the temperature [266-267]

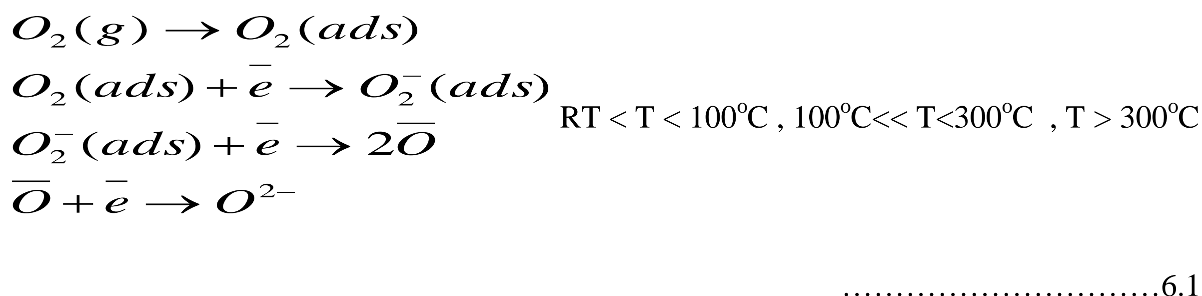

$$O_2(g) \rightarrow O_2(ads)$$
$$O_2(ads) + \bar{e} \rightarrow O_2^-(ads)$$
$$O_2^-(ads) + \bar{e} \rightarrow 2\bar{O}$$
$$\bar{O} + \bar{e} \rightarrow O^{2-}$$

$RT < T < 100^oC$, $100^oC << T < 300^oC$, $T > 300^oC$

…………………………6.1

As a result of capturing of electron on the surface of Zn, a depletion layer will be formed, which has a higher resistance than bulk of ZnO due to decrease of electron. When the ZnO sensor is exposed to NO_2 gas, the electrophile NO_2 molecule can either directly abstract electron from the conduction band of ZnO, or react with the absorbed oxygen ions, resulting in a decrease of the electron concentration and increase of depletion layer width, which eventually increases the sensor resistance. During the recovery period the adsorbed NO_2 species are desorbed, and the resistance comes back its initial value. The interactions are shown in equations 6.1 and 6.2 respectively [266-267].

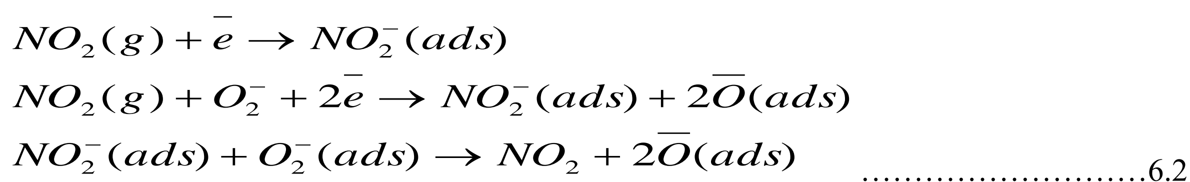

$$NO_2(g) + \bar{e} \rightarrow NO_2^-(ads)$$
$$NO_2(g) + O_2^- + 2\bar{e} \rightarrow NO_2^-(ads) + 2\bar{O}(ads)$$
$$NO_2^-(ads) + O_2^-(ads) \rightarrow NO_2 + 2\bar{O}(ads)$$

………………………6.2

The gas sensing mechanism of the semiconductors metal oxides gas sensor was based on the variation of electrical resistance resulting from gas adsorption and desorption from the active surface area. The oxidizing nature of the NO_2 gas is responsible for the transfer of electrons from ZnO to the NO_2 gas molecules. Hence NO_2 adsorption increases the resistance of ZnO material which is shown in Figure.6.11 (a). More over the gas sensitivity enhances with an increase in the target gas concentration was depicted in Figure.6.11 (b). The gas sensitivity values observed are higher than reported values. The response time decreases with an increase in the gas concentration, which was attributed to large amount of gas species available at 10 ppm to react with ZnO nanostructures. The recovery time increases with an increase in the gas concentration, it may due to species in larger quantities. Along with the gas sensitivity, operating temperature response and recovery time, the selectivity or the cross sensing of gas sensor to a particular gas is also very important aspect of a gas sensor for its commercial applications. Therefore, the selectivity of ZnO for 10 ppm LPG, ethanol, SO_2, H_2S and CO was also studied at an operating temperature of 200^oC as shown in Figure.6.11 (f) and 6.12 (f). Therefore the ZnO based sensor has good selectivity and high sensitivity for NO_2 gas at 200^oC. Thus ZnO nanostructures are very promising due to their large surface area, which make them ideal candidate for gas sensing material. Another important parameter in metal oxide sensors is the repeatability which is shown in Figure.6.11 (e). It is observed that both sample shows nearly same response upon the exposure 10 ppm NO_2, ie both shows highest repeatability which is one of the characteristics of a good gas sensor.

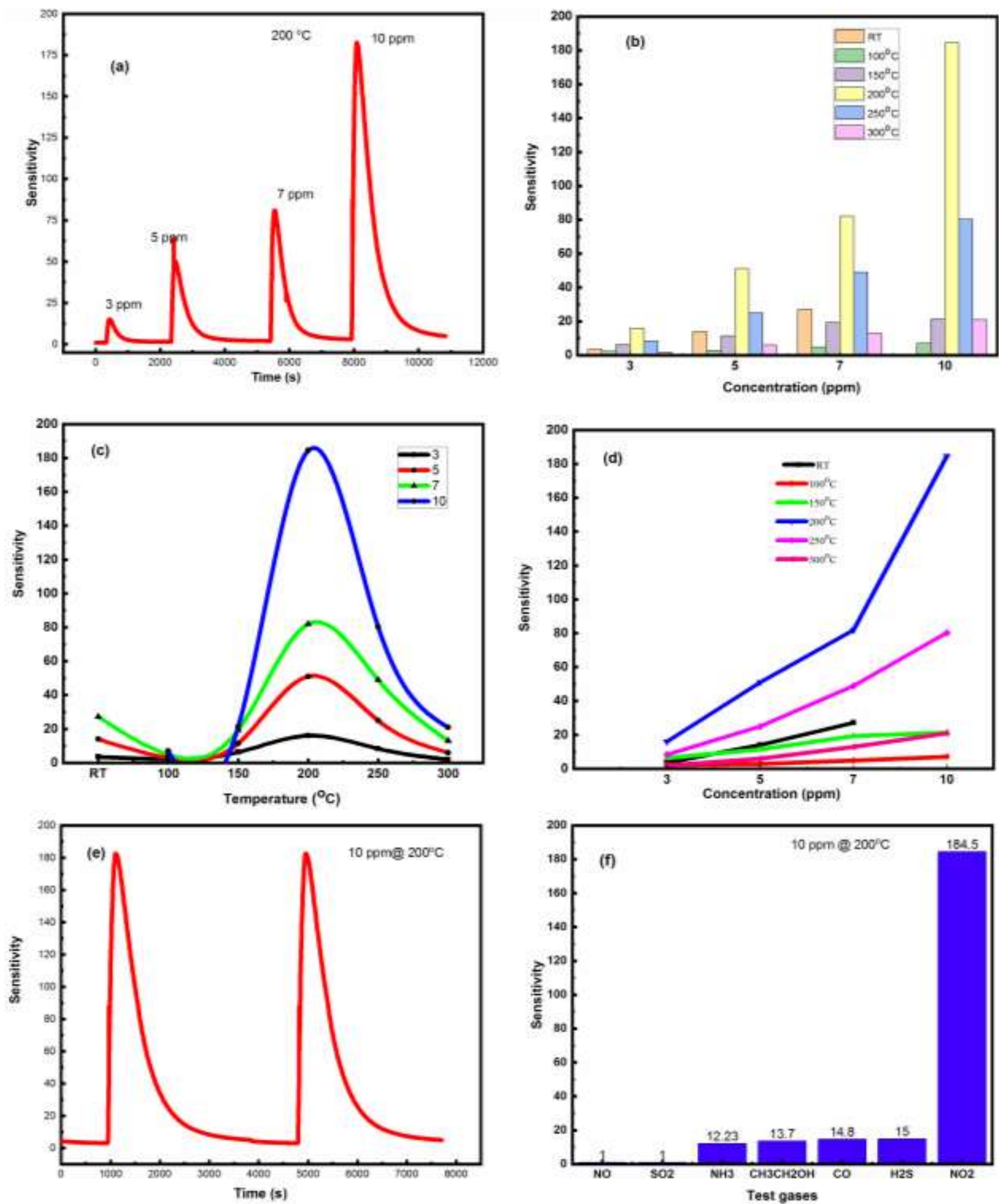

Figures.**6.11** (a-f)) correspond to sensitivity plots of Z1 samples on exposure of NO_2 gas at different temperature & different concentrations

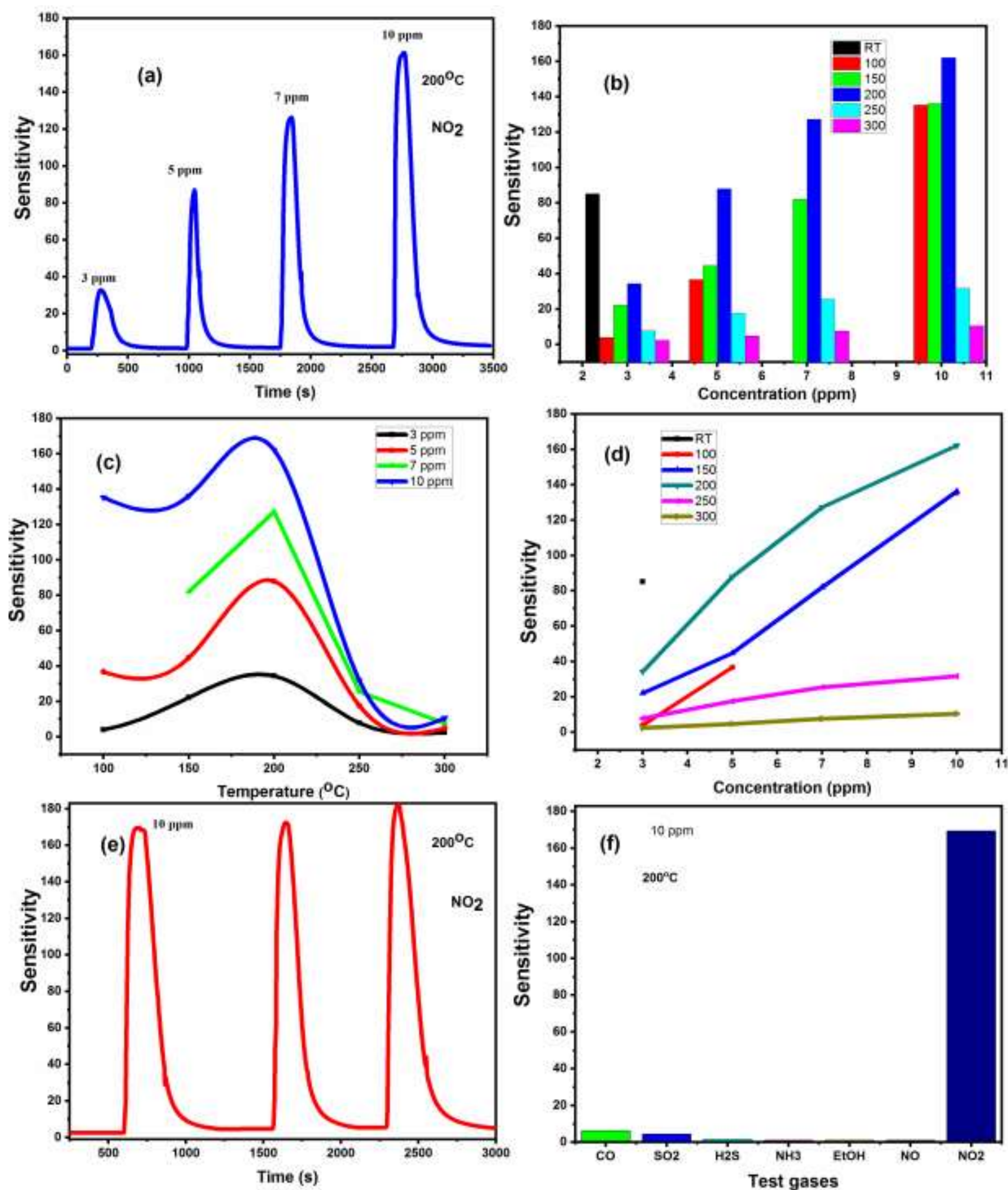

Figures.**6.12** (a-f)) correspond to sensitivity plots of Z2 samples on exposure of NO_2 gas at different temperature & different concentrations

6.4. Conclusion

In conclusion, ZnO nanostructures were synthesized using cost effective methods like sol-gel and hydrothermal methods. XRD pattern showed that all the films shows different peaks with hexagonal wurtzite structure. FESEM showed that they are homogeneous, uniformly distributed over the surface. Gas sensing studies revealed that the sensor response was strongly affected by the operating temperature and concentration. The sensors showed high selectivity to NO_2 with fast response and recovery characteristics. Oxygen vacancies in the lattice were also seen to help in improvement of sensor response. The results demonstrate that these films prepared by low cost method, can be utilized for fabrication of NO_2 gas sensors in the 0–10 ppm range with very high selectivity, sensitivity and repeatability.

CHAPTER 7

Summary and future work

The research work embodied in this thesis was undertaken primarily to explore the possibility of using a powder target in RF magnetron sputtering to prepare ZnO and doped ZnO thin films and their characterization. By proper optimization of deposition parameters such as RF power, Gas ratio, Pressure, temperature etc, it was possible to get reproducible, good quality and strongly adherent ZnO films. Taking into account the optimized parameters of film deposition and with proper selection of dopants, doped ZnO thin films were successfully deposited using various dopants with different concentration. The roles of different dopant towards luminescent properties and also on other physical properties have been investigated deeply. Pristine, single (Li, Sb, P, In, Ga) and codoped ZnO thin films are deposited by RF magnetron sputtering. Sputtering targets were prepared in-house using powders of ZnO and other oxides like Sb_2O_3, P_2O_5, Ga_2O_3, etc for doped ZnO films. All the thin films exhibited typical wurtzite structure with a strong (002) preferred orientation. EDS and XPS analysis confirmed the presence of the oxidized dopants in each film. The excellent optical properties reveal a great promise for the proposed thin films for visible light emission applications.

Both undoped and Lithium doped ZnO films have a single phase wurtzite structure with strong orientation along c-axis, as confirmed by XRD and Raman studies. A blue shift observed in the band gap energy of LZO might be due to the incorporation of Li into the ZnO lattice. Photoluminescence spectra exhibited multiple defect emissions in the visible region in addition to NBE in LZO, indicating that Li doped ZnO films might be useful for white light-emitting devices in optoelectronic applications.

Sb and P doped ZnO thin films have been deposited using RF sputtering technique. XRD analysis reveals that doped ZnO thin films exhibit hexagonal wurtzite structure with preferred orientation. PL results have shown and confirmed that for SZO samples exhibit UV emission peak accompanied by a peaks in the blue region. Thus these films are useful for luminescent thin film applications, particularly where blue emission is required. XRD patterns showed that all the films were preferentially oriented along the c-axis with a strong Bragg reflection corresponding to (002) orientation. PL and XPS analysis confirmed the signatures of oxygen interstitials and vacancies defects in SZO and PZO films. All the films exhibited >90% optical transmittance in

the visible range. These studies provide a pathway for tuning the material properties of ZnO based devices to achieve the desired performance

All the IZO films were highly crystalline with standard hexagonal wurtzite structure and exhibited a preferred orientation along the c-axis. The intensity of (002) peak tended to decrease with the indium content. The XRD spectra revealed that In atoms substituted Zn in the hexagonal lattice. PL emission across the visible light region of IZO films was attributed to a range of structural defects, such as oxygen vacancies, oxygen interstitials, zinc interstitials and zinc vacancies formed during indium doping. PL results suggested that by controlling the doping amount it was possible to achieve white light emission. The average transmittance of IZO films in the visible region was above 90% and the band gap decreased with doping content. Homojunction devices fabricated with IZO/SZO bilayers showed rectifying type I-V characteristics with knee voltage of 1.87 V, 3.16 V and 3.54 V for 1%, 5% and 10% IZO/SZO respectively.

The transmittance of ZnO and GZO films was higher than 90% in the visible region, and the optical band gap of film became wider with increasing Ga content, because of the Burstein-Moss effect. The photoluminescence showed that the doping with ZnO altered the band emission due to zinc vacancies, oxygen vacancies and surface defects. In addition to increasing oxygen vacancies in neutral (V_o) and ionized (V_o^+) states, a number of other effects are generates, which include Zn interstitials (Zn_i), neutral ionized Zn vacancy(V_{zn}) and oxygen antisite (O_{zn}) as the dynamic acceptor defects which act as the defect origins of different visible PL components classified in the UV- violet, violet- blue and green-yellow regions. UV luminescence and visible emission of the GZO films are extremely useful for many optoelectronic devices along with TCO layers.

Pristine, single (In, Ga) and codoped ZnO thin films were deposited on glass substrates by RF magnetron sputtering. All the thin films exhibited typical wurtzite structure with a strong (0 0 2) preferred orientation. XPS analysis and Raman line shifts confirmed the presence of the oxidized dopants in each film. The peak attributed to the oxygen vacancy defect in Raman spectra is consistent with that observed from PL spectra and XPS. Among doped films, IGZO film showed better morphology, crystallinity and PL emission. All the films had very high optical transmittance of the order of 95% in the visible range. The excellent optical properties

reveal a great promise for the proposed thin films with applications in various optoelectronic devices.

Second part of the thesis is focused on the gas sensing properties of prepared nanostructures. Gas sensing studies revealed that the sensor response was strongly affected by the operating temperature and concentration of indium. Among the all fabricated IZO gas sensors, 10 wt% shows the highest sensitivity for H_2S at an operating temperature of 250°C. The 10 wt% sensor showed high selectivity to H_2S with fast response and recovery characteristics and this doping level considered to be optimum for sensing H_2S. The above results suggest that IZO has the potential for use in practical applications such as white light source, LED devices and H_2S gas sensors.

ZnO nanostructures were synthesized using cost effective methods like sol-gel and hydrothermal methods. XRD pattern showed that all the films shows different peaks with hexagonal wurtzite structure. FESEM showed that they are homogeneous, uniformly distributed over the surface. Gas sensing studies revealed that the sensor response was strongly affected by the operating temperature and concentration. The sensors showed high selectivity to NO_2 with fast response and recovery characteristics. Oxygen vacancies in the lattice were also seen to help in improvement of sensor response. The results demonstrate that these films prepared by low cost method, can be utilized for fabrication of NO_2 gas sensors in the 0–10 ppm range with very high selectivity

In future there are possibilities for the use of other dopants such as Mg, Co, Fe, etc. to study optical, electrical and magnetic properties of ZnO nanostructures and to fabricate homojunction/heterojunction using the dopants and other metal oxides. Similarly there are possibilities to study gas sensing and gas selectivity of doped ZnO films and other future aspects are given in the Figure.

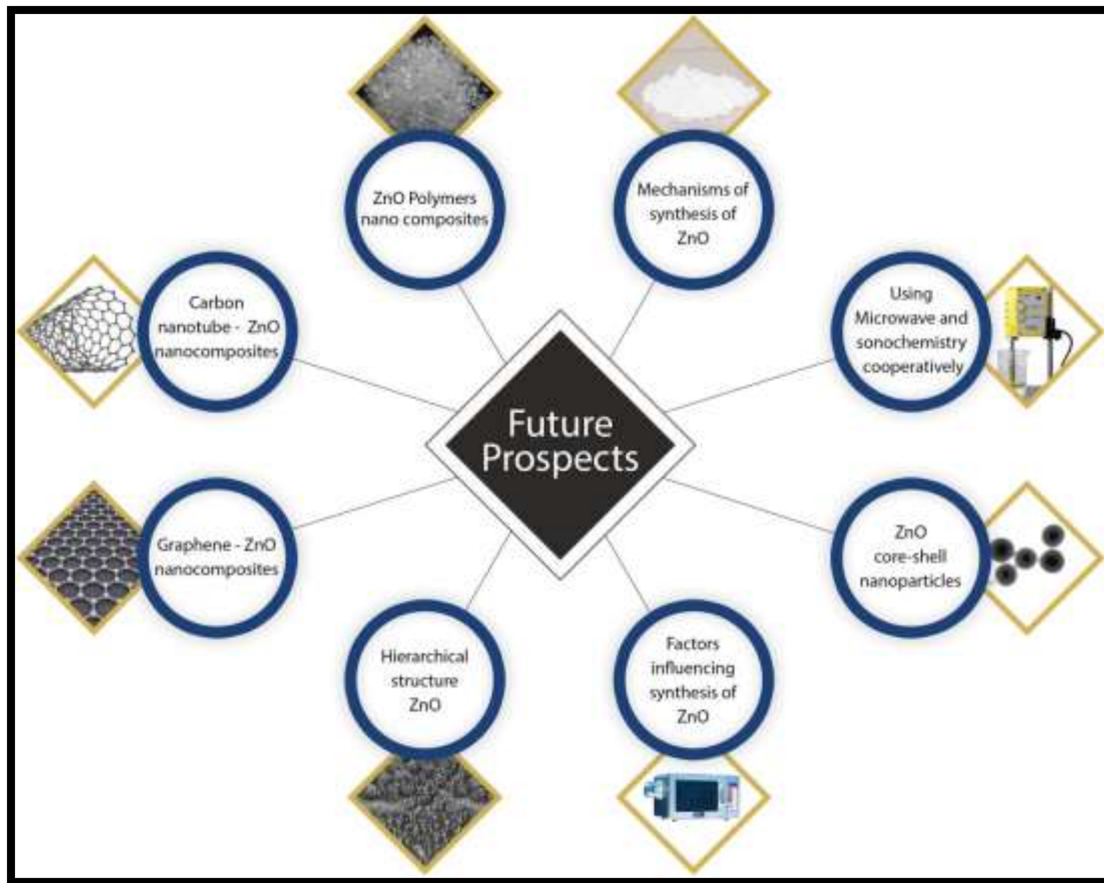

Conceptual diagram related to the possible areas for development and expansion of future research in the field semiconducting oxide.

References

1. Lawrence sylaja vikas and Madabi. K. Jayaraj , C-axis oriented growth of ZnO nanorods over Mg:GaN for improved heterojunction device performance, Aip Advances 9 (2019) 105318
2. Look.D.C.., Recent advances in ZnO materials and devices., Mater.Sci.and Eng B 80 (2001) 383-387
3. Hanada T, Yao T and Hong S.K. Basic properties of ZnO, GaN and Related materials In: Oxide and nitride semiconductors. Advances in Material Research, 12. Springer
4. Brown M E (ed) ZnO—Rediscovered (New York: The New Jersey Zinc Company) 1957
5. E. J. Boyd and S. A. Brown, "Nanotechnology" 20 (2009) 425201
6. H. Morkoç and Ü. Özgür, Zinc oxide: fundamentals, materials and device technology: John Wiley & Sons, 2008
7. Yangyang zhang, Manoj K. Ram, Elias K.stefanakos, and D.Yogigoswami., Synthesis, Characterisation and applications of ZnO nanowires, J.nanomaterials (2012) 624520.
8. Webofscience Available:http://apps.webofknowledge.com/WOS_GeneralSearch_input.do?product=WOS&search _mode=GeneralSearch&SID=2FFBfx8uRFUOCI3JHNx&preferencesSaved=
9. S.J. Pearton, D.P. Norton, K. Ip, Y.W. Heo, T. Steiner, Recent progress in processing and properties of ZnO, Progress in Materials Science 50 (2005) 293-340
10. Z. Fan and J. G. Lu, Zinc Oxide Nanostructures: Synthesis and properties, J. Nanosci Nanotechnol. 5 (2005) 1561-73.
11. S. Singh, P Thiyagarajan, K. Mohan Kant, D. Anita, S. Thirupathiah, N Rama, Brajesh Tiwari, M. Kottaisamy and M. S. R. Rao, Structure, microstructure and physical properties of ZnO based materials in various forms: bulk, thin film and nano, J. Phys. D: Appl. Phys. 40 (2007) 6312-6327
12. J. Cui, Zinc oxide nanowires, Materials Characterization 64 (2012) 43-52.
13. C. Klingshirn, ZnO: From basics towards applications, Phys. Stat. Sol. 244 (2007) 3027-3073
14. Z. L. Wang, Zinc oxide nanostructures: growth, properties and applications, J. Phys.:Condens. Matter 16 (2004) R829-R858.
15. E. P. Etape, J. F. Tendo, L. J. Ngolui, B. V. Namondo, F. C. Yollande, and M. Borel N. Nguimezong., Structural Characterization and Magnetic Properties of Undoped and Ti-

Doped ZnO Nanoparticles Prepared by Modified Oxalate Route, J.Nanomaterials (2018) Article ID 9072325

16. X. G. Zhao and Z. Tang., Magnetic properties of ZnO nanoclusters, J. Applied Phys 111 (2012) 084321 https://doi.org/10.1063/1.4707946
17. Omri J. E Ghoul O. M. Lemine M. Bououdin, B. ZhangdL. E Mir Magneti., Magnetic and optical properties of manganese doped ZnO nanoparticles synthesized by sol–gel technique, Superlattices and Microstructures 60 (2013) 139-147.
18. J. S. Tawale, K. K. Dey, R. Pasricha, K. N. Sood and A. K. Srivastava, Synthesis and characterization of ZnO tetrapods for optical and antibacterial applications, Thin Solid Films 519 (2010) 1244-1247
19. Amiruddin. R and Kumar MCS., Enhanced visible emission from vertically aligned ZnO nanostructures by aqueous chemical growth process. J. Lumin (2014) 155: 149-155
20. Aleksandra B. Djurišić, Xinyi Chen, Yu Hang Leung and Alan Man Ching Ng , ZnO nanostructures: growth, properties and applications J. Mater. Chem. 22 (2012) 6526-6535
21. Michał A. Borysiewicz., ZnO as a Functional Material, a Review Crystals 9 (2019) 505; doi:10.3390/cryst9100505
22. H. Morkoc and U. Ozgur, General properties of ZnO, Zinc Oxide: Fundamentals, materials and device technology, Wiley-Vch Verlag (2009) p.1-2.
23. Xiao Wei Sun and Yi yang, ZnO nanostructures and their applications, (2012) CRC press.
24. Ü. Özgür, Y. I. Alivov, C. Liu, A. Teke, M. A. Reshchikov, S. Dogan, V. Avrutin, S. J. Cho, and H. Morkoc., A comprehensive review of ZnO materials and devices, J. Appl. Phys., vol. 98 (2005)
25. Z. C. Feng, Handbook of Zinc Oxide and Related Materials, Materials. 1 (2012)
26. K. Ellmer, A. Klein, and B. Rech, Transparent Conductive Zinc Oxide: Basics and Applications in Thin Film Solar Cells, 460 (2007)
27. A. Pimentel, J. Rodrigues, P. Duarte, D. Nunes, F. M. Costa, T. Monteiro, R. Martins, and E. Fortunato. Effect of solvents on ZnO nanostructures synthesized by solvothermal method assisted by microwave radiation: a Photocatalytic study. J. Mater. Sci. (2015) 50(17).
28. Kumar. R., Kumar.G, and Umar. A. Zinc oxide nanomaterials for photocatalytic degradation of mmethyl orange: a review. Nanoscience and Nanotechnology Letters, 6(8) (2014) 631-650

29. A. Kobayashi, O. F. Sankey, S. M. Volz, and J. D. Dow, Semiempirical tight-binding band structures of wurtzite semiconductors: AlN, CdS, CdSe, ZnS, and ZnO, Phys. Rev. B, 28 (1983) 935–945
30. Naji Al Dahoud, Comparative study of highly dense aluminium- and gallium-doped zinc oxide transparent conducting sol–gel thin films, Bull. Mater. Sci., 37 (2014) 1243–1248.
31. S. Horzum, F. Iyikanat, R. T. Senger, C. Çelebi, M. Sbeta, A. Yildiz and T. Serin., Monitoring the characteristic properties of Ga-doped ZnO by Raman spectroscopy and atomic scale calculations., J. Molecular Structure 1180 (2019) 505-511
32. L. C. Kuang Liau and J. S. Huang, Effect of indium- and gallium-doped ZnO fabricated through sol-gel processing on energy level variations, Materials Research Bulletin 97 (2018) 6–12.
33. Yang Liua, and Siming Zhub., Preparation and characterization of Mg, Al and Ga co-doped ZnO transparent conductive films deposited by magnetron sputtering, Results in Physics 14 (2019) 102514
34. A. Samavati, Z. Samavati, A. F. Ismail, M. H. D. Othman, M. A. Rahman, A. K. Zulhairuna and I. S. Amiri, Structural, optical and electrical evolution of Al and Ga co-doped ZnO/SiO_2/glass thin film: role of laser power density, RSC Adv. 7 (2017) 35858–35868
35. Chen-Hui Zhai, Rong-Jun Zhang, Xin Chen, Yu-Xiang Zheng, Song-You Wang, Juan Liu, Ning Dai and Liang-Yao Chen., Effects of Al Doping on the Properties of ZnO Thin Films Deposited by Atomic Layer Deposition, Nanoscale Research Letters (2016) 11:407
36. M. U. Shahid, K. M. Deen, A. Ahmad, M. A. Akram, M. Aslam, W. Akhtar, Formation of Al-doped ZnO thin films on glass by sol–gel process and characterization, Appl Nanosci (2016) 6:235–241
37. M. K. Hamza Taha, O. Boisron, B. Canut, P. Melinon, J. Penuelas, M. Gendry and B. Masenelli., Control of the compensating defects in Al-doped and Ga-doped ZnO nanocrystals for MIR plasmonics, RSC Adv (2017) 7 28677
38. S. Edinger, N. Bansal, M. Bauch, R. A. Wibowo, G. U´ jva´ ri, R. Hamid, G. Trimmel, and T. Dimopoulos., Highly transparent and conductive indium-doped zinc oxide films deposited at low substrate temperature by spray pyrolysis from water-based solutions, J. Mater. Sci (2017) 52:8591–8602

39. W. Zhu, S. Kitamura, M. Boffelli, E. Marin, E. Della Gaspera, M. Sturaro, A. Martucci and G. Pezzotti., Analysis of defect luminescence in Ga-doped ZnO nanoparticles, Phys. Chem. Chem. Phys. (2016) 10.1039/c6cp00746e
40. S. H. Lee, J. S. Lee, W. BaeKo, J. I. Sohn, S. N. Cha, J. M. Kim, Y. J. Park, J. P. Hong, Photoluminescence Analysis of Energy Level on Li-Doped ZnO Nanowires Grown by a Hydrothermal Method, Appl. Phys. Express 5 (2012) 095002
41. L. M. Mahajan, C. K. Kasar and D.S. Patil., Investigation of optical and electrical properties of lithium doped ZnO nano films, Mater. Res. Express 6 (2019) 045053 https://doi.org/10.1088/2053-1591/aafd65.
42. J. S. Lee , S. N. Cha, J. M. Kim, H. W. Nam, S. H. Lee, W. B. Ko, K. L. Wang, J. G. Park, and J. P. Hong., p-Type Conduction Characteristics of Lithium-Doped ZnO Nanowires, Adv. Mater. (2011) XX, 1–5 DOI: 10.1002/adma.201101376.
43. A. Saaedi, R. Yousefi, F. Jamali-Sheini, M. Cheraghizade, A. K. Zak and N. M. Huang, Optical properties of Group-I- doped ZnO nanowires, Ceramic Intern. 40 (2014) 4327- 4332
44. LuYue, Zhiqiang Zhang, YanyanMa, and Wenhui Zhang., Effect of Na Doping on the Nanostructures and Electrical Properties of ZnO Nanorod Arrays, J. Nanomaterials (2016) Article ID 3040536, 5 http://dx.doi.org/10.1155/2016/3040536.
45. Linhua Xua, Fang Gua, Jing Sua, Yulin Chena, Xiangyin Li and Xiaoxiong Wang., The evolution behavior of structures and photoluminescence of K-doped ZnO thin films under different annealing temperatures, J. Alloys and Compds 509 (2011) 2942–2947.
46. Min-Suk Oh and R. Navamathava., Hydrogen incorporation effect in phosphorus doped p-type ZnO thin films grown by radiofrequency magnetron sputtering, RSC Adv., 7 (2017) 16119.
47. K. Zhang, M. R. Hao, W. Guo, T. Heeg, D.G. Schlom, W.Z. Shen and X.Q. Pan., Low temperature electron transport in phosphorus-doped ZnO films grown on Si substrates Physica B 407 (2012) 2825–2828.
48. J. W. Kang, Y. S. Choi, M. Choe, N. Y. Kim, T. Lee, B. J. Kim, C. W. Tu and S. J. Park., Electrical and structural properties of antimony-doped p-type ZnO nanorods with self-corrugated surfaces, Nanotechnology 23 (2012) 495712.

49. S. K. Pandey, S. K. Pandey, V. Awasthi, A. Kumar, M. Gupta, U. P. Deshpande et al., Influence of in-situ annealing ambient on p-type conduction in dual ion beam sputtered Sb-doped ZnO thin films., Appl. Phys. Lett. 103 (2013) 072109 doi: 10.1063/1.4818819
50. T. Tohsophon, N. Wattanasupinyo, B. Silskulsuk, N. Sirikulrat Effect of aluminum and indium co-doping on zinc oxide films prepared by dc magnetron sputtering, Thin Solid Films 520 (2011) 726–729
51. V. K. Jayaraman, A. M. Álvarez, M. de la luz and O. Amador., Effect of substrate temperature on structural, morphological, optical and electrical properties of IGZO thin films., Physica E 86 (2017) 164–167
52. F. H. Wang and C. L. Chang., Effect of substrate temperature on transparent conducting Al and F co-doped ZnO thin films prepared by rf magnetron sputtering, App. Surf. Sci. 370 (2016) 83–91
53. D. S. Y. Jayathilake, T. A. Nirmal Peiris, Jagdeep S. Sagu, Dominic B. Potter, K. G. U. Wijayantha, C. J. Carmalt, and D. J. Southee., Microwave-Assisted Synthesis and Processing of Al-Doped, Ga Doped, and Al, Ga Codoped ZnO for the Pursuit of Optimal Conductivity for Transparent Conducting Film Fabrication, ACS Sustainable Chem. Eng. 5 (2017) 4820−4829 DOI:10.1021/acssuschemeng.7b00263
54. D. Snigurenko, E. Guziewicz, T. A Krajewski, R. Jakiela, Y. Syryanyy, K. Kopalko and W. Paszkowicz., N and Al co-doping as a way to p-type ZnO without post-growth annealing, Mater. Res. Express 3 (2016) 125907
55. Dominic B. Potter, Michael J. Powell, Ivan P. Parkin and Claire J. Carmalt Aluminium/gallium, indium/gallium, and aluminium/indium co-doped ZnO thin films deposited via aerosol assisted CVD., J. Mater. Chem. C 6 (2018) 588
56. C. L. Heng, W. Xiang, W. Y. Su, H. C. Wu, Y. K. Gao, P. G. Yin, and T. G. Finstad, Strong near band edge emission of (Ce, Yb) co-doped ZnO thin films after high temperature annealing, Optical Materials Express 7 (2017) 3042
57. Kittel C Introduction to Solid State Physics 8th edn (2005) (New York: Wiley)
58. Erhart. P, Klein. A. and Albe. K, First-principles study of the structure and stability of oxygen defects in zinc oxide. Physical Review B, 72(8) (2005) 085213
59. McCluskey MD and Jokela S.J, Defects in ZnO. J Appl Phys 106 (2009) 071101 1-13.

60. A. Janotti and C. G. Van De Walle, Native point defects in ZnO, Phys. Rev. B - Condens. Matter Mater. Phys., 76 (2007) 1–22.
61. A. F. Kohan, G. Ceder, D. Morgan Chris and G van de Walle., First principle study of native point defects in ZnO., Physical review B 61 22 (2000) 15019.
62. Van de Walle C G and Neugebauer., First-principles calculations for defects and impurities: Applications to III-nitrides, J. Appl. Phys. 95 (2004) 3851 https://doi.org/10.1063/1.1682673
63. Janotti A and Van de Walle C G., New insights into the role of native point defects in ZnO J. Cryst. Growth 287 (2006) 58 https://doi.org/10.1016/j.jcrysgro.2005.10.043.
64. Tuomisto F, Saarinen K, Look D C and Farlow G C, Introduction and recovery of point defects in electron-irradiated ZnO, Phys. Rev. B 72 (2005) 085206 https://doi.org/10.1103/PhysRevB.72.085206.
65. I. T. Drapak, Visible luminescence of ZnO-Cu_2O heterojunction. Semiconductors 2 (1968) 624-625.
66. J. H. Lim, C. K. Kang, K. K Kim, I. K. Park., Electroluminescence emission from ZnO light emitting diodes grown by high temperature radio frequency sputtering, Adv. Mater., 18 (2006) 2720-2724
67. S. P. Chang and T. H. Chang., Use of the Thermal Chemical Vapor Deposition to Fabricate Light-Emitting Diodes Based on ZnO Nanowire/p-GaN Heterojunction, J. Nanomaterials (2011) 903176
68. W. Z. Xu, Z. Z. Ye,a Y. J. Zeng, L. P. Zhu, B. H. Zhao, L. Jiang, J. G. Lu, and H. P. He., ZnO light-emitting diode grown by plasma-assisted metal organic chemical vapor deposition, Appl. Phys. Lett. 88 (2006) 173506.
69. M. A. Abbasi, Z. H. Ibupoto, M. Hussain, O. Nur and M. Willander., The fabrication of white light-emitting diodes using the n-ZnO/NiO/p-GaN heterojunction with enhanced luminescence, Nanoscale Research Letters (2013) 8:320.
70. S. B Bashar, M. Suja, M. Morshed, F. Gao and J. Liu., An Sb-doped p-type ZnO nanowire based random laser diode, Nanotechnology 27 (2016) 065204.
71. C. Panatarani, S. Fitriyadi, N. Balasubramanian, N. S. Parmar, and I. M. Joni., Preparation and characterizations of electroluminescent p-ZnO:N/n-ZnO:Ga/ ITO thin films by spray pyrolysis method, Aip Advances 6 (2016) 025121.

72. G. C. Park, S. M. Hwang, S. M. Lee, J. H. Choi, K. M. Song, H. Y. Kim, H. S. Kim, S. J. Eum, S. B. Jung, J. H. Lim and J. Joo, Hydrothermally Grown In-doped ZnO Nanrods on P-GaN films for color-tunable Heterojunction Light- emitting- diodes, Sci. Rep, 5 (2015) 10410
73. H. Long, G. Fang, H. Huang, X. Mo, W. Xia, B. Dong, X. Meng and X. Zhao., Ultraviolet electroluminescence from ZnO/NiO-based heterojunction light-emitting diodes, Appl. Phys. Letts 95 (2009) 013509
74. M. Zhong, G. Shan, Y. Li and G. Wang., Synthesis and luminescence properties of Eu^{3+} doped ZnO nanocrystal by a hydrothermal process, Mater. Chem and Physics 106 (2007) 305-309
75. S. D. Baek, P. Biswas, J. W. Kim, Y. C. Kim, T. I. Lee, and J. M. Myoung, Low-Temperature Facile Synthesis of Sb-Doped p-Type ZnO Nanodisks and Its Application in Homojunction Light-Emitting Diode, ACS Appl. Mater. Interfaces 8 (2016) 13018−13026
76. S. D. Baek, Y. Porte, Y. Cheol Kim, and J. M. Myoung., ZnO Homojunction-based Color-Switchable Bidirectional LEDs by Using Hydrothermal Growth Method, J. Mater. Chem. C 5 (2017) 9479-9487
77. Rui Li, Chunyan Yu, Hailiang Dong, Wei Jia, Tianbao Li, Zhuxia Zhang and Bingshe Xu, Effects of $Ga_xZn_{1-x}O$ nanorods on the photoelectric properties of n-ZnO nanorods/p- GaN heterojunction light-emitting diodes., RSC Adv., 7 (2017) 49613
78. N. H. Alvi, Kamran ul Hasan, Omer Nur, Magnus Willander., The origin of the red emission in n-ZnO nanotubes/p-GaN white light emitting diodes, Nanoscale Research Letters 2011, 6:130
79. B.Y. Oh, M.C. Jeong, T.H. Moon, W. Lee, J.M. Myoung, J.Y. Hwang, and D.S. Seo. Transparent conductive Al-doped ZnO films for liquid crystal displays. J. Appl. Physics, 99(12) (2006) 124505
80. Muslih E.Y and Kim K.H, Preparation of zinc oxide (ZnO) thin film as transparent conductive oxide (TCO) from zinc complex compound on thin film solar cells: A study of O_2 effect on annealing process. IOP Conference Series: Materials Science and Engineering 214 (2017) 012001 DOI: 10.1088/1757-899X/214/1/012001.

81. P. K. Nayak, J. A. Caraveo-Frescas, U. S. Bhansali, and H. N. Alshareef., Homo-junction ferroelectric field-effect-transistor memory device using solution-processed lithium-doped zinc oxide thin films, Appl. Phys. Letts 100 (2012) 253507.
82. K. Kim, S. Y. Park, K. H. Lim, C. Shin, J. M. Myoung and Y. S. Kim., Low temperature and solution-processed Na-doped zinc oxide transparent thin film transistors with reliable electrical performance using methanol developing and surface engineering., J. Mater. Chem. 10.1039/c2jm33790h 2012.
83. Hsin-Chiang You, Indium Doping Concentration Effects in the Fabrication of Zinc-Oxide Thin-Film Transistors, Int. J. Electrochem. Sci., 8 (2013) 9773 – 9784.
84. Han.D, Zhang.Y, Cong.Y, Wen Yu, Xing Zhang and Yi Wang, Fully transparent flexible tin-doped zinc oxide thin film transistors fabricated on plastic substrate. Sci Rep 6 (2016) 38984. https://doi.org/10.1038/srep38984
85. I. Lee, S. J. Choi, K. M. Park, S. S. Lee, S. Choi, I. D. Kima, C. O. Park., The stability, sensitivity and response transients of ZnO, SnO_2 and WO_3 sensors under acetone, toluene and H_2S environments., Sensors and Actuators B 197 (2014) 300–307.
86. G. Heiland., Homogeneous semiconducting gas sensors, Sensors and Actuators 2 (1982) 343.
87. Z. Jing and J. Zhan, Fabrication and gas-sensing properties of porous ZnO nanoplates, Adv. Mater. 20 (2008) 4547-4551
88. C. Hong, Qu Zhou, Z. Lu, A. Umar, R. Kumar, Z. Wei, X. Wu, L. Xu, and S. H. Kim., Ag-doped ZnO nanoellipsoids based highly sensitive gas sensor, Mater. Express, 7 (2017).
89. R. Dhahri , M. Hjiri , L. El Mir , H. Alamri, A. Bonavita, D. Iannazzo, S.G. Leonardi, . Neri CO sensing characteristics of In-doped ZnO semiconductor Nanoparticles, J. Sci: Adv Mater and Devices 2 (2017) 34-40
90. K.G. Girija, K. Somasundaram, A.K. Debnath, Anita Topkar and R.K. Vatsa, Enhanced H_2S sensing properties of Gallium doped ZnO nanocrystalline films as investigated by DC conductivity and impedance spectroscopy J. Mater. Chem. Phys, 214 (2018) 297 – 305
91. Junjie Qi, Hong Zhang, Shengnan Lu, Xin Li, Minxuan Xu, and Yue Zhang High Performance Indium-Doped ZnO Gas Sensor., J. Nanomaterials 6 (2015) 954747 http://dx.doi.org/10.1155/2015/954747

92. M. A. Basyooni, M. Shaban and Adel M. E Sayed., Enhanced Gas Sensing Properties of Spin-coated Na-doped ZnO Nanostructured Films., Scientific Reports | 7:41716 | DOI: 10.1038/srep41716
93. M. Kaur, S. V. S. Chauhan, S. Sinha, M. Bharti, R. Mohan, S. K. Gupta, and J. V. Yakhmi, Application of Aligned ZnO Nanowires/Nanobelts as a Room Temperature NO Gas Sensor, J. Nanosci. Nanotech 9 (2009) 5293–5297.
94. Sumati Pati, P. Banerji and S. B. Majumder., Properties of indium doped nanocrystalline ZnO thin films and their enhanced gas sensing performance, RSC Adv., 5 (2015) 61230
95. A. Sanger, S. B. Kang, M. H. Jeong, M. J.Im, I. Y. Choi, C. U. Kim, H. Lee, Y. Min Kwon, J. M. Baik, H. W. Jang, and K. J. Choi., Morphology-Controlled Aluminum-Doped Zinc Oxide Nanofibers for Highly Sensitive NO_2 Sensors with Full Recovery at Room Temperature, Adv.Sci.5 (2018) 1800816
96. J. W. Kim, Y. Porte, K. Y. Ko, H. Kim, and J. M. Myoung., Micropatternable double -Faced ZnO Nanoflowers for Flexible Gas Sensor., ACS Appl. Mater. Interfaces 9 (2017) 32876−32886 DOI: 10.1021/acsami.7b09251
97. Nisha. R, K. N. Madhusoodanan, T.V. Vimalkumar and K. P. Vijayakumar., Gas sensing application of nanocrystalline zinc oxide thin films prepared by spray pyrolysis, Bull. Mater. Sci., 38 (2015) 583–591.
98. V. L. Patil, S. A. Vanalakar, A. S. Kamble, S. S. Shendage, J. H. Kim and P. S. Patil., Farming of maize-like zinc oxide via a modified SILAR technique as a selective and sensitive nitrogen dioxide gas sensor, RSC Adv., 6 (2016) 90916.
99. K. Anand, O. Singh, M. P. Singh, J. Kaur and R. C. Singh, Hydrogen sensor based on graphene/ZnO nanocomposite., Sensors and Actuators B 195 (2014) 409–415.
100. H. W. Kim, Y. J. Kwon, A. Mirzaei, S. Y. Kang, M. S. Choi, J. H. Bang and S. S. Kim., Synthesis of zinc oxide semiconductors-graphene nanocomposites by microwave irradiation for application to gas sensors, Sensors and Actuators B 249 (2017) 590–601.
101. V. L. Patil, S.A. Vanalakar, P. S. Patil and J. H. Kim., Fabrication of nanostructured ZnO thin films based NO_2 gas sensor via SILAR technique, Sensors and Actuators B 239 (2017) 1185–1193.
102. M. Hjiri, L. El Mira, S.G. Leonardi, A. Pistone, L. Maviliad, G. Neri., Al-doped ZnO for highly sensitive CO gas sensors, Sensors and Actuators B 196 (2014) 413–420.

103. R. Sankar ganesh , M. Navaneethan , Ganesh Kumar Mani , S. Ponnusamy, K. Tsuchiya, C. Muthamizhchelvan, S. Kawasaki and Y. Hayakawa, Influence of Al doping on the structural, morphological, optical, and gas sensing properties of ZnO nanorods, J. Alloys and Comp. 698 (2017) 555-564.
104. M. S. Choi, A. Mirzaei, J. H. Bang, W. Oum, Y. J. Kwon, J. H. Kim, S. W. Choi, S. S. Kim and H. W. Kim., Selective H_2S-sensing performance of Si nanowires through the formation of ZnO shells with Au functionalization, Sensors & Actuators: B. Chemical 289 (2019) 1–14.
105. M. Wang, Q. Luo, S. Hussain, G. Liu, G. Qiao and E. Jung Kim., Sharply-precipitated spherical assembly of ZnO nanosheets for low temperature H_2S gas sensing performances, Mater. Sci. Semicond. Proce. 100 (2019) 283–289.
106. C. Han, Xiaowei Li, Changlu Shao, Xinghua Li, Jiangang Ma, Xintong Zhang and Yichun Liu., Composition-controllable p-CuO/n-ZnO hollow nanofibers for high performance H_2S detection, Sensors & Actuators: B. Chemical 285 (2019) 495–503.
107. K. Shingange, H.C. Swart, G.H. Mhlongo, H_2S detection capabilities with fibrous-like La-doped ZnO nanostructures: A comparative study on the combined effects of La-doping and post-annealing, J. Alloys and Comp. 797 (2019) 284-301.
108. I. Y. Habib, A. A. Tajuddin, H. A. Noor, C. M. Lim, A. H. Mahadi and N. T. R. N. Kumara, Enhanced Carbon monoxide sensing properties of Chromium doped ZnO nanostructures, Scientific Reports (2019) 9:9207 https://doi.org/10.1038/s41598-019-45313-w.
109. H. I. Chen, C. Yu Chi, W. C. Chen, I. P. Liu, C. H. Chang, T. C. Chou and W. C. Liu., Ammonia Sensing Characteristic of a Pt Nanoparticle/Aluminum-Doped Zinc Oxide Sensor, Sensors and Actuators B chemical 267 (2018) 145-154.
110. P. S. Kolhe, A. B. Shinde, S.G. Kulkarnia, N. Maiti, P. M. Koinkar, K. M. Sonawane, Gas sensing performance of Al doped ZnO thin film for H_2S detection, J. Alloys and Comp 748 (2018) 6-11.
111. Y. T. Tsai, S. J. Chang, L. W. Ji, Y. J. Hsiao, I. T. Tang, H. Y. Lu, and Y. L. Chu., High Sensitivity of NO Gas Sensors Based on Novel Ag-Doped ZnO Nanoflowers Enhanced with a UV Light-Emitting Diode, ACS Omega 3 (2018) 13798−13807.

112. N. Vorobyeva, M. Rumyantseva, D. Filatova, F. Spiridonov, V. Zaytsev, A. Zaytseva and A. Gaskov, Highly Sensitive ZnO (Ga, In) for Sub-ppm Level NO_2 Detection: Effect of Indium Content, Chemosensors 5 (2017) 18.
113. Buddha Deka Boruah, Zinc oxide ultraviolet photodetectors: rapid progress from conventional to self-powered photodetectors, Nanoscale Adv., 1 (2019) 2059-2085.
114. Y. H. Leung, Z. B. He, L. B. Luo, C. H. A. Tsang, N. B. Wong, W. J. Zhang, and S. T. Lee ZnO nanowires array p-n homojunction and its application as a visible-blind ultraviolet photodetector, Applied Physics Letters 96 (2010) 053102.
115. Shaivalini Singh, Yogesh Kumar, Hemant Kumar, Sumit Vyas, Chinnamuthan Periasamy, Parthasarathi Chakrabarti, Satyabrata Jit, and Si-Hyun Park, A study of hydrothermally grown ZnO nanorod-based metal-semiconductor metal UV detectors on glass substrates, Nanomaterials and Nanotechnology 7 (2017) 1-5.
116. C. L. Hsu, K.Chao Chen, and T. Jen Hsueh, A Homojunction Based On p-Type Sb-Doped ZnO Nanoparticles UV Photodetector of and n-Type ZnO Nanowires, IEEE Transactions On Electron Devices, 61 (2014) 5
117. D. Kim, Ilgu Yun and Hyung jun Kim, Fabrication of rough Al doped ZnO films deposited by low pressure chemical vapor deposition for high efficiency thin film solar cells Current Applied Physics 10 (2010) S459–S462.
118. O. Lupan, S. Shishiyanu, V. Ursaki, H. Khallaf, L. Chow, T. Shishiyanu, V. Sontea, E. Monaico and S. Railean, Synthesis of nanostructured Al-doped Zinc oxide films on Si for solar cells applications, Solar Energy Materials & Solar Cells 93 (2009) 1417–1422.
119. Jinxia Duan, Qiu Xiong, Jinghua Hu and Hao Wang, Electric-Field-Assisted Growth of Ga-Doped ZnO Nanorods Arrays for Dye-Sensitized Solar Cells, J. Power and Energy Engineering, 3 (2015) 11-18.
120. S. Noda, H. Shima and H. Akinaga, Cu_2O/ZnO Heterojunction Solar Cells Fabricated by Magnetron-Sputter Deposition Method Films Using Sintered Ceramics Targets, J. Phys: Conference Series 433 (2013) 012027.
121. Pal. M, Bera. S, Khan. H and Jana. S, Effect of Ga doping on Microstructural, Optical and Photocatalytic Properties of Nanostructured Zinc Oxide Thin Films, Kenk Nanotec Nanosci 1 (2015) 40-50.

122. Feng Zhang, Wenjuan Zhang, Xiaolin Luo, Guodong Feng and Li Fang Zhao, Electrodeposition of ZnO Film With Enhanced Photocatalytic Activity Towards Methylene Blue Degradation, Int. J. Electrochem. Sci., 12 (2017) 3756 – 3764 doi: 10.20964/2017.05.62
123. A. Fujishima and K. Homda, Electrochemical Photolysis of Water at a Semiconductor Electrode, Nature 238 (1972) 37-38.
124. Yang. L. L. Zhao and Willander. M, Size-controlled growth of well-aligned ZnO nanorod arrays with two-step chemical bath deposition method. J. Alloys and Comp. 469 (2009) 623.
125. Wang. G, Yang. X, Qian, F. Zhang.J. Z, and Li. Y, Double-sided CdS and CdSe quantum dot co-sensitized ZnO nanowire arrays for photoelectrochemical hydrogen generation, Nano Letters, 10 (2010) 1088.
126. Miao.J, Yang. H. B, Khoo. S.Y and Liu.B, Electrochemical fabrication of ZnO-CdSe core shell nanorod arrays for efficient photoelectrochemical water splitting. Nanoscale, 5 (2013) 11118.
127. W. Kern and K.K. Schuegraf, Deposition Technologies and Applications: Introduction and Overview, Handb. Thin-Film Depos. Process. Tech. i (2002).
128. C. Moore, Z. Yu, L.R. Thompson and G.J. Collins, Laser and Electron Beam Assisted Processing, (2001) 349–379. doi:http://dx.doi.org/10.1016/B978-081551442-8.50014-6.
129. W.S. Knodle and R. Chow, Molecular Beam Epitaxy: Equipment and Practice, Handb. Thin Film Depos.Process. Tech. Second Ed. (2001) 381–461. doi:http://dx.doi.org/10.1016/B978-081551442-8.50015-8
130. T. Film, G. Process, Thin Film Processes, in: n.d. doi:10.1016/B978-0-8155-1483-1.50003-4.
131. D. Depla, S. Mahieu, J. Greene, Sputter deposition processes, Handb. Depos. Technol. Film. Coatings. 281 (1991) 253–296.
132. S. Yield, Sputtering Phenomena, in: Energy, 1852. doi:10.1016/B978-0-8155-1483-1.50004-6.
133. S. Rossnagel, Sputtering and Sputter Deposition, Handb. Thin-Film Depos. Process. Technol. (2001) 319–348. doi:10.1002/ange.19891010662
134. J. A. Thornton, “Magnetron sputtering: basic physics and application to cylindrical magnetrons”, J. Vacuum Science & Technology 15 (1978) 171–177.
135. K. L. Chopra and S. R. Das in “Thin Film Solar Cells” (Plenum Press, New York, 1983).

136. Brinker C. J. and G. W. Scherer, Sol-gel science: the physics and chemistry of sol-gel processing. 1990, San Diego, CA, USA: vol. 8, academic Inc. Press.
137. Danks A. E., S. R. Hall and Z. Schnepp, The evolution of sol-gel chemistry as a technique for materials synthesis, Mater. Horiz., 3 (2016) 91.
138. A. C. Pierre, Introduction to Sol-gel Processing, 1st edition. Springer Science Business Media New York Originally, 1998
139. Sunandan Baruah and Joydeep Dutta, topical review: Hydrothermal growth of ZnO nanostructures Sci. Technol. Adv. Mater. 10 (2009) 013001.
140. http:// serc. carleton. edu/ research_education/ geochemsheets/ techniques /XRD.html, 10 October 2014, http://www.absoluteastronomy.com/topics/X-ray_crystallography, 10 October 2014. http://prism.mit.edu/xray/oldsite/training.htm#chronological, 10 October 2014.
141. M. Birkholz, Principles of X-ray Diffraction, Thin film analysis by X-ray scattering, WILEY-VCH Verlag GmbH & Co. KGaA, Weinheim, (2006) 10-11
142. M.N.H. Mia , M.F. Pervez , M. Khalid Hossain , M. Reefaz Rahman , M. Jalal Uddin , M.A. Al Mashud ,H.K. Ghosh and Mahbubul Hoq Influence of Mg content on tailoring optical bandgap of Mg-doped ZnO thin film prepared by sol-gel method Results in Physics 7 (2017) 2683–2691
143. Dayakar. T, V. Rao. K, Bikshalu. K, Rajendar.V, and Park. S. H, Novel synthesis and structural analysis of zinc oxide nanoparticles for the non enzymatic glucose biosensor. Mater. Sci. Engg C, 75 (2017) 1472–1479 doi:10.1016/j.msec.2017.02.032.
144. T. Srinivasulu, K. Saritha and K.T. Ramakrishna Reddy, Synthesis and characterization of Fe-doped ZnO thin films deposited by chemical spray pyrolysis, Modern. Electr. Mater 3 (2017) 76–85.
145. B.D. Cullity, In “Elements of X-ray Diffraction” Addison- Wesley Publisimg Co-Inc., 1982
146. J. García Solé, L. E. B., D. Jaque, An Introduction to the Optical Spectroscopy of Inorganic Solids. John Wiley & Sons Ltd: England, (2005).
147. https://www.sas.upenn.edu/~crulli/TheRamanSpectrophotometer.html
148. J. Yu, Y. Lai, Y. Wang, S. Cheng, and Y. Chen, "Polarized Raman scattering of single ZnO nanorod," J. Applied Physics, 115 (2014) 033505.

149. W. Zhou, R. Apkarian, Z. L. Wang, D. Joy, Fundamentals of scanning electron microscopy (SEM), Scanning microscopy for nanotechnology: Techniques and applications, Springer, New York (2007) 1-40.
150. Abou-Ras, D., T. Kirchartz, and U. Rau, Advanced characterization techniques for thin film solar cells. (2010), Weinheim, Germany: Wiley-VCH
151. J. F. Moulder, W. F. Stickle, P. E. Sobol, K. D. Bomben, Handbook of X-ray Photoelectron Spectroscopy, ULVAC-PHI, Inc Japan and Physical Electronics USA, (1995).
152. J. Chastain, and Roger C. King Jr., Introduction, Handbook of X-ray photoelectron spectroscopy, Physical Electronics USA, Inc., (1995) 9-10.
153. Watts, J.F. and J. Wolstenholme, An introduction to surface analysis by XPS and AES. (2003), Chichester, UK: John Wiley & Sons Ltd.
154. Vij. D. R, Handbook of applied solid state spectroscopy (2006), New York; USA: Springer
155. Z. Chen et al, UV-vis spectroscopy, photoelectrochemical water splitting, Springer Briefs in Energy (2013) 49.
156. A. H. Hammad, M. Sh.Abdel-wahab, Sajith Vattamkandathil, Akhalakur Rahman Ansari, Structural and optical properties of ZnO thin films prepared by RF sputtering at different thicknesses, Physica B: Condensed Matter 540 (2018) 1-8.
157. G. D. Gilliland, Photoluminescence spectroscopy of crystalline semiconductors, Materials Science and Engineering: R: Reports, 18 (1997) 99 – 399.
158. W. Y. Liang, "Excitons," Physics Education, 5 226–228, 197.
159. H. M. Chiu, Y. T. Chang, W. W. Wu, and J. M. Wu, Synthesis and Characterization of One-Dimensional Ag-Doped ZnO/Ga-Doped ZnO Coaxial Nanostructure Diodes, ACS Appl. Mater. Interfaces 6 (2014) 5183−5191
160. S.P. Patil, V.L. Patil, S.S. Shendage, N.S. Harale, S.A. Vanalakar, J.H. Kim, et al., Spray pyrolyzed indium oxide thick films as NO_2 gas sensor, Ceram. Int. 42 (2016) 16160-16168.
161. L. Zhu and W. Zeng, A novel coral rock-like ZnO and its gas sensing. Mater. Lett. 209 (2017) 244246.
162. C. Wang and W. Zeng, New insights into multi-hierarchical nanostructures with size-controllable blocking units for their gas sensing performance, J. Mater. Sci.: Mater. Electron. 28 (2017) 10847-10852.

163. Y.H. Navale, S.T. Navale, N.S. Ramgir, F.J. Stadler, S.K. Gupta, D.K. Aswal, et al., Zinc oxide hierarchical nanostructures as potential NO_2 sensors, Sens. Actuators B: Chem. 251 (2017) 551563.

164. J. Jonca, J. Harmel, L. Joanny, A. Ryzhikov, M.L. Kahn, P. Fau, B. Chaudret, et al., Au/MOx (M = Zn, Ti) nanocomposites as highly efficient catalytic filters for chemical gas sensing at room temperature and in humid atmosphere, Sens. Actuators B: Chem. 249 (2017) 357-363.

165. C. L. Hsu, L. F. Chang and T. J. Hsueh, Light-activated humidity and gas sensing by ZnO nanowires grown on LED at room temperature, Sens. Actuators B: Chem. 249 (2017) 265-277

166. C. Wagner, K. Hauffe, The stationary state of catalysts in homogeneous reactions. Ztschr. Elektrochem. 33, 172 (1938)

167. T. Seiyama, A. Kato, K. Fujiishi, M. Nagatani, A new detector for gaseous components using semiconductive thin film, Anal. Chem. 34(11) (1962) 1502–1503. doi:10.1021/ac60191a001

168. N. Yamazoe, New approaches for improving semiconductor gas sensors. Sens. Actuators B 5(1–4) (1991) 7–19. doi:10.1016/ 0925-4005(91)80213-4

169. H. J. Kim and J. H. Lee, Highly sensitive and selective gas sensors using p-type oxide semiconductors: Overview. Sensors and Actuators B: Chemical. 192 (2014) 607-627.

170. M. E. Franke, T. J. Koplin, and U. Simon, Metal and metal oxide nanoparticles in chemiresistors: Does the nanoscale matter? Small. 2 (1) (2006) 36-50

171. Ravi. N, Pulsed adsorption gas sensor system, (2006) M.S., Sate University of New York at Buffalo, Ann Arbor.

172. H.V. Han, N.D. Hoa, P.V. Tong, H. Nguyen and N.V. Hieu, Single crystal zinc oxide nanorods with nanovoids as highly sensitive NO_2 nanosensors. Mater. Lett. 94 (2013) 41–43. doi:10.1016/j.matlet.2012.12.006

173. C. J. Chang, C. Y. Lin, J. K. Chen and M. H. Hsu, Ce-doped ZnO nanorods based low operation temperature NO_2 gas sensors, Ceram. Int. 40(7) (2014) 10867–10875. doi:10.1016/j.ceramint. 2014.03.080

174. S. Bai, L. Chen, S. Chen, R. Luo, D. Li, A. Chen and C.C. Liu, Reverse microemulsion in situ crystallizing growth of ZnO nanorods and application for NO_2 sensor, Sens. Actuators B: Chem. 190 (2014) 760–767. doi:10.1016/j.snb.2013.09.032
175. T. V. Kolekar, S. S. Bandgar, S. S. Shirguppikar and V. S. Ganachari, Synthesis and characterization of ZnO nanoparticles for efficient gas sensors. Arch. Appl. Sci. Res. 5(6) (2013) 20–28.
176. D. Yan, M. Hu, S. Li, J. Liang, Y. Wu and S. Ma, Electrochemical deposition of ZnO nanostructures onto porous silicon and their enhanced gas sensing to NO_2 at room temperature. Electrochim. Acta 115 (2014) 297–305. doi:10.1016/j.electacta.2013.10.007
177. M. Salah, S. Azizi, A. Boukhachem, C. Khaldi, M. Amlouk and J. Lamloumi, Structural, morphological, optical and photodetector properties of sprayed Li-doped ZnO thin films, J. Mater. Sci. Energy materials s10853 (2017) 017-1218. DOI 10.1007/s10853-017-1218-z
178. L.Tang, B. Wang, Y. Zhang and Y. Gu, Structural and electrical properties of Li-doped p-type ZnO thin films fabricated by RF magnetron sputtering, Mater.Sci. Engg. B 176 (2011) 548-551.
179. Rajendran, A. Rakesh and S. Balakumar, Structural, electrical transport and optical studies of Li ion doped ZnO nanostructures, Proc. and Appl. of Cer 8 (2014) 7-13.
180. A.V. Vasin, A.V. Rusavsky, E.G. Bortchagovsky, Y.V. Gomeniuk, A.S. Nikolenko, V. V. Strelchuk, R. Yatskiv, S. Tiagulskyi, S. Prucnal, W. Skorupa and A.N. Nazarov, Methane as a novel doping precursor for deposition of highly conductive ZnO thin films by magnetron sputtering, Vacuum 174 (2020) 109199.
181. S. Polarz, A. Orlov, A. Hoffmann, M .R. Wagner, C. Rauch, R. Kirste, W. Gehlhoff, Y. Aksu, M. Driess, M. W. E. Van den Berg and M. Lehmann, A systematic study on zinc oxide materials containing I metals (Li, Na, K)-Synthesis from Organometallic Precursors, Characterization, and Properties, Chem. Mater 21 (2009) 3889-3897.
182. S. Dhara and P. K. Giri, Stable p-type conductivity and enhanced photoconductivity from nitrogen-doped annealed ZnO thin film, Thin Solid Films 520 (2012) 5000–5006.
183. J. A. de Campos, T. Viseu, A. G. Rolo, N. P. Barradas, E. Alves, T. de Lacerda- Arôso and M. F. Cerqueira., Electrical and Raman scattering studies of ZnO:P and ZnO:Sb thin films, J.Nanosci. Nanotech 10 (2010) 2620–2623.

184. S. H. Nam, S. J. Cho and J. H. Boo, Physical properties of metal-doped zinc oxide films for surface acoustic wave application, Nanoscale. Res. Lett (2012) 7:25
185. L. X. Chen, S. Liu, C. M. Li and Y. C. Wang, J. L. Liu and J. J. Wei, Enhanced deposition of ZnO films by Li doping using radio frequency reactive magnetron sputtering, Inter. J. Miner. Meta and Mater 22 (2015) 1108.
186. M. Hjiri, M. S. Aida, O. M. Lemine, L. El Mir, Study of defects in Li-doped ZnO thin films, Mater. Sci. Semi. Proces. 89 (2019) 149–153
187. J. G. Lu, Y. Z. Zhang, Z. Z. Ye, Y. J. Zeng, H. P. He, L. P. Zhu, J. Y. Huang, L. Wang, J. Yuan, B. H. Zhao and X. H. Li, Control of p-type and n type conductivities in Li-doped ZnO thin films, Appl. Phy. Lett 89 (2006) 112-113.
188. D. Wang, J. Zhou and G. Liu, Effect of Li-doped concentration on the structure, optical and electrical properties of p type ZnO thin films prepared by sol-gel method, J. Alloys and Comp 481(2009) 802-805.
189. S. D. Senol, Influence of Mg doping on the structural, optical, and electrical properties of $Zn_{0.95}Li_{0.05}O$ Nanoparticle, Int J Appl Ceram Technol. 16 (2019) 138–145.
190. P. Chand, A. Gaur, A. Kumar and U. K. Gaur, Structural, morphological and optical study of Li doped ZnO thin films on Si (100) substrate deposited by pulsed laser deposition, Ceramic. Inter 40 (2014) 11915-11923.
191. M. Wang, E. J. Kim and S. H. Hahn Photoluminescence study of undoped and Li-doped ZnO thin films grown by sol–gel technique, J. Lumin 131 (2011) 1428–1433.
192. O. Lupan, L. Chow, L. K. Ono, B. R. Cuenya, G. Chai, H. Khallaf, S. Park and A. Schulte, Synthesis and characterization of Ag- or Sb doped ZnO nanorods by a facile hydrothermal route, J. Phys. Chem. C 114 (2010) 12401-12408.
193. R. Al-Gaashani, S. Radiman, A.R. Daud, N. Tabet, Y. Al-Douri, XPS and optical studies of different morphologies of ZnO nanostructures prepared by microwave methods, Ceramics International 39 (2013) 2283–2292
194. Z. Lin, J. Chang, C. Zhang, J. Zhang, J. Wu and Y. Hao, Low temperature aqueous solution-processed Li doped ZnO buffer layers for high performance inverted organic solar cells, J. Mater. Chem. C 4 (2016) 6169-6175.

195. S. Y. Park, K. Kim, K. H. Lim, B. J. Kim, E. Lee, J. H. Cho and Y. S. Kim, The structural, optical and electrical characterization of high-performance, low-temperature and solution-processed alkali metal-doped ZnO TFTs, J. Mater. Chem. C 1 (2013) 1383-1391.
196. I. Thakur, S. Chatterjee, S. Swain, A. Ghosh, S. K. Behera and Y. S. Chaudhary, Facile synthesis of single crystalline n-/p-type ZnO nanorods by lithium substitution and their photoluminescence, electrochemical and photocatalytic properties, New J. Chem 39 (2015) 2612-2619.
197. S. Dellis, N. Pilatsikas, N. Kalfagiannis, O. Lidor-Shalev, A. Papaderakis, G. Vourlias, S. Sotiropoulos, D. C. Koutsogeorgis, Y. Mastai and P. Patsalas, Broad band luminescence in defect-engineered electrochemically produced porous Si/ZnO nanostructures, Scientific Reports 8 (2018) 6988.
198. A. Zendehnam, M. Mirzaee and S. Miri, Influence of deposition rate on PL spectrum and surface morphology of ZnO nanolayers deposited on Si (100) substrate, Bull. Mater. Sci 37 (2014) 179-183.
199. S. Vempati, J. Mitra and P. Dawson, One step synthesis of ZnO nanosheets: a blue- white flurophore, Nanoscale Res. Lett.7 (2012) 470.
200. S. K. Pandey, S. K. Pandey, V. Awasthi, A. Kumar, U. P. Deshpande, M. Gupta, and S. Mukherjee, P-type conduction from Sb-doped ZnO thin films grown by dual ion beam sputtering in the absence of oxygen ambient, J. Appl. Phys 114 (2013) 163107.
201. H. B. Fan, S.Y. Yang, P.F. Zhang, H.Y. Wei, X.L. Liu, C.M. Jiao, Q.S. Zhu, Y.H. Chen, and Z.G. Wang, Investigation of Oxygen Vacancy and Interstitial Oxygen Defects in ZnO Films by Photoluminescence and X-Ray Photoelectron Spectroscopy, Chin. Phys. Lett. 24 (2007) 2108 https://doi.org/10.1088/0256-307X/24/7/089
202. S. Limpijumnong, S. B. Zhang, S. H. Wei, and C. H. Park, Doping by Large-Size-Mismatched Impurities: The Microscopic Origin of Arsenic or AntimonyDoped p -Type Zinc Oxide, Phys. Rev. Lett. 92 (2004) 155504 https://doi.org/10.1103/PhysRevLett.92.155504
203. S. D. Baek, Y. C. Kim and J. M. Myoung, Sb-doped p-ZnO quantum dots: Templates for ZnO nanorods homojunction white light-emitting diodes by low-temperature solution process, App. Surf. Sci 480 (2019) 122–130.

204. Shashi B. Rana Amarpal Singh, Navneet Kaur, Structural and optoelectronic characterization of prepared and Sb doped ZnO nanoparticles, J Mater Sci: Mater Electron 24 (2013) 44–52.
205. Mahmood, M. A., Baruah, S. and Dutta, Enhanced visible light photocatalysis by manganese doping or rapid crystallization with ZnO nanoparticles, Mater. Chem. Phys. 130 (2011) 531–535 https://doi.org/10.1016/j.matchemphys.2011.07.018.
206. Wang. Y. S, Thomas. P. J. and P. O'Brien, Optical Properties of ZnO Nanocrystals Doped with Cd, Mg, Mn, and Fe Ions, J. Phys. Chem. B 110 (2006) 21412–21415 https://doi.org/10.1021/jp0654415
207. Lee. J. H. and Park. B. O, Transparent conducting ZnO:Al, In and Sn thin films deposited by the sol–gel method, Thin Solid Films 426 (2003) 94–99 https://doi.org/10.1016/S0040-6090(03)00014-2
208. Lee. W. J, Kang. J and Chang. K. J, Defect properties and p -type doping efficiency in phosphorus doped ZnO, Phys. Rev. B 73 (2006) 024117 https://doi.org/10.1103/PhysRevB.73.024117
209. Gong. H, Hu J. Q, Wang J. H, Ong. C. H. and Zhu. F. R., Nano-crystalline Cu-doped ZnO thin film gas sensor for CO, Sens. Actuators. B-Chem. 115 (2006) 247–251.
210. Anandan.S, A. Vinu, T. Mori, N. Gokulakrishnan, P. Srinivasu, V. Murugesan and K. Ariga, Photocatalytic degradation of 2, 4, 6-trichlorophenol using lanthanum doped ZnO in aqueous suspension, Catal. Commun. 8 (2007)1377–1382 https://doi.org/10.1016/j.catcom.2006.12.001
211. P. Sharma, A. Gupta, K. V. Rao, F. J. Owens, R. Sharma, R. Ahuja, J. M. Osorio Guillen , B. Johansson and G. A. Gehring, Ferromagnetism above room temperature in bulk and transparent thin films of Mn-doped ZnO, Nat. Mater. 2 (2013) 673–677.
212. J. Gao, Q. Zhao, Y. Sun, G. Li, J. Zhang and D. Yu, A Novel Way for Synthesizing Phosphorus-Doped Zno Nanowires, Nanoscale Res Lett 6 (2011) 45.
213. P. Tao, Q. Feng, J. Jiang, H. Zhao, R. Xu, S. Liu, M. Li, J. Sun and Z. song, Electroluminescence from ZnO nanowires homojunction LED grown on Si substrate by simple Chemical vapor deposition, Chem. Phys. Letts 22 (2012) 92-95.

214. T. V. Vimalkumar, N. Poornima, C. Sudha Kartha and K. P. Vijayakumar, On tuning the orientation of grains of spray pyrolysed ZnO thin films, Appl. Surf. Sci. 256 (2010) 6025–6028.
215. S. Major, A. Banerjee and K. L. Chopra, Highly transparent and conducting indium doped zinc oxide films by spray pyrolysis, Thin solid Films, 108 (1983) 333-340.
216. Z. Wang, Oxide nanobelts and nanowires—growth, properties and applications, J.Nanosci. and Nanotech, 8 (2008) 27–55
217. T. Pauporte, O. Lupan, B. Viana , L. Chow and M. T. Chernycheva, Controlling the properties of electrodeposited ZnO nanowire arrays for light emitting diode, photodetector and gas sensor applications, Proc. of SPIE Vol. 8987 89871R-1
218. J. C. Wang, F. C. Cheng, Y. T. Liang, H. I. Chen, C. Y. Tsai, C. H. Fang and T. E. Nee, Anomalous luminescence phenomena of indium-doped ZnO nanostructures grown on Si substrates by the hydrothermal method, Nanoscale. Res. Lett. 7 (2012) 270.
219. Tang Kun, Gu Shu-Lin, Ye Jian-Dong, Zhu Shun-Ming, Zhang Rong, Zheng You-Dou. Recent progress of the native defects and p-type doping of zinc oxide. Chinese Physics B, 26 (2017) 047702.
220. R. Wu, W. Zhang, H. Zhang, D. Song, Q. Maa, J. Liu, X. Ma, L. Zhang, L. Zhang, H. Song, Investigation of aluminum and gallium co-doped ZnO powders and their effects on the properties of targets, Mater. Sci. Semi. Proce. 19 (2014) 24–31.
221. D. P. Norton, M. Ivill, Y. Li, Y.W. Kwon, J. M. Erie, H. S. Kim, K. I, S. J. Pearton, Y.W. Heo, S. Kim, B. S. Kang, F. Ren, A. F. Hebard and J. Kelly, Charge carrier and spin doping in ZnO thin films, Thin Solid Films 496 (2006) 160 – 168.
222. K.G. Girija, K. Somasundaram, Anita Topkar and R.K. Vatsa, Highly selective H_2S gas sensor based on Cu-doped ZnO nanocrystalline films deposited by RF magnetron sputtering of powder target, J.Alloy.Comp. 684 (2016) 15-20.
223. S. A. M. Lima, M. R. Davolos, W. G. Quirino, C. Legnani, and M. Cremona, Low-voltage electroluminescence of europium in zinc oxide thin films, Appl. Phys. Lett. 90 (2007) 023503.
224. Mahmood, K. Khalid, A. Ahmad and S.W. Mehran, Indium-doped ZnO mesoporous nanofibers as efficient electron transporting materials for perovskite solar cells, Surf. Coat. Tech, 352 (2018) 231-237

225. Y. R. Park , E. K. Kim , D. Jung , T. S. Park, Y. S. Kim, Growth of transparent conducting nano-structured In doped ZnO thin films by pulsed DC magnetron sputtering, Appl. Surf. Sci 254 (2008) 2250–2254.
226. S. S. Badadhe and I. S. Mulla, H_2S gas sensitive indium-doped ZnO thin films: Preparation and Characterization, Sensors. Actuator B 143 (2009) 164-170.
227. P. Bindu and Sabu Thomas, Estimation of lattice strain in ZnO nanoparticles: X-ray peak profile analysis, J. Theor. Appl. Phys 8 (2014) 123–134.
228. R. K. Chava and M. Kang, Improving the photovoltaic conversion efficiency of ZnO based dye sensitized solar cells by indium doping, J. Alloys Compd 692 (2017) 67-76, http://dx.doi.org/10.1016/j.jallcom.2016.09.029.
229. G. C. Park, S. M. Hwang, J. H. Choi, Y. H. Kwon, H. K. Cho, S. W. Kim, J. H. Lim, and J. Joo, Effects of In or Ga doping on the growth behavior and optical properties of ZnO nanorods fabricated by hydrothermal process, Phys. Status Solidi A 210 (2013) 1552–1556 DOI 10.1002/pssa.201200907.
230. A. F. Lotus, Y. C. Kang, R. D. Ramsier and G. G. Chase, Investigation of the physical and electronic properties of indium doped zinc oxide nano fibers synthesized by electrospinning, J. Vzc. Sci. Technol. B 27 (2009) 2331.
231. S. U. Awan, S. K. Hasanain, M. F. Bertino, and G. H. Jaffari, Ferromagnetism in Li doped ZnO nanoparticles: The role of interstitial Li, J. Appl. Phys. 112, (2012) 103924.
232. A. Singh, S. Chaudhary and D. K. Pandya, High conductivity indium doped ZnO films by metal target reactive co-sputtering, Acta Mater. 111 (2016) 1-9
233. K. G. Saw, N. M. Aznan, F. K. Yam, S. S. Ng and S. Y. Pung , New Insights on the Burstein-Moss Shift and Band Gap Narrowing in Indium-Doped Zinc Oxide Thin Films, Plos one 10 0141180.
234. S. Y. Bae, C. W. Na, J. H. Kang, and J. Park, Comparative structure and optical properties of Ga, In and Sn doped ZnO nanowires synthesized via thermal evaporation, J. Phys. Chem. B, (2005) 2526-2531
235. K. Vanheusden, W. L. Warren, C. H Seager, D. R. Tallant, J. A. Voigt, and B. E. Gnade, Mechanism behind green photoluminescence in ZnO phosphor powders, J. Appl. Phys, (1996) 7983-7990.

236. K. Mahmood, S. B. Park and H. Jin Sung, Enhanced photoluminescence, Raman spectra and field-emission behavior of indium-doped ZnO nanostructures, J. Mater. Chem.C, 1 (2013) 3138

237. T. Kılıçoğlu, Effect of an organic compound (Methyl Red) interfacial layer on the calculation of characteristic parameters of an Al/Methyl Red/p-Si sandwich Schottky barrier diode, Thin Solid Films 516 (2008) 967–970.

238. Kim. K. M, H. R. Kim, K. Choi, H. J. Kim and J. H. Lee, Design Of Highly Sensitive C_2H_5OH Sensors Using Self-Assembled Zno Nanostructures, sensors 11 (2011) 9685.

239. H. C. Park, D. Byun, B. Angadi, D. H. Park, W. K. Choi, J. W. Choi and Y. S. Jung, Photoluminescence of Ga-doped ZnO film grown on c-Al_2O_3 by plasma- assisted molecular beam epitaxy, J. Appl. Phy., 2007, 102,073114.

240. D. Meljanac, K. Juraic, V. Mandic, H. Skenderovic, S. Bernstorff, J. R. Plaisier, A. Santic, A. Gajovic, B. Santic, D. Gracina, The influence of thermal annealing on the structural, optical and electrical properties of AZO thin films deposited by magnetron sputtering, Surf. Coat. Tech. 321 (2017) 292–299.

241. T. C. Li, C. F. Han, T. H. Kuan, and J. F. Lin, Effects of sputtering-deposition inclination angle on the IGZO film microstructures, optical properties and photoluminescence, Optical Materials Express 6 (2016) 343 | Doi:10.1364/Ome.6.000343 |

242. Lim.J, Lee.S, Kim. H, H. Y. Kim, J. Park, S. B. Jung, G. C. Park, J. Kim and J. Joo, Synergistic effect of Indium and Gallium co-doping on growth behavior and physical properties of hydrothermally grown ZnO nanorods. Sci Rep 7 41992 (2017). https://doi.org/10.1038/srep41992

243. F. Mitsugi, Y. Umeda, N. Sakai and T. Ikegami, Uniformity of gallium doped zinc oxide thin film prepared by pulsed laser deposition, Thin Solid Films 518 (2010) 6334–6338.

244. Qing Yang, Xiaohong Zhang, Xiaohong Zhou, and Shuhua Liang., Growth of Ga-doped ZnO films by thermal oxidation with gallium and their optical properties., AIP Advances 7 (2017) 055106.

245. B.J. Jin, S. Im, S.Y. Lee, Violet and UV luminescence emitted from ZnO thin films grown on sapphire by pulsed laser deposition, Thin Solid Films 366 (2000) 107.

246. Ming Gao, Jinghai Yang, Lili Yang , Yongjun Zhang , Jihui Lang ,Huilian Liu , Hougang Fan , Yunfei Sun, Zhiqiang Zhang and Hang Song, Enhancement of optical properties and donor-related emissions in Y-doped ZnO, Superlattice Microstructure 52 (2012) 84–91.
247. Nanda Shakti, Chandni Devi, A. K. Patra, P. S. Gupta, and Sandeep Kumar, Lithium doping and photoluminescence properties of ZnO nanorods, Aip Advances 8 (2018) 015306.
248. V. Khomchenko, M. Sopinskyy, M. Mazin, V. Danko, O. Lytvyn and Y. Priyantinkii, The violet luminescence band in ZnO and ZnO-Ag thin films, J.Lumin. 213 (2019) 519-524.
249. G. X. Zhu, Y. J. Liu, C. Zhang, Z. l. Zhu and Z. Xu, Fabrication and Enhanced Rectifying Performance of $Zn_{1-x}Co_xO$ Nanowall Vertically Growing on Si Wafer, Chem. Lett., 39 (2010) 994–995 https://doi.org/10.1246/cl.2010.994
250. I. Rahim, M. Shah, M. Iqbal, F. Wahab, A. Khan, S.H. Khan, Fabrication and electrical characterizations of graphene nanocomposite thin film based heterojunction diode, Physica B 524 (2017) 97.
251. Hayder J, Al-Asedu, Noriah Bidis, Sharug A, Al Khafaji, Hazar Bakhtiar, Sol-gel grown aluminum/gallium co-doped ZnO nanostructures: Hydrogen gas sensing attributes, Mat. Sci. in Semicon. Proc. 77 (2018) 50.
252. M. Benhaliliba, C. E. Benouis, M. S. Aida, F. Yakuphanoglu and A. Sanchez Juare, Indium and aluminium-doped ZnO thin films deposited onto FTO substrates: nanostructure, optical, photoluminescence and electrical properties, J. Sol-Gel Sci Technol 55 (2010) 335.
253. M. Rouchdi, E. Salmani, B. Fares, N. Hassanain and A. Mzerd, Synthesis and characteristics of Mg doped ZnO thin films: Experimental and ab-initio study, Results Phys 7 (2017) 620
254. Saraswathi Chirakkara and S. B. Krupanidhi, Gallium and indium co-doped ZnO thin films for white light emitting diodes, Phy. Status Solidi RRL,6 (2011) 34.
255. Fang-Hsing Wang, Jen-Chi Chao, Han-Wen Liu, and Tsung-Kuei Kang, Physical Properties of ZnO Thin Films Codoped with Titanium and Hydrogen Prepared by RF Magnetron Sputtering with Different Substrate Temperatures, J. Nanomater (2015) 936482
256. A. Amala Rani and S. Ernest, Structural, Morphological, Optical and Compositional Characterization of Spray deposited Ga doped ZnO thin film for Dye-Sensitized Solar Cell Application, Superlattices and Microstructures 75 (2014) 398-408.

257. B. Allabergenov, S. H. Chung, S. M. Jeong, S. Kim and B. Choi, Enhanced blue photoluminescence realized by copper diffusion doping of ZnO thin films, Opt. Mater. Express 3 (2013) 1733.
258. Z. Liang, X. Yu, B. Lei, P. Liu, W. Mai, Novel blue-violet photoluminescence from sputtered ZnO thin films, J. Alloy. Compds 509 (2011) 5437–5440
259. Kleinerman, J. Rynbrandt and D. Lung, Proteolytic activity and serum protease inhibition after NO_2 exposure, Arch. Environ. health (1976) 313741
260. A.I. Ismail and M.J.Abdullah, The structural and optical properties of ZnO thin films prepared at different RF sputtering power, J.KingSaud.Univ.Sci.25 (2013) 209–215
261. K.A. Alim, V.A. Fonoberov and A.A. Balandin, Origin of the phonon frequency shifts in ZnO quantum dots, Appl. Phys. Lett. 86 (2005) 053103
262. M. Chen, X.Wang, Y.H.Yu and Z.L.Pei, X-ray photoelectron spectroscopy and auger electron spectroscopy studies of Al-doped ZnO films, Appl. Surf. Sci., 158 (2000) 134.
263. Zendehnama, M. Mirzaeec, S. Miri., Effect of annealing temperature on PL spectrum and surface morphology of zinc oxide thin films. Appl. Surf. Sci 270 (2013) 163–168
264. S.A Vanalakar, V.L Patil, N.S. Harale, S.A Vhanalakar, M.G Gang, J.X. Kim, P.S. Patil and J.H. Kim, Controlled growth of ZnO nanorod arrays via wet chemical route for NO_2 gas sensor applications, Sensors and Actuators B 221 (2015) 1195-1201.
265. N. Qin, Q. Xiang, H. Zhao, J. Zhang and J. Xu, Synthesis of highly surface-textured ZnO thin films by aerosol assisted chemical vapour deposition, Cryst. Eng Commn, 16 (2014) 7062.
266. Mirzaei, S. Park, G.J. Sun, H. Kheel, C. Lee, CO gas sensing properties of $In_4Sn_3O_{12}$ and TeO_2 composite nanoparticle sensors, J. Hazard. Mater. 305 (2016) 130–138.
267. Mirzaei, M. Bonyani, S.G. Leonardi, K. Janghorban, B. Hashemi, G. Neri, Highly stable and selective ethanol sensor based on Fe_2O_3 nanoparticles prepared by Pechini sol–gel method, Ceram. Int. 42 (2016) 6136–614416.